University of Southampton Research Repository

UNIVERSITY OF SOUTHAMPTON

FACULTY OF PHYSICAL SCIENCES AND ENGINEERING
ELECTRONICS AND COMPUTER SCIENCE

An Investigation into Electrical Degradation Mechanisms within Air-Filled Cavities in Solid Dielectric Materials

by

Thanarat Tanmaneeprasert

Thesis for the degree of Doctor of Philosophy

October 2018

UNIVERSITY OF SOUTHAMPTON

ABSTRACT

FACULTY OF PHYSICAL SCIENCES AND ENGINEERING
ELECTRONICS AND COMPUTER SCIENCE

Doctor of Philosophy

An Investigation into Electrical Degradation Mechanisms within Air-Filled Cavities in Solid Dielectric Materials

by Thanarat Tanmaneeprasert

Degradation and failure mechanisms in electrical insulation systems (EIS) in high voltage apparatus are not only caused by the thermal and mechanical stresses but also by the electrical stress during operational service. Imperfections in terms of cavities, craters, contaminants and electrical trees might seriously affect in insulation material of HV equipment due to the changes in microstructural levels at these defects under the enhancement of electric fields. Air-filled cavities embedded in solid dielectric material have been considered to be one of the most complicated issues that partial discharge (PD) activity plays an important role, which induces progressive deterioration processes in the cavity from localised erosion to complete failure. Phase-resolved partial discharge (PRPD) analysis is an effective condition monitoring tool for diagnosing the identifiable stages of degradation mechanisms in the relationship between PD characteristics and morphological changes in an air-filled cavity within the insulation.

The main aim of this thesis is to experimentally investigate the progressive degradation mechanisms within an air-filled cavity embedded in polymers by PD analysis. The samples used in the PD experiment are made from two different shaped cavities embedded in solid polymers regarding a cylindrical flat-shaped cavity and a spherical-shaped cavity. Based on the results, the recognisable variation in PRPD patterns and PD statistical quantities can be directly linked to distinguish the progressive levels of localised erosion on the surface wall inside an enclosed cavity in terms of surface erosion, erosion depth, electrical tree growth and upcoming failure. Interestingly, the results also show that the distinct PD characteristics can be analysed to accurately validate the presence of corrosive by-products regarding micro-craters and electrical tree initiation within the cavity wall before the treeing growth progressively propagates towards the whole dielectric between parallel electrodes, leading to total failure. The findings from these studies are further examined to explore the microscopic structure on the cavity surface due to accelerated ageing processes by various analytical techniques of microanalysis instruments used for additional prognoses in terms of physical, thermal and chemical properties. In particular, the noticeable PRPD patterns and PD diagnostic quantities, i.e. the average apparent charge, the maximum apparent charge and the average number of PDs per cycle are reproduced through a PD model with good agreement between measurement and simulation results.

Contents

Declaration of Authorship

I, Thanarat Tanmaneeprasert, declare that the thesis entitled *an Investigation into Electrical Degradation Mechanisms within Air-Filled Cavities in Solid Dielectric Materials* and the work presented in this thesis are my own, and has been generated by me as the result of my own original research. I confirm that:

1. This work was done wholly or mainly while in candidature for a research degree at this University;
2. Where any part of this thesis has previously been submitted for a degree or any other qualification at this University or any other institution, this has been clearly stated;
3. Where I have consulted the published work of others, this is always clearly attributed;
4. Where I have quoted from the work of others, the source is always given. With the exception of such quotations, this thesis is entirely my own work;
5. I have acknowledged all main sources of help;
6. Where the thesis is based on work done by myself jointly with others, I have made clear exactly what was done by others and what I have contributed myself;
7. Parts of this work have been published as conference proceedings, colloquium presentations and journal papers:

- T. Tanmaneeprasert, P. L. Lewin, and J. A. Hunter. Influence of internal discharges in a cavity within polymeric insulating material caused by partial discharge mechanisms. IEEE Conference on Electrical Insulation and Dielectric Phenomena (CEIDP), Ann Arbor, USA, 18 - 21 October 2015, pp. 342-345.
- T. Tanmaneeprasert and P. L. Lewin. The use of partial discharge analysis for the diagnosis of electrical ageing in polymeric insulation containing cavities. IEEE Electrical Insulation Conference (EIC), Montreal, Canada, 19 – 22 June 2016.
- T. Tanmaneeprasert and P. L. Lewin. Investigation into accelerated ageing and failure mechanisms of cavities in polyethylene materials using partial discharge techniques. IEEE Condition Monitoring and Diagnosis (CMD), Xi'an, China, 25-28 September 2016.
- T. Tanmaneeprasert and P. L. Lewin. Electrical treeing and ageing characteristics in cavities of low-density polyethylene dielectrics on partial discharge measurements. IEEE Conference on Electrical Insulation and Dielectric Phenomena (CEIDP), Toronto, Canada, 16 - 19 October 2016.
- T. Tanmaneeprasert, P. L. Lewin and G. Callender. Analysis of degradation mechanisms of silicone insulation containing a spherical cavity using partial discharge detection. IEEE Electrical Insulation Conference (EIC), Baltimore, USA, 11 – 14 June 2017.

- T. Tanmaneeprasert, P. L. Lewin and G. Callender. Measuring and simulating partial discharge activity in a spherical cavity during electrical ageing processes. IEEE International Conference on Dielectrics (ICD), Hungary, 1-5 July 2018.
- T. Tanmaneeprasert, P. L. Lewin and G. Callender. Electrical tree growth by partial discharges within a spherical cavity under accelerated life tests. Universities High Voltage Network (UHVnet) Colloquium, Winchester Guildhall, UK, 15-16 January 2018.
- T. Tanmaneeprasert, P. L. Lewin and G. Callender. Investigation into electrical deterioration mechanisms of surface erosion and erosion depth by partial discharges within a spherical cavity under electrical ageing test. IEEE Transactions on Dielectrics and Electrical Insulation, 2018. (Submitted)
- T. Tanmaneeprasert, P. L. Lewin and G. Callender. Analysis of micro-craters and electrical tree initiation mechanisms by partial discharges within a spherical cavity under accelerated ageing processes. IEEE Transactions on Dielectrics and Electrical Insulation, 2018. (In draft)
- G. Callender, T. Tanmaneeprasert and P. L. Lewin. Simulating partial discharge activity in a cylindrical void using a model of plasma dynamics. Journal of Physics D: Applied Physics, 2018. (Submitted)

Signed: ....

Date: ....

Acknowledgements

Firstly, I would like to express my sincerest appreciation to my first supervisor: Prof. Paul Lewin for his supervision, opportunity, support, encouragement, and kindness throughout my PhD journey and also extends to my second supervisor: Dr Jack Hunter for his supervision, guidance and kindness during my first year.

I would also like to express my sincere thanks to my thesis committee: Prof. Alun Vaughan, Dr Thomas Andritsch and Prof. John Fothergill for their invaluable advice and comments to improve this research.

Many thanks to Dr George Callender for his contribution, discussion and suggestion regarding a PD model in Matlab and simulation data in Comsol.

My thanks also to many people within the Tony Davies High Voltage Laboratory group during my study, especially, Dr Demetres Evagorou for his help and guidance at the beginning for the experimental set-up, Dr Ian Hosier, Dr Celia Yeung, Dr James Pilgrim, Dr Matt Praeger and Dr Suvi Virtanen for their technical expertise with training and advice, Mr Neil Palmer, Mr Brian Rogers, Mr Mike Smith, Mr Michael Hickey, Mr Ian Virtanen, Mrs Liz Tillotson and Dr Nik Hakimi Bin Nik Ali for their technical support and also goes to Mr Alistair Clark for his training and assistance using scanning electron microscopy coupled with energy dispersive X-ray spectroscopy at the university's chemistry faculty.

A special acknowledgement goes to Rajamangala University of Technology Phra Nakhon, Thailand to give me an opportunity to enhance my study in a PhD degree and Ministry of Science and Technology of Thailand for providing a scholarship. My thanks is also extended to Asst. Prof. Dr Komson Petcharaks and Dr Channarong Banmongkol at Chulalongkorn University, Thailand for their advice and recommendation letters for applying a PhD program in electronics and computer science at the University of Southampton.

Last but not least, I would like to thank my parents for their unconditional love and all support.

Nomenclature

A_{dt}	Surface area at the emitting point (mm^2)
A_e	Electron emission at the surface area (mm^2)
A'	Constant parameter (kV/kPa·m)
B_i	Ionisation parameter in the gas ($m^{1/2}Pa^{1/2}$)
B'	Constant parameter (kV)
C_d	Rate of chemical reactions for evaluating degradation processes
C_i	Ionisation parameter in the gas ($m^{1/2}Pa^{1/2}$)
C'	Constant parameter
D_{dis}	Dissociating half of CH bonds of the cavity surface thickness (mm)
E	Electric field ($kV\cdot mm^{-1}$)
E_B	Electric breakdown ($kV\cdot mm^{-1}$)
E_{cav}	Electric field inside a cavity ($kV\cdot mm^{-1}$)
E_{cav0}	Electric field inside a cavity without the surface charge ($kV\cdot mm^{-1}$)
E_{ch}	Electric field along a channel by the streamer discharge ($kV\cdot mm^{-1}$)
E_{cr}	Critical electric field for a self-sustained discharge in the gas ($kV\cdot mm^{-1}$)
E_e	Electric field due to the surface emission ($kV\cdot mm^{-1}$)
E_{inc}	Inception electric field in a cavity ($kV\cdot mm^{-1}$)
E_o	Background electric field ($kV\cdot mm^{-1}$)
E_q	Electric field due to dipolar charges on the cavity surface ($kV\cdot mm^{-1}$)
E_{res}	Residual electric field ($kV\cdot mm^{-1}$)
ΔE	Electric field collapse across a cavity ($kV\cdot mm^{-1}$)
F_{eff}	Fraction of hot electrons damaging chemical bonds of the polymer surface
F_{hot}	Fraction of hot electrons impinging chemical bonds of the polymer surface
F(c)	Ageing function of insulation material
$F(c_F)$	Ageing function of insulation material after failure
$F(t_B)$	Failure probability (%)

L_A	Lifetime rate
L_o	Initial lifetime
L_{cr}	Lifetime for the formation at localised erosion
L'	Cavity thickness (m)
K_B	Scale parameter of the Weibull cumulative distribution
K_d	Dimensionless factor
M_o	Constant factor of dielectric material
N_{CH}	Number of CH bonds in the damaged zone
N_{dt}	Number of detrappable charges on the cavity surface
$\dot{N}_e$	Initial electron generation rate (s^{-1})
$\dot{N}_{erad}$	Electron emission rate of the radiative ionisation (s^{-1})
$\dot{N}_{ewall}$	Electron emission rate on the cavity surface (s^{-1})
H_o	Activation energy for chemical reactions occurring in dielectric material
p	Pressure (kPa)
P'	gas pressure inside a cavity (kPa)
R_{dis}	Rate of progressive damage on the cavity surface (mm)
R_{el}	Rate of electrons colliding the polymer surface
R_o	Gas constant
S_d	Total length of all treeing branches (mm)
S_e	Surface charge emission on the cavity surface ($C{\cdot}m^{-3}$)
T_{az}	Angle of treeing initiation in the Z-axis (degree)
T_c	Crystallisation temperature (°C)
T_d	Treeing length from an initial point (mm)
T_g	Glass transition temperature (°C)
T_L	Treeing length (mm)
T_m	Melting temperature (°C)
T_n	Average length of treeing channels (mm)

T_p	Intersection of temperature between TGA and DSC curves (°C)
T_w	Treeing width (mm)
U_{app}	Applied voltage amplitude (kV)
U_{inc}	Applied inception voltage amplitude (kV)
d_c	Cavity diameter (mm)
d_{cr}	Critical levels of eroded depth on the cavity surface by the enhancement of electric fields (mm)
d_h	Cavity height (mm)
d_L	Fractal dimension of branched and bushed trees
d_m	Dielectric material in a thickness (mm)
e	Electric charge by electrons (C)
f_c	Field enhancement factor in a cavity
f(t)	Function of time dependence by the emission of trapped electrons on the cavity surface
g(E)	Function of field dependence by the emission of trapped electrons on the cavity surface
k_B	Boltzmann constant ($J{\cdot}K^{-1}$)
q_o	Transferred charge by a PD event (pC)
q_s	Dipolar charge on the cavity surface (pC)
q'	Induced charge or apparent charge (pC)
r_a	Cavity radius in the parallel axis of the background field (mm)
r_b	Cavity radius in the perpendicular axis of the background field (mm)
r_c	Cavity radius (mm)
t	Time (s)
t_A	Ageing time (s)
t_B	Time to breakdown (s)
t_{ch}	Time of treeing channel propagation (s)
t_{dis}	Time of dissociating half of CH bonds on the cavity surface thickness (s)
t_F	Time to failure (s)
Λ_o	Velocity coefficient of chemical processes

β_B	Shape parameter of breakdown
β_t	Shape parameter of failure
β_E	Shape parameter of breakdown field
ε_o	Relative permittivity of vacuum
ε_r	Relative permittivity of dielectric material
ε_c	Relative permittivity inside a cavity
ε_{PE}	Relative permittivity of polyethylene material at 50 Hz
ε_{Si}	Relative permittivity of silicone material at 50 Hz
ε_T	Relative permittivity of electrical tree growth
κ_s	Surface conductivity (S)
η	Gas attachment coefficient
η_o	Voltage endurance coefficient
ν	Order of chemical reactions
υ_o	Phonon frequency (cm^{-1})
γ	Ionisation parameter of air
α	Gas ionisation coefficient
α_B	Scale parameter of breakdown
Φ_e	Effective work function (eV)
Φ_{rad}	Flux density of radiative ionisation ($J\cdot m^{-2}\cdot s^{-1}$)
$\Delta\Phi$	Difference of heat flow rates ($W\cdot m^{-2}$)
$\nabla\lambda_o$	Gradient of dimensionless scalar field

Abbreviations

AC	Alternating current
AFM	Atomic force microscopy
Al	Aluminium
Au	Gold
BSE	Back-scatter electrons
CCD	Charge-coupled device
DSC	Differential scanning calorimetry
EDX	Energy dispersive X-ray
EPR	Ethylene propylene rubber
EPDM	Ethylene propylene diene monomer
FEA	Finite element analysis
FTIR	Fourier-transform infrared spectroscopy
GC	Gas chromatography
HV	High voltage
IEC	International electrotechnical commission
K	Potassium
LDPE	Low-density polyethylene
N	Nitrogen
Na	Sodium
O	Oxygen
PD	Partial discharge
PDEV	Partial discharge extinction voltage
PDIV	Partial discharge inception voltage
PDMS	Polydimethylsiloxane
PE	Polyethylene
PET	Polyethylene terephthalate

PP	Polypropylene
PRPD	Phase-resolved partial discharge
PVC	Polyvinylchloride
RMS	Root mean square
SBFSEM	Serial block-face scanning electron microscopy
SE	Secondary electrons
SEM	Scanning electron microscope
Si	Silicon
SPMDs	Swarming pulsive micro-discharges
Ta	Tantalum
TGA	Thermogravimetric analysis
TDHVL	Tony davies high voltage laboratory
XCT	X-ray computed tomography
XLPE	Cross-linked polyethylene
XPS	X-ray photoelectron spectroscopy

Chapter 1 Introduction

Polymers are important materials used for many parts in high voltage insulators of the electrical power apparatus [1-3]. Although these polymers have generally been designed to withstand the physical environment in terms of electrical, thermal and mechanical stresses, failure still happens prior to their design life expectancy [2-5], which might be caused by the appearance of unavoidable defects embedded in dielectric material, i.e. cavities, cracks and contaminants [5-7]. Air-filled cavities within solid insulation might be formed during the manufacturing process and lead to a decrease of insulation performance during operational service of HV equipment [5, 8-10] because the enhancement of electric fields inside the cavity is higher than the surrounding insulation [6, 11]. An understanding of progressive deterioration mechanisms within the cavity from localised erosion to total failure, which is driven by partial discharge (PD) activity, is necessary for providing a prognosis of the degradation stages before an upcoming failure [11-14]. PD detection has been used as an effective condition monitoring tool for diagnosing deterioration processes due to defects in insulation for more than a half-century [15-16]. The classification of localised sites such as internal discharges, treeing discharges, corona discharges and surface discharges can be distinguished by PD analysis [17-18]. In particular, the electrical discharges in a cavity between parallel electrodes are defined as [19]: “partial discharges (PDs) in cavities or at the edges of conducting inclusions in solid or liquid insulation. The cavity may be entirely enclosed in insulation, or it may be covered on one side by a conductor”.

1.1 Research motivation

A number of researches were undertaken to investigate PD activity induced degradation processes caused by a cavity embedded in solid dielectric materials [20-27]. The electrical discharge signals from two different shaped voids, i.e. flat-shaped and square-shaped voids embedded in dielectric materials as a function of various void sizes were monitored to diagnose the relationship between optical discharge images and pulse shapes related to morphological changes on the void surface during elapsed time of ageing. The observed differences in terms of PD magnitudes and shaped discharges can be distinguished to three consecutive stages of localised degradation on the void surface regarding streamer-like, Townsend-like and pit mechanisms [20, 28-29]. The stages of deterioration processes on the cavity wall by PD activity were interpreted to associate them with phase-resolved partial discharge (PRPD) patterns and PD statistical quantities [30-35]. The typical characteristics of internal discharges in a cavity were distinguished into two typical shapes in terms of rabbit-like and turtle-like patterns [30-32, 36]. A phenomenon of electrical tree growth from the cavity wall embedded in solid insulation by PD activity has been considered to be one of the most important causes for an upcoming failure of the whole insulation [37]. Most investigations of treeing behaviour in polymers have commonly used between needle and plate electrodes embedded in solid insulation to form progressive treeing from initiation until breakdown [34, 38-39]. One of the recognisable PD detection methods for analytical techniques of electrical tree growth links to the PD characteristic of a wing-like pattern with the appearance of minimum magnitude discharges, which is associated with the mechanism of swarming pulsive micro-discharges (SPMDs) [40-42].

1.2 Contributions of this thesis

The main contributions of this thesis are to develop a clear understanding of the progressive degradation mechanisms within an air-filled cavity embedded in polymers by PD analysis. In particular, literature reviews have indicated that a hypothesis of electrical tree initiation from an enclosed cavity has not been evidenced experimentally. The two substantial objectives of this research are reported in summary:

I. Analysis of degradation mechanisms by PD activity within a cylindrical flat-shaped cavity in polyethylene material:

PD activity of each sample containing a cylindrical flat-shaped cavity in the centre of the middle layer embedded in three layers of low-density polyethylene (LDPE) film was investigated to analyse the PD quantities from twenty test samples in terms of the partial discharge inception voltage (PDIV), the average number of PDs per cycle and the average apparent charge. All of these samples were further investigated PD characteristics over an accelerated ageing test. Also, the evolution of PRPD patterns can be distinguished the states of the cavity formation from localised erosion to total failure. Various techniques of microanalysis were used to find out the changes in the morphological cavity due to the effect of the ageing process in terms of dielectric, thermal and chemical properties, i.e. optical microscopy, dielectric spectroscopy, differential scanning calorimetry (DSC), Fourier-transform infrared spectroscopy (FTIR), scanning electron microscopy (SEM) and energy-dispersive X-ray (EDX) spectroscopy. Moreover, PD characteristics of distinct PRPD patterns and PD diagnostic quantities, i.e. the average apparent charge and the average number of PDs per cycle were examined to establish if they were useful indicators of degradation processes from visible evidence in terms of the localised erosion site, electrical tree growth and upcoming failure.

II. Analysis of degradation mechanisms by PD activity within a spherical cavity in silicone rubber material:
PD activity of each sample containing different spherical cavity diameters in the centre of silicone material was investigated to analyse the PD quantities from thirty-five test samples in terms of the PDIV, the average number of PDs per cycle, the average apparent charge, the inception electric field and pressure, where the simulation results of the average apparent charge as a function of different cavity diameters were compared with the measurement results. All of these samples were further investigated the evolution of PD characteristics due to the accelerated electrical ageing. Comparison of PRPD patterns and φ-q-n plots as a function of different voltage amplitudes was presented in both

measurement and simulation results. Moreover, PD characteristics from two samples containing different cavity sizes were conducted to compare the measured PRPD patterns and the statistical quantities, i.e. the average apparent charge, the maximum apparent charge and the average number of PDs per cycle. Furthermore, the deposited by-products on the cavity surface due to the accelerated ageing were further analysed by the chemical technique of Raman spectroscopy. Another investigation into three samples containing different cavity diameters was undertaken to reveal visible evidence of erosion depth inside the enclosed cavity in vertical cross-section views caused by loss of hydrophobicity due to the electrical ageing processes. Thermogravimetric analysis (TGA) was used for diagnosis of the thermal property of test samples at various ageing times, where the presence of corrosive by-products on the cavity surface by PD activity was analysed. Also, the dielectric property of test samples at different cavity sizes was measured by the real relative permittivity and the tan delta at 50 Hz. Furthermore, the recognisable variation in noticeable PD characteristics and PD diagnostic quantities can be analysed to validate a direct link of the localised erosion sites regarding the micro-craters and the electrical tree initiation on the cavity surface. The findings from these studies differed considerably from the PD source of typical cavity discharges in regular issues, i.e. rabbit-like and turtle-like patterns. Notable evidence from corrosive by-products was further examined to explore the microscopic levels by analytical techniques of scanning electron microscopy (SEM) and energy dispersive X-ray (EDX) systems. The result indicates that the chemical compound of nitrogen inside a cavity plays a key role, resulting in a large amount of detectable nitrogen at the localised sites of both micro-craters and electrical tree initiation, whereas nitrogen was undetectable in bulk of a virgin cavity. The variation in PRPD patterns was distinguished the morphological changes from localised erosion to total failure, which visible evidence of growing protrusions on the outer cavity surface can be correlated to PD statistic quantities, i.e. the average apparent charge, the maximum apparent charge and the average number of PDs per cycle, the distinct PRPD patterns were also reproduced through a PD model with good agreement between measurement and simulation results.

1.3 Thesis outline

A brief overview of contents of this thesis is divided into six chapters as follows:

- Chapter 1 gives an introduction based on the interrelated background research, the motivation and contributions for this research.
- Chapter 2 details the fundamental background, literature reviews and theoretical physics of discharge mechanisms within a gas-filled cavity in solid dielectric materials due to PD activity.
- Chapter 3 describes the preparation of test samples produced by two different shaped cavities regarding a cylindrical flat-shaped cavity and a spherical-shaped cavity embedded in various polymers, the methodologies and procedures of the PD experiment set-up and the accelerated

ageing test, including microanalysis techniques for additional diagnosis by scanning electron microscopy (SEM) and energy dispersive spectroscopy X-ray (EDX) instruments.

- Chapter 4 presents the experimental results of a cylindrical flat-shaped cavity embedded in polyethylene material regarding PDIV and ageing levels, the variation in PRPD patterns related to the cavity formation and various techniques used in analysis of dielectric, thermal and chemical properties for characteristic changes of test samples due to ageing processes. Moreover, the evolution of PRPD patterns related to degradation mechanisms on the cavity surface in terms of the localised erosion site, the electrical tree growth and the upcoming failure.
- Chapter 5 presents the measurement and simulation results of a spherical-shaped cavity embedded in silicone rubber of PD characteristics at various conditions in terms the PDIV as a function of various cavity diameters, the accelerated ageing test as a function of different cavity diameters, different voltage amplitudes and various ageing times. Moreover, the distinct PRPD patterns and PD statistical quantities related to visible evidence of surface erosion and erosion depth on the wall inside an enclosed cavity, including analysis of thermal and dielectric properties. Furthermore, the evolution of PRPD patterns and PD diagnostic quantities related to the localised erosion sites regarding the micro-craters and the electrical tree initiation on the cavity surface, including microanalysis techniques of SEM and EDX systems.
- Chapter 6 discusses the overview, conclusions and future work resulting from this thesis.

Chapter 2 Degradation Mechanisms in a Cavity within Solid Dielectric Materials

The beginning of this chapter introduces the fundamental classification of PD activity that involves a brief overview of various PD phenomena. The theoretical foundation of physical discharges inside an air-filled cavity is considered based on the past reported studies in the literature. Degradation processes within a cavity in solid dielectric materials caused by PD mechanisms are discussed in relation to the electrical ageing and life models, leading to the growth of electrical tree initiation from the cavity. A summary of the chapter is detailed in the last section.

2.1 A fundamental classification of partial discharges

PD detection is an effective tool for the diagnosis of localised defects within dielectric material of HV equipment. Generally, discharge mechanisms between parallel electrodes can be distinguished into four types: internal discharges, treeing discharges, corona discharges and surface discharges [43] as shown in Figure 2.1. The phenomenon of internal discharges inside a gas-filled cavity in solid dielectric material is the main focus of this chapter, whereas other types of discharges are also briefly discussed.

Internal discharges usually occur at weak points within solid insulation material such as air-filled cavities, where the electrical breakdown strength of air is lower than the surrounding dielectric [44-45]. The electric field inside a cavity depends on various factors, i.e. size, shape, location and material [46]. The degradation mechanisms within a cavity by PD activity gradually deposit chemical by-products on the cavity surface, i.e. oxalic acid and liquid droplets, which form conducting layers at the localised erosion site to complete failure of the insulation [44]. The phenomenon of electrical tree initiation from the cavity wall can be identified as the significant signal before an upcoming failure that the progressive propagation of treeing growth is induced by the enhancement of local electric fields at deposited by-products on the cavity surface [47-48]. The progressive levels of tree growth in dielectric material depended on circumstances of applied voltage magnitudes and elapsed time [49-51]. In the case of surface discharges or surface tracking, this discharge from a pointed conductor can occur along the interface or surface boundaries of dielectric material in gases or liquid medium [52-53]. Otherwise, corona discharges usually occur around a sharp conductor in air or liquid under a sufficiently high electric field [44, 54-55].

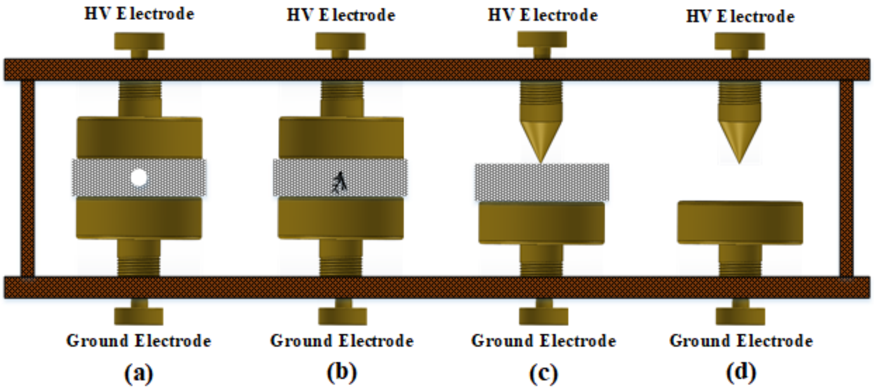

Figure 2.1: Classification of discharge mechanisms: (a) internal discharges, (b) discharges by electrical trees, (c) surface discharges and (d) corona discharges.

All of these discharges can cause degradation processes until complete failure in solid dielectric material between two parallel conductors under electrical stresses as shown in Figure 2.2. For example, when internal discharges dominate electrical degradation within a cavity, the chemical by-products are formed by localised erosion and progressed to pits or cracks corresponding to an increase in dielectric loss in the dielectric insulation. Subsequently, the propagation of tree growth takes place and eventually leads to failure [56-58].

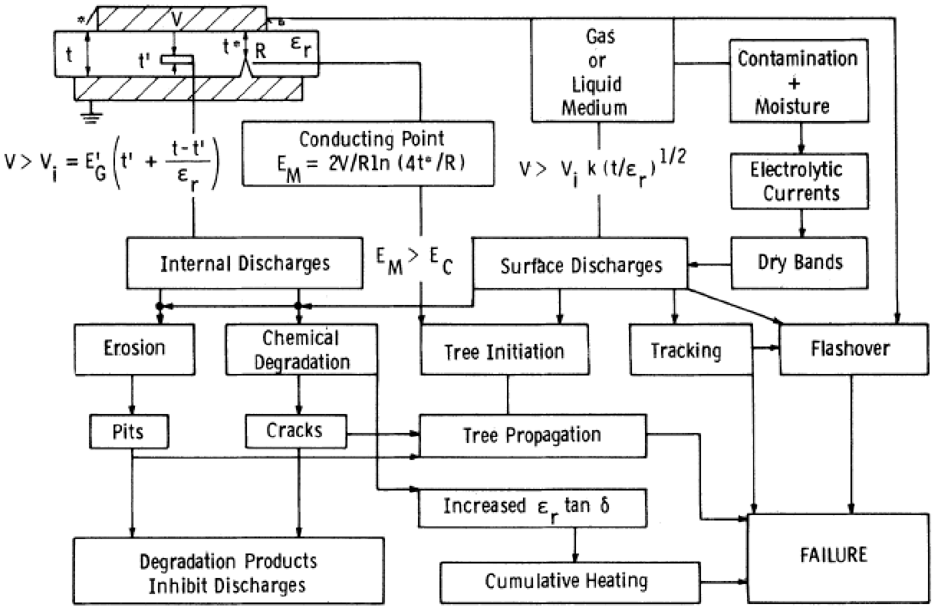

Figure 2.2: Schematic diagram of failure by various discharge mechanisms [17].

2.2 Gaseous discharge mechanisms in solid insulation

This section considers the partial discharge mechanisms related to a gaseous cavity within solid insulation.

2.2.1 Paschen’s law

Paschen’s curve for air at 1 atm illustrates the relationship between the breakdown voltage as a function of gas pressure and gap length between parallel electrodes [59-61]. The inception voltage can be estimated by the applied voltage level across a small gap to exceed a minimum value for a PD occurrence as shown in Figure 2.3.

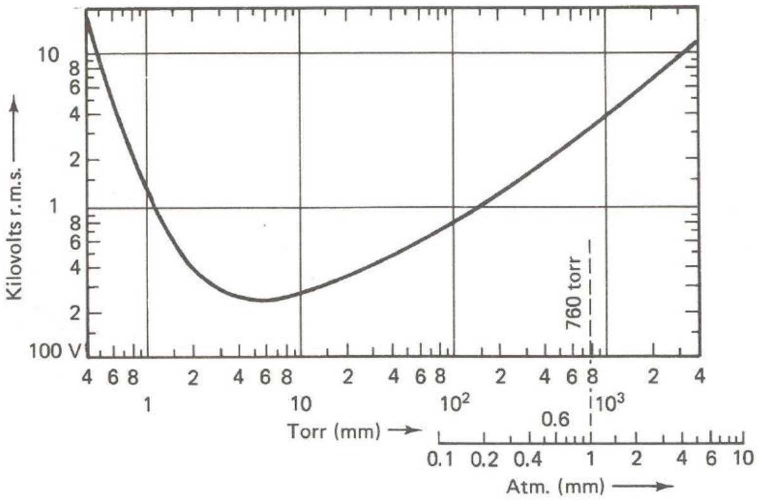

Figure 2.3: Paschen’s curve [59].

2.2.2 A single avalanche

A single avalanche in a cloud chamber is generated by ionisation processes as shown in Figure 2.4 (a). The collision of electrons produces positive and negative ions between parallel plate electrodes. Some electrons are emitted and released from the cathode electrode under a sufficiently high electric field. The front motion of electrons forms this mechanism and followed by the positive ions with a long tail toward the anode electrode. A distortion of localised electric field is produced during the electron avalanche in the gap. An actual single avalanche is shown in Figure 2.4 (b).

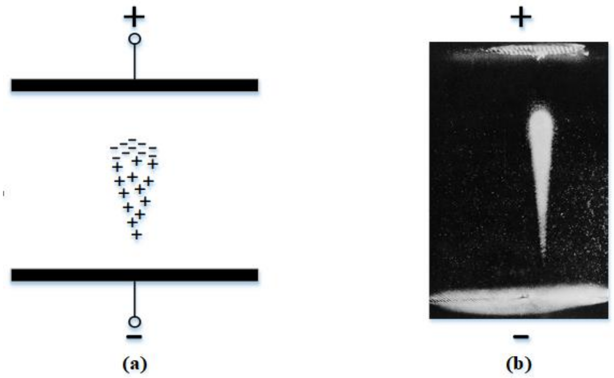

Figure 2.4: An electron avalanche: (a) the local distribution of electrons and positive ions and (b) photograph of an actual avalanche by Raether [62].

2.2.3 Townsend discharges

In the presence of a gas discharge between parallel plate electrodes, the initial electron can be generated by a detachment of background radiation from the cathode electrode [63]. An electron multiplication mechanism can generate an avalanche mechanism by electron collisions, this process is called primary electron avalanche of Townsend discharges as shown in Figure 2.5. The transition from non-self-sustained to self-sustaining discharges depends on the process of secondary electron avalanche to create a repetitive mechanism [64]. Therefore, there are two significant mechanisms to maintain for gas discharges that the initial electron avalanche is excited by a self-sustained high electric field to induce the ionisation process and the continuous mechanism by secondary ionisation processes [65].

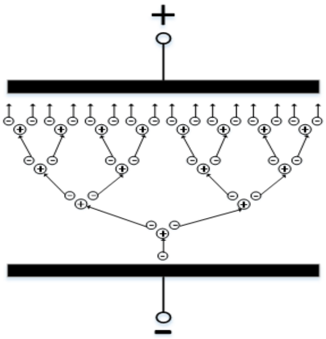

Figure 2.5: Development of an electron avalanche in uniform fields [67].

2.2.4 Streamer discharges

The steamer mechanism was established by Loeb and Meek [63] and Raether [62]. If an electron avalanche significantly grows, the high enhancement of local electric fields occurs with a separation between electrons and positive ions that high electric fields are formed ahead of the region of positive charge and a self-sustaining ionising wave propagates across the air gap as shown in Figure 2.6 (a). The wave is propagated by numerous secondary electron avalanches ahead of the wave providing seed charges as shown in Figure 2.6 (b). The secondary electron avalanches are generated by photoemission and secondary ionisation such that the streamer discharge occurs across the gap to form a conducting channel between two parallel electrodes as shown in Figure 2.6 (c).

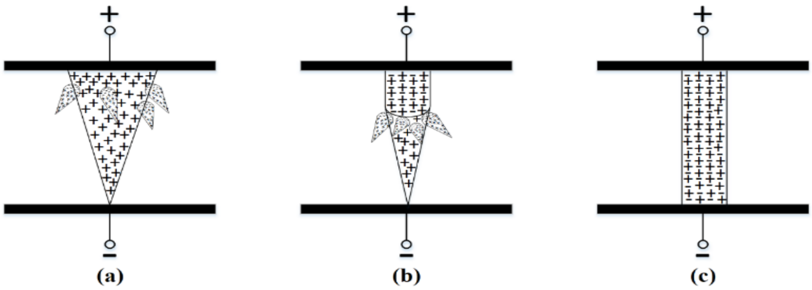

Figure 2.6: Transition from an electron avalanche to a streamer across the gap [66].

2.3 Discharge mechanisms inside a cavity

The theoretical background of partial discharges in a cavity associates various factors so that the variation in PD behaviour of a cavity in insulation can be determined by various factors such as gas pressure, inception field, shaped cavities, cavity sizes, locations, and materials as further detailed in this section. The occurrence of a PD event in a cavity depends on the fulfilment of two main conditions. Firstly, an initial electron must be produced to start an ionisation avalanche mechanism and secondly, the electric field in a cavity must exceed a minimal inception voltage of a self-sustained discharge [68-69]. For the generation of electron emission mechanism within a gas-filled cavity in solid dielectric material, the first electron production rate consists of radiative ionisation such as natural cosmic and gamma radiation or X-rays and electron emission from the cavity surface by a previous discharge. The first electron emission can be defined as [70]:

$$\dot{N}_{e} = \dot{N}_{erad} + \dot{N}_{ewall} \tag{2.1}$$

The rate of radiative ionisation is proportional to the cavity radius, which is determined as [70]:

$$\dot{N}_{erad} \propto \pi r_c^2 \Phi_{rad} \tag{2.2}$$

The rate of electron emission on the cavity surface is given by [70]:

$$\dot{N}_{ewall} \propto q_o f(t) g(E) \tag{2.3}$$

where r_c is the cavity radius, Φ_{rad} is the flux density of the ionising radiation, q_o is the transferred charge by a previous PD event, f(t) and g(E) are the functions of time and field dependence controlling the emission of trapped electrons on the cavity surface.

The first electron production can be emitted from the cavity surface by ion impact and photoionisation processes within the gaseous cavity. The rate of surface emission is also described by specific factors in terms of an effective work function, Φ_e, an emitting surface area, A_e, and a surface charge emission of detachment from the cavity surface, S_e that all of these parameters relate to the electric field at the localised emission is high sufficiently to release an electron on the surface dielectric material. Therefore, the rate of first electron emission can be expressed as [71]:

$$\dot{N}_{e} = \frac{A_e}{e} S_e \exp - \left[\frac{\Phi_e - \sqrt{eE_e/(4\pi\varepsilon_o)}}{k_B T} \right] \left(1 - \frac{\eta}{\alpha} \right) \tag{2.4}$$

where e is the electric charge by electrons, E_e is the electric field due to the surface emission, ε_o is the relative permittivity of vacuum, k_B is Boltzmann constant, T is temperature, η is gas attachment coefficient, and α is gas ionisation coefficient.

The surface charge emission of detachment from the cavity surface can be determined by [71]:

$$S_e = \upsilon_o e \frac{N_{dt}}{A_{dt}} \tag{2.5}$$

Where υ_o is the fundamental phonon frequency with an approximate value of 10^{13} to 10^{14} s^{-1}, e is the elementary charge, N_{dt} is the number of detrappable charges at a PD site, A_{dt} is the surface area at the emitting point.

Before a PD occurs as shown in Figure 2.7 (a), the deployment of dipolar charges along the cavity surface is induced by the local enhancement of the applied background field, E_o. When the electric field inside a cavity without the surface charge, E_{cav0} is less than the inception field, E_{inc}, prior to a discharge, the electric field is due to dipolar charges on the cavity surface from a previous PD event, E_q, and is initially opposed by the field of f_cE_o, where f_c is the factor of the field enhancement in the cavity, depending on the shaped cavity and the relative permittivity of dielectric material. Hence, the electric field inside a cavity, E_{cav} can be defined as [70-71]:

$$E_{cav} = f_c E_o + E_q \tag{2.6}$$

When a PD occurs as shown in Figure 2.7 (b), the electric field inside a cavity, E_{cav} rapidly drops to the residual field, E_{res}. Hence, the electric field drop inside a cavity, ΔE is the channel field of the streamer discharge based on the applied electric field until the discharge takes place and the local electric field from previous PD activity, the electric field collapse across a cavity due to discharges can be determined as [72]:

$$\Delta E = f_c E_o + E_q - E_{res} \tag{2.7}$$

The residual electric field inside the cavity, E_{res} is directly related to the electric field along the channel of the propagating streamer discharge, E_{ch}, which is proportional to the critical electric field of a self-sustained discharge in the gas, E_{cr}. Thus, the residual field can be defined as [72]:

$$E_{res} = E_{ch} = \gamma E_{cr} \tag{2.8}$$

where γ is the dimensionless factor for air, which is equal to 0.2 for a positive streamer and 0.5 for a negative streamer.

After a PD occurs as shown in Figure 2.7 (c), the charge movement along the cavity surface induces the surface conductivity and the surface charge decay [73]. The electric field due to dipolar charges on the cavity surface from a previous PD event, E_q can be determined as [72]:

$$E_q = \frac{q_s}{\varepsilon_o \pi r_b^2 \left[1 + \varepsilon_r (K_d - 1)\right]} \tag{2.9}$$

Where q_s is the dipolar charge on the cavity surface, r_b is the cavity radius in the perpendicular axis of the background field, ε_r is the permittivity of the surrounding dielectric, K_d is a dimensionless factor [71-72].

The inception electric field inside a cavity as shown in Figure 2.8, E_{inc} can be given by the criterion of streamer discharge mechanism that the applied field in a cavity must be exceeded the critical threshold of a self-sustained discharge as [72]:

$$E_{inc} = E_{str} = (E/p)_{cr} p \left[1 + \frac{B_i}{(2pr_a)^{C_i}} \right] \tag{2.10}$$

Where $(E/p)_{cr}$ is the pressure reduced critical field, B_i and C_i are the specific factors of ionisation processes in the gas, p is the gas pressure, r_a is the cavity radius in the parallel axis of the background field. For an air-filled cavity, the values of $(E/p)_{cr} = 25.2\ VPa^{-1}m^{-1}$, $B_i = 8.6\ Pa^{1/2}m^{1/2}$ and $C_i = 0.5$.

An increase in surface conductivity can occur during the charge deployment due to the conducting path across a cavity. The dipolar surface charge on the cavity surface, $\pm q_s$ can be expressed as [71-72]:

$$\pm q_s = \pi \varepsilon_o r_b^2 [1 + \varepsilon_r (K_d - 1)] \Delta E \tag{2.11}$$

Furthermore, the surface charge density of the charge deployment after a PD event increases the surface conductivity that the distribution of charge decay might be influenced from the diffusion inside a cavity or the deep trap in dielectric material. The rate of dipolar charge decay on the cavity surface can be given as [72]:

$$-\frac{dq_s}{dt} = (\pi/2) \kappa_s E 2 r_a \tag{2.12}$$

Where $E2r_a$ is the instantaneous potential drop along the cavity surface and κ_s is the surface conductivity, which has been obtained as 5×10^{-13} Siemens for a spherical cavity of diameter in the range of millimetres. It is assumed to be varying magnitudes with the range of 10^{-12} to 10^{-11} Siemens for an ageing cavity and 10^{-14} to 10^{-16} Siemens for a virgin cavity [72].

PD quantities from the positive and negative charges on the cavity surface can be detected by the transformation of PD signals from the localised site between parallel electrodes through the coupling device of PD measurement as shown in Figure 2.9. The induced charge or apparent charge can be given by [71-72]:

$$q' = -\frac{4}{3} \pi r_a r_b^2 \varepsilon_o \varepsilon_r K \Delta E \nabla \lambda_o \tag{2.13}$$

Where $\nabla\lambda_o$ is the gradient of dimensionless scalar fields, which the factor λ_o is the coupling PD signals from the localised cavity to the parallel electrodes.

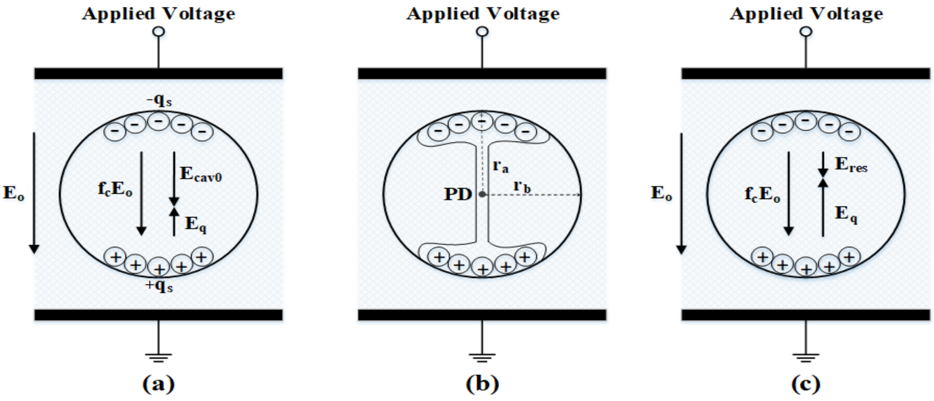

Figure 2.7: Schematic diagram of PD charge deployment on the cavity surface: (a) before a PD event, (b) during a PD event and (c) after a PD event [71].

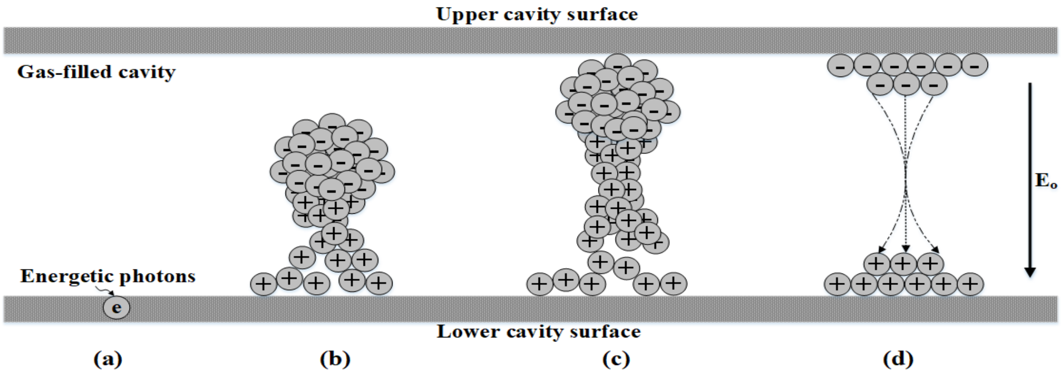

Figure 2.8: Discharge mechanisms within a gas-filled cavity: (a) the start of first electron production from the cavity surface, (b) the form of electrons and positive ions, (c) the movement of electrons and positive ions towards the upper cavity surface, and (d) the conducting channel by a streamer discharge [71].

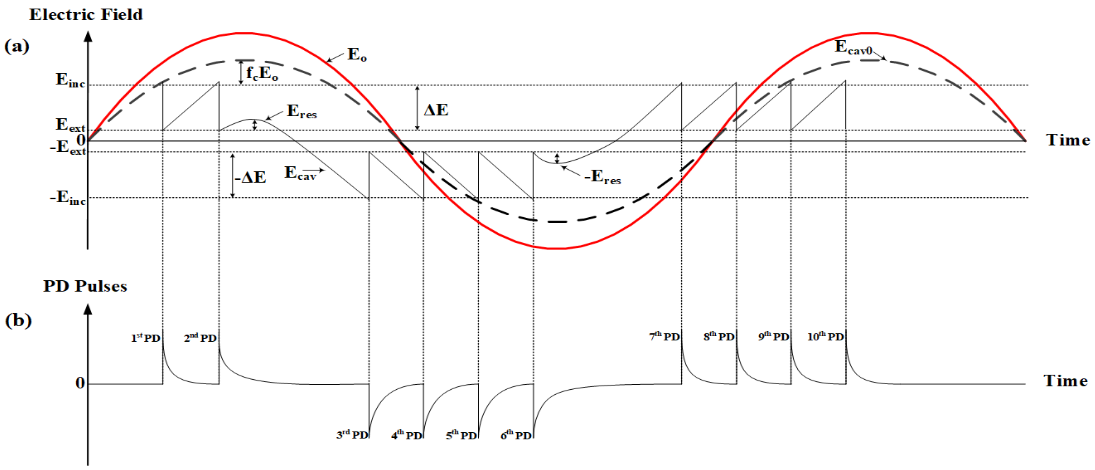

Figure 2.9: PD sequence within a cavity under an AC applied voltage as a function of time: (a) the waveform of electric fields and (b) PD pulses [59, 74].

To describe the concept of a current pulse across a small gap by PD measurement [75-76], the main elements of electrons and ions are considered such that the velocity of electrons in gas is much higher than that of other ions. Therefore, the pulse shape of a single discharge exhibits the waveform of a steep front with a short time period of just under 1 ns by the electronic portion and follows by its tail with a lower magnitude pulse in a longer time period of about 100 ns by the latter of ionic portion as shown in Figure 2.10.

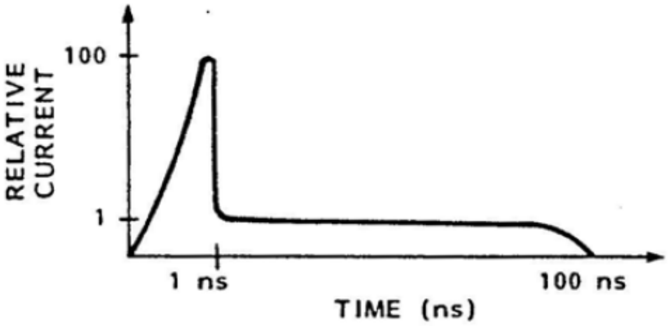

Figure 2.10: Principle shape of a current pulse across a small gap [76].

2.3.1 Surface charge decay

The accumulation of surface charge decay on the cavity wall gradually deposited by the consecutive PD events over a period of ageing, which increased the conductivity of gaseous compounds and decreased the electric field in the cavity [77-78]. Moreover, an amount of surface charge distribution by PD was examined regarding cavity sizes, shaped cavities [79] and variable pressure [80]. The measurement of surface conductivity related to various ageing times by PD was undertaken under the electrical stress for just over 900 h, where the surface conductivity in a cavity tended to increase with elapsed time of ageing [81]. An investigation into PD pulse mechanisms within the cavity can be distinguished two main types in terms of a streamer-like discharge and a Townsend-like discharge, which associated with the relationship between their PD pulse shape and amplitude. The evolution of discharge mechanisms from the streamer-like to Townsend-like can be formed the narrow pulse with the high magnitude discharge to the wide pulse with the low magnitude discharge due to an increase of the surface conductivity on the cavity wall and a decrease of the statistical time lag with elapsed time of ageing [82]. A discharge mechanism in a virgin cavity, the movement of charges decays on the cavity surface, which depends on the direction between the applied field inside a cavity without the surface charge decay, Ecav0 and the electric field inside a cavity, Ecav. After a previous PD event at the positive half-cycle of an alternating current source, the polarities of both local and applied fields are the same direction of the background field, Eo while the polarity of electric field due to the cavity surface, Eq is opposite the background field such that the distribution of charges move towards the polar cavity wall, resulting in an increased conduction along the cavity surface as shown in Figure 2.11(a). After a previous PD event at the negative half-cycle of an alternating current source, the polarities of both local and applied fields are the same direction of the background field while the field due to the surface charge remains unchanged, which the dipole charges move recombination on the cavity surface as shown in Figure 2.11(b).

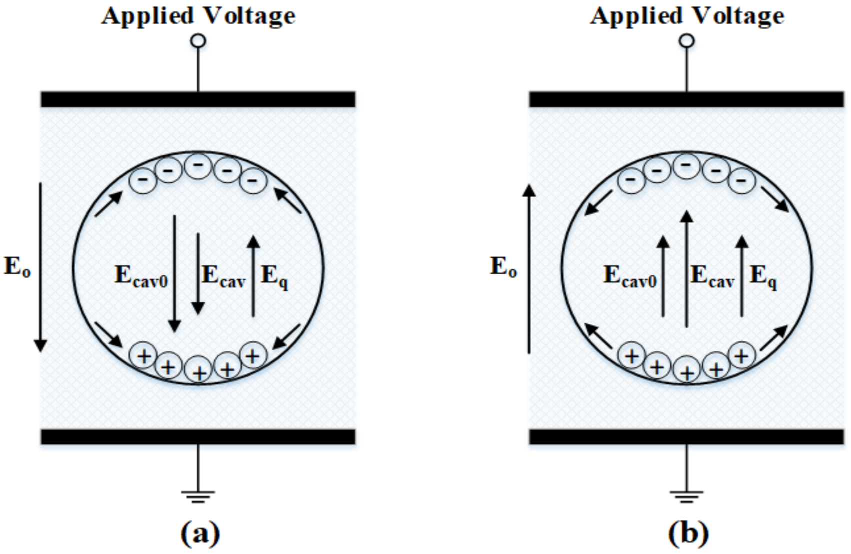

Figure 2.11: Directions of charge movements along the cavity surface: (a) the decay of surface charges at the positive half-cycle of an applied voltage and (b) the recombination of surface charges at the negative half-cycle of an applied voltage [83].

2.3.2 Influence of variation in gas pressure

The presence of PD activity in a cavity depends on two main mechanisms regarding an initial electron and a self-sustained high electric field at the local site. The PD characteristics are concerned various factors such as gas pressure [84-87], gas composites [88-89], applied field [86, 90], frequency [91-92], temperature [86, 93-96], shaped cavities [97-99], cavity sizes [96, 100], cavity locations [101-102] and dielectric materials [103-104]. The variation in gas pressure and gaseous elements within a cavity influences the changes of PD characteristics that the volume of gas pressure inside a spherical cavity can be measured by gas capture from a micro-puncture of the cavity wall and the identification of gaseous compounds using gas chromatography from the inner cavity. This approach obtained the gas composites such as nitrogen, oxygen, including a small volume of cyclohexene, dicarboxylic acid and moisture that the variation in gas pressure and nitrogen compound inside a cavity were investigated from different cavity sizes. A sample containing an air-filled cavity of diameter 8.2 mm after ageing was occupied with gas pressure of 0.71 bar and 97% of nitrogen while another sample embedded an air-filled cavity of diameter 7.9 mm after ageing was obtained by gas pressure of 0.76 bar and 90% of nitrogen [105]. Another investigation into the variation of gas pressure in a cavity related to the change of PRPD patterns as a function of ageing time was undertaken using polyethylene material of three layers containing a disc-shaped cavity diameter 5 mm in the middle layer with 2 mm in thickness. The variation in gas pressure within the cavity was measured by the movement of silicone oil in a cylindrical glass tube through a micro-puncture of the cavity wall during PD activity [32]. The result shows that the variation in gas pressure within a cavity can be divided into four stages as a function of ageing time as shown in Figure 2.12. The gas pressure rapidly dropped by 20% from 100% at the first stage and followed by a steep rise of 95% at the second stage. Subsequently, the trend slightly declined to just over 87% and suddenly increased before breakdown during the third-fourth stages respectively.

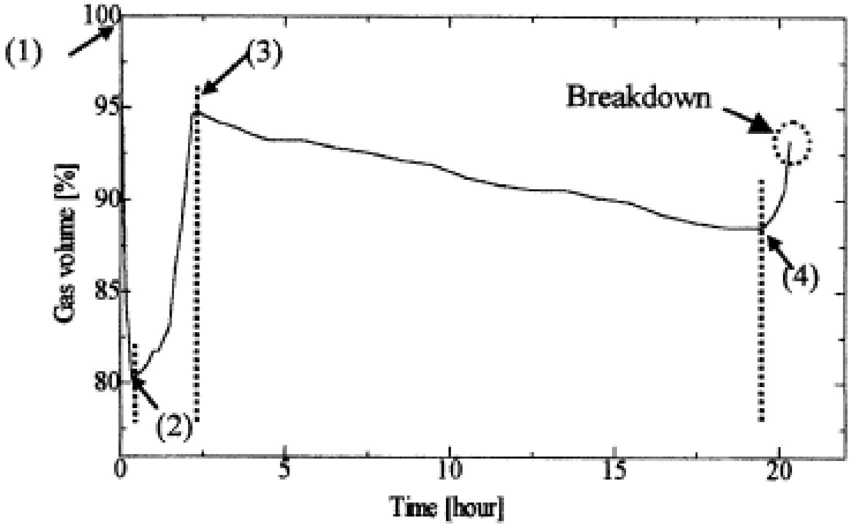

Figure 2.12: Variation in gas pressure within a cavity [32].

2.3.3 Electric field distribution within a cavity

The enhancement of electric fields within an air-filled cavity is higher than the surrounding insulation When the electric field inside a cavity exceeds the inception value, a discharge mechanism within a cavity occurs, leading to conductivity on the cavity surface after a PD event [106]. According to a detailed description [107], the electric field inside a cavity is dropped during a discharge mechanism. Referring to Figure 2.13 (a), the cavity turns into a non-conducting wall before a PD event while the cavity surface turns into a conducting wall after a PD event as shown in Figure 2.13 (b).

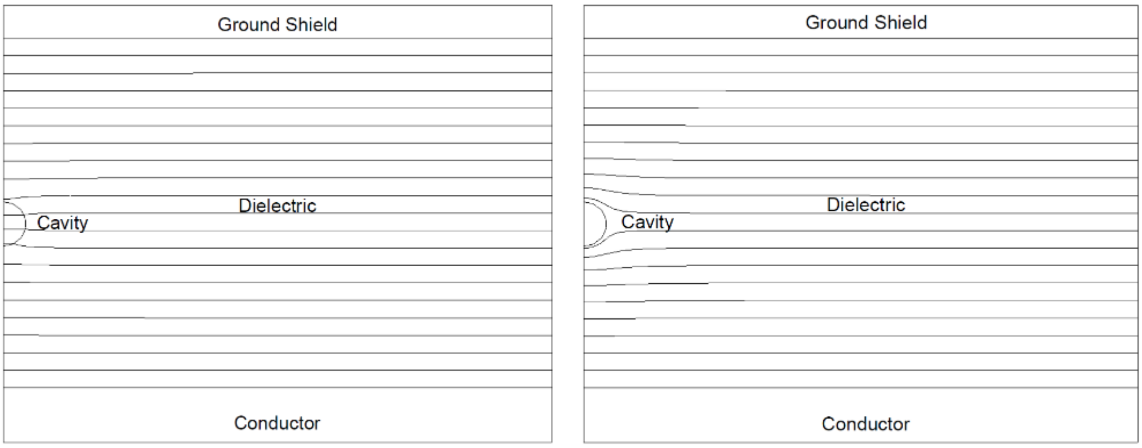

(a) (b)

Figure 2.13: Electric field distribution of a cavity embedded in cross-linked polyethylene (XLPE) material: (a) before a PD event and (b) after a PD event [107].

2.3.4 Influence of various cavity geometry

The electric field distribution in a cavity depended on various conditions, i.e. shape, location, thickness and diameter [108]. A comparison of different shaped cavities embedded in dielectric material, i.e. a cylindrical cavity and a spherical cavity was investigated the characteristic discharges related to the localised erosion sites on the cavity surface, including a calculation to find out the influence of various cavity geometry in terms of ellipses, cylinders and spheres [17]. An investigation into PD behaviour as a function of different shaped voids, i.e. ellipsoidal and spheroidal geometry was analysed using characteristic PD signals [109]. Furthermore, the inception field as a function of various shaped cavities within solid dielectric material between parallel plate electrodes was determined as reported in [59]. If a cylindrical flat-shaped cavity is a tall diameter in the parallel direction of electric fields, the field enhancement in the cavity tends to be equal to times the dielectric constant of the surrounding insulation as shown in Figure 2.14 (a). If a cylindrical flat-shaped cavity is a broad diameter in the perpendicular direction of electric fields, the field enhancement in the cavity tends to be equal to times the dielectric constant of the surrounding insulation as shown in Figure 2.14 (b). In a spherical-shaped cavity, the field enhancement in the cavity tends to be equal to 1.5 times the dielectric constant of the surrounding insulation as shown in Figure 2.14 (c).

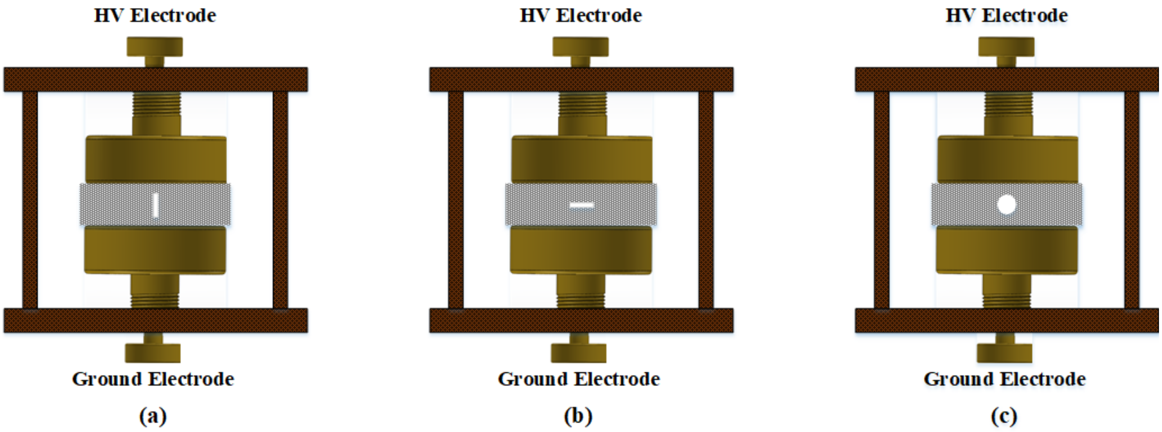

Figure 2.14: Various shaped cavities in solid insulation: (a) a tall flat-shaped cavity, (b) a broad flat-shaped cavity and (c) a spherical-shaped cavity.

2.3.5 Influence of electric field magnitudes in different cavity sizes

The induced charge from a cavity embedded in insulation material by PD activity is governed by the transformation of electric fields from the localised cavity to parallel electrodes. It is assumed that if an electric dipole by a PD event remains stable, some induced charges that can be detected with increasing the cavity lengths, which the enhancement of electric fields in the vertical direction at the localised site between the cavity surface and the surrounding dielectric material is proportional to increase in the cavity sizes [110] as shown in Figure 2.15.

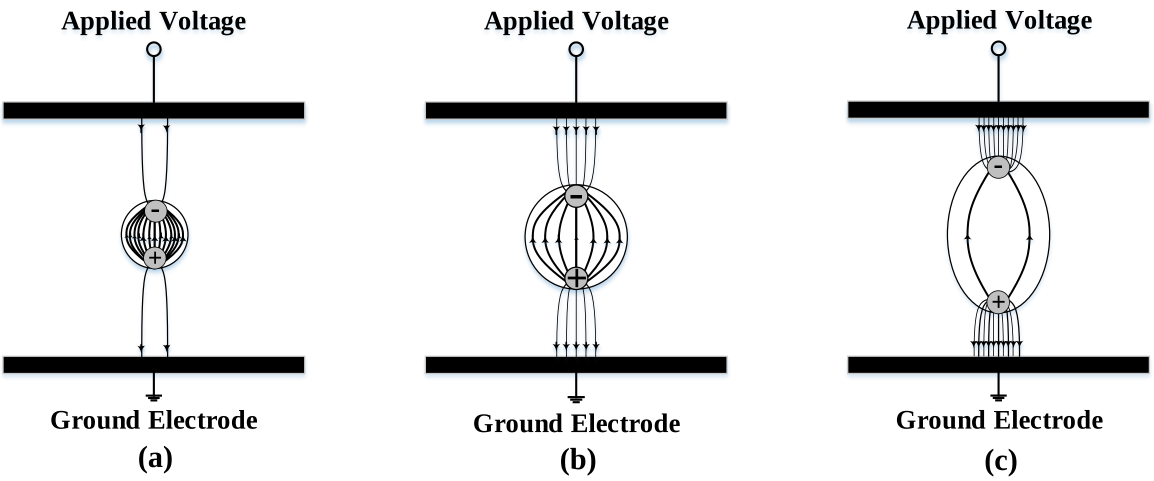

Figure 2.15: Electric field magnitudes as a function of different cavity sizes [111].

2.4 PD measurement

Electrical discharges are described by international electrotechnical commission (IEC) 60270 standard that do not entirely bridge through insulation material between parallel electrodes, which are well-known partial discharges [112]. The components used for the PD detection are shown in Figure 2.16.

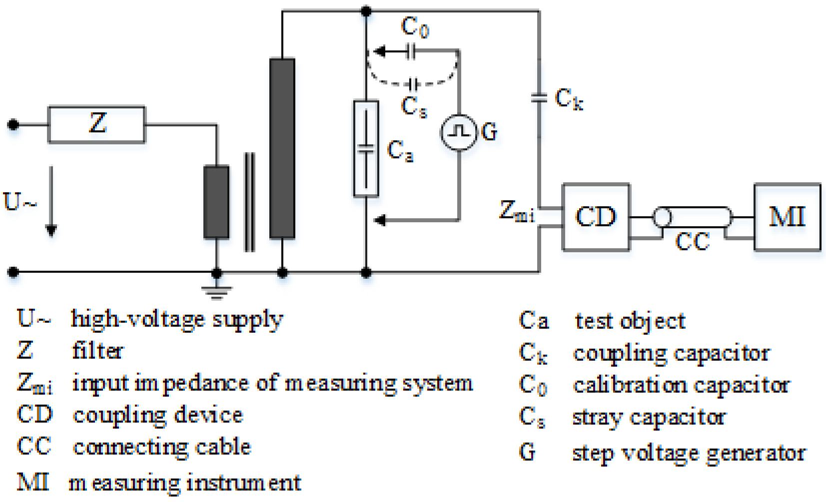

Figure 2.16: Schematic diagram of the PD arrangement according to IEC 60270-2000 [112].

In general, the arrangement of test circuits and measuring instruments used in PD detection can be divided into two types, which depend on the connected components in series with the coupling device. Regarding the indirect type circuit, when the coupling capacitor is directly linked to the coupling device, the PD event occurs in the opposite polarity of an alternating current waveform as shown in Figure 2.17 (a). As regards a direct type circuit, when the test object is connected in series with the coupling device, the PD event occurs in the same polarity of an alternating current waveform as shown in Figure 2.17 (b).

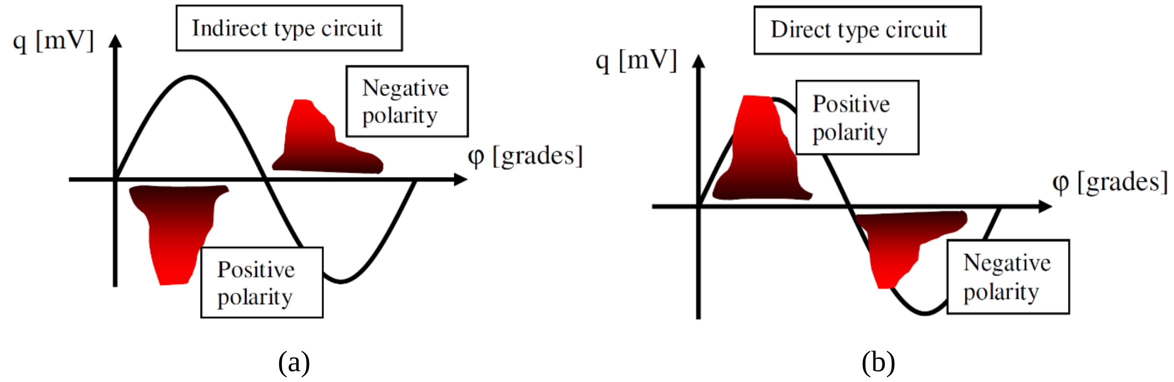

Figure 2.17: Schematic representation of the polarity of discharges depending on the connected components: (a) the case of a coupling device in series with a coupling capacitor and (b) the case of a coupling device in series with a test object [113].

2.4.1 Recognition of phase-resolved PD patterns

Generally, the technical method of interpretable PD measurement data is PRPD analysis, which can be used to diagnose typical defects such as cavities, protrusions and trees in solid dielectric material and can be used to determine degradation states for predicting the remaining lifetime of insulation system. The PRPD pattern is a scatter plot of phase angle over a single voltage cycle in the horizontal axis and apparent charge magnitude in the vertical axis. The number of PD pulses per second is illustrated with the different intensity of histogram colours. Figure 2.18 shows a detailed description of a PRPD pattern.

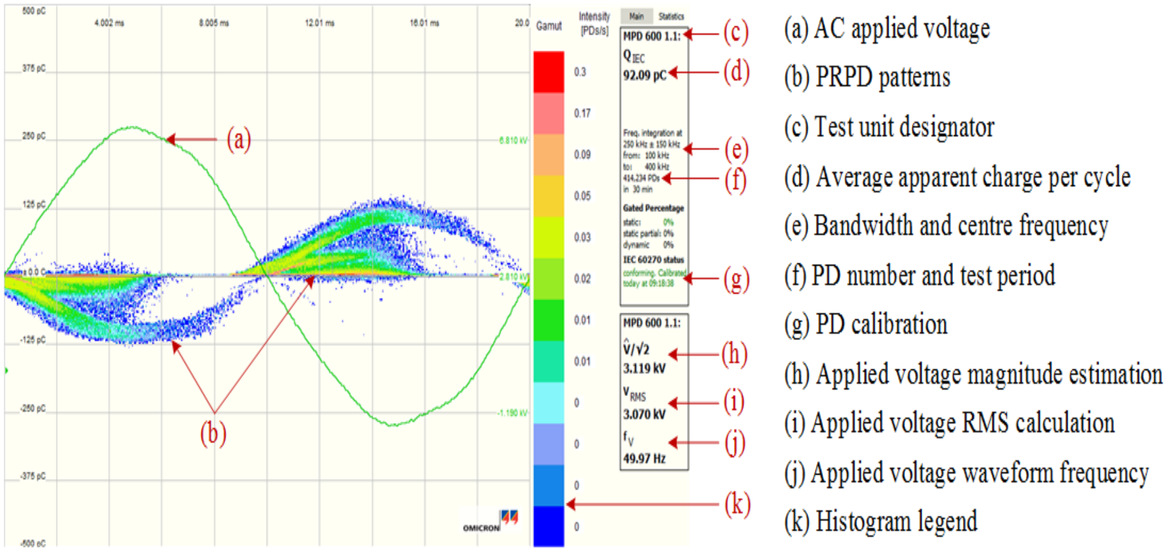

Figure 2.18: A detailed description of a PRPD pattern.

An understanding of progressive deterioration mechanisms in a cavity from localised erosion to failure, driven by PD activity, is essential for providing the diagnosis before an upcoming breakdown [114-115]. An investigation into the variation in PRPD patterns was distinguished during degradation processes in conjunction with visible evidence of the cavity formation [31]. The typical PD shapes of PRPD patterns by internal discharges were distinguished as a rabbit-like pattern and a turtle-like pattern [30, 32, 116-117]. These characteristic plots are shown in Figures 2.19 (a) and 2.19 (b) respectively. The changes of PRPD shapes by internal discharges in a cavity depended on various factors, i.e. gas pressure, gaseous composites or relative humidity. The charge bombardment can release moisture at the localised site during the degradation process. The transition of PRPD patterns from the turtle-like pattern to the rabbit-like pattern was associated with significant absorption of moisture by electron attachment, where the rabbit-like pattern with a large ear was due to an increase of the statistical time lag by PD activity [36, 89, 118-119]. The transition of rabbit-like patterns from a long ear to a short ear was observed with a reduction of oxygen content in a cavity due to oxidative ageing processes [117]. The role of relative humidity was identified in the diagnosis of PD quantities, where relative humidity increased from 35% to 98%, PD characteristics of PDIV, PD magnitude and statistical time lag tended to decrease, whereas the number of PD pulses increased [120]. Furthermore, an investigation into the influence between PD magnitude and humidity of a cavity as a function of ageing time has indicated that the maximum magnitude discharges tended to increase, whereas humidity tended to gradually decrease with elapsed time of ageing [121].

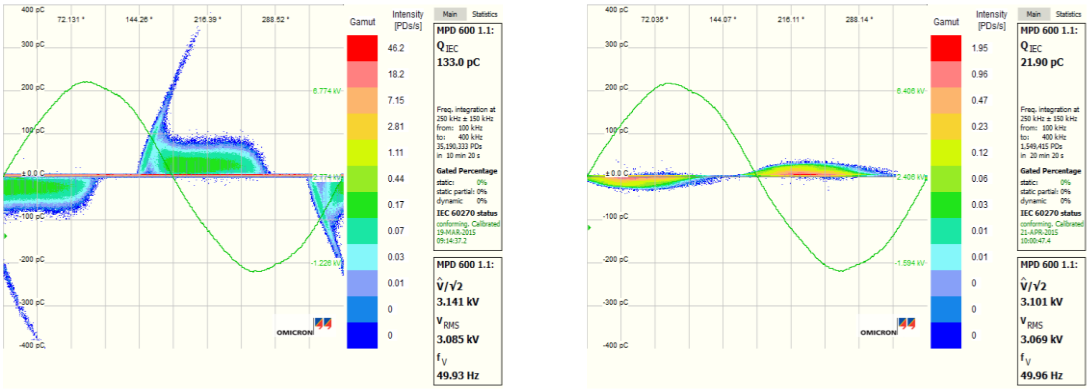

(a)

MPD 600 1.1:
Q_{IEC}
133.0 pC

Freq. integration at 250 kHz ± 150 kHz
from: 100 kHz
to: 400 kHz
35,190,333 PDs
in 10 min 20 s

Gated Percentage
static: 0%
static partial: 0%
dynamic 0%

IEC 60270 status
conforming. Calibrated 19-MAR-2015 09:14:37.2

MPD 600 1.1:
$\hat{V}/\sqrt{2}$
3.141 kV
V_{RMS}
3.085 kV
f_V
49.93 Hz

(b)

MPD 600 1.1:
Q_{IEC}
21.90 pC

Freq. integration at 250 kHz ± 150 kHz
from: 100 kHz
to: 400 kHz
1,549,415 PDs
in 20 min 20 s

Gated Percentage
static: 0%
static partial: 0%
dynamic 0%

IEC 60270 status
conforming. Calibrated 21-APR-2015 10:00:47.4

MPD 600 1.1:
$\hat{V}/\sqrt{2}$
3.101 kV
V_{RMS}
3.069 kV
f_V
49.96 Hz

Figure 2.19: Typical PRPD patterns: (a) a rabbit-like pattern and (b) a turtle-like pattern.

The treeing phenomenon is a recognised degradation mechanism prior to failure of insulation material [122]. Electrical tree initiation can be generated by a needle electrode embedded in insulation, where the PD characteristic of PRPD pattern linked to a wing-like shape correlated with the appearance of minimum magnitude discharges, namely swarming pulsive micro-discharges (SPMDs) [123-126]. Furthermore, the wing-like PRPD shape was also exhibited in a sample with an artificial tree channel embedded in a polyethylene block, which was formed as a cylindrical channel with a diameter of 10 µm and 2 mm in length [127]. Figure 2.20 shows the relationship of electrical tree growth initiation from a needle tip electrode related to the PD characteristic of a wing-like pattern.

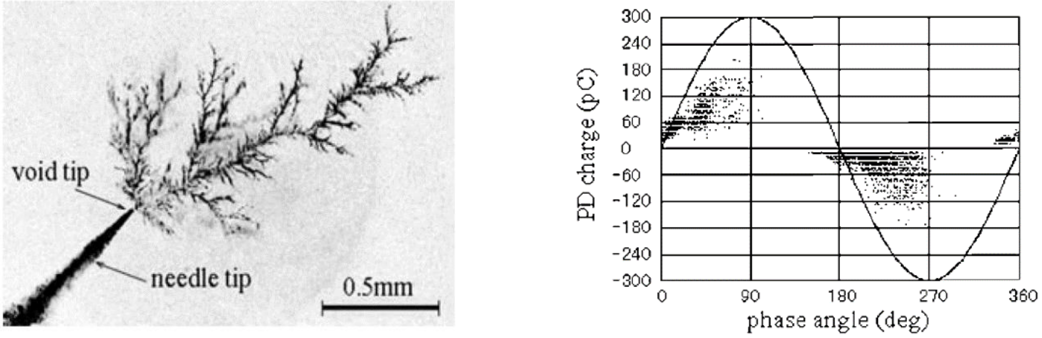

(a)

(b)

Figure 2.20: Tree growth from a needle tip and (b) PD characteristic of a wing-like pattern [125].

The changes of oxygen and nitrogen inside a cavity were investigated the progressive propagation of tree growth from localised erosion on the cavity surface that when the production of oxygen was completely consumed by the chemical reaction due to oxidative degradation, nitrogen, moisture and other gases compounds were replaced for generating pits at the localised site, where swarming micro partial discharges occurred [58]. Figure 2.21 shows the evolution of wing-like patterns with the mechanism of SPMDs [30].

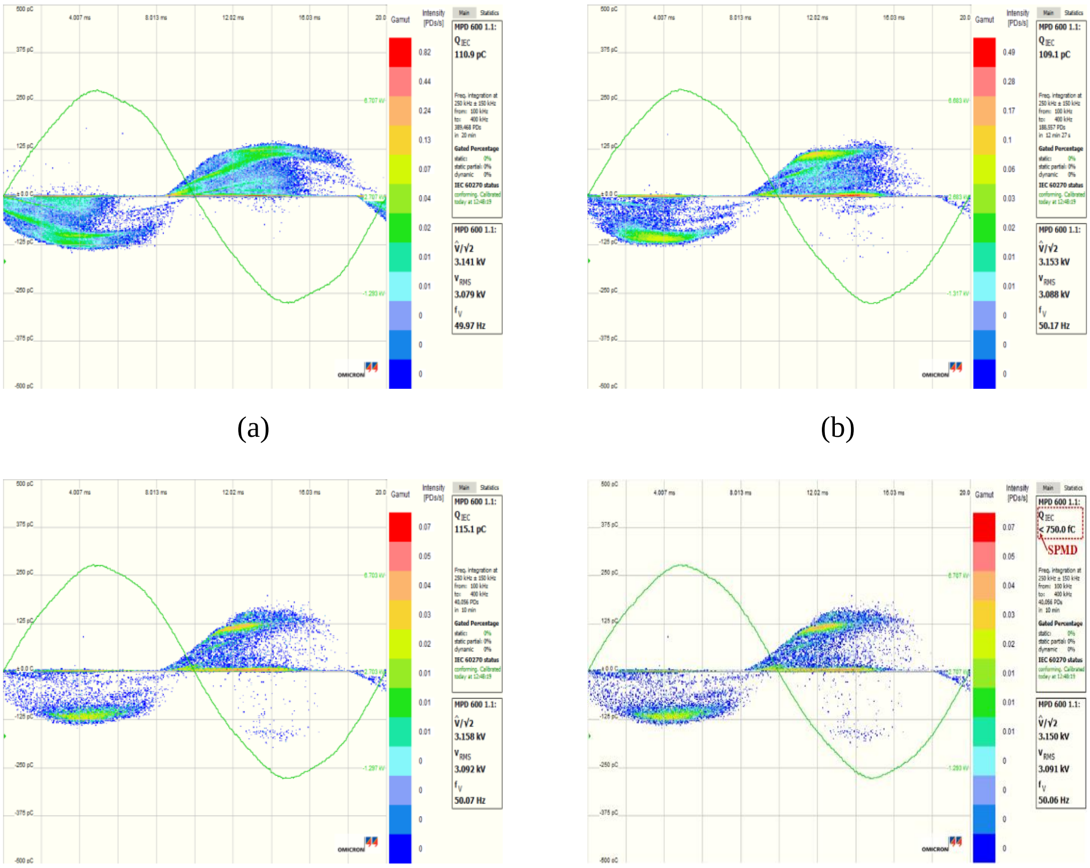

(a)

(b)

(c)

(d)

Figure 2.21: Evolution of PRPD plots of treeing initiation on the cavity surface: (a) a turtle-like pattern, (b) a turtle-like pattern, (c) a wing-like pattern and (d) a wing-like pattern with SPMDs.

2.5 Degradation processes of polymers

Polymeric materials can be basically divided into two main categories, natural and synthetic compounds, according to the structures of their molecular chains and their electrical, chemical, mechanical and thermal properties. Polymers can also be grouped in terms of thermoplastics, thermosets and elastomers. Thermoplastic polymers comprise linear chains without cross-linked structures, i.e. polyethylene (PE), polyethylene terephthalate (PET), polypropylene (PP), polyvinylchloride (PVC). When heating processes form these plastics, the process by which these plastics are produced is reversible [128]. In thermosetting polymers, the chemical molecules consist of long chains with cross-linked structures, i.e. epoxy resins, polyester resins. When these polymers are melted by heating processes, the process by which these plastics are produced is irreversible [128]. The rubber elastomer is the flexible polymer which the molecular structures compose a low cross-link density, i.e. silicone rubber, ethylene propylene rubber (EPR), ethylene propylene diene monomer (EPDM) [129]. Referring to Figure 2.22, the polymer molecule microstructure consists of semi-crystalline and amorphous regions. The semi-crystalline polymers are aligned with a regular layer with their neighbours while the irregular coordination with their surroundings obtains the amorphous structures.

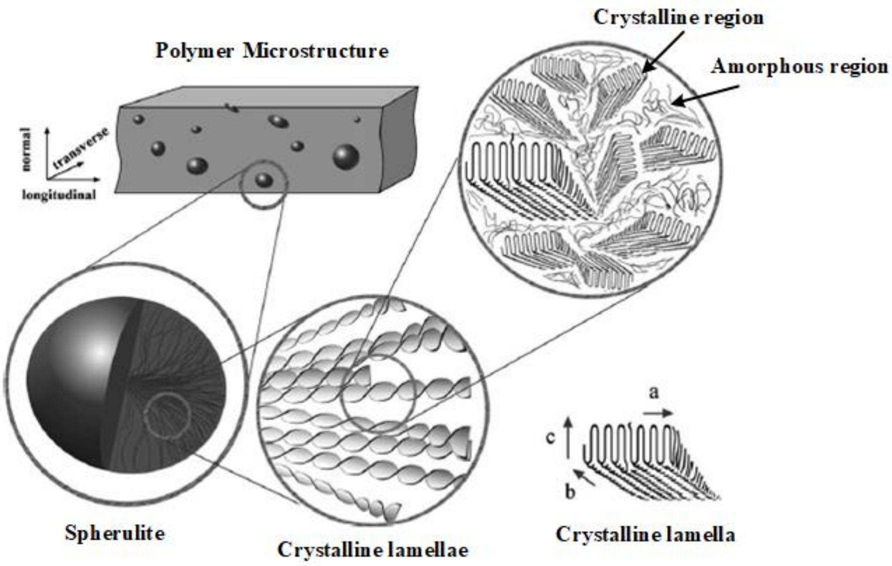

Figure 2.22: Microstructure of crystalline polyethylene [131].

The chemical structure of polyethylene is composed of a single monomer molecule of ethylene (C_2H_4), where the molecular chains hydrogen are linked to a long chain of carbon [130]. The schematic structure of polyethylene is illustrated in Figure 2.23. The microstructure of semi-crystalline consists of a spherical structure of spherulites with a diameter of approximately 10 µm that their compositions are comprised of crystalline lamellae layers, which each lamellar stack is about 100 nm in a wide range with a thickness about 20 nm in length as shown in Figure 2.24.

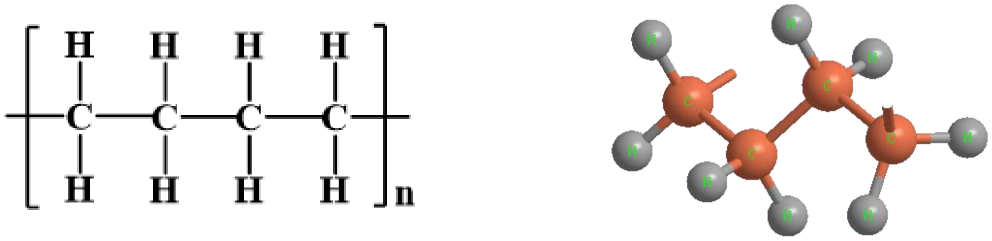

Figure 2.23: Chemical structure of polyethylene material: (a) two dimensions of molecular chains and (b) three dimensions of molecular chains.

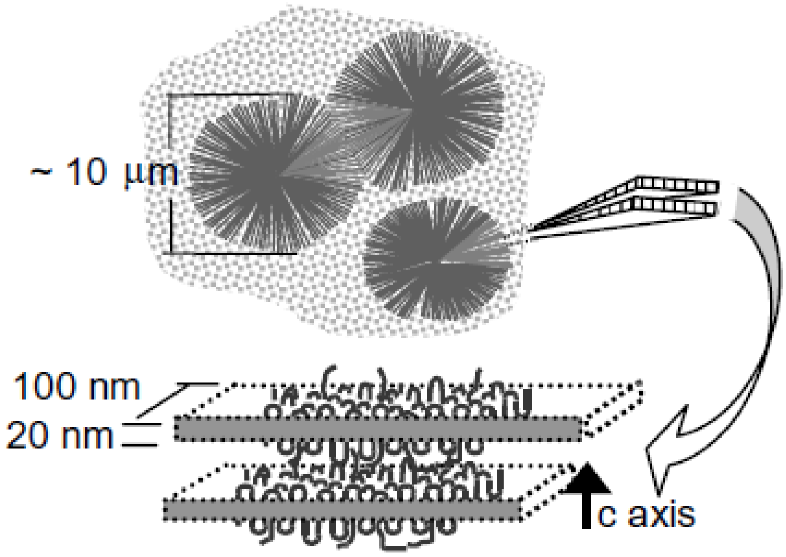

Figure 2.24: Microstructure of semi-crystalline polyethylene [132].

Silicones can be categorised as a synthetic polymer [130], where the molecular chains consist of silicon and oxygen, combining with the covalent bonds of a carbon atom and three hydrogen atoms as shown in Figure 2.25. For example, the structure of silicone elastomer is polydimethylsiloxane (PDMS) with a repeating unit, where a silicon atom is linked with an oxygen atom and surrounded by an organic group of methyl containing a single carbon atom bonded to three hydrogen atoms. The molecular structure of silicone elastomer material is illustrated in Figure 2.26

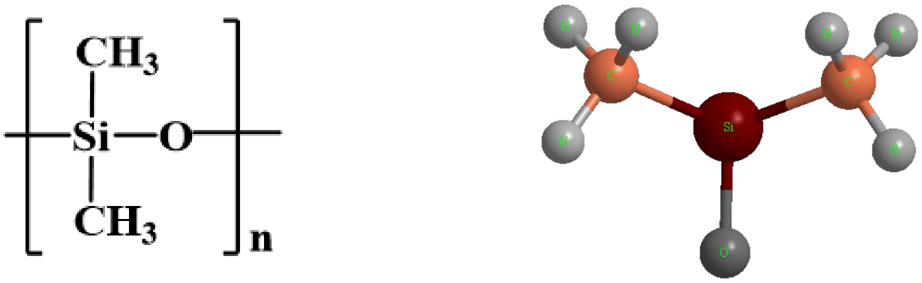

Figure 2.25: Chemical structure of silicone rubber: (a) two dimensions of molecular chains and (b) three dimensions of molecular chains.

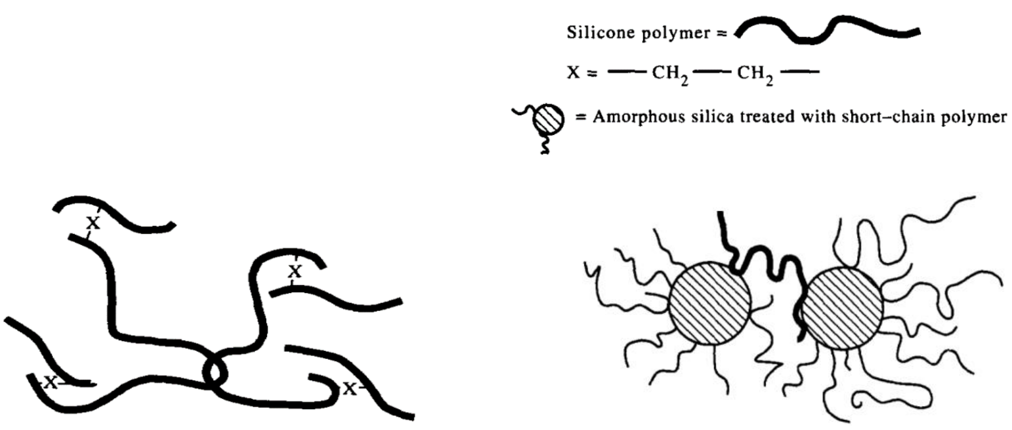

(a) (b)

Figure 2.26: Molecular structure of silicone rubber: (a) silicone polymer obtained a covalent cross-link and (b) silicone polymer obtained amorphous silica with short chains [133].

2.5.1 Electrical ageing and lifetime models

The influence of accelerated ageing in a cavity by PD activity and oxidation reactions leads to breaking of chemical bonds of polymers. The essential sequence of failure in polymeric materials can be mainly organised from two conditional processes in terms of electrical ageing and degradation mechanisms as shown in Figure 2.27.

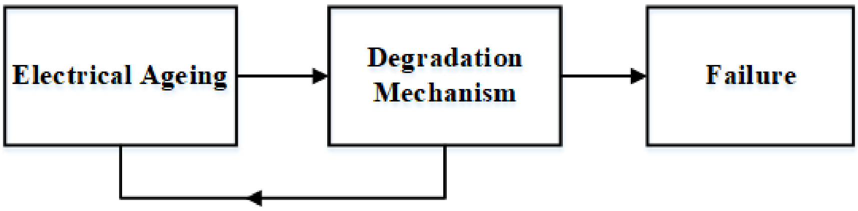

Figure 2.27: Sequence diagram of degradation mechanisms until failure of dielectric material.

During electrical ageing, characteristic properties in the bulk of polymers is reconstructed by breaking the microstructure of chemical bonds [134]. According to the Dakin model, the rate of chemical reactions for evaluating degradation processes can be expressed by [135-136]:

$$\frac{\mathrm{dC_d}}{\mathrm{dt}} = -\Lambda_{\mathrm{o}} \mathrm{C_d^{\nu}} \tag{2.14}$$

Where C_d is the variable number per unit volume, Λ_o is the velocity coefficient of chemical processes and ν is the order of the chemical reaction. The coefficient of Λ_o can be also given by the Arrhenius equation as [136]:

$$\Lambda_o = M_o \exp\left(-\frac{\mathrm{H}_o}{R_o T}\right) \tag{2.15}$$

Where T is temperature, R_o is the gas constant, M_o is the constant factor of dielectric material and H_o is the activation energy for chemical reactions occurring in dielectric material.

In the voltage-life test, the sample is electrically stressed by applying a constant voltage level until time to breakdown. Therefore, the ageing function of insulation material due to the electrical stress as a function of lifetime can be expressed as [137]:

$$F(c) = \Lambda_o(E) \cdot t_A \tag{2.16}$$

$$F(c_F) = \Lambda_o(E) \cdot L_A \tag{2.17}$$

Where F(c) is the ageing function of insulation material, $F(c_F)$ is the ageing function of insulation material after failure, Λ_o (E) is the deterioration rate or ageing rate, E is the electrical stress, t_A and L_A are ageing time and lifetime respectively.

In the accelerated lifetime, an inverse-power of electrical lifetime model used for predicting the remaining lifetime of insulation material is given by [137-138]:

$$L_A = L_o E^{-\eta_o} \tag{2.18}$$

Where L_A is the lifetime rate, L_o is the initial lifetime, E is the electric field and η_o is the voltage endurance coefficient.

Generally, the Weibull probability function for predicting failure of insulation material under applying a constant voltage level or variable levels of electrical stresses is determined as [139-142]:

$$F(t_B) = 1 - \exp\left[-\left(\frac{t_B}{\alpha_B}\right)^{\beta_B}\right] \tag{2.19}$$

Where $F(t_B)$ is the probability of failure, t_B is the variation of time to breakdown, α_B is the scale parameter, and β is the shape parameter of breakdown.

The Weibull distribution based on time to failure, t_F and electric breakdown, E_B can be given by an inverse-power model in [137], for example, the probability of failure over electrical lifetimes as shown in Figure 2.28 (a). Furthermore, analysis of insulation failure rate as a function of time can be described by a bathtub curve for failure rate, which is proportional to variable values of the shape parameter of failure, β_t as shown in Figure 2.28 (b), and is determined by:

$$F(t_F, E_B) = 1 - \exp[-(K_B t_F^{\beta_t} E_B^{\beta_E})] \tag{2.20}$$

where β_t and β_E are the shape parameters of time to failure and electric breakdown respectively, and K_B is related to the scale parameter of the Weibull cumulative distribution.

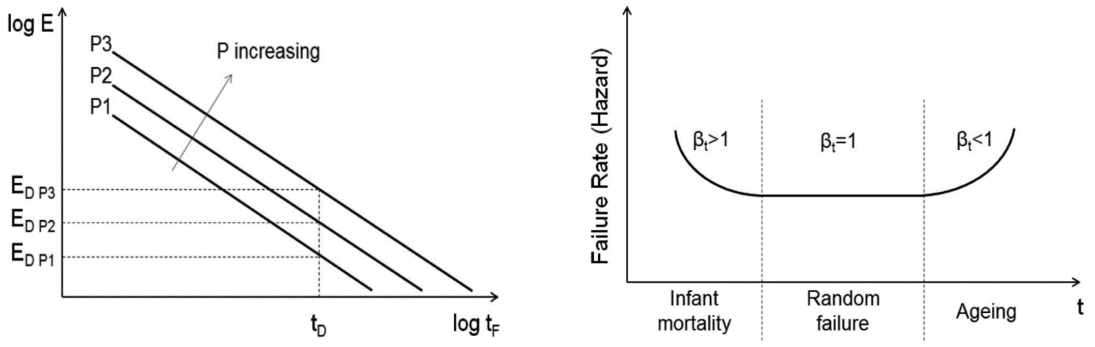

(a) (b)

Figure 2.28: Electrical lifetimes: (a) failure probability based on an inverse-power model and (b) bathtub curve for failure rate as a function of time under the electrical stress [137].

2.5.2 Models of degradation processes in a cavity

Electrical degradation and failure mechanisms by internal discharges inside an air-filled cavity of polyethylene insulation are complex issues caused by the interaction between chemical reactions and ion bombardment on the cavity surface [32, 57-58], resulting from the degradation processes of oxidative reactions [143-144]. The progression of degradation by-products on the cavity surface by PD activity can be gradually formed during ageing processes in terms of gaseous, liquid droplet and solid by-products [56-57]. In the initial stage, the interaction of charge bombardment and gaseous by-products in a cavity increased both surface conductivity and surface roughness on the inner cavity surface [31, 56-57, 145]. In the latter process, the influence of electric field enhancement at the localised erosion site by a combination of charge bombardment and chemical reactions produced corrosive by-products in the form of crystal growth on the cavity surface such that electrical tree growth might be initially generated and then progressed to failure [56-57, 146]. The model of electrical tree growth by PD activity from localised erosion to pit and electrical breakdown is shown in Figure 2.29 (a). The degradation processes on the cavity surface can be divided into five stages as shown in Figure 2.29 (b). At the first stage, the interaction between moisture and dissociation of the gaseous cavity by PD activity increases the surface conductivity. Subsequently, localised erosion on the cavity surface occurred due to an increase in the surface roughness by PD bombardment. The chemical by-products of crystals are formed due to the enhancement of electric field at the localised site, leading to electrical tree growth and complete breakdown of solid insulation. The deterioration mechanisms from the eroded surface to complete failure are illustrated in Figure 2.29 (c). The high-energy ions by internal discharges gradually decreased the thickness of a cavity surface by breaking chemical bonds and led to the growth of pits. The electric fields concentrated in this localised site, where the initial tree was generated before an upcoming failure of insulation. Furthermore, degradation processes in a cavity consumed oxygen by PD activity in the initial ageing due to oxidation reactions, leading to the presence of localised erosion of pits and progressive tree initiation prior to failure of dielectric material as shown in Figure 2.29 (d).

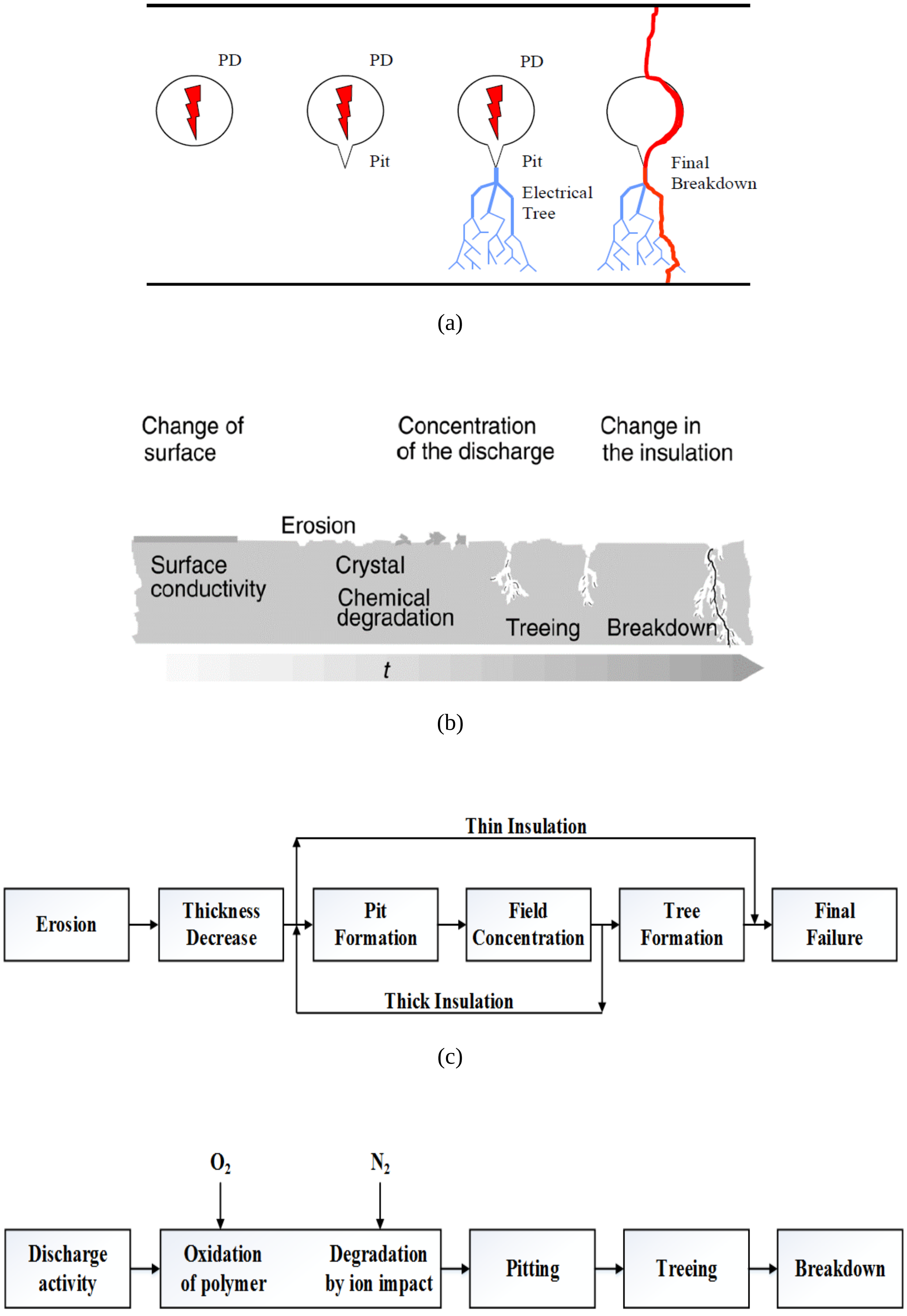

(a)

(b)

(c)

(d)

Figure 2.29: Various models of degradation mechanisms within a cavity from localised erosion to complete failure: (a) Montanari's model [37], (b) Temmen's model [57], (c) Tanaka's model [58] and (d) Morshuis's model [20].

2.5.3 Oxidation reactions

The oxidative degradation mechanism in polyethylene polymer by irradiation processes can dissociate the polymeric chains of C-H or C-C bonds as a result in the presence of free radicals, C=C, cross-links and cyclization. For example, the initial oxidation process of polyethylene material occurs, when decomposition of chemical reactions gradually degrades molecular chains in the bulk of the polymer surface by consuming oxygen. The formation of polymeric radical, $R^{\cdot}$ is formed in this initial process. Subsequently, the absorption and diffusion by oxygen on the cavity surface due to oxidative reactions react with polymer radicals to produce peroxides, $ROO^{\cdot}$, which lead to the production of hydroxyl radicals with oxygen until hydroperoxides, ROOH, are produced by the decomposition of chemical bonds due to oxidation reactions [2, 147-148]. The hydroperoxide reactions induce chemical by-products containing $^{\cdot}OH$ groups and water, H_2O [150]. When all the oxygen is consumed, an antioxidant reaction is taken place to prevent degradation processes of the polymer [147-149] as shown in Figure 2.30. Moreover, when oxygen inside a cavity was consumed by discharge mechanisms due to oxidation reactions until nitrogen take place of oxygen, leading to the initiation of tree growth prior to failure. Oxidation reactions of polyethylene material during ageing processes are detailed as follows:

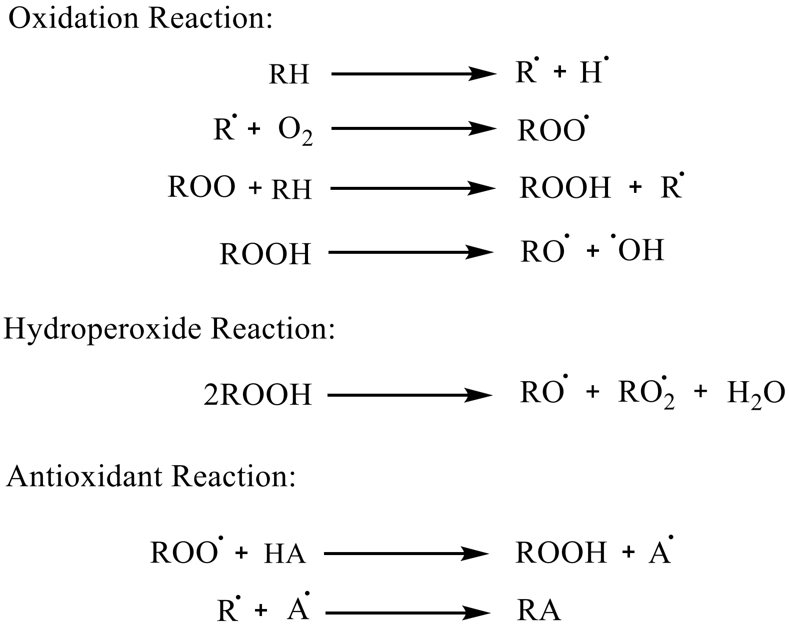

Figure 2.30: Degradation mechanisms of polyethylene material due to oxidative ageing [147].

The influence of accelerated degradation by the interaction of charge bombardment and chemical reactions lead to the breaking of chemical bonds of the polymer surface, resulting in the rate of progressive damage on the cavity surface, R_{dis} is given by [137, 151]:

$$R_{dis} = D_{dis}/t_{dis} \tag{2.21}$$

For time of dissociating half of CH bonds on the cavity surface thickness, t_{dis} can be given by [137, 151]:

$$t_{dis} = N_{CH} / (2R_{el}F_{eff}F_{hot}) \tag{2.22}$$

Where N_{CH} is the number of CH bonds in damaged zone, R_{el} is the rate of electrons colliding the polymer surface, F_{eff} is the fraction of hot electrons damaging chemical bonds of the polymer surface and F_{hot} is the fraction of hot electrons impinging chemical bonds of the polymer surface, which requires electron energies in excess of 8 eV.

Regarding the growth of electrical trees, the critical level of eroded depth on the polymer surface to start electrical trees by the local field enhancement, d_{cr} and the lifetime for the formation at localised erosion can be determined as [137, 151]:

$$L_{cr} = d_{cr} / R_{dis} \tag{2.23}$$

The mechanism of electric tree growth progressively develops from the cavity wall by PD activity. It is assumed that the formation on the polymer surface was dissociated chemical bonds at the localised site by the combination of hot electrons and chemical reactions due to the oxidation degradation [152-153]. The role of oxygen inside a cavity accelerated the scissor chains of the surface polymer. If the damaged zone is formed with a large void on the surface, the tree initiation will take place at localised erosion [154-155] as shown in Figure 2.31.

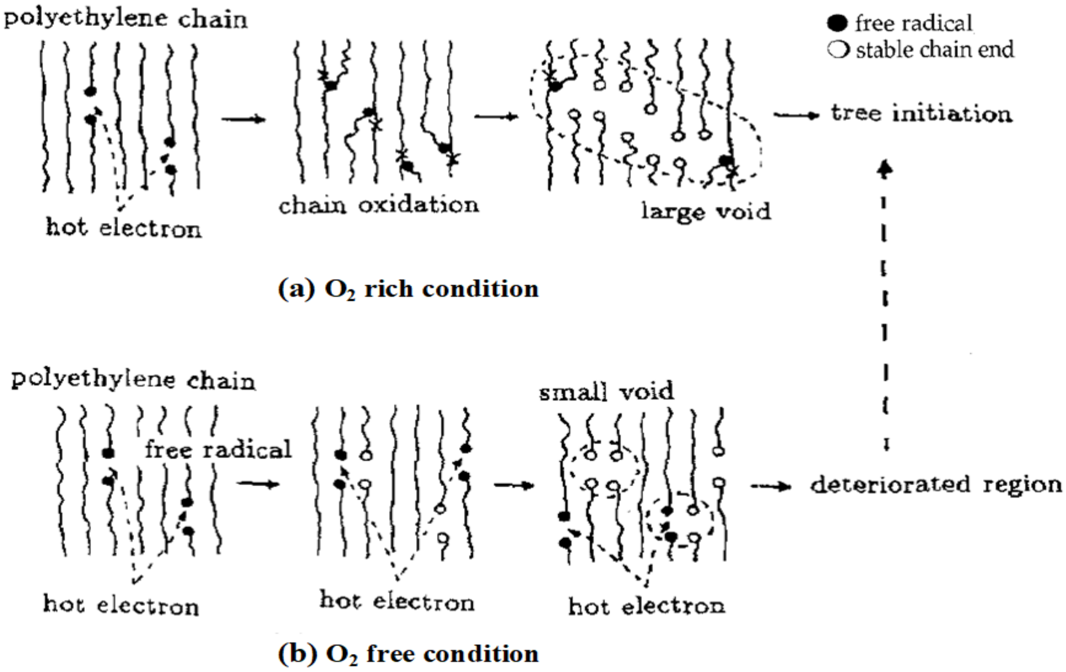

Figure 2.31: Degradation processes of electrical tree initiation at localised erosion [154].

An investigation into degradation processes within a cavity in epoxy material due to ageing was undertaken to find out deposited by-products on the cavity wall in terms of droplets and crystals [88, 156]. The presence of droplets occurred after oxidative ageing from 20 h to 100 h while the appearance of crystals was observed after prolonged exposure of just over 900 h by PD activity [157]. The chemical composites of degradation products on the epoxy surface after ageing were identified as hydrogen oxalate hydrate ($C_2H_2O_4{\cdot}2H$) of crystals [157] and organic elements such as formic, acetic and carboxylic acids of liquid droplets [156-157]. The deposited products of liquid droplets and crystals on a void surface in polyethylene material was observed after ageing 80 h as shown in Figure 2.32 (a). Another investigation into the chemical by-products in a cavity embedded in polyethylene material by PD activity was reported the progressive growth of crystals, which consisted of the chemical elements in terms of hydrogen, carbon and oxygen as shown in Figure 2.32 (b).

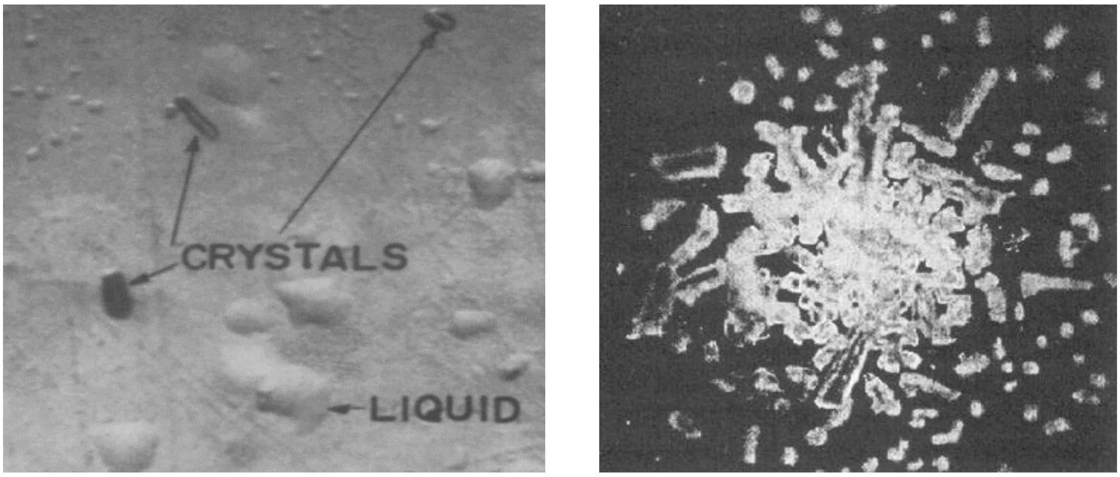

(a) (b)

Figure 2.32: Deposited by-products on the cavity surface of polyethylene material caused by internal discharges: (a) crystals and liquid droplets [158] and (b) a cluster of crystals [56].

Oxidative ageing is one of the significant causes of deterioration mechanisms of dielectric material. In the case of silicone polymers, the degradation processes of polydimethylsiloxane (PDMS) by oxidation reactions were investigated through consideration of the changes of microstructure by thermal ageing, photo-ageing and acid vapour ageing [159]. Generally, the chemical structure of silicone comprises Si-O bonds with methyl groups. After the oxidation mechanism occurs, the methyl compound of PDMS is replaced by a silanol group and liquid water as shown in Figure 2.33 (a). If the oxidation process also continues, the chemical compounds change to a gel (cross-linked) material as shown in Figure 2.33 (b).

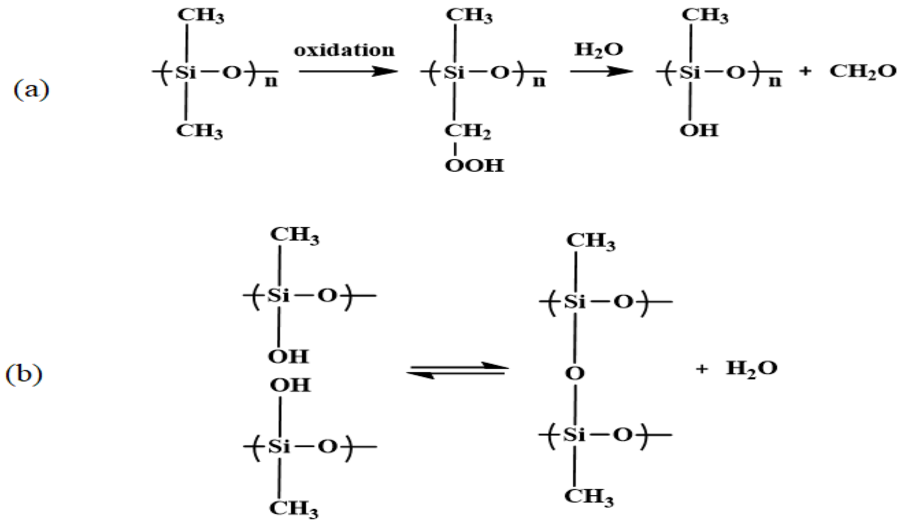

Figure 2.33: Degradation mechanisms of silicone material due to oxidative ageing [160].

Internal discharges can occur in a gaseous cavity within solid insulation and may lead to failure of dielectric material before its life expectancy. Degradation by-products in an enclosed cavity can be initially formed in terms of liquid droplets and solid by-products by reactions of gaseous composites and PD activity [161]. The proportion of gaseous composites in air contains 78.09% nitrogen, 20.95% oxygen, and amounts of other gases. In the initial stage of ageing, the substantial gaseous products in air between oxygen and nitrogen molecules are dissociated by internal discharges. The chemical by-products of nitrate radical, NO_3 with oxygen, O_2 molecules are predominantly produced by reactions of nitrogen dioxide, NO_2 with ozone, O_3 during the generation of channel discharge across a cavity. The chemical reactions between NO_2 and NO_3 are regenerated during processes of oxidative ageing to form the deposited by-product of dinitrogen pentoxide, N_2O_5. In the case of discharge mechanisms in air, the letter 'M' represents as oxygen and nitrogen molecules. The liquid droplets, H_2O on the cavity surface can be released and evaporated due to the breaking of chemical bonds in the bulk material by PD bombardment. The additional reaction of N_2O_5 with liquid droplets attributes the cause of localised erosion in the bulk cavity surface by corrosive nitric acid, HNO_3. An amount of nitric acid can be reformed by the termination reaction of chemical compounds between hydroxyl radical, OH and nitrogen dioxide as shown in Figure 2.34. The possible mechanisms of chemical reactions for the occurrence of liquid droplets containing nitric acid on the cavity surface by internal discharges are detailed as follows: [162]:

$$NO_2 + O_3 \longrightarrow NO_3 + O_2$$

$$NO_2 + NO_3 + M \longrightarrow N_2O_5 + M$$

$$N_2O_5 + H_2O \longrightarrow 2HNO_3$$

$$OH + NO_2 + M \longrightarrow HNO_3 + M$$

Figure 2.34: Chemical reactions for the occurrence of liquid droplets containing nitric acid [162].

The behaviour of morphological changes in polydimethylsiloxane (PDMS) based on silicone elastomer was investigated under increasing high electric fields [163]. The virgin surface of PDMS film was first observed as shown in Figure 2.35 (a). The significant deformation under these mechanisms can be mainly distinguished into two physical changes based on the applied voltage. The appearance of creases initiation on the surface was observed followed by creases of growing size after the magnitudes of the applied voltage from 8.8 kV to 9.7 kV as shown in Figures 2.35 (b) and 2.35 (c) respectively. Some creases on the surface formed of craters after expanding voltage of 10.5 kV as shown in Figure 2.35 (d). The transition from all creases to craters was entirely deformed and replaced by the oversized craters after increasing the voltage level from 13.3 kV to 15.6 kV as shown in Figures 2.35 (e) and 2.35 (f) respectively.

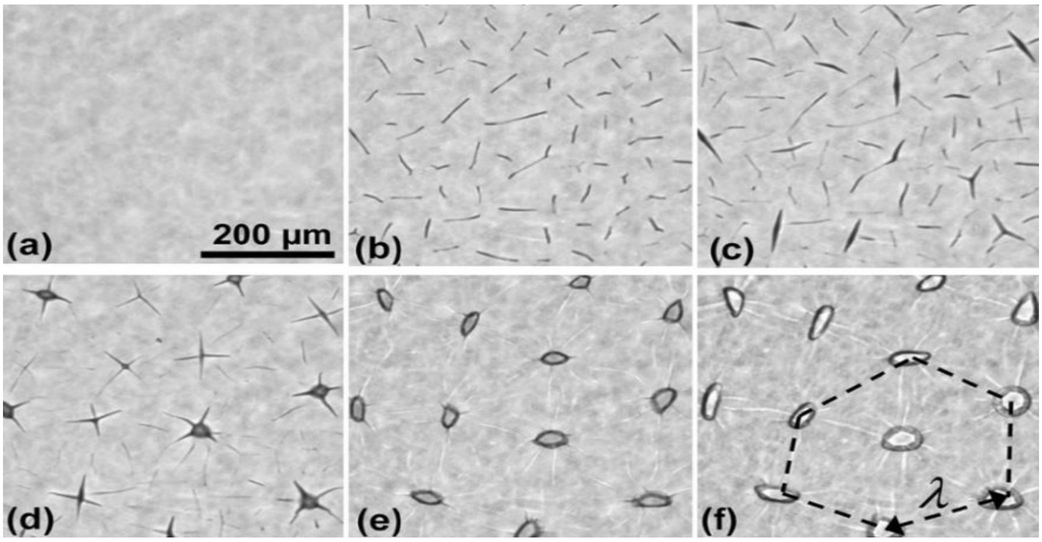

Figure 2.35: Morphological changes of chemical by-products on PDMS material under the electrical stress: (a) a virgin surface at 7 kV, (b) a creased state at 8.8 kV, (c) a crease coarseness at 9.7 kV, (d) coexistence of both creases and craters at 10.5 kV, (e) a crater state at 13.3 kV and (f) craters with a large diameter at 15.6 kV [164].

2.5.4 Electrical tree growth in solid dielectric material

The degradation processes by internal discharges of a cylindrical flat-shaped cavity with 0.1 mm in height and 3 mm in diameter embedded polyethylene material were observed the form of pits on the cavity wall. This mechanism indicates that localised erosion and deposited by-products on the cavity surface gradually evolved with elapsed time and amplitude of the test voltage due to the charge bombardment at the localised site [17]. Tree growth in solid dielectric material generally results from imperfections or protrusions in the dielectric, which might be mostly initiated from these localised sites. The behaviour of electrical trees by internal discharges within a cavity by the enhancement of local electric fields is considered to be one of the usual causes of electrical breakdown in polymeric materials [165-166]. The two most common tree structures in polymeric insulation are bow-tie trees and the vented trees, i.e. water trees, electrical trees [167-170]. The bow-tie tree normally grows within insulation material, where this tree does not bridge the electrodes until the occurrence of electrical breakdown [171]. In the vented trees, the path of tree growth within dielectric material might progress along the direction of electric fields until failure of the whole insulation failure [171]. The classification of typical trees such as water trees, electrical trees and bow-tie trees was observed inside the polymer insulation after a long-term period of operational service [172-173]. Another physical explanation of the cavity formation in solid dielectric is that it may be caused by electrical discharges, i.e. electrons and ions bombard at the localised site, where the gaseous channels were produced the conductive track along the cavity surface and replaced by the form of initial craters in these channels. When the erosion depth of the crater increased, the localised discharges led to induce the progressive propagation of electrical trees prior to failure as shown in Figure 2.36 (a). In the case of electric tree initiation from pits by PD activity, the progressive degradation mechanisms from localised erosion to tree initiation of a cavity in epoxy material is shown in Figure 2.36 (b).

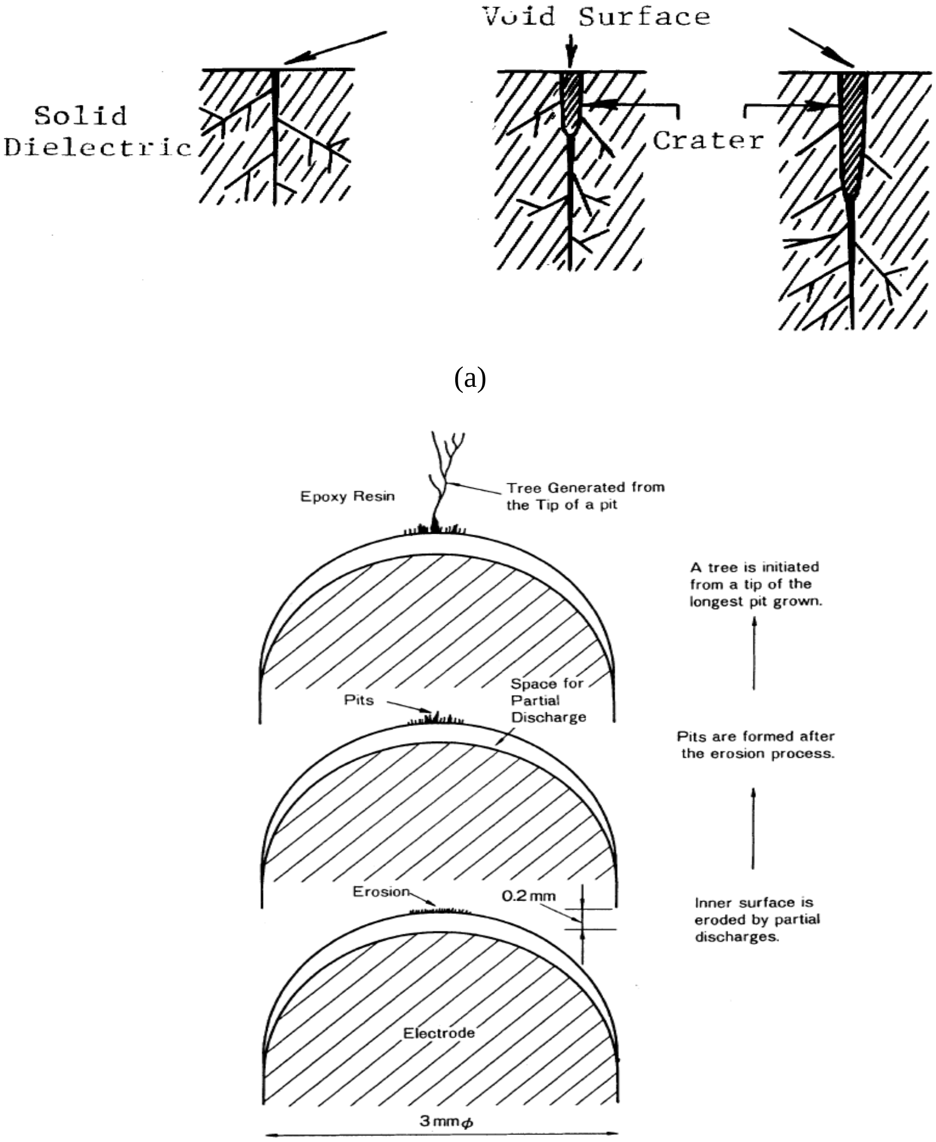

(a)

(b)

Figure 2.36: Hypothetical explanation of electrical tree growth on the cavity surface: (a) tree initiation from a crater [174] and (b) tree initiation from pits [58].

The progressive processes of tree growth in epoxy material were generated by using a needle tip and can be categorized into three main stages. The initial trees were observed in the first stage. In the second-third stages, these trees with small branches propagated towards the ground electrode and subsequently became wider structures of branches and channels after electrical breakdown with diameters between 1 µm and 10 µm for small branches and between 60 µm and 150 µm for tree channels as shown in Figure 2.37 (a). The growth of trees in silicone rubber between the needle tip and plate electrodes was classified according to their shapes as single branch tree, branch tree, bush tree and blend tree. As an example, the appearance of bush tree growth after breakdown is illustrated in Figure 2.37 (b) and shows that the physical propagation of this tree resulted in the carbonised track between the needle tip and ground electrodes.

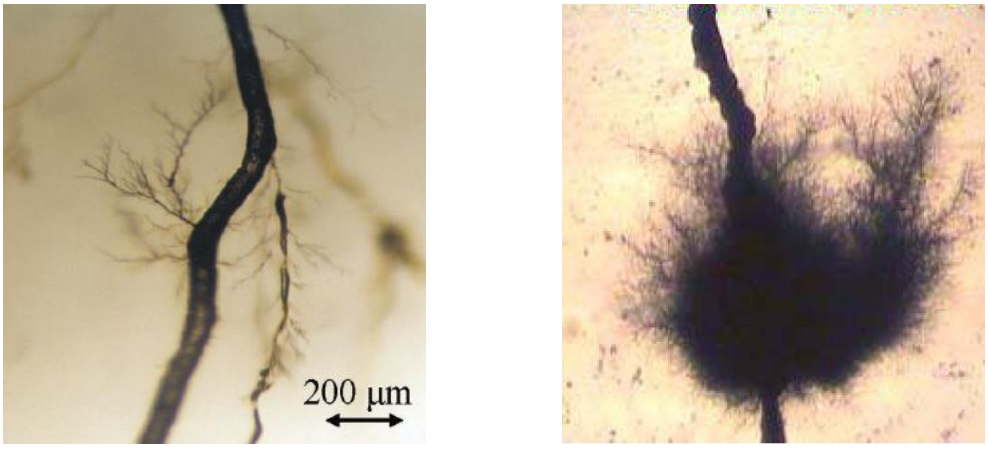

(a) (b)

Figure 2.37: Electrical tree growth in solid dielectric material by using a needle tip: (a) treeing channel and branches in epoxy material [175] and (b) treeing propagation in silicone rubber after breakdown [176].

The relationship between the progressive growth of trees with different lengths and the types of trees can be determined as [177]:

$$S_d = \left[T_d / T_n \right]^{d_L} \tag{2.24}$$

Where S_d is the total length of all tree branches, T_d is the treeing length from an initial point, T_n is the average length of treeing channels and d_L is the fractal dimension in the range from 1.2 to 1.8 for branched trees and from 2.4 to 3 for bushed trees.

In the case of the progressive propagation of tree growth under an applied alternating current stress, the conducting behaviour of tree channels can be expressed as [177]:

$$S_d(t) = \left[T_d / T_n \right]^{d_L} = t_A / t_{ch} \tag{2.25}$$

Where t_A is the ageing time and t_{ch} is the time of treeing channel propagation.

SEM micrographs of tree channels were closely examined in a cross-section view of tree channels using a microtome for cutting specimens into thin slices [178]. One of these trees was bush-like in polyethylene material, and another structure of treeing was produced in blended polyethylene by Yong Zhao as shown in Figures 2.38 (a) and 2.38 (b) respectively. Another investigation into electrical tree growth in ethylene propylene diene monomer (EPDM) [179], the observation of tree channel after breakdown by SEM indicates that this channel obtained by the black bulk within the inner surface with diameters between 392 µm and 430 µm as shown in Figure 2.39. It is likely that the inner tree channel was covered with conducting carbonisation as a result of breaking chemical bonds of polymeric chains, leading the progressive growth of tree channel before breakdown mechanism.

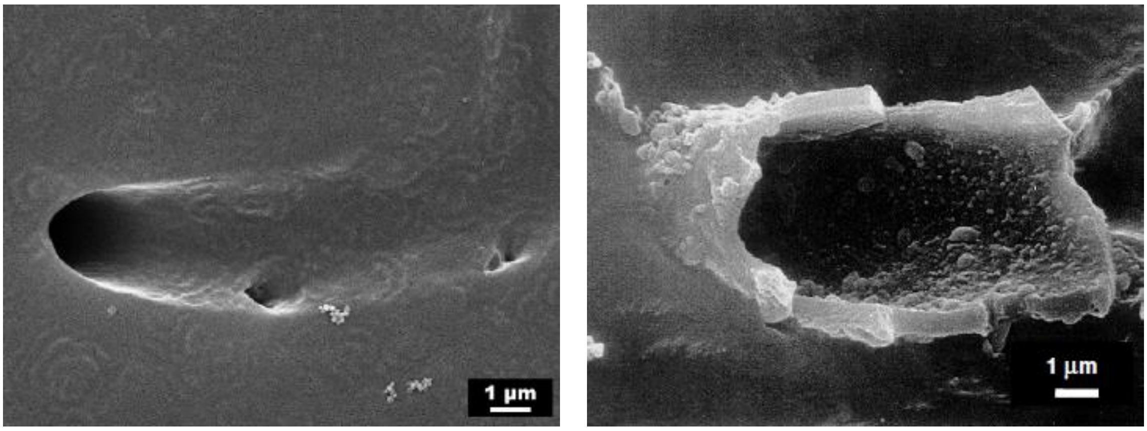

(a) (b)

Figure 2.38: SEM micrographs of treeing channel structures: (a) a cross-section view of tree channel in polyethylene material and (b) a cross-section view of tree channel in blended polyethylene material [178].

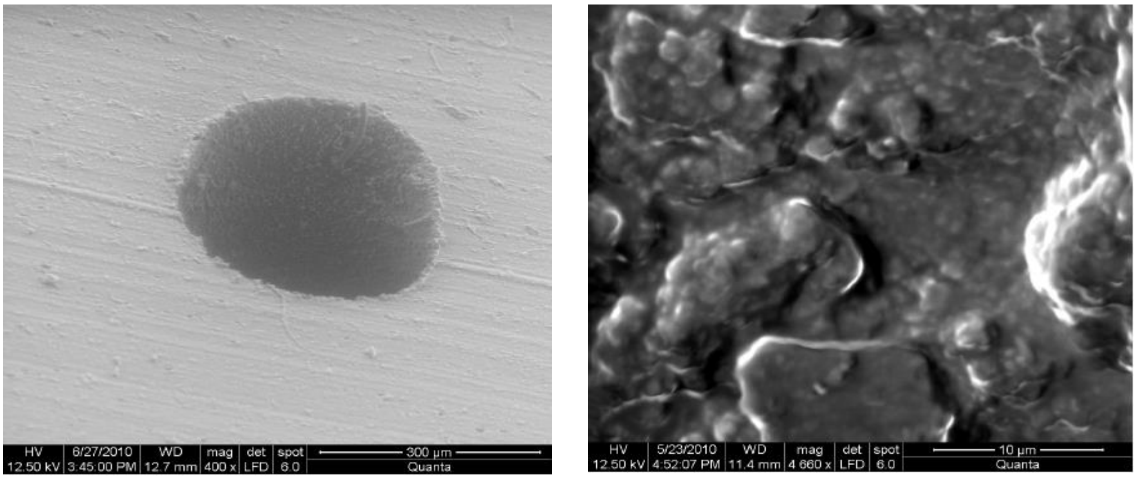

(a) (b)

Figure 2.39: SEM micrographs of treeing channel surface in ethylene propylene diene monomers (EPDM) material: (a) a treeing channel after breakdown and (b) an inner wall within the treeing channel [179].

2.6 Summary

This chapter details the principal concepts of PDs within an air-filled cavity in solid dielectric and the degradation processes caused by PD activity. Firstly, the classification of discharge mechanisms can be sorted into four categories in terms of the internal discharges, the treeing discharges, the corona discharges and the surface discharges. The overview of gaseous discharge mechanisms inside a cavity has discussed the evolution of discharge phenomena, i.e. a single avalanche, Townsend discharges and streamer discharges. The theoretical background of internal discharges inside a cavity by PD was also detailed, including the influence of various factors such as surface charge decay, gas pressure, electric fields, shaped cavities and cavity sizes. Furthermore, the PRPD analysis can be used for diagnosis of the variation in PD characteristics of a cavity that the typical cavity discharge linked to a rabbit-like pattern and a turtle-like pattern. The treeing discharges linked to wing-like patterns and SPMDs. Regarding the degradation processes within a cavity, some examples of electrical ageing and lifetime models have reported that the degradation processes on the cavity surface caused by PD activity can be divided into five main stages. At the first stage, the interaction between moisture and gaseous dissociation inside a cavity by charge bombardment increased the surface conductivity. Subsequently, localised erosion of the surface roughness on the cavity surface was noticed. The chemical by-products of crystals were formed due to the enhancement of electric fields at the localised site, leading to electrical tree initiation before failure of insulation material.

Chapter 3 Methodologies and Experimental Procedures

The objective of this chapter is to describe in detail the technical methodologies and measurements used in the experimental work in this thesis. The preparation procedures of samples containing a single air-filled cavity are divided into two different shaped cavities embedded in polymers. One type containing a flat-shaped cavity in the centre of the middle layer of three layers is made from polyethylene material while the other containing a spherical-shaped cavity is made from silicone rubber elastomer material. The PD experiment is primarily to allow PRPD analysis of the test sample during the ageing process. Also, the details of the test cell and calibration are provided in this section. The ageing experiment uses a constant applied voltage level such that the field is slightly higher than the breakdown strength of a cavity. This ageing test is specifically designed to stress twenty test samples using multiple test cells. Analysis of PD characteristics during the ageing process in a cavity is performed in the correlation with microanalysis techniques, which employ fundamental instruments to investigate the changes in physical, thermal and chemical properties, i.e. optical microscopy, dielectric spectroscopy, differential scanning calorimetry (DSC), thermogravimetric analysis (TGA), Fourier-transform infrared spectroscopy (FTIR), Raman spectroscopy, scanning electron microscopy (SEM) and energy dispersive X-ray (EDX). A summary of this chapter is given in the last section.

3.1 Procedures for producing test samples

The preparation of suitable samples for ageing is an important part of this thesis. To ensure measurable similarity before testing samples that are not contamination or contained other defects every cure has been taken in ensuring samples are manufactured in a clear environment.

3.1.1 LDPE samples

The technical procedures for producing the test samples were carefully undertaken in a chemical preparation room at the Tony Davies High Voltage Laboratory (TDHVL) to avoid contamination of dielectric material, which might occur in the form of micro-defects, i.e. contaminants, dust particles, impurity or voids. The samples used in this experiment were made using three layers of LDPE film manufactured by Goodfellow Cambridge Ltd. with a thickness of 300 μm and a flat-shaped cavity of diameter 2 mm in the centre of the middle layer. The cavity is obtained by removing the centre part of the polyethylene layer leaving a circular shape using a micro drill bit. This layer is placed in the middle layer between the top and bottom layers as shown in Figure 3.1 (a and b). The three layers of polyethylene film are put in the middle of a rectangular steel mould, which is used to control the sample thickness during the pressing. All of them are set between aluminium plates and then inserted between heat plates of a press machine at 96 °C with a pressure of 0.145 bar for 10 minutes as shown in Figure 3.1 (c and d). After the pressing process is complete, the LDPE sample is taken out from the press machine, and the sample thickness after the press is measured using a micrometre to ensure that the total thickness, which remains close to 300 µm as shown in Figure 3.1 (e and f). All samples have the same dimensions of 50 mm^2 with an embedded cavity with a diameter of 2 mm and 100 µm in height. The characteristic properties of LDPE film are listed in Table 3.1.

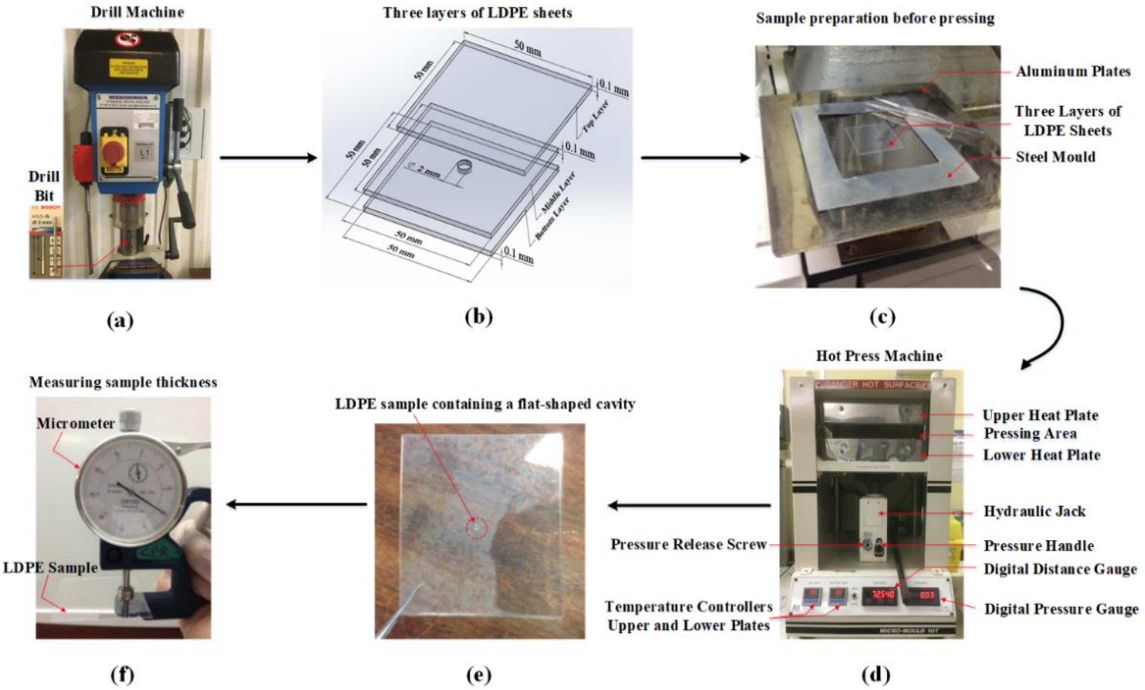

Figure 3.1: Procedures for producing a polyethylene sample containing a flat-shaped cavity.

Table 3.1: Characteristic properties of LDPE film [180].

Material Type	Dielectric Strength [kV/mm]	Dielectric Constant at 1 MHz	Dissipation Factor at 1 MHz
LDPE (100 µm in thickness)	27	2.2-2.35	0.0003

3.1.2 Silicone samples

The samples used for this experiment are produced from a Dow Corning Sylgard® 184 Silicone Elastomer, which is manufactured by Ellsworth Adhesives Ltd. This product comprises of two colourless liquid compartments containing the silicone rubber and the hardener. During the curing process, silicone rubber with its hardener is stirred thoroughly with a mix ratio of 10 to 1. The weight of the mixture is 5 g, which is measured using an electronic weight balance as shown in Figure 3.2 (a). Air bubbles in the mixture are removed in a vacuum oven for 60 minutes at room temperature as shown in Figure 3.2 (b). The viscosity of the mixture is increased by a pre-heating cure in a fan oven for 10 minutes at 60 ˚C before a controlled volume of air is injected with a syringe. The syringe is a Hamilton precise syringe 600 series, 2.5 µL manufactured by Sigma Aldrich and is used for making a spherical cavity in the middle mixture as shown in Figure 3.2 (c and d). A post-heating cure is performed immediately after a cavity is injected using a fan oven for 35 minutes at 100 ˚C. To ensure that the position of a cavity remains fixed in the middle of the sample as shown in Figure 3.2 (e). After a complete curing process, the silicone sample is removed from the container as shown in Figure 3.2 (f). The cavity size is determined using optical microscope, and the sample thickness is measured using a digital vernier calliper as shown in Figure 3.2 (g). The characteristic properties of silicone elastomer material are listed in Table 3.2.

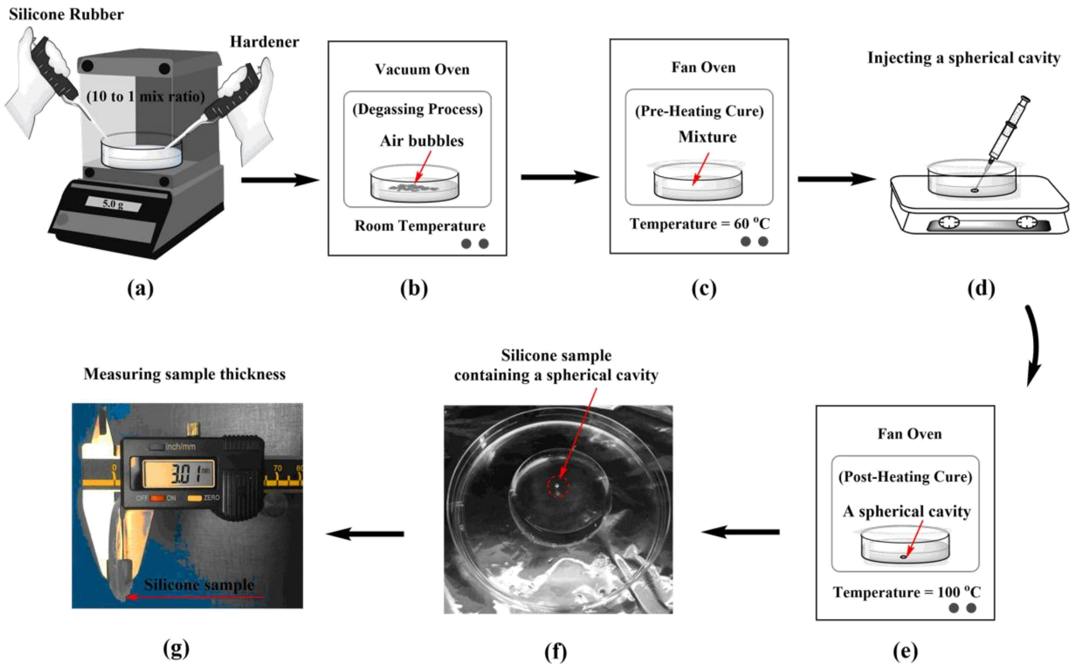

Figure 3.2: Procedures for producing a silicone sample containing a spherical cavity.

Table 3.2: Characteristic properties of Sylgard® 184 silicone rubber elastomer material [181].

Material Type	Dielectric Strength [kV/mm]	Dielectric Constant at 100 Hz	Dissipation Factor at 100 Hz
Silicone Elastomer	19	2.72	0.00257

3.2 PD measurement technique

PD activity can occur at the localised site, where the electric field stress exceeds a minimal inception field. In solid dielectrics, the deterioration processes initially associated with internal discharges in gas-filled cavities that these mechanisms influence in descending the remaining lifetime and material performances, which might depend on the enhancement of electric fields inside a cavity and elapsed time of ageing. The recognition of PD characteristics can be used to identify the status of dielectric insulation material during the time-evolution of PD activity obtains by PD quantities, i.e. the average apparent charge, the maximum apparent charge and the average number of PDs per cycle for the diagnosis of measurement results. Therefore, it is important to understand the method of PD detection for an effective interpretation of experimental results.

3.2.1 PD experimental set-up

The PD experimental set-up is placed in a Faraday cage as shown in Figure 3.3. The main components consist of a HV transformer, a PD system, a test cell and a test sample. The power transformer is equipped with a filter for eliminating high-frequency noise provided a HV AC supply. For the PD detection system, a PD acquisition and a battery charger unit are coupled to a measuring impedance for detecting PD signals such that when a discharge occurs in the test sample, the voltage across the test sample drops rapidly [182]. Thus, the charge is transferred to the coupling capacitor from the test sample to conserve charge. Both the test sample and a test cell are immersed in a silicone oil bath to prevent surface discharges and connected in parallel with the coupling capacitor. All HV connections have been made using copper pipes in order to suppress corona discharges.

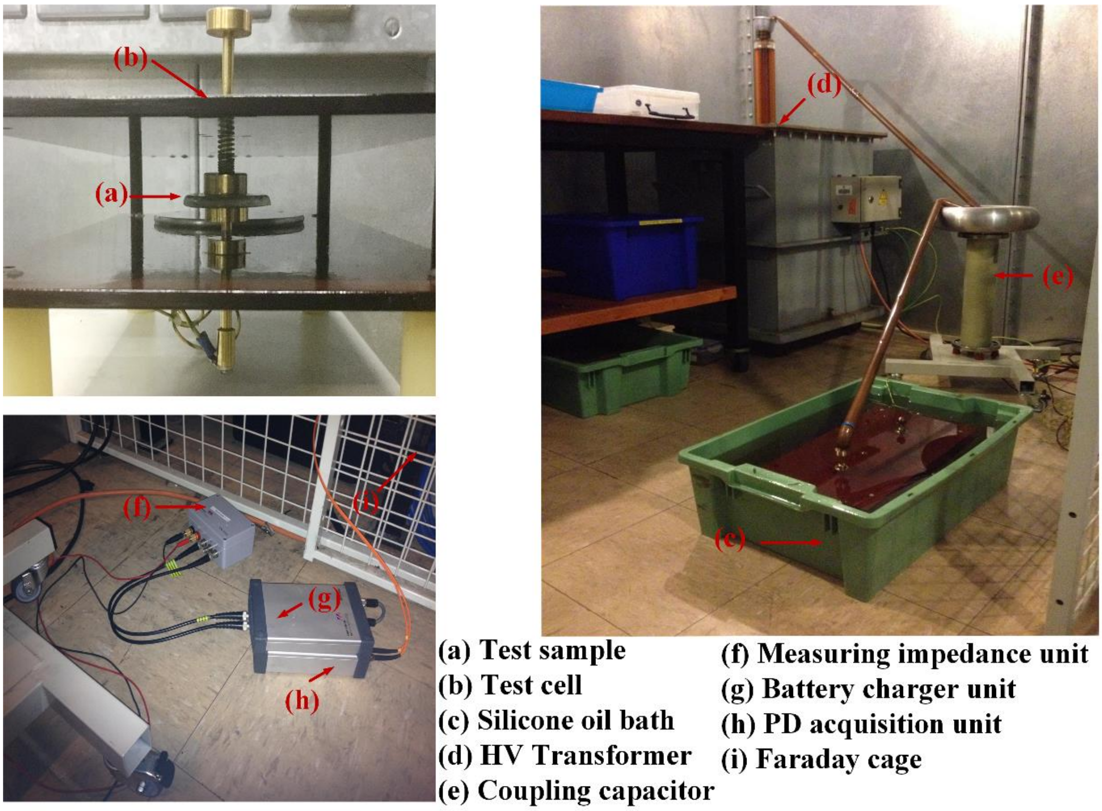

Figure 3.3: Photographs of the PD experimental set-up in a Faraday cage.

3.2.2 PRPD analysis

The PD detection used for a conventional monitoring system in this thesis is the technique of PRPD analysis using Mtronix MPD 600 manufactured by Omicron. The equivalent circuit of PD system is shown in Figure 3.4. The PD experimental set-up is calibrated before the beginning of PD measurement by using a charge calibrator, Mtronix CAL 542, where a known amount of apparent charge, in the range of pico-coulombs (pC), is injected into the terminals of the test sample according to the IEC 60270 standard. The PD measuring system is supplied by an alternating current source from a HV transformer in the maximum rating of 100 kV. The PD detection equipment operates in the frequency range between 100 kHz and 400 kHz to identify PD signals. The MPD 600 system used for the acquisition of PD events is supplied with a Lithium DC battery pack, MPP 600 with charging and discharging rates of 12.6 V, 4 A and 9-11.1 V, 4 A respectively. The MPD 600 unit is connected to the control unit, MCU 502 via fibre optic bus controllers, which is used for converting optical signals from the MPD into electrical signals of PD activity via the USB port. The measured phase-resolved PD data is stored as streams, which can be displayed or cut individually to focus on significant PD events. Statistical quantities of PD activity can be determined by exporting PD data using MATLAB code in Appendix D.1, common measures include the average apparent charge, the maximum apparent charge and the average number of PDs per cycle. The coupling capacitor has a rating of 1 µF, 50 Hz is used reduce reflective signals during the PD measurement and is connected in series with the measuring impedance unit, CPL 542. The test sample held in a test cell is connected in parallel with the coupling capacitor.

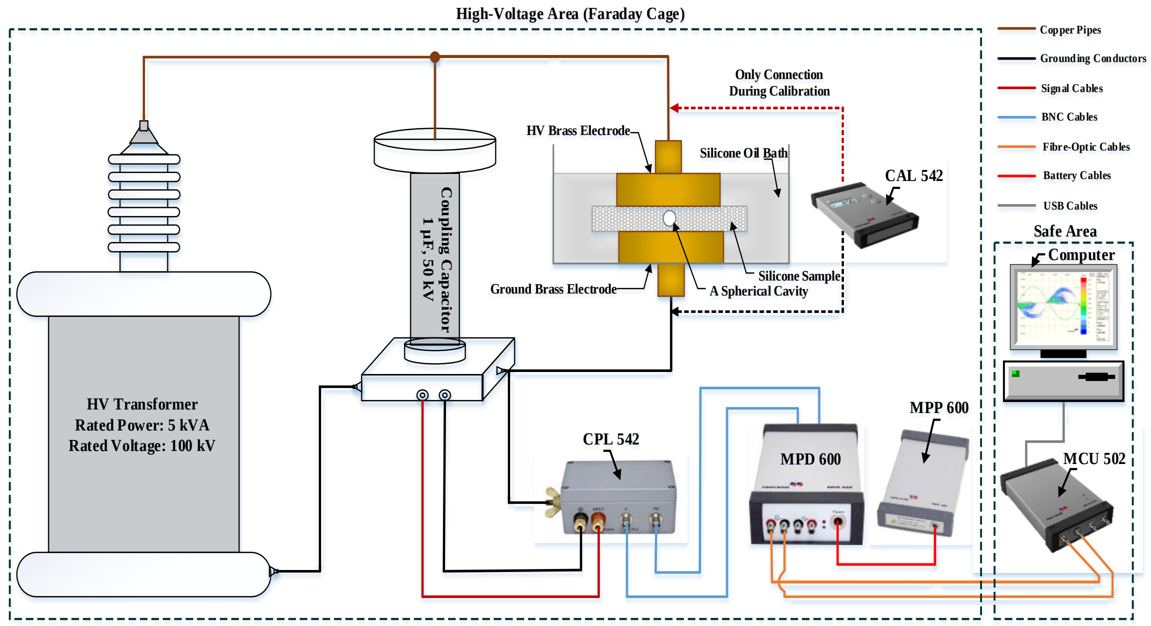

Figure 3.4: Schematic arrangement of the PD measurement.

3.2.3 Single test cell for the PD measurement

The schematic geometry of a single test cell for the PD measurement is provided as shown in Figure 3.5. A silicone sample is used for this example, which contains a single spherical cavity embedded in the centre of a cylindrical dielectric material of diameter 50 mm with 3 mm in thickness. The parallel electrodes are made from the cylindrical brass, which consists of diameter 23.4 mm with 10.4 mm in thickness for the top electrode and diameter 23.4 mm with 8 mm thickness for the bottom electrode. Both test sample and parallel electrodes are held between two rectangular plates of paxolin insulation board, which are joined to each other by a plastic leg at each edge. All components are immersed in a silicone oil bath in order to prevent surface discharges. The upper electrode is connected to a 50 Hz HV AC supply and the lower electrode is connected to earth.

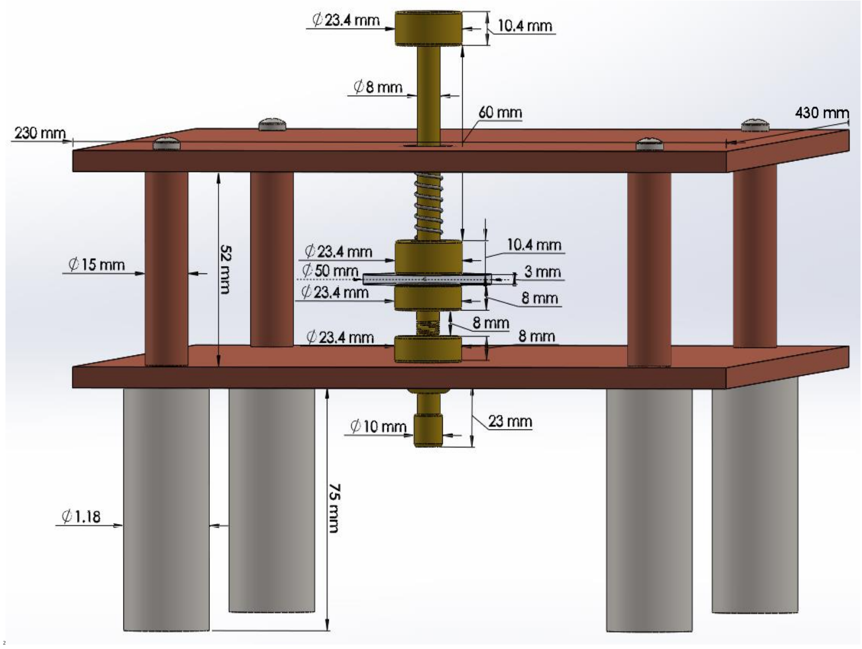

Figure 3.5: Schematic geometry of a test cell and a test sample for the PD measurement.

3.2.4 Calibration for the PD experiment

A calibration process must be performed for every time before the PD experiment is started. The PD system is calibrated by a charge calibrator, where a known quantity of apparent charge is injected into the test object for calibration [183] so that the PD measurement is verified accurately in the experiment result. It should be noted that the magnitude of measured apparent charge is not equal to an amount of real charge at the localised site, which is induced to the terminal electrodes for the PD detector. The charge amplitude for the calibrator is set equal to 10 pC for injecting into the test sample for calibration of a PD system as shown in Figure 3.6.

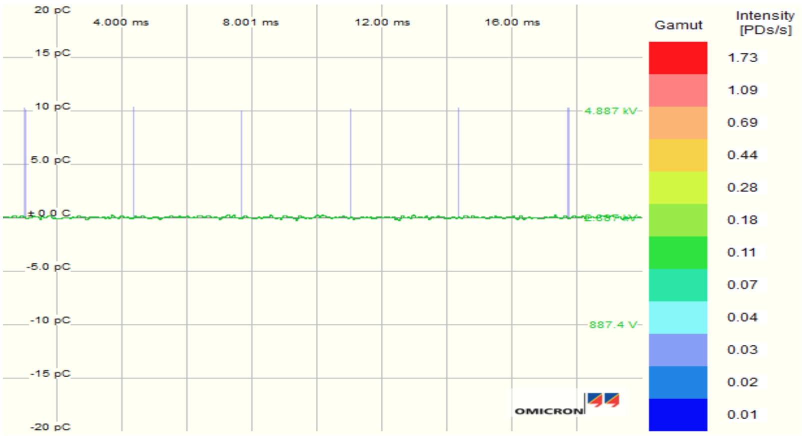

Figure 3.6: PD calibration.

3.3 Accelerated ageing test

Electrical degradation mechanisms of an air-filled cavity embedded in solid dielectric material can be induced by the enhancement of electric field stress caused by the accelerated ageing test. An investigation into the cavity formation by PD activity at the localised site is experimentally undertaken to clarify the relationship between microstructural changes and time-evolution from surface erosion to electrical tree initiation, leading to complete failure.

3.3.1 Experimental set-up for the ageing test

The accelerated ageing test is undertaken at a constant applied voltage level, which is higher than the inception voltage of a cavity. The ageing set-up is specifically designed for twenty test samples with multiple test cells. Each test cell consists of ten parallel brass electrodes, which are immersed in a silicone oil bath to eliminate surface discharges. Each test cell is connected in parallel with a 20 kV, 25 mA HV transformer. The voltage level for the ageing test is controlled using a digital voltmeter outside a Faraday cage, which is connected to a HV probe with maximum rating of 25 kV that has a input:output voltage ratio of 1000 V to 1V as shown in Figure 3.7.

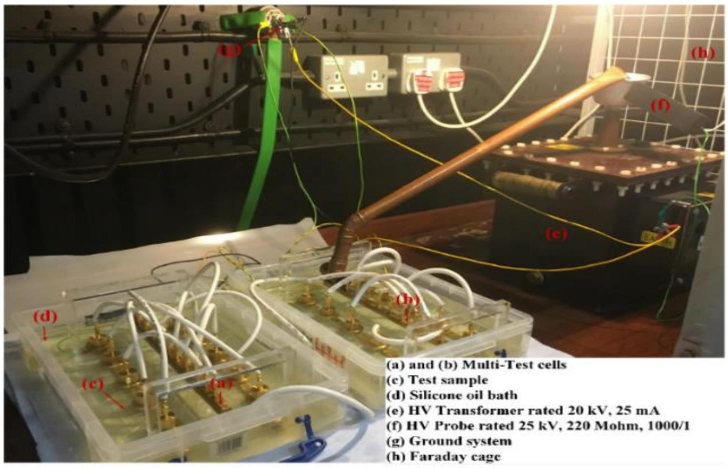

Figure 3.7: Photograph of the experimental set-up for the ageing test in a Faraday cage.

3.3.2 Multiple test cells for the ageing test

The schematic diagram of the multiple test cells and components for the ageing test is showed in Figure 3.8. Each test cell contains ten test samples, each sample places between parallel electrodes, where the upper electrode is connected to the brass bus bar, and the bottom electrode is connected to the ground brass bar. The HV transformer supplies each test cell via a copper pipe. The schematic geometry of a single test cell with the test sample is illustrated in Figure 3.9. The sample containing a cavity is placed between parallel electrodes, which consist of the upper electrode of diameter 18 mm with 25 mm in height and the lower electrode of diameter 20 mm with 5 mm in height. The RMS applied voltage over the AC cycle constant for the accelerated ageing test is set by increasing the average PDIV of test samples, where the PDIV for each sample is gradually increased the voltage level until the initiation of a PD event occurs. All components are placed in a Faraday cage.

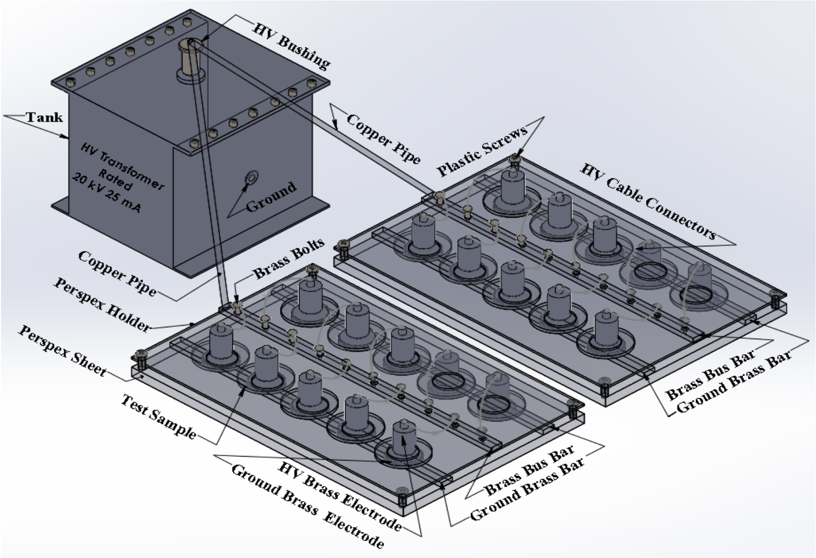

Figure 3.8: Schematic arrangement of multiple test cells and components for an accelerated ageing.

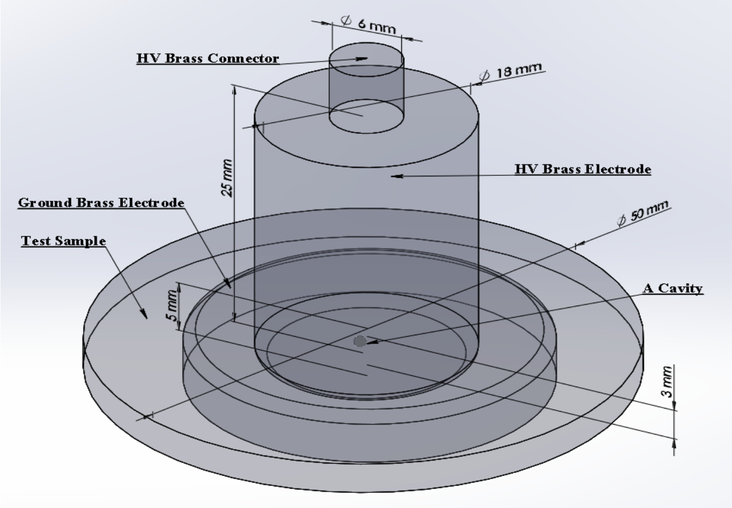

Figure 3.9: Schematic geometry of a single test cell and a test sample.

3.4 Methodologies for an investigation into polymer degradation

The deterioration processes in solid dielectrics are induced under an electric field stress that can lead to the loss of insulating properties. In the case of gas-filled cavities within polymers, the degradation reactions by internal partial discharges are most likely to cause insulation failure that these mechanisms influence both dielectric performance and the remaining lifetime. An investigation into the cause before an upcoming failure is essential for predicting the degradation stages of the polymer. Analysis of PD characteristics during deterioration processes in a cavity embedded in dielectric material can be correlated using microanalysis techniques that allow investigation into the changes in the microstructure, i.e. physical, thermal and chemical properties can alter during the ageing processes, i.e. optical microscopy, dielectric spectroscopy, differential scanning calorimetry (DSC), thermogravimetric analysis (TGA), Fourier transform infrared spectroscopy (FTIR), Raman spectroscopy, scanning electron microscopy (SEM) and energy dispersive X-ray (EDX) spectroscopy. Further details are provided in the following sections.

3.4.1 Optical microscopy

Optical microscopy is carried out using a Leitz Aristomet optical microscope, coupled Leitzlar objective lens, which can be also combined with a charge-coupled device (CCD) detector for collecting images at the focused area as shown in Figure 3.10. The optical properties of polymers used in the test samples are transparent, which facilitates observation of a cavity embedded in the insulation. The sample can be examined through a magnification of objective lens under the luminescence of scatter light, which can be operated in both refraction or transmission modes. In the accelerated ageing process, conventional optical microscopy is used to observe the morphological changes of test samples to identify the stages of degradation mechanisms before an upcoming failure. The sample preparation used for optical microscope is performed by using a soft cotton swab for wiping the surface of the test sample in both upper and lower sides and then used liquid acetone to remove small particles and the fine layer of silicone oil.

Figure 3.10: Photograph of the optical microscopy instrument.

3.4.2 Gold sputter coater

A gold coating is used for preparing samples to increase their electrical conductivity before performing scanning electron microscopy or dielectric spectroscopy. The surface of test sample is coated using an Emitech K550X sputter coater as shown in Figure 3.11. It is adjusted to ensure the automatic cycle for venting gas in the chamber to atmosphere and setting at 25 mA for 2 minutes and a vacuum of 0.1 millibars for coating gold layer on the surface with the deposition thickness of 20 nm.

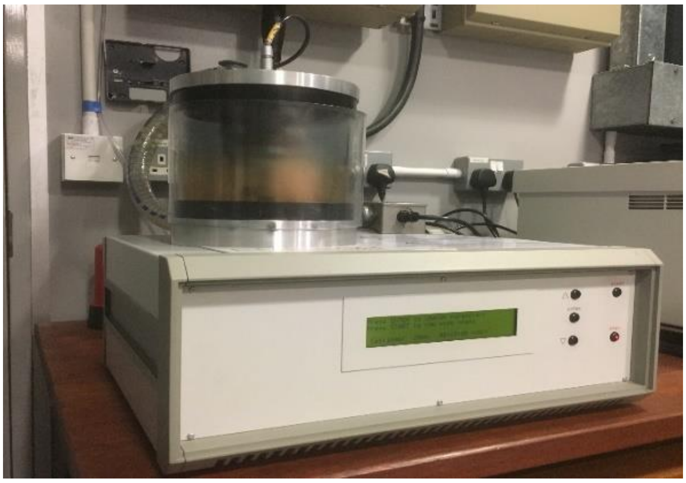

Figure 3.11: Photograph of the gold sputter coater instrument.

3.4.3 Dielectric spectroscopy

The characteristic property of dielectric material under an applied alternating current is related to the complex permittivity, ε^*, which depends on two parameters as a function of frequency between the real relative permittivity, ε' and the imaginary relative permittivity, ε''. The dielectric constant, ε' is the real part of the complex permittivity, which is a measure of the energy storage in the bulk material while the dielectric loss, ε'' is the imaginary part of the complex permittivity, which the electric energy transfer is dissipated in insulation material. The dissipation factor or tan delta can be defined as $\varepsilon''/\varepsilon'$ and is proportional to a ratio of energy loss and energy storage [184]. Dielectric spectroscopy is performed using a Solatron 1296 dielectric interface combined with a Schlumberger SI 1260 impedance/phase gain analyser as shown in Figure 3.12. The sample preparation used for dielectric spectroscopy is performed by coating gold layers of the centre part of the test sample with a circular diameter of 30 mm in both upper and lower sides. This sample is place between parallel brass electrodes in a chamber to shield the sample from the surrounding noise during the measurement. At the beginning of the measurement for Solatron should be set to sweep for collecting integrated data over 10 cycles at 10 points per decade in the range of frequency between 10^{-1} Hz and 10^{6} Hz, including a frequency of 50 Hz.

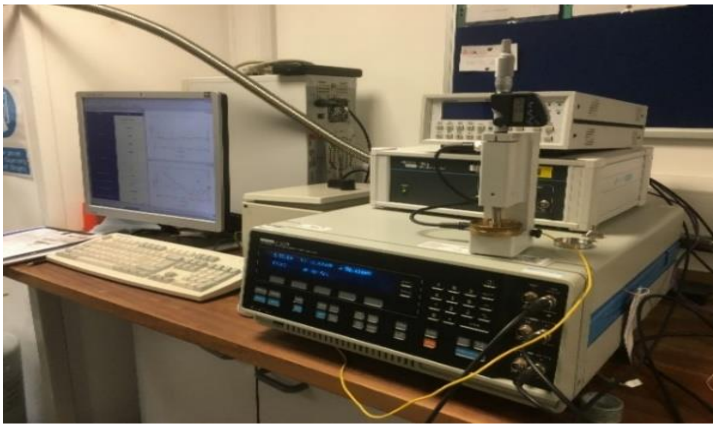

Figure 3.12: Photograph of the dielectric spectroscopy instrument.

3.4.4 Differential scanning calorimetry

Differential scanning calorimetry (DSC) is the typical method used for thermal analysis [185-186]. The basic DSC system is the measurement of the difference of heat flow rates, $\Delta\Phi$, from two pans that the sample pan and the reference pan are maintained with a gradual increase at the same rate of temperature as shown in Figure 3.13. As an example, the characteristic for a semi-crystalline polymer is plotted the heat flow rate as a function of temperature obtained by the melting temperature, T_m, crystallisation temperature, T_c and glass transition temperature, T_g as shown in Figure 3.14. When the thermal transition changes the state from solid phase to liquid phase, the heated absorption of the sample is higher than the reference. The DSC curve of the heat flow as a function of temperature is generally obtained by two reactions between an endothermic melt and an exothermic crystallisation, where the thermal energy of the sample is absorbed and released respectively. The DSC instrument is obtained using a PerkinElmer DSC 7 with Pyris analysis software as shown in Figure 3.15, which can be set to measure over a range of temperatures between -180 °C and 600 °C. The sample preparation used for DSC test is performed by using a steel razor blade for cutting the centre portion of the cavity surface from the bottom layer of the test sample. The mass of a sample should be weighted less than 10 mg, which contained in an enclosed aluminium can and covered with an aluminium lid. For reliable measurement, this instrument is calibrated before beginning use by selecting indium material, which is known to have a melting point of 157.8 °C with setting the heating rate at 10 °C/min as shown in Figure 3.16.

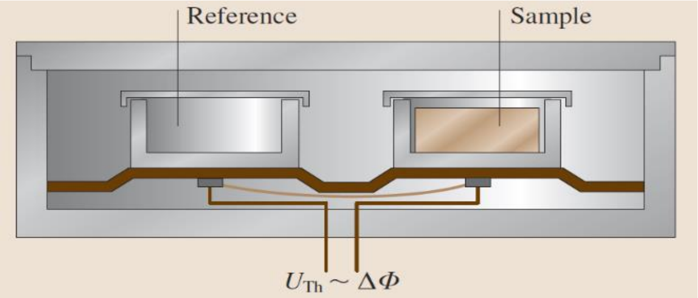

Figure 3.13: Schematic diagram of the differential scanning calorimetry [187].

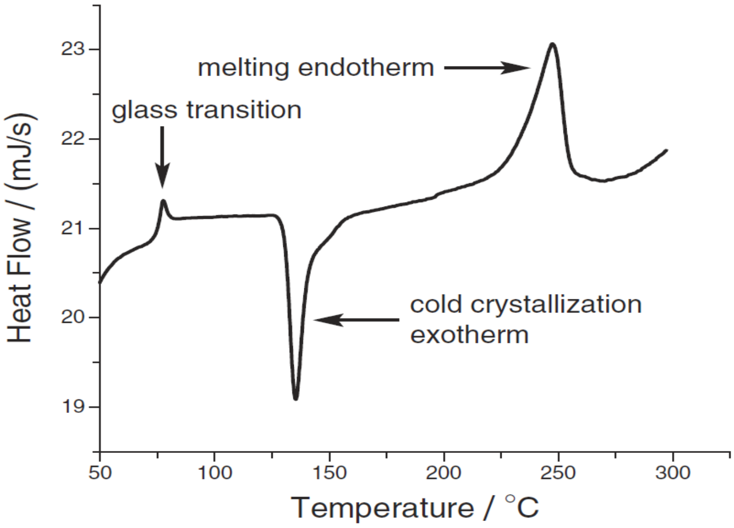

Figure 3.14: DSC curve of thermal transition from PET material [188].

Figure 3.15: Photograph of the differential scanning calorimetry instrument.

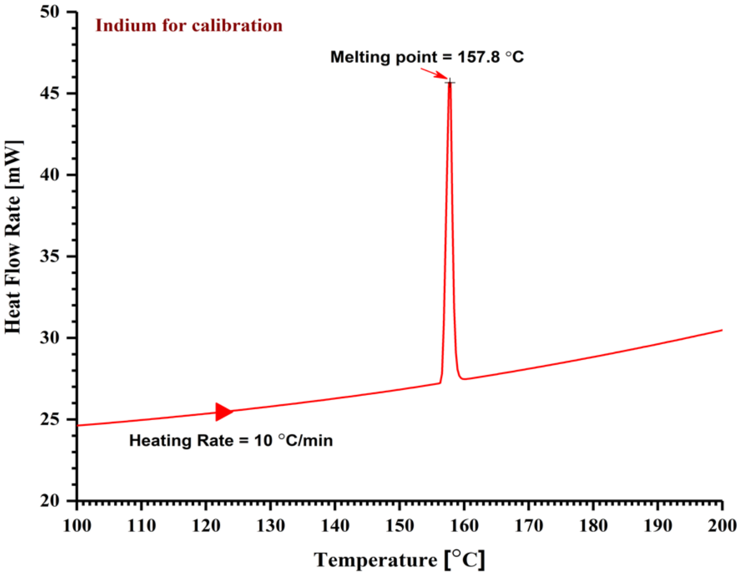

Figure 3.16: Indium material for calibration used in the DSC experiment.

3.4.5 Thermogravimetric analysis

Thermogravimetric analysis (TGA) is a technique for thermal analysis, where a substance is heated in a furnace and monitoring the rate of change in the mass loss as a function of temperature. TGA measurement was equipped using a PerkinElmer Pyris 1 TGA instrument, operated with Pyris thermal software from room temperature to 900 °C at a heating rate of 10 °C/minute in an inert atmosphere as shown in Figure 3.17. The sample preparation used for TGA test is performed by using a thin stainless steel razor blade for cutting the whole part of the cavity from the test sample. The mass of a sample should be weighted less than 50 mg, which contained in an aluminium pan and hanged by the sample holder. As an example, analysis of the decomposition process for PDMS polymers was initially undertaken, where the coincidence of a TGA curve and a DSC curve is marked at the intersection of temperature, T_p as shown in Figure 3.18.

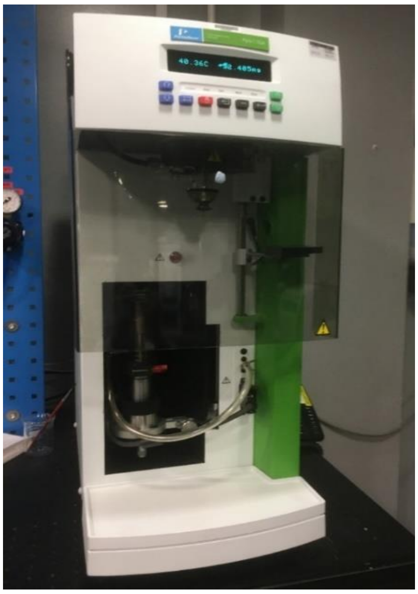

Figure 3.17: Photograph of the thermogravimetric analysis instrument.

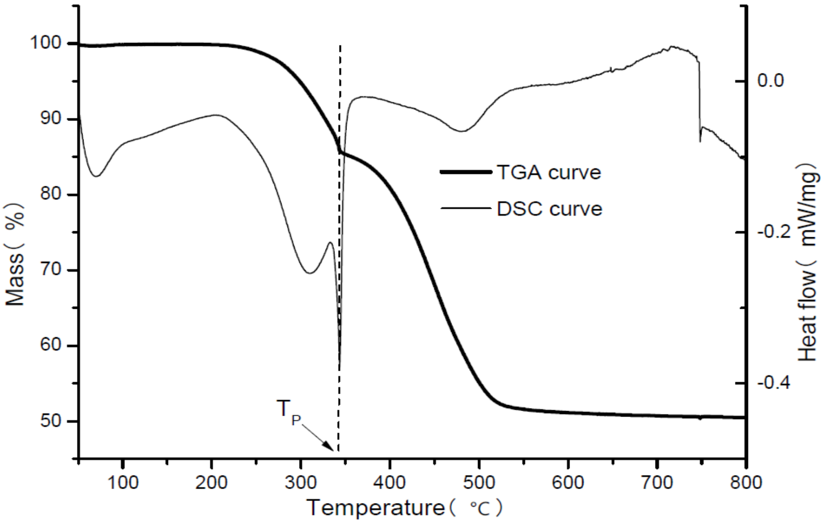

Figure 3.18: TGA and DSC curves of PDMS samples as a function of temperature [189].

3.4.6 Fourier transform infrared spectroscopy

Fourier transform infrared spectroscopy (FTIR) is an analytical technique used to identify the structure of molecular composites [190]. The operating principle is that when the sample absorbs radiation at a focal point of an infrared incident, energy is transferred from the incident radiation to the molecular bulk of the sample. Vibrational energy levels correspond to the wavelengths of the characteristic molecule that are directly absorbed by the sample. The infrared spectrometer is a PerkinElmer Spectrum GX instrument as shown in Figure 3.19 that can be operated in both reflection or transmission modes. When the transmission mode is selected, the radiation is generated by a source through the interferometer, which comprises two infrared beams between the transmitted beam and the reflected beam. Subsequently, this beam is transmitted from the condenser Cassegrain reflector to the sample and carried to forward from the objective Cassegrain reflector to the remote aperture. Finally, the signal is transferred to the detector or the optical viewer. On the other hand, when the reflection mode is used, the infrared beam is continually carried from the reflectance mirror to the objective Cassegrain reflector and reaches to the sample through the substrate. Afterwards, this beam is reversed to the sample and emitted from the sample surface to proceed towards the detector as shown in Figure 3.20. Each FTIR spectra is obtained in the mid-infrared range of wavelengths between 4000 cm^{-1} and 580 cm^{-1} over 32 scans at a resolution of 4 cm^{-1}. The FTIR system is calibrated, which background spectrum of an infrared beam is transmitted directly without any sample towards the detector in atmosphere before the sample is placed in the sample holder. The single-channel intensity from calibration is illustrated as shown in Figure 3.21.

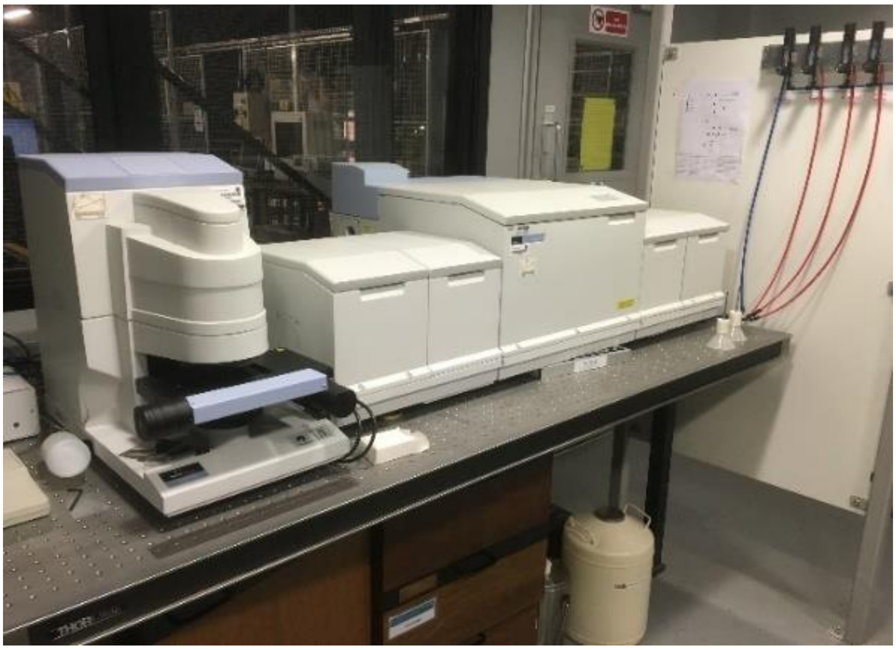

Figure 3.19: Photograph of the Fourier transform infrared spectroscopy instrument.

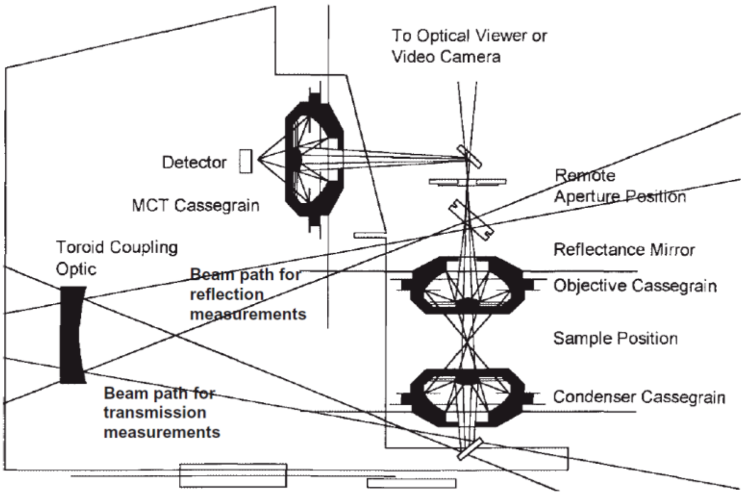

Figure 3.20: Schematic diagram of the FTIR experiment [191].

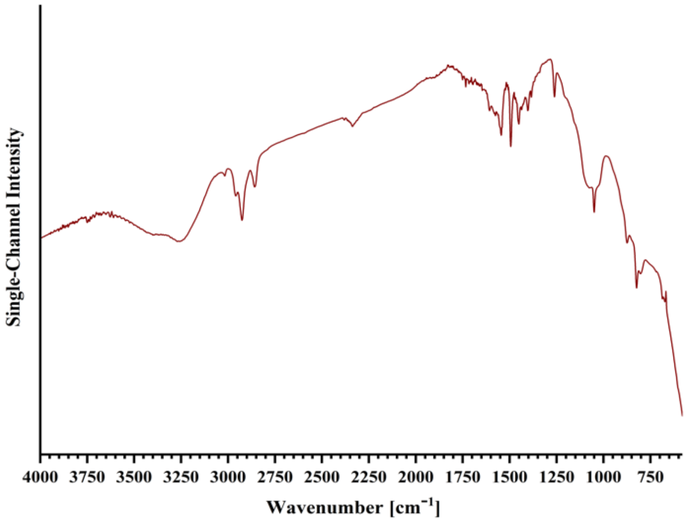

Figure 3.21: FTIR background spectrum obtained from calibration.

3.4.7 Raman microscopy

Raman microscopy is a vibrational spectroscopic method for identifying molecular compounds in the bulk of dielectric material, where a focal point on the sample surface can be magnified for observation through optical microscope [192-193]. The infrared spectrum is produced by the incident radiation from a laser beam to the test sample, which determines the characteristics of chemical composites. The light back-scattering obtained is transmitted from the notch filter to the beam splitter, and the laser beam is directed towards the sample along the vertical axis of the microscope, which is placed between two lenses. One lens observes the signal from the sample and another lens is used as a focal point of the signal towards the spectrometer as shown in Figure 3.22. The Raman spectrometer used is a Renishaw Raman RM1000 instrument combined with a Leica microscope and an excitation source of 785 nm diode laser with a rated power of 25 mW as shown in Figure 3.23.

Each Raman spectra is set a maximum intensity of a laser beam at 100 % with scanning an accumulation of 25 scans at 10 seconds in the wavelength between 3200 cm^{-1} and 100 cm^{-1}. The system is calibrated using silicon, where this peak is obtained at Raman shift of 520 cm^{-1} as shown in Figure 3.24.

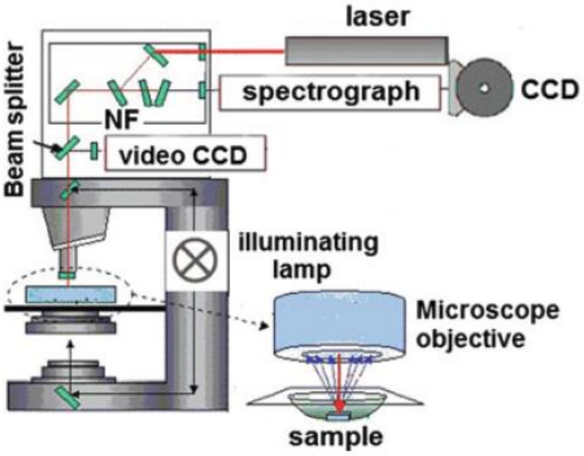

Figure 3.22: Schematic diagram of the Raman experiment [194].

Figure 3.23: Photograph of the Raman spectroscopy instrument.

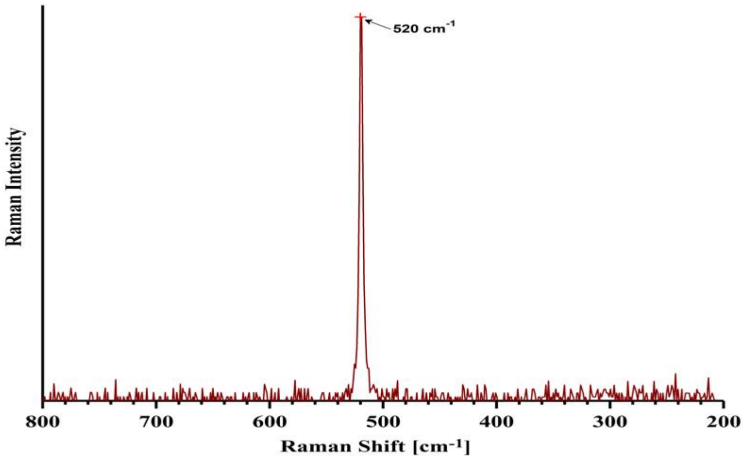

Figure 3.24: Raman spectrum of silicon material obtained from calibration.

3.4.8 SEM and EDX microanalysis

The technical high-resolution images and chemical microanalysis for small sample sizes are generally obtained by using scanning electron microscopy (SEM) and energy dispersive X-ray (EDX) instruments [195]. The SEM and EDX systems for microanalysis of test samples in this research is implemented by using a Philips FEI XL30 ESEM instrument with visual display monitors and a vacuum chamber as shown in Figure 3.25. The sample preparation used for SEM microanalysis is performed by using a steel razor blade for cutting the focused area within the cavity of the test sample. The specimen is placed on an aluminium stub and firmly attached to a conductive carbon tape for a good conductive contact and then coated by gold layers to increase the surface conductivity. This test sample is placed on an aluminium holder in a vacuum chamber before undertaking microanalysis. The SEM detector in cooperation with X-ray spectrometer is a method for analysis of microstructure and identification of elemental composites in bulk materials. The details of SEM micrographs are displayed on the monitor from a local scan at a focused region of the topographical surface, which is obtained from the signal due to the interaction between the high-energy beam of electrons with the atomic bulk on the sample surface. The X-ray spectrum is acquired at the localised site of the sample such that X-ray peaks can be identified to perform quantitative analysis of chemical compounds in the energy range from 0 to 5 keV. When the focused electron beam from an electron gun interacts to excite molecules in the sample, several types of signals are emitted: secondary electrons (SE), back-scatter electrons (BSE), Auger electrons and characteristic X-rays. The secondary electrons can be formed predominantly from the two major signals between primary electrons and Auger electrons, which emerge from the sample surface. The scanned images provide information about test samples can be produced by the emission of secondary electrons and backscatter electrons. The X-ray spectrum can be used to identify the quantities of chemical constituents as a result from the emission of energies in the sample excited by Auger electrons and the pointed locations of spectral peaks obtained by characteristic X-rays as shown in Figure 3.26.

(a) (b)

Figure 3.25: Microanalysis instruments: (a) scanning electron microscope (SEM) and energy dispersive X-ray (EDX) with visual display monitors and (b) test samples in a vacuum chamber.

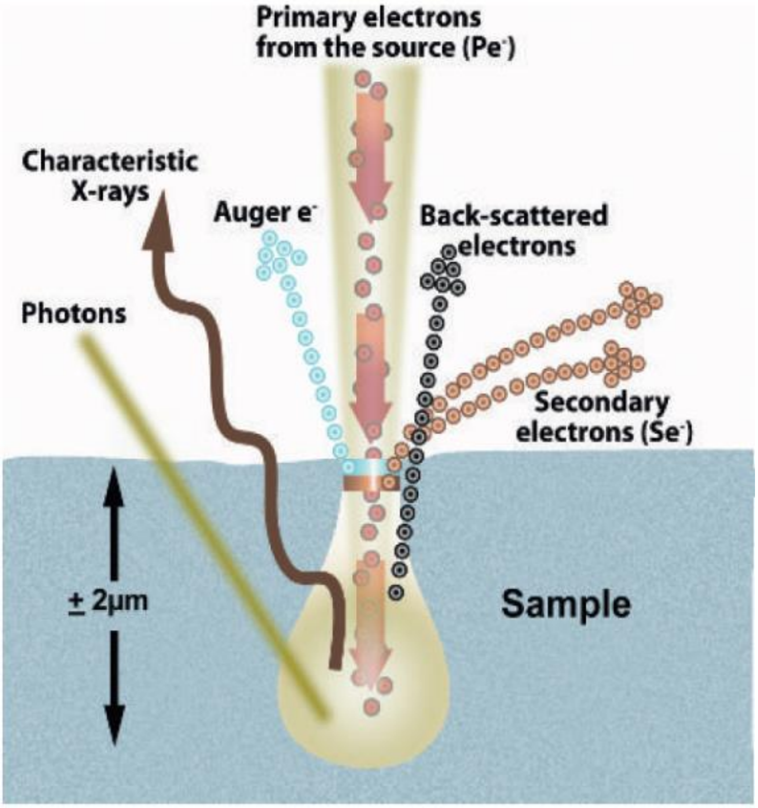

Figure 3.26: Interaction of a beam of incident electrons in the bulk of dielectric material [196].

3.5 Summary

This chapter has detailed the methodological and experimental procedures of the PD measurement and the accelerated ageing process. Firstly, the preparation procedures for test samples have been detailed. The PD experimental set-up was performed to facilitate PRPD analysis, which detected the PD signals from Mtronix MPD 600 and also provided information of the calibration method, including the details of the PD test cell and multiple test cells. Various techniques of microanalysis were used to investigate the changes in physical, electrical, thermal and chemical properties of the test samples caused by PD activity during the ageing test with specific technical instruments. These techniques have been briefly introduced and explained.

Chapter 4 Analysis of Degradation Mechanisms by PD activity within a Cylindrical Flat-Shaped Cavity in Polyethylene Material

The purpose of this chapter is to present an investigation into a cylindrical flat-shaped cavity embedded in polyethylene material undergoing accelerated ageing. The PD characteristics of PDIV and accelerated ageing levels are analysed from twenty samples. The evolution of PRPD patterns is undertaken to reveal degradation processes on the cavity surface due to the effect of a long-term period of ageing. The various techniques for microanalysis are performed to explore the causes of localised erosion such as corrosive by-products and the black bulk on the cavity surface regarding physical, thermal and chemical properties, i.e. dielectric spectroscopy, differential scanning calorimetry (DSC), Fourier transform infrared spectroscopy (FTIR), scanning electron microscopy (SEM) and energy dispersive X-ray (EDX). Moreover, analytical results of PD characteristics in both PRPD patterns and PD quantities related to diagnosis of degradation mechanisms on the cavity surface are reported, which can be distinguished into three significant cases in terms of deterioration mechanisms, electrical tree initiation and upcoming failure. The last section is given a summary of this chapter.

4.1 PD Characteristics at the PDIV level

An experimental investigation into the characteristics of PDIV measurement was determined by finding the average PDIV of twenty test samples, each containing a flat-shaped cavity of diameter 2 mm and 0.3 mm in thickness. All samples were tested by increasing the voltage until each sample exhibited the initiation of PD activity and then PD data was recorded for 10 min. The PDIV as a function of twenty test samples is illustrated in Figure 4.1 (a). The results show that the maximum and minimum values were 1.787 kV and 1.287 kV respectively while the average value was 1.486 kV. The average number of PDs per cycle was obtained with maximum and minimum values of 9 and 2.27 respectively while the average value was just over 5 as shown in Figure 4.1 (b). Also, an amount of average apparent charge was 21.74 pC with the highest value of 48.10 pC and the lowest value of 8.55 pC as shown in Figure 4.1 (c) while the scatter distribution of apparent charge in three-dimensional axes is illustrated in Figure 4.1 (d), which the front waveform showed a steep magnitude at the initial measurement and followed by the tail with lower magnitude charges. It is suggested that the discharge behaviour depended on the changes in gas pressure and chemical composites inside the cavity [33, 182].

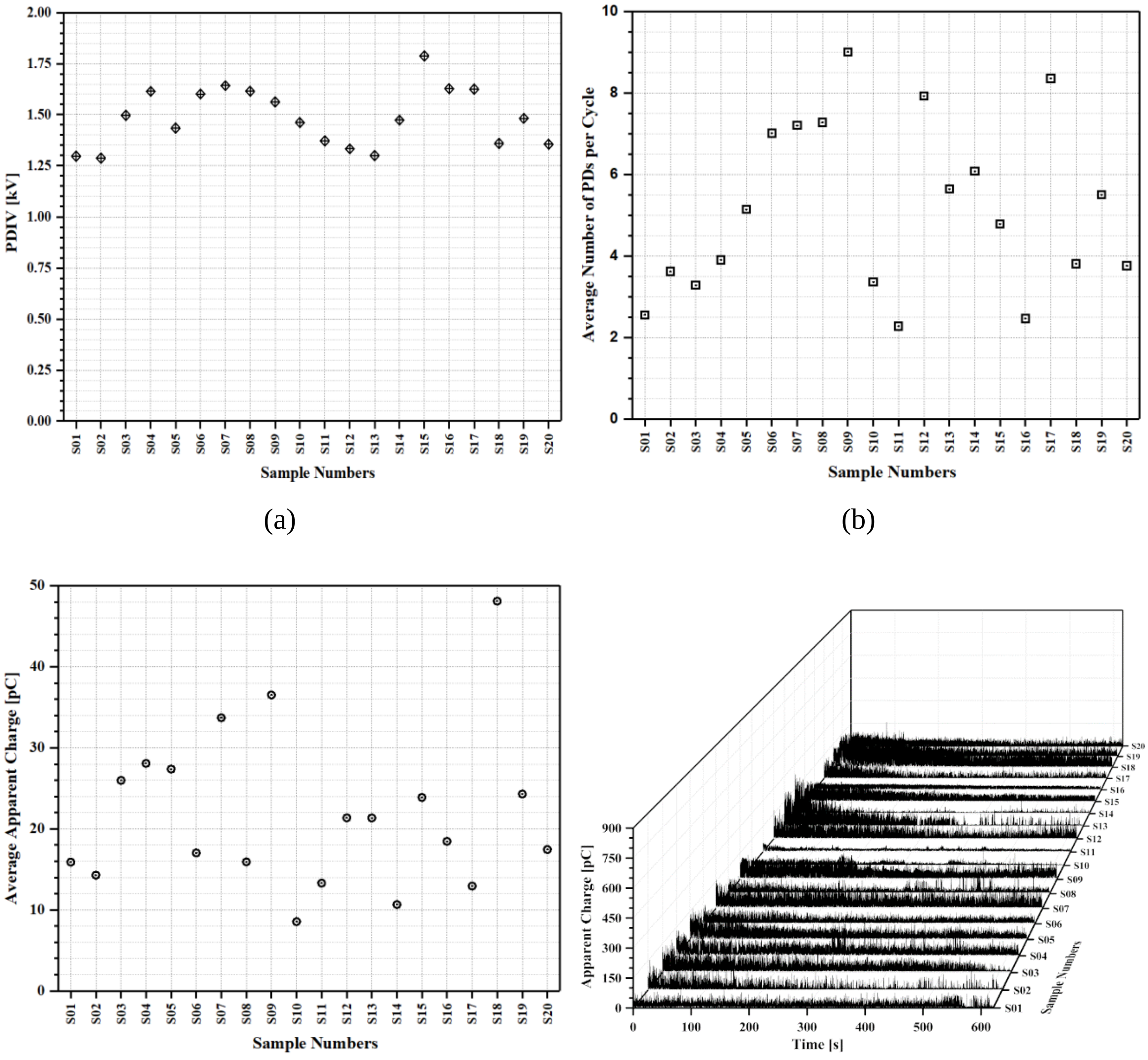

(a) (b)

(c) (d)

Figure 4.1: PD data of twenty test samples at the PDIV level: (a) the PD inception voltage, (b) the average number of PDs per cycle, (c) the average apparent charge and (d) the scatter distribution of apparent charge.

4.2 PD characteristics at the accelerated ageing level

After measuring PDIV, the PD characteristics from twenty samples were performed by increasing the level voltage for the accelerated ageing process. The applied voltage level was obtained from the PDIV measurement of twenty samples. The ageing voltage magnitude level for the ageing test was set by increasing the average PDIV by 68% for the accelerated degradation process induced by PD within an air-filled cavity for all samples. In this experiment, each sample containing a single flat-shaped cavity was aged by increasing the voltage magnitude of 2.5 kV, 50 Hz and then acquired the PRPD patterns for 10 min, which this data can be exported both PRPD patterns and PD quantities through MATLAB code (Appendix D.1). The samples were electrically stressed with the constant voltage level using the multi-test cells for a long-term period of ageing as detailed in Sections 3.3.1

and 3.3.2. The scatter plot of average apparent charge as a function of twenty samples is illustrated in Figure 4.2 (a), where the average apparent charge was 26.63 pC with maximum and minimum values about 44.93 pC and 6.40 pC respectively. The average number of PDs per cycle was obtained with maximum and minimum values of 15 and 2 respectively while the average value was just over 8.5 as shown in Figure 4.2 (b). The scatter distribution of apparent charge in three-dimensional axes are shown in Figure 4.2 (c). Comparison of PD characteristics between accelerated ageing and PDIV levels shows that the average apparent charge under the accelerated ageing was slightly more than the PDIV while the average number of PDs per cycle at the ageing stage was higher than the PDIV stage. The scatter distribution of apparent charge at the accelerated ageing exhibited larger magnitudes, compared with the PDIV level.

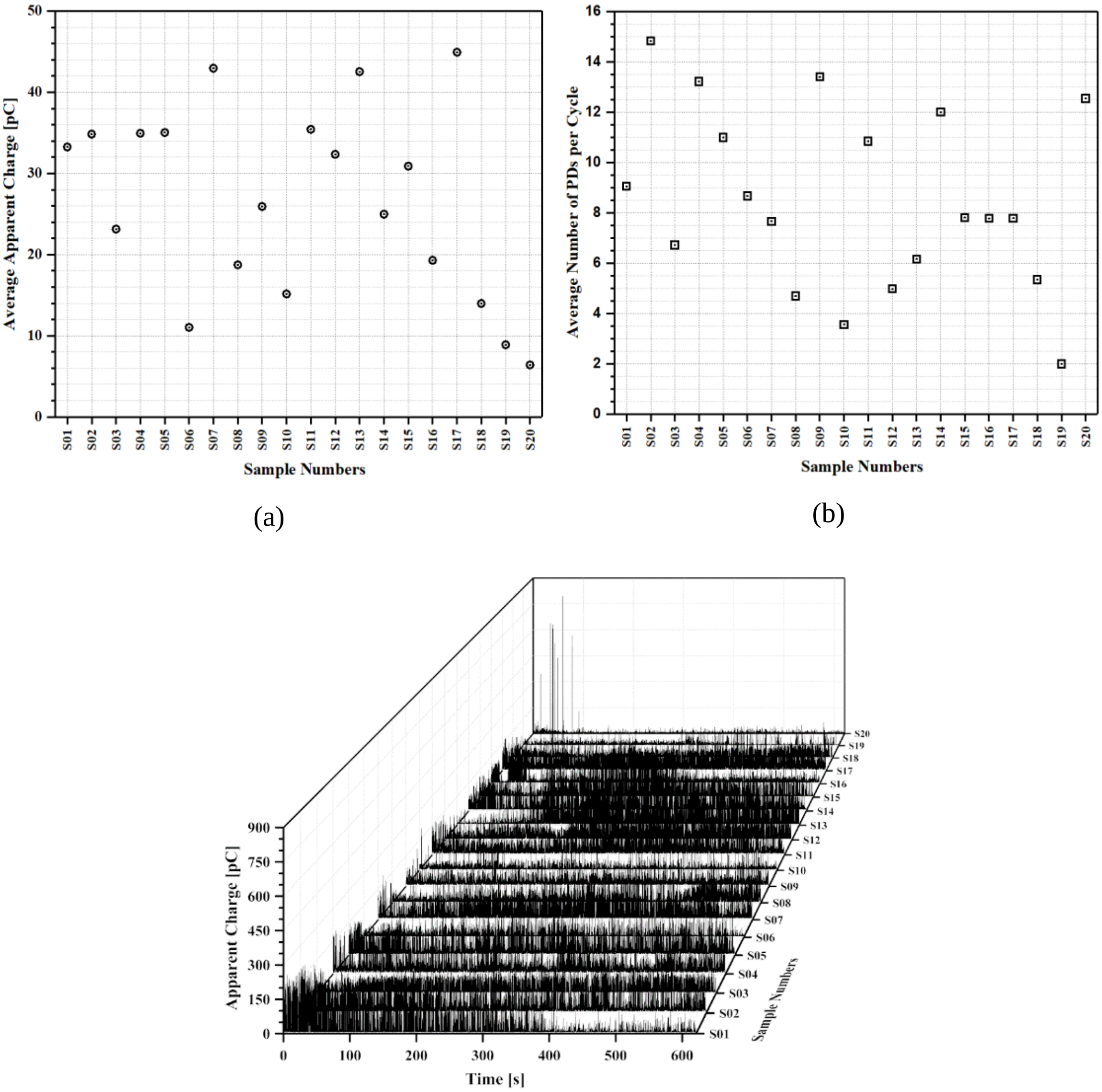

(a)

(b)

(c)

Figure 4.2: PD data of twenty test samples at the accelerated ageing level at the applied voltage level of 2.5 kV, 50 Hz: (a) the average apparent charge, (b) the average number of PDs per cycle and (c) the scatter distribution of apparent charge.

4.3 PD characteristics of degradation mechanisms in a cavity

An investigation into PD characteristics in an air-filled cavity under ageing tests related to the cavity formation was examined to explore the cause of deterioration mechanisms within the cavity surface.

4.3.1 Optical microscopy

Before measuring PD, the test sample containing a flat-shaped cavity of diameter 2 mm was observed a virgin cavity as shown in Figure 4.3 (a). The cavity formation of corrosive by-products and some deposited by-products in the centre location on the cavity surface was formed after ageing 308 h and 409 h respectively as shown in Figures 4.3 (b) to 4.3 (d). After further ageing of just over 1000 h, the cavity surface at this localised erosion was obtained with large deposited by-products as shown in Figures 4.4 (e) and the initiation of electrical trees as shown in 4.4 (f). The deposited by-products inside a cavity occur due to PD induced the oxidative degradation [197], where chemical by-products of the bulk on the cavity surface was identified as liquid droplets and crystals as reported in [157, 198], which the chemical element of hydrogen can be detected by using a technique of gas chromatography analysis [199]. It has also been reported that after a prolonged period of ageing, some micro-protrusions were formed on the centre cavity surface due to the enhancement of electric fields [200] and the growth of tree-like structure was found at localised erosion of crystals on the cavity surface [145].

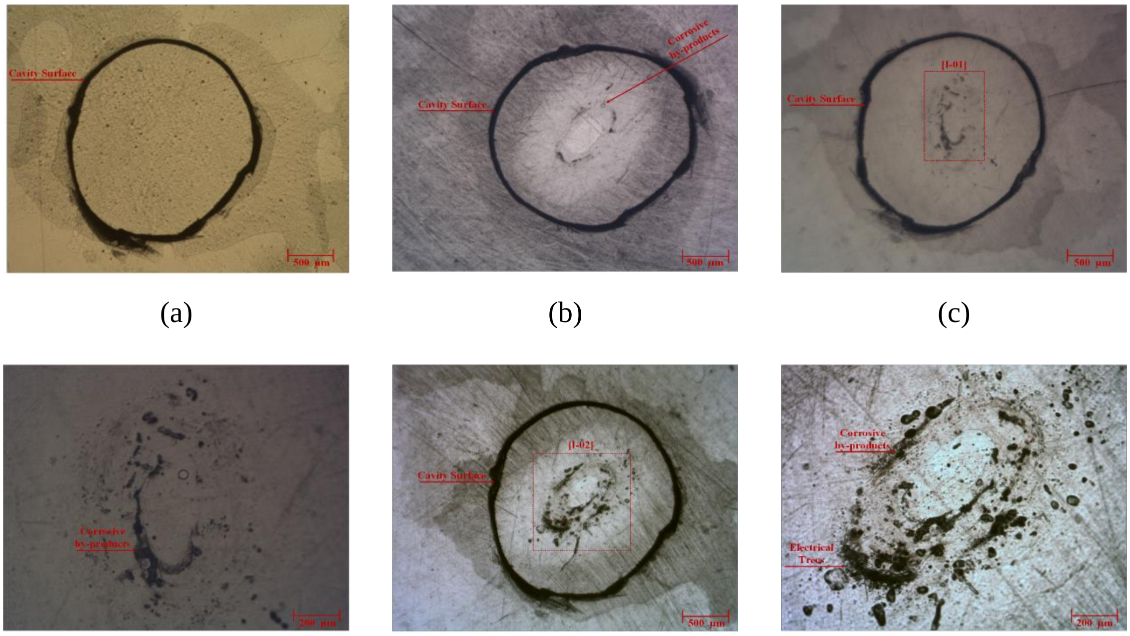

(a) (b) (c)

(d) (e) (f)

Figure 4.3: Morphological changes of the polyethylene sample containing a flat-shaped cavity of diameter 2 mm at various ageing times: top-section views of (a) a virgin cavity, (b) 308 h, (c) 409 h, (d) a high-magnification in the micrograph (c), (e) 1004 h and (f) a high-magnification in the micrograph (e).

4.3.2 Measurement of PD activity

The line graph between average apparent charge and average number of PDs per cycle was acquired continuously to record every 30 minutes during the ageing process from 10 min to 6 h, which tended to decrease from 13 pC to 3 pC and from 15.5 to 2 respectively as shown in Figure 4.4 (a). Moreover, these quantities over ageing from 409 h to 419 h tended to increase from 15 pC to 27 pC and from 9 to 12 respectively as shown in Figure 4.4 (b). The evolution of PD characteristics in the sample containing a flat-shaped cavity related to the cavity formation from a virgin cavity to electric tree initiation was distinguished into three distinct PRPD patterns. The initial ageing of PRPD patterns linked to the rabbit-like pattern with a long ear, resulting from the long time lag for the occurrence of a PD event [36, 119] and this pattern then changed to a shorter ear after ageing 4 h as shown in Figures 4.5 (a) and 4.5 (b) respectively. After further ageing 308 h and 409 h, the transition from this pattern to the turtle-like pattern was observed, resulting in the short time lag for the occurrence of a PD event [36, 119] as shown in Figures 4.5 (c) and 4.5 (d) respectively. The significant consequence of PRPD patterns exhibited the wing-like patterns with SPMDs, which appeared slight magnitude discharges both positive and negative half-cycle after ageing of just over 1000 h as shown in Figures 4.5 (e) and 4.5 (f). Otherwise, the scatter distribution of apparent charge is illustrated as shown in Figures 4.6 (a) and the bar chart between average apparent charge and average number of PDs per cycle is shown in Figure 4.6 (b). It is suggested that PRPD characteristics of typical cavity discharges were identified as the rabbit-like pattern and the turtle-like pattern [201] while the wing-like pattern associated with the growth of electrical trees in dielectric material [34].

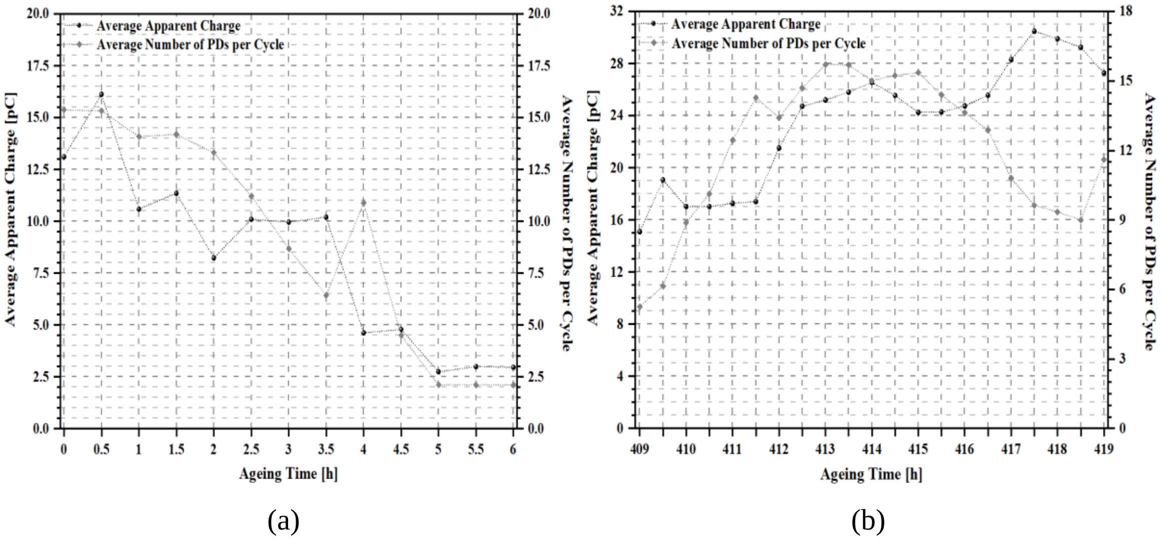

Figure 4.4: PD sequences of the polyethylene sample embedded a flat-shaped cavity of diameter 2 mm: (a) and (b) the line graph between average apparent charge and average number of PDs per cycle as a function of elasped time of ageing from 10 min to 6 h and from 409 h to 419 h respectively.

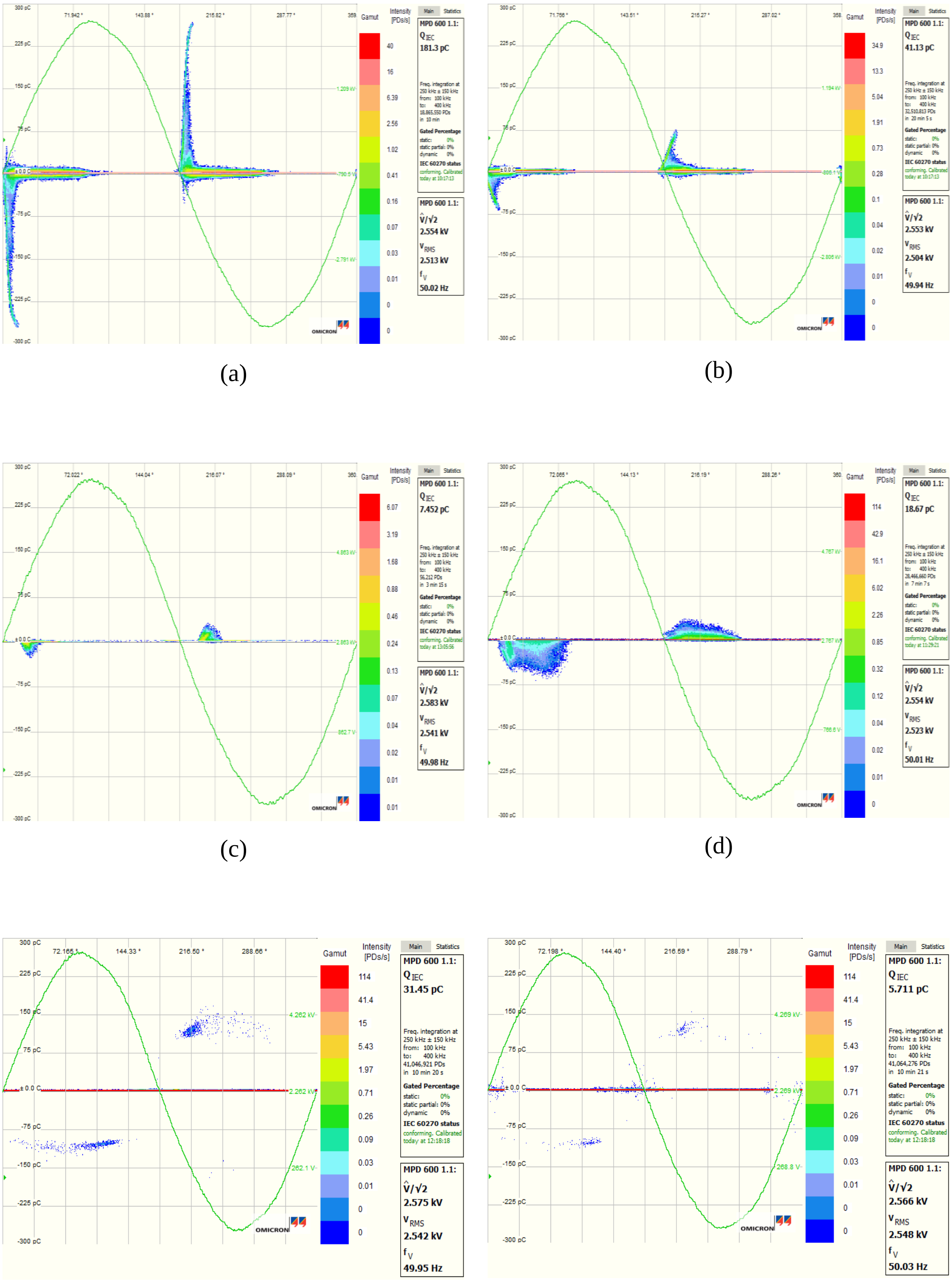

(a) (b)

(c) (d)

(e) (f)

Figure 4.5: Variation in measured PRPD patterns of the polyethylene sample containing a flat-shaped cavity of diameter 2 mm at various ageing times: (a) a rabbit-like pattern at ageing 10 min, (b) a rabbit-like pattern at ageing 4 h, (c) a turtle-like pattern at ageing 308 h, (d) a turtle-like pattern at ageing 409 h, (e) and (f) wing-like patterns after ageing 1004 h and 1005 h respectively.

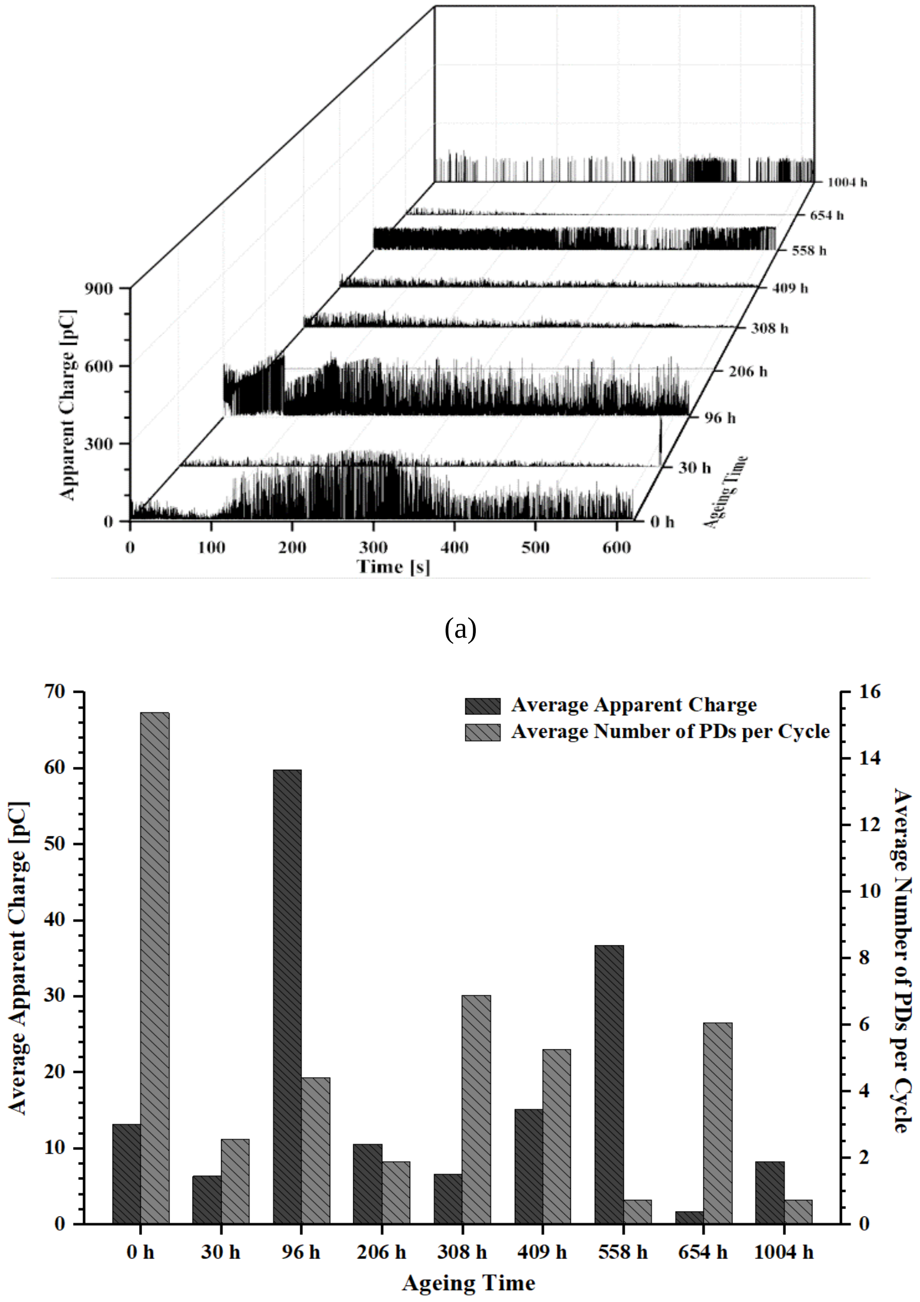

(a)

(b)

Figure 4.6: PD data of the polyethylene sample containing a flat-shaped cavity of diameter 2 mm as a function of various ageing times: (a) the scatter distribution of apparent charge and (b) the bar charge between average apparent charge and average number of PDs per cycle.

4.3.3 Dielectric spectroscopy

Dielectric spectroscopy was applied to analyse the dielectric property of the virgin sample and the test samples at various ageing times. The line graph between real relative permittivity and tan delta was measured as shown in Figures 4.7 (a) and 4.7 (b). The result shows that the sample containing a flat-shaped cavity of diameter 2 mm and the sample without a cavity were obtained to provide as a reference while the line curves of test samples after ageing were obtained by two samples at various ageing times of 139 h and 180 h. All of these samples were obtained the values of real relative permittivity in the range between 2.41 and 2.54 and the tan delta in the range between 1x10^{-3} and 7x10^{-3} while the real relative permittivity at 50 Hz of the samples after ageing 180 h was slightly higher than the sample after ageing 139 h while the tan delta at 50 Hz after ageing 180 h were larger than ageing 139 h as shown in Figure 4.7 (c). This result indicates that the trend of tan delta tended to increase with elapsed time of ageing processes, compared with an increase of dielectric loss due to thermal ageing as reported in other researches [202].

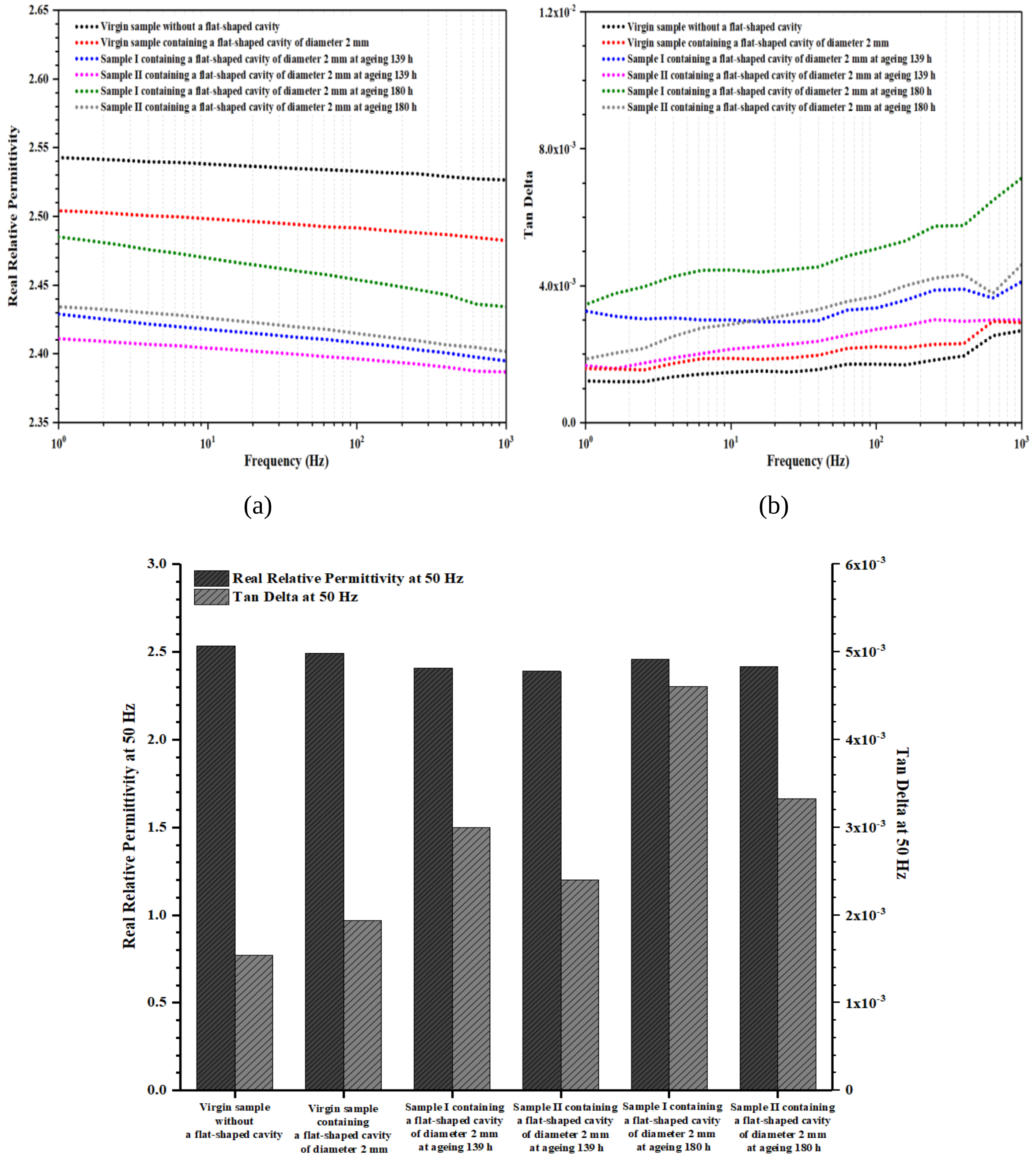

(a) (b)

(c)

Figure 4.7: Dielectric characteristics of test samples obtained from various ageing times: (a) the real relative permittivity as a function of frequency, (b) the tan delta as a function of frequency and (c) the bar chart between real relative permittivity and tan delta at 50 Hz.

4.3.4 Differential scanning calorimetry

The DSC technique was applied to examine for thermal analysis of the test samples to find out the effect of deterioration processes on the cavity surface, i.e. deposited by-products by charge bombardment. The DSC curve is illustrated both heating and cooling rates at 10 °C/min. The specimen for this DSC test was performed by using a razor blade for cutting the centre portion of the cavity surface from the bottom layer of the test sample, which the mass of this specimen should be weighted less than 10 mg and obtained in an aluminium can before undertaking the experiment. The DSC results for all samples showed the relationship between endothermic melting and exothermic crystallisation as a function of temperature in both virgin sample and test samples at various ageing times. The line graph of a virgin sample was provided as a reference, where temperatures of the melting peak, T_m and the cooling peak, T_c were obtained at 107.7 °C and 94.2 °C respectively as shown in Figure 4.8 (a). Also, the line graphs of test samples at various ageing times, the sample after ageing 50 h was obtained the appearance of three melting peaks at temperatures of 92.7 °C, 102.0 °C and 108 °C as shown in Figure 4.8 (b). In the samples after further ageing, temperatures of two melting peaks were observed at 98.5 °C and 108.6 °C for ageing 102 h and 97.8 °C and 107.8 °C for ageing 206 h, 97.3 °C and 108.1 °C for ageing 308 h, and 96.6 °C and 107.6 °C for ageing 409 h as shown in Figures 4.8 (c) to 4.8 (f) respectively. For the cooling peaks of all sample, the average value was 93.43 °C.

Interestingly, the transition of multiple melting peaks for test samples after ageing processes caused by the rearrangement of microstructural crystallisation due to the oxidative reaction. It is considered that the occurrence of multiple melting peaks were noticed with an increase of annealing temperature of polypropylene material as reported in [203]. It has been demonstrated that the transition from the endothermic melting to the exothermic crystallisation involved the change of heat energy in bulk material due to the breaking and formation of chemical bonds, which the endothermic reaction absorbed heat from its surroundings while the exothermic reaction released heat into its surroundings. The rate of heat flow can be determined by integrating the area of melting and crystallisation processes on the baseline [183]. The DSC result indicates that the virgin sample exhibited the single melting peak while the test samples after ageing processes exhibited the multiple melting peaks due to the breaking of chemical bonds in the bulk material by charge bombardment during the process of oxidative ageing.

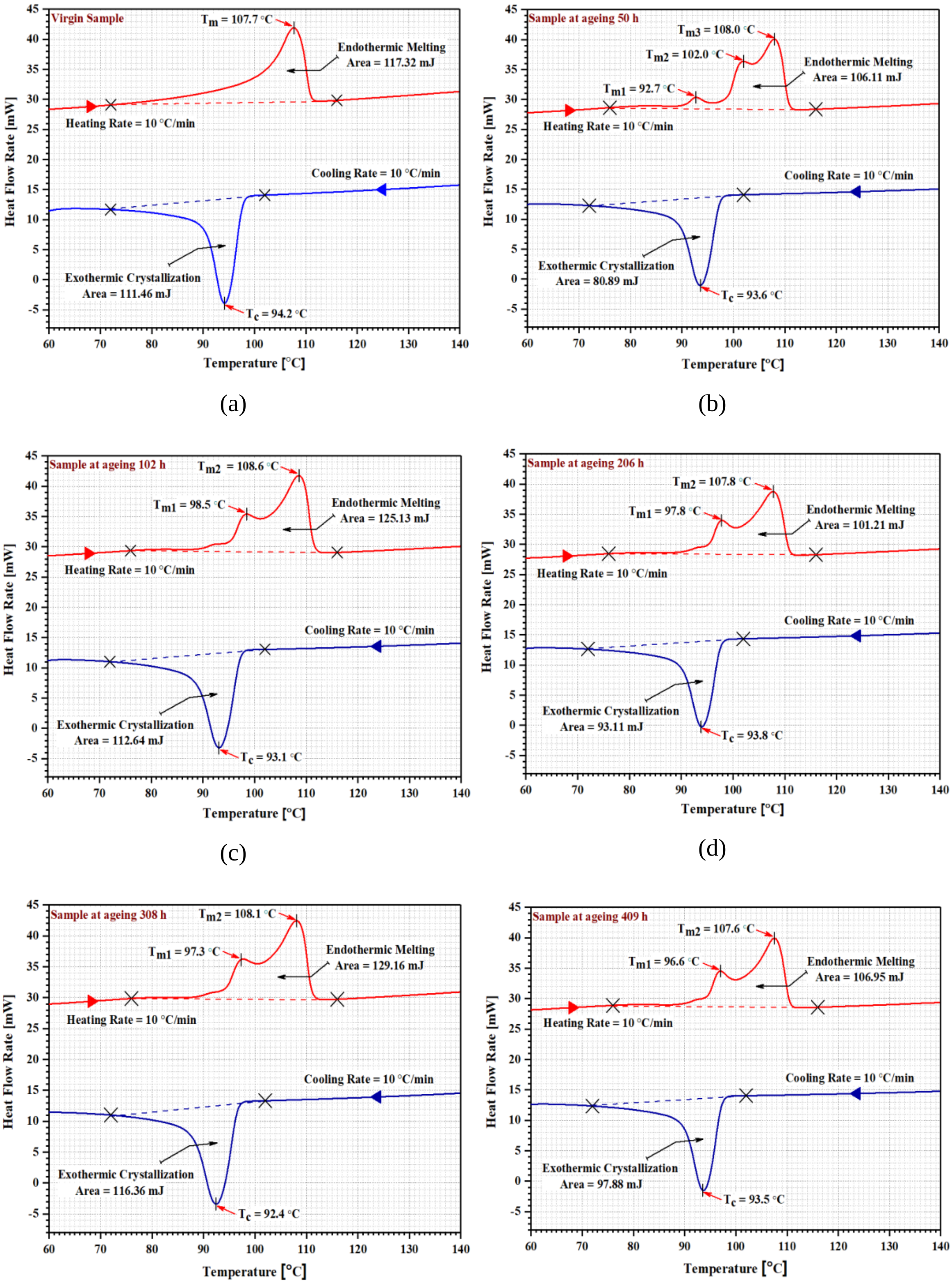

(a)

(b)

(c)

(d)

(e)

(f)

Figure 4.8: DSC curves of polyethylene samples obtained from various ageing times: (a) 0 h, (b) 50 h, (c) 102 h, (d) 206 h, (e) 308 h and (f) 409 h.

4.3.5 Fourier transform infrared spectroscopy

The application of infrared spectroscopy was used to analyse chemical composites in both a virgin sample and test samples at various ageing times in the range of wavenumbers from 4000 cm^{-1} to 580 cm^{-1}. The FTIR characteristics of strong peaked spectra and their functional groups obtained from LDPE material are listed in Table 4.1. A comparison of peak spectra between the virgin sample and the test sample at ageing 180 h is illustrated in Figure 4.9 (a), which the virgin sample was obtained to provide as spectral reference. The infrared spectra of test samples at various ageing times were obtained at 108 h, 308 h and 1004 h. The results show that the samples after ageing were obtained the wider-ranging wavenumber between 2990 cm^{-1} and 2800 cm^{-1} while the spectrum for the virgin sample was obtained the wavenumber between 2960 cm^{-1} and 2830 cm^{-1} as shown in Figure 4.9 (b). Interestingly, the presence of a new peak for all test samples after the accelerated ageing process was found as carboxylic acids at the wavenumber of 1727 cm^{-1}, whereas the absence of this peak was obtained for the virgin sample as shown in Figure 4.9 (c). With reference to the literature, a possible explanation for the appearance of a new peak was found for test samples after ageing that an investigation into localised erosion in the forms of small voids and tree growth was undertaken using a needle tip embedded in a polyethylene block, where occurred the absorption of a new peak at the wavenumber of 1730 cm^{-1} caused by the enhancement of electric field at the needle tip to break chemical bonds in the bulk polymer during the oxidation reaction [204]. The influence of gaseous mixture between oxygen and nitrogen in a void was investigated deterioration mechanisms on the polyethylene surface due to ageing, where the localised site of pitting growth exhibited the spectrum of a new peak at the wavenumber of 1715 cm^{-1} [205].

Table 4.1: FTIR characteristics of peak spectra and their functional groups obtained from LDPE.

Peak spectra (cm^{-1})	**Frequency (cm^{-1})**	**Functional groups**		**Ref.**
3644 and 3604	3650 - 3600	O−H	Alcohols, Phenols (Free OH)	[213]
3371	3400 - 3200	O−H	Alcohols, Phenols (H-bonded OH)	[213]
2990 - 2800	3000 - 2800	C−H	Aldehyde	[213]
2663	2800 - 2600	−CHO	Aldehydes (Fermi doublet)	[214]
2344 and 2019	2400 - 2000	C≡C	Alkynes	[214]
1727	1730 - 1700	C=O	Carboxylic acids	[214]
1468, 1377 and 1303	1550 - 1300	C−H	Alkanes, Alkenes	[214]
1080	1300 - 1000	C−O	Ethers, Esters	[213]
888 and 721	1000 - 650	C−H	Alkenes	[213]

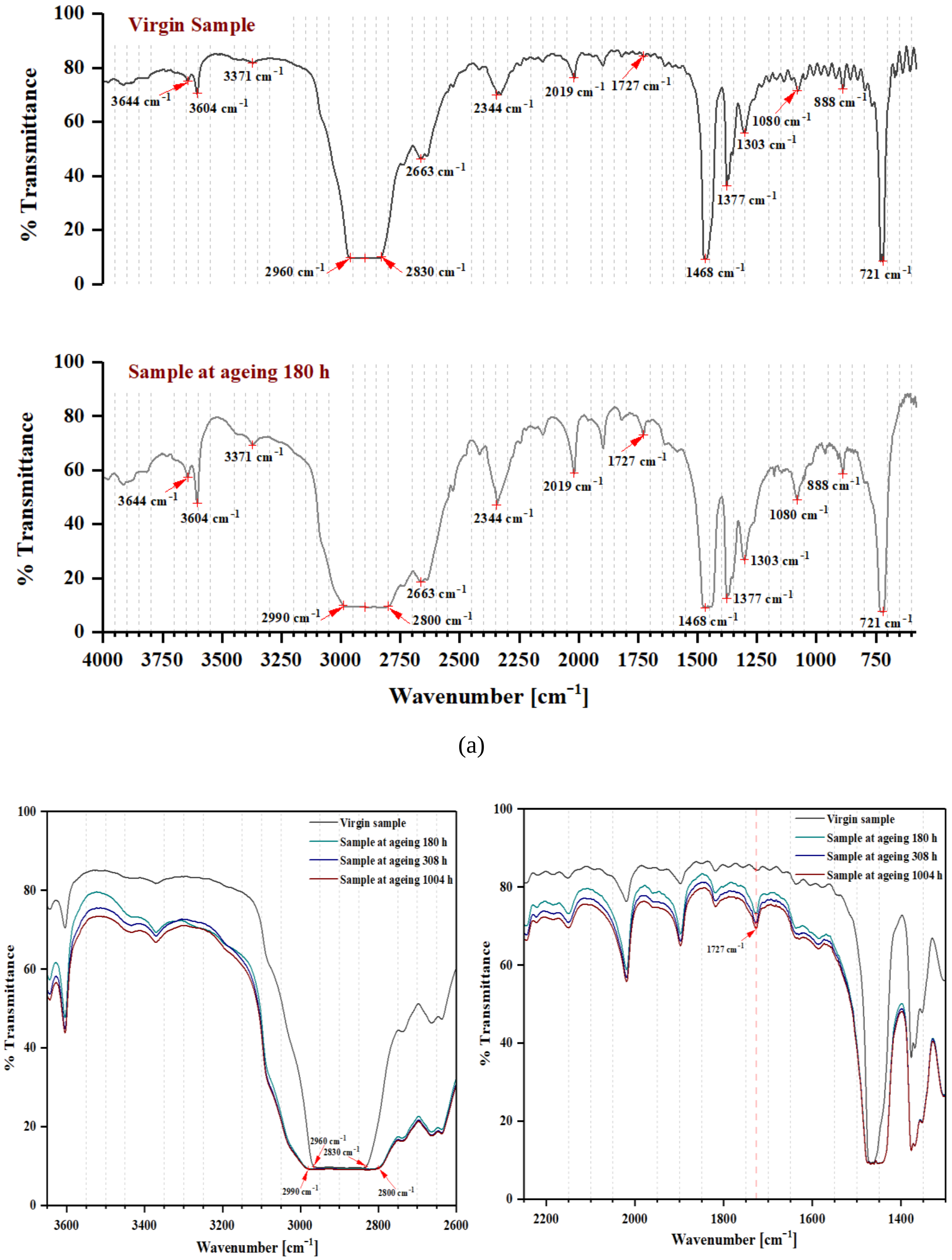

(a)

(b)

(c)

Figure 4.9: Infrared spectra of polyethylene samples obtained from various ageing times: (a) comparison between a virgin sample and a test sample at ageing 180 h, (b) and (c) comparison of spectra at the wavenumber from 3650 cm^{-1} to 2600 cm^{-1} and from 2250 cm^{-1} to 1300 cm^{-1} respectively.

4.4 PD characteristics and chemical microanalysis

The influence of internal discharges within a cavity under the accelerated ageing test lead to the changes in chemical microstructures in bulk on the cavity surface. Therefore, an investigation into PD characteristics related to microanalysis of the cavity formation was examined to reveal the cause of localised erosion on the cavity wall due to PD activity during the ageing process. In this section, three test samples were investigated to establish the evolution of PRPD characteristics related to the morphological changes on the cavity surface, including chemical microanalysis by using the combined techniques of SEM and EDX systems to explore microstructural images and chemical elements at the localised erosion sites on the cavity surface prior to failure of insulation material.

4.4.1 Optical microscopy: the polyethylene sample (I)

The polyethylene sample (I) containing a cavity diameter of 2 mm was observed the morphology of a virgin cavity as shown in Figure 4.10 (a). The appearance of surface roughness at the centre area on the cavity surface was noticed after ageing 96 h as shown in Figure 4.10 (b). After further ageing 206 h, the progressive of corrosive by-products was formed at the centre location on the inner cavity surface, where is marked by a rectangle as shown in Figure 4.10 (c) and a high-magnification at this localised site is shown in Figure 4.10 (d).

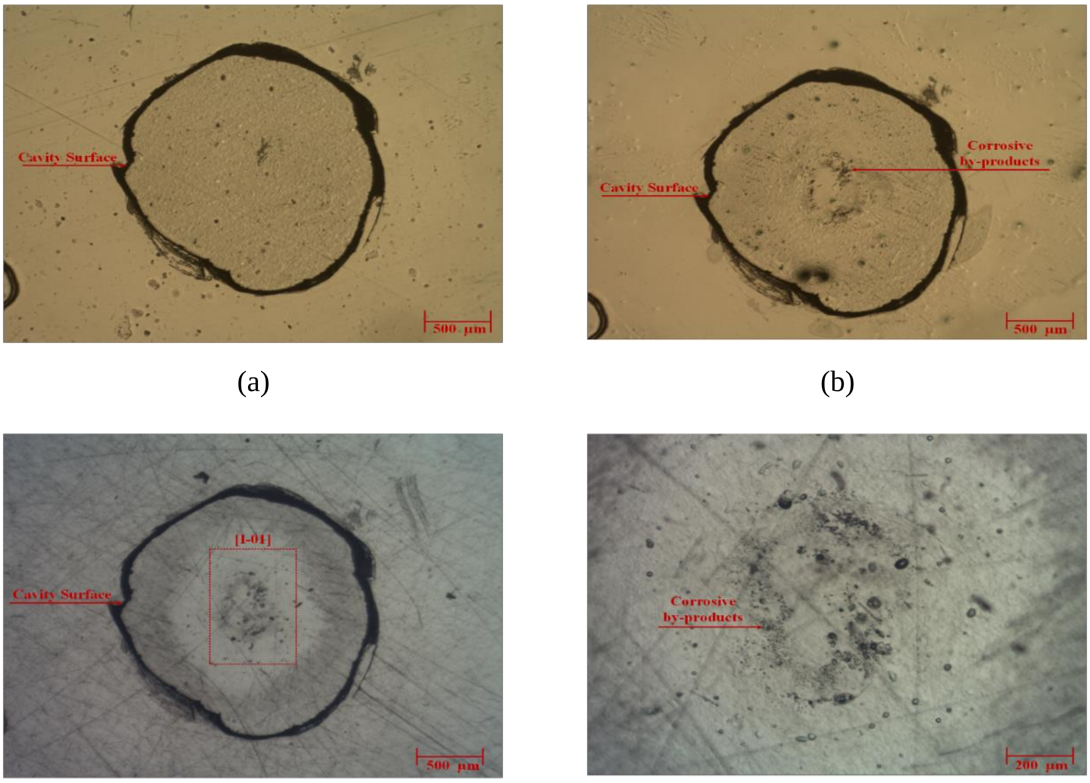

(a) (b)

(c) (d)

Figure 4.10: Morphological changes of the polyethylene sample (I) containing a flat-shaped cavity of diameter 2 mm at various ageing times: top-section views of (a) a virgin cavity, (b) 96 h, (c) 206 h and (d) a high-magnification in the micrograph (c).

4.4.2 Measurement of PD activity: the polyethylene sample (I)

PRPD characteristics exhibited the rabbit-like pattern at the initial ageing and this pattern remained unchanged with high magnitude discharges after ageing 206 h as shown in Figures 4.11 (a) and 4.11 (b) respectively. The scatter distribution of apparent charge as a function of various ageing times showed high discharge magnitudes at the initial ageing, followed by minimum discharges during further ageing 30 h and 96 h. Subsequently, the distribution of apparent charge was detected with large discharges after ageing 206 h as shown in Figure 4.12 (a). The bar chart between average apparent charge and average number of PDs per cycle can be divided into three main stages at various ageing stages as shown in Figure 4.12 (b). The result shows that the average apparent charge tended to decline from just over 30 pC at the initial ageing to just over 10 pC at ageing 30 h and followed by a steep increase from just under 6 pC at ageing 96 h to just over 70 pC at ageing 206 h while the average number of PDs per cycle tended to decrease from just over 14 to about 2 during further ageing 30 h and 96 h respectively and the figure was obtained subsequent to a high magnitude discharge of just over 4 at ageing 206 h. It is suggested that the changes of discharge magnitudes as a function of ageing time caused by the variation in pressure inside a cavity and an increase of conductivity on the cavity wall, where the characteristic discharges steeply increased before an upcoming breakdown [5].

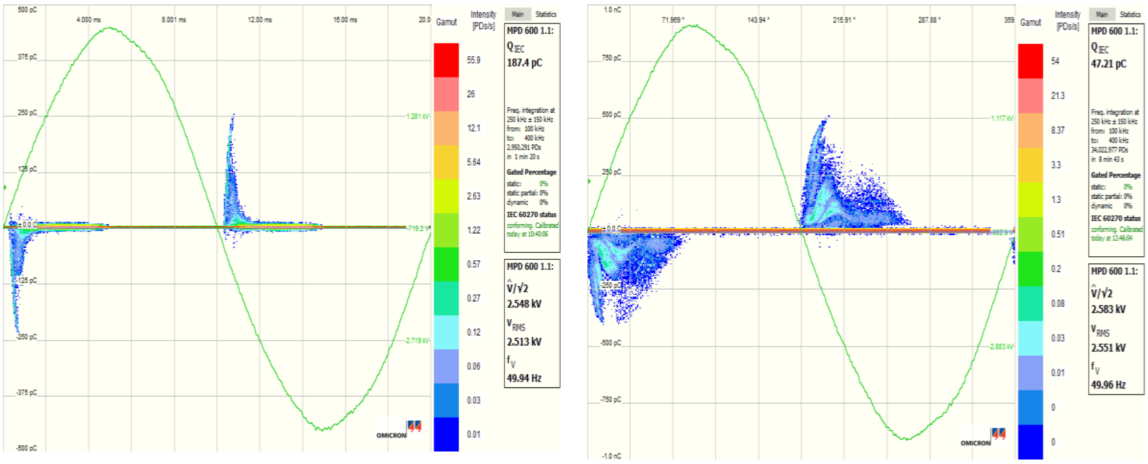

(a) (b)

Figure 4.11: Measured PRPD patterns of the polyethylene sample (I) containing a flat-shaped cavity of diameter 2 mm at various ageing times: (a) a rabbit-like pattern at ageing 10 min and (b) a rabbit-like pattern at ageing 206 h.

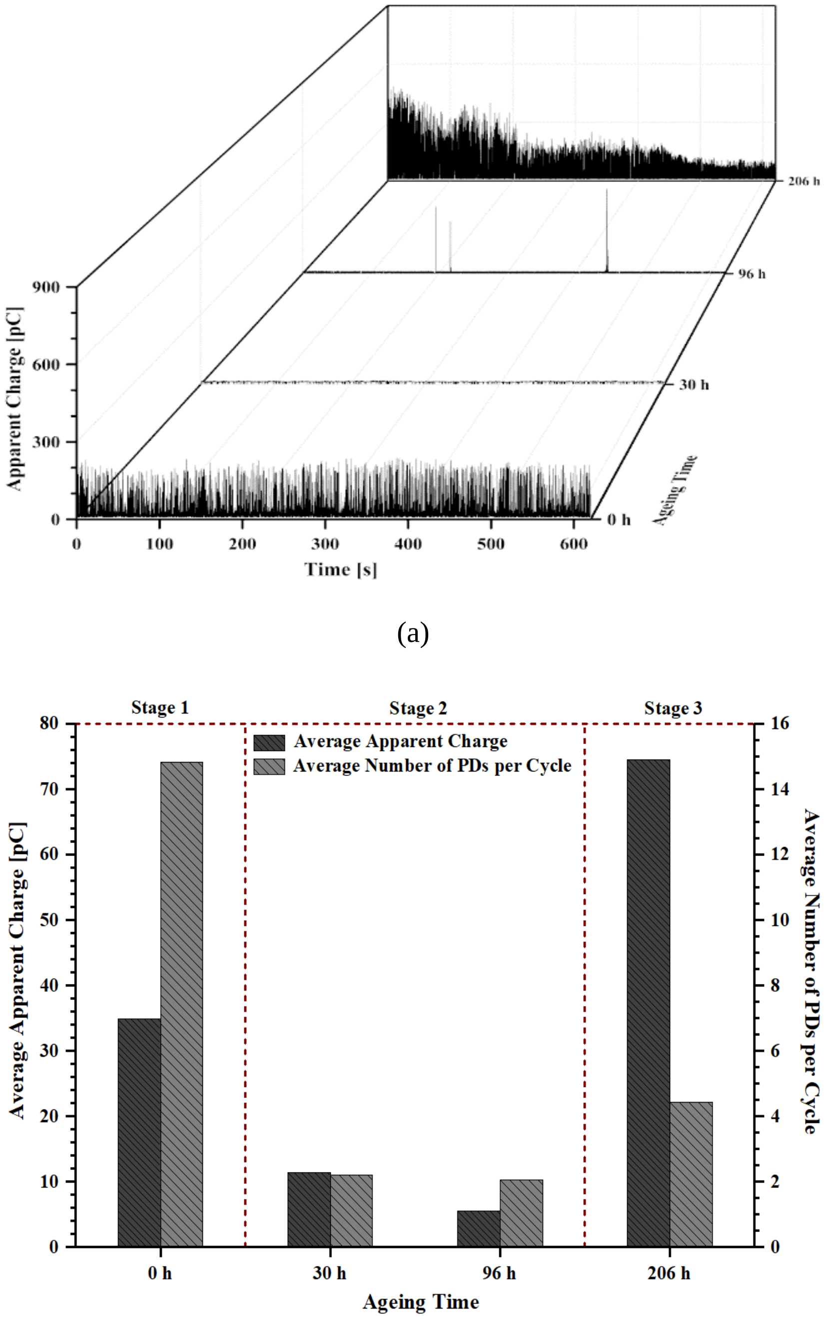

(a)

(b)

Figure 4.12: PD data of the polyethylene sample (I) containing a flat-shaped cavity of diameter 2 mm as a function of various ageing times: (a) the scatter distribution of apparent charge and (b) the bar chart between average apparent charge and average number of PDs per cycle.

4.4.3 SEM and EDX analysis: the polyethylene sample (I)

The techniques of SEM and EDX microanalysis were applied to analyse the microstructure and chemical elements in bulk of the localised erosion site on the cavity surface. The sample preparation used for SEM microanalysis was performed by removing the upper layer of the test sample for coating gold layer to increase the surface conductivity before undertaking technical microanalysis. The SEM micrograph of a virgin cavity showed in Figure 4.13 (a) that EDX analysis of chemical composites of this micrograph was spotted both centre and outer cavity of the localised sites at I-01 and I-02 as shown in Figures 4.13 (b) and 4.13 (c) respectively. The EDX result indicates that these localised spots were obtained by carbon elements of 100%.

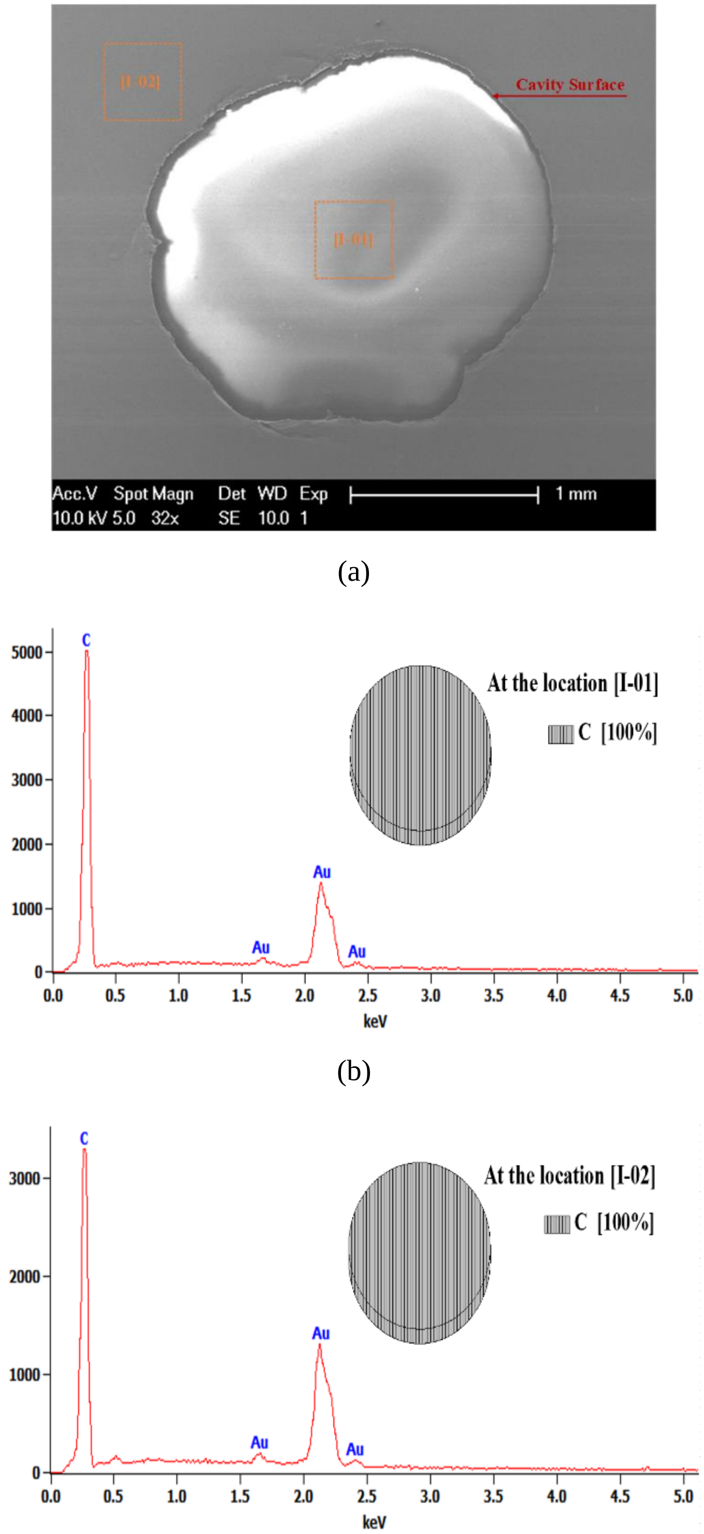

(a)

(b)

(c)

Figure 4.13: Microanalysis of a virgin sample: (a) a SEM image, (b) and (c) EDX analysis of chemical composites at the localised spots of I-01 and I-02 in the micrograph (a).

For the test sample after the ageing test, the SEM image at localised erosion on the cavity surface is illustrated in Figure 4.14 (a), images are for three different locations in terms of surface roughness, crystal growth and corrosive by-products at the localised spots of I-01, I-02 and I-03 respectively as shown in Figure 4.14 (b). All of these spots were examined chemical compounds, which composed of five chemical composites in terms of carbon, C, nitrogen, N, oxygen, O, sodium, Na, and silicon, Si. In the localised spot I-01, the chemical elements consisted 97.9% of carbon and 2.1% of oxygen, whereas this spot was undetected an amount of nitrogen, sodium and silicon as shown in Figure 4.15 (a) while the major proportion of carbon was obtained by 77.5% and 82.1% at the localised spots I-02 and I-03 respectively as shown in Figures 4.15 (b) and 4.15 (c). The ratio of nitrogen comprised of 9.6%, compared with 8.3 % at the localised spots I-02 and I-03 respectively. The percentage of oxygen was obtained by just over 10% at the spot I-02 and just under 8% at the localised spot I-03. It is likely that an amount of sodium was only found of 0.1% at both localised spots I-02 and I-03 while silicon was obtained by 2.6% and 1.6% at the localised spots I-02 and I-03 respectively, which these chemical elements might be from contamination during the sample preparation for chemical analysis or the inside of a vacuum chamber because the upper layer of the test sample was opened for coating gold before undertaking microanalysis of SEM and EDX. It should be noted that the changes of nitrogen and oxygen inside a cavity were consumed during PD activity, where oxygen was consumed at the initial ageing by PD bombardment, leading to the surface roughness on the cavity surface. It can be assumed that when the consumption of oxygen inside a cavity is nearly exhausted due to oxidation reactions, nitrogen ions act to induce the initial growth of pits at localised erosion and electrical tree initiation gradually evolves at localised pits, resulting from the enhancement of electric fields [56, 58].

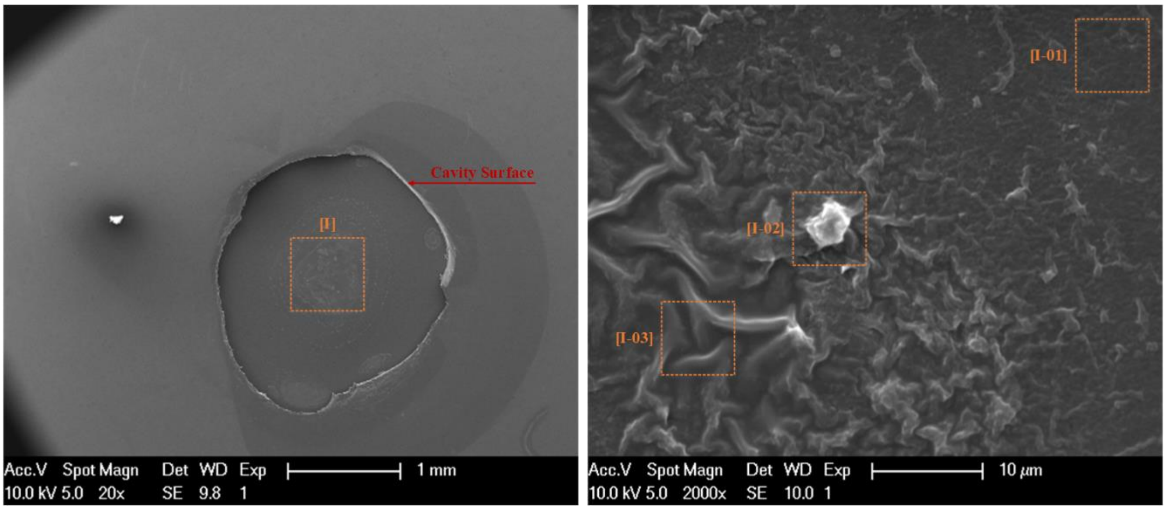

(a) (b)

Figure 4.14: Microanalysis of SEM micrographs: (a) a localised spot of the polyethylene sample (I) containing a flat-shaped cavity of diameter 2 mm at ageing 206 h and (b) a high-magnification at the localised spot of I in the micrograph (a).

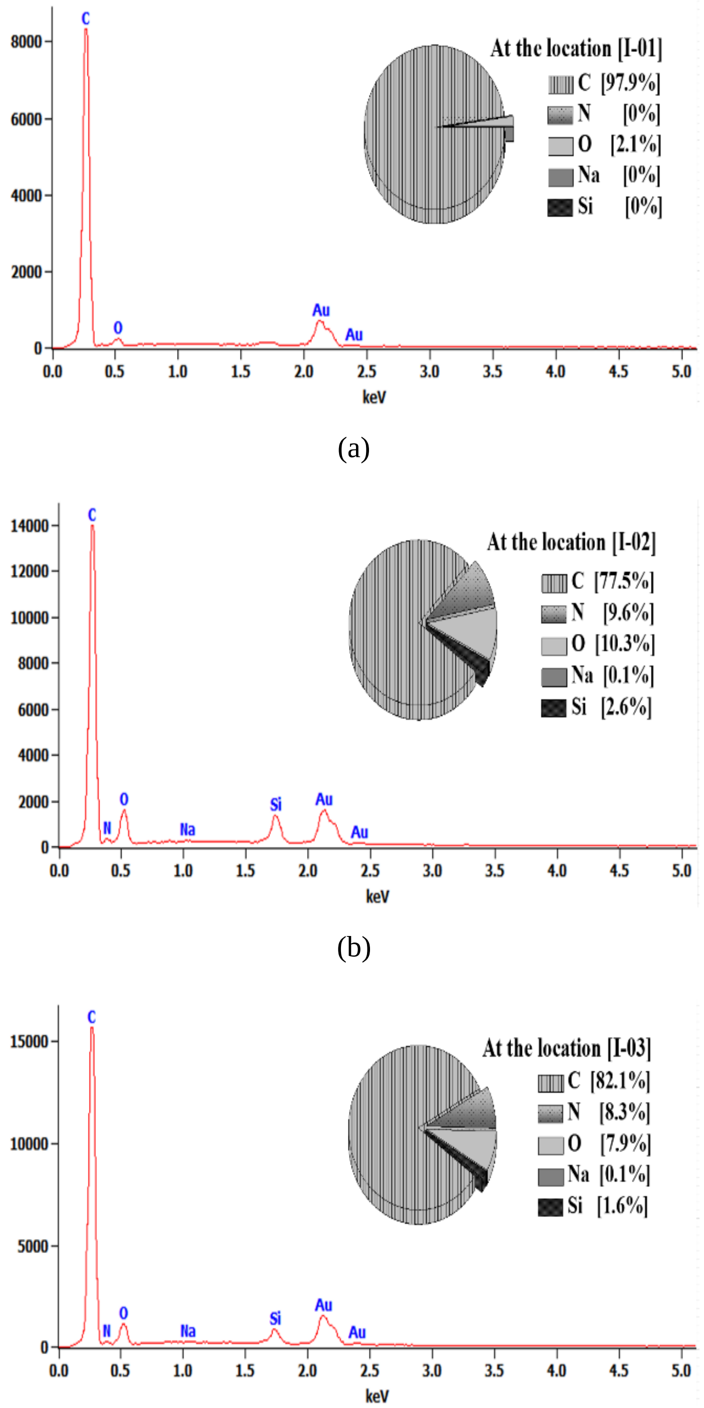

(a)

(b)

(c)

Figure 4.15: EDX analysis of chemical composites in Figure 4.14 (b) at the localised spots of I-01, I-02 and I-03.

4.4.4 Optical microscopy: the polyethylene sample (II)

An investigation into the polyethylene sample (II) containing a cavity diameter of 2 mm was performed to find out the cause of the degradation mechanisms before failure. The morphology of a virgin cavity was observed before the accelerated ageing test as shown in Figure 4.16 (a). The appearance of the surface roughness at the centre area on the cavity surface was observed after ageing

96 h as shown in Figure 4.16 (b). After further ageing of 206 h, the progressive degradation of localised erosion was formed the black bulk at the centre area of the inner cavity surface, where is marked by a rectangle as shown in Figure 4.16 (c) and a high-magnification at this localised site is shown in Figures 4.16 (d). It is likely that the interaction between PD bombardment and chemical reactions inside a cavity gradually degraded the localised erosion site to make the black bulk with progressive erosion on the cavity surface, leading to the growth of tree initiation prior to complete failure [208].

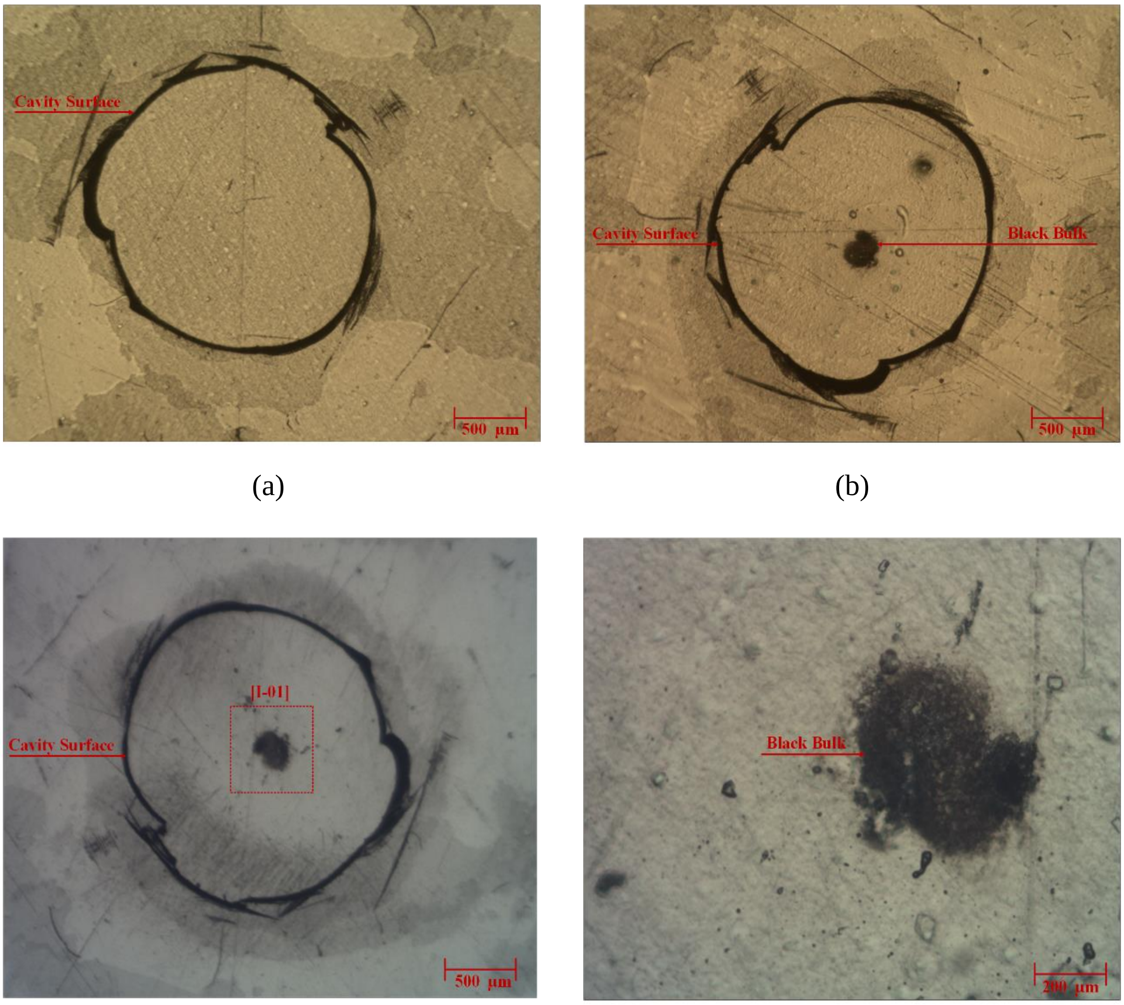

(a) (b)

(c) (d)

Figure 4.16: Morphological changes of the polyethylene sample (II) containing a flat-shaped cavity of diameter 2 mm at various ageing times: top-section views of (a) a virgin cavity, (b) 96 h, (c) 206 h, (d) a high-magnification in the micrograph (c).

4.4.5 Measurement of PD activity: the polyethylene sample (II)

The characteristics of PRPD patterns exhibited the rabbit-like shape with a long ear at the initial ageing and this pattern remained as a rabbit-like shape with a shorter ear after ageing 206 h as shown in Figures 4.17 (a) and 4.17 (b) respectively. The scatter distribution of apparent charge at various ageing times illustrated the high magnitude discharges at the initial ageing and followed by minimum discharges during further ageing 30 h and 96 h. After further ageing 206 h, high magnitude discharges were detected again as shown in Figure 4.18 (a). The bar chart between average apparent charge and average number of PDs per cycle can be divided into three main stages as a function of various ageing times as shown in Figure 4.18 (b). The results show that the average apparent charge tended to decrease from just over 30 pC at the initial ageing to 10 pC and 2 pC after ageing 30 h and 96 h respectively. Subsequently, the discharge magnitude rapidly increased to just over 40 pC after ageing for 206 h. For the average number of PDs per cycle, the average was 5 at the initial ageing and slightly increasing to just over 7 at ageing 30 h. Subsequently, reducing to 3 at ageing 96 h and followed by a remaining stable about 3 after further ageing 206 h.

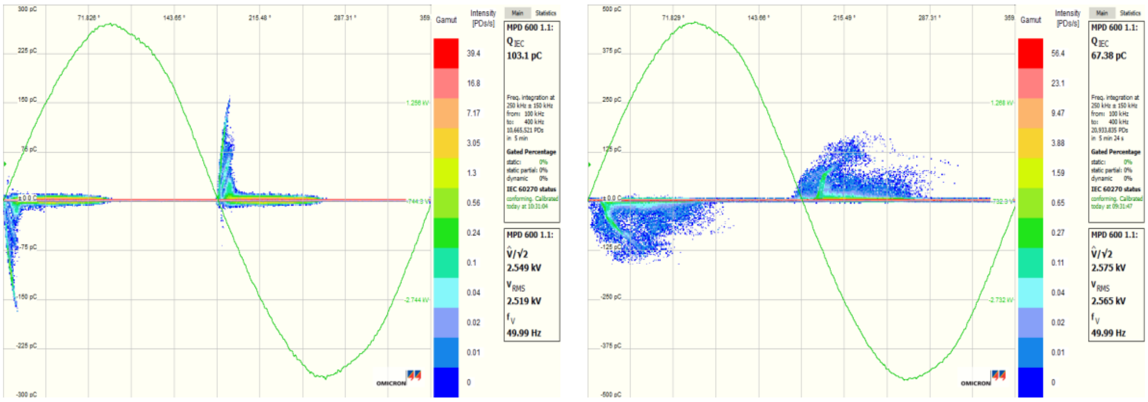

(a) (b)

Figure 4.17: Measured PRPD patterns of the polyethylene sample (II) containing a flat-shaped cavity of diameter 2 mm at various ageing times: (a) a rabbit-like pattern at ageing 10 min and (b) a rabbit-like pattern at ageing 206 h.

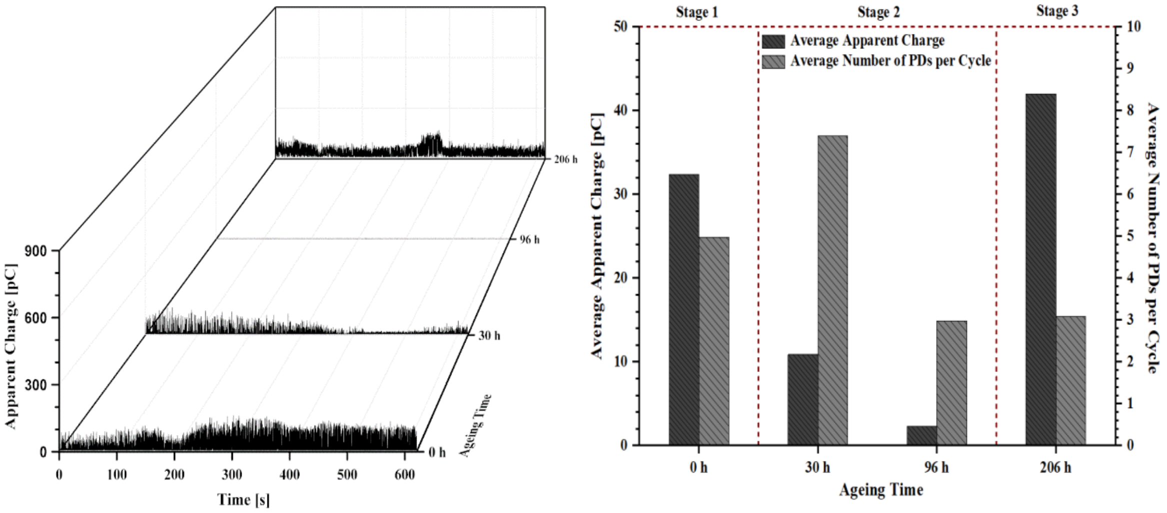

(a) (b)

Figure 4.18: PD data of the polyethylene sample (II) containing a flat-shaped cavity of diameter 2 mm as a function of various ageing times: (a) the scatter distribution of apparent charge and (b) the bar chart between average apparent charge and average number of PDs per cycle.

4.4.6 SEM and EDX analysis: the polyethylene sample (II)

The SEM micrograph of localised erosion on the cavity surface was revealed the localised spot of I as shown in Figure 4.19 (a), which can be subdivided three different regions of progressive deterioration mechanisms at the localised spots of I-01, I-02 and I-03 as shown in Figure 4.19 (b). All these spots were examined the chemical elements in terms of carbon, C, oxygen, O, potassium, K, sodium, Na, and silicon, Si as shown in Figures 4.20 (a) to 4.20 (c). The percentage of carbon was obtained by just over 90% of all localised spots while the large ratio of oxygen was detected by 6% at the localised spot of I-02, compared with this chemical compound of 4.2% and 5.3% at the localised spots of I-01 and I-03 respectively. It is likely that the variation in oxygen at each localised spots depended on the relative levels of localised erosion in the bulk on the cavity surface. Interestingly, a large amount of oxygen was obtained the localised site of high corrosive by-products, resulting in the oxidative ageing during PD activity [208]. The proportion of potassium, sodium, and silicon, there were only found little quantities at the localised spots of I-01, I-02 and I-03 that these chemical elements might be from contamination during the sample preparation for chemical analysis or the inside of a vacuum chamber because the upper layer of the test sample was opened for coating gold before undertaking microanalysis of SEM and EDX systems.

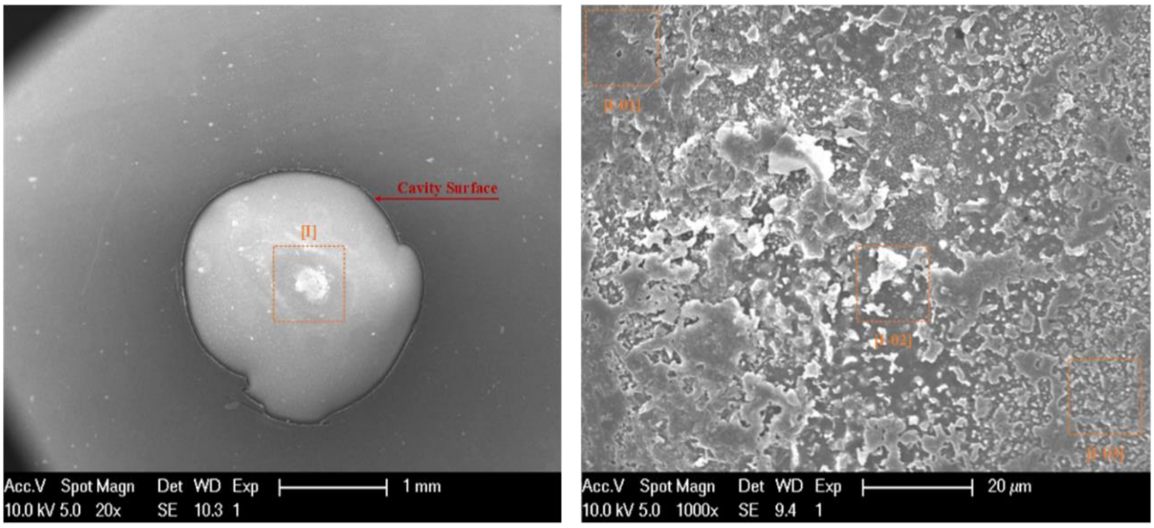

(a) (b)

Figure 4.19: Microanalysis of SEM micrographs: (a) a localised spot of the polyethylene sample (II) containing a flat-shaped cavity of diameter 2 mm at ageing 206 h and (b) a high-magnification at the localised spot of I in the micrograph (a).

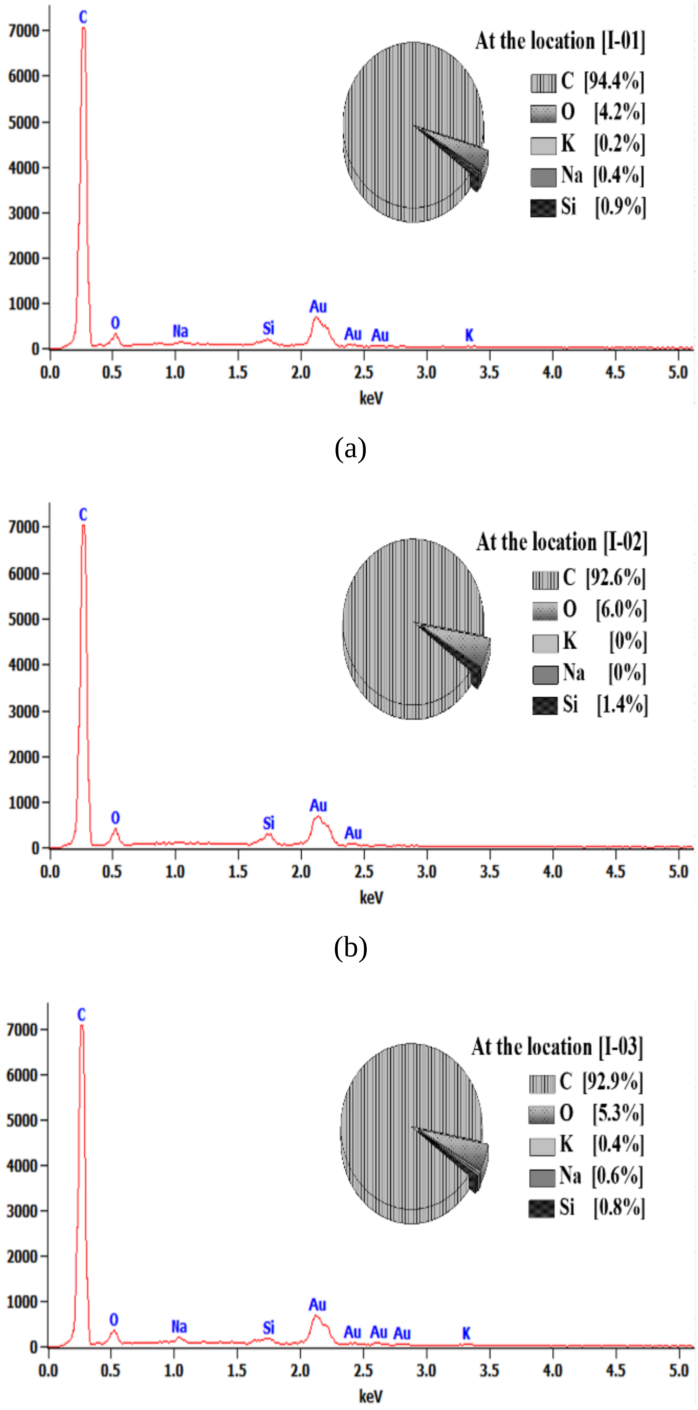

(a)

(b)

(c)

Figure 4.20: EDX analysis of chemical composites in Figure 4.19 (b) at the localised spots of I-01, I-02 and I-03.

4.4.7 Optical microscopy: the polyethylene sample (III)

Another investigation into the polyethylene sample (III) containing a cavity diameter of 2 mm was undertaken to find out the cause of cavity formation before total failure. The morphology of a virgin cavity was recorded before the accelerated ageing process as shown in Figure 4.21 (a). The appearance of the surface roughness at the centre area on the cavity surface was observed after ageing 96 h as shown in Figure 4.21 (b). After further ageing 206 h, the progressive erosion of corrosive by-products was formed the black bulk at the centre location of the inner cavity surface, where is marked by a rectangle as shown in Figure 4.21 (c) and a high-magnification at this localised site is shown in Figures 4.21 (d). It is likely that PD activity continually bombarded at the localised site of the black bulk on the cavity, leading to the further eroded depth at this localised site until complete failure of the test sample.

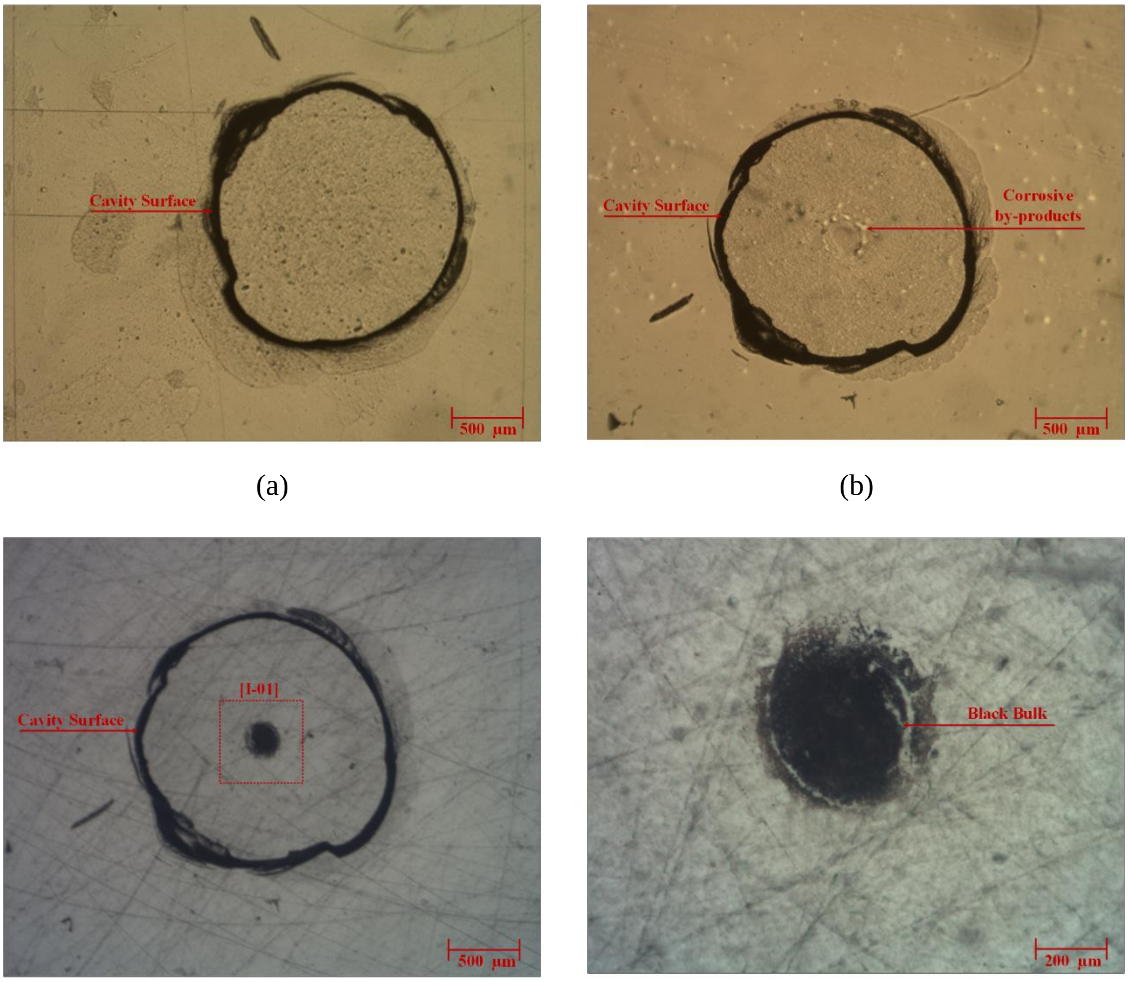

(a) (b)

(c) (d)

Figure 4.21: Morphological changes in the polyethylene sample (III) containing a flat-shaped cavity of diameter 2 mm at various ageing times: top-section views of (a) a virgin cavity, (b) 96 h, (c) 206 h, (d) a high-magnification in the micrograph (c).

4.4.8 Measurement of PD activity: the polyethylene sample (III)

The characteristics of PRPD patterns exhibited the rabbit-like shape with a long ear at the initial ageing and this pattern remained unchanged by the rabbit-like shape with a shorter ear after further ageing 206 h as shown in Figures 4.22 (a) and 4.22 (b) respectively. The scatter distribution of apparent charge as a function of various ageing times showed high magnitude discharges at the initial ageing stages, followed by minimum discharges after further ageing of 30 h and 96 h. After further ageing 206 h, high magnitude discharges were detected again as shown in Figure 4.23 (a). The bar chart between average apparent charge and average number of PDs per cycle can be divided into three main stages as a function of various ageing times as shown in Figure 4.23 (b). The result shows that the average apparent charge tended to decline from just over 40 pC at the initial ageing to just over 11 pC at ageing 96 h and followed by a steep increase from just over 20 pC at ageing 96 h to just under 40 pC at ageing 206 h while the average number of PDs per cycle tended to decrease from just over 6 at the initial ageing stage to just under 5 after ageing 30 h and reducing to 3 after ageing 96 h before increasing to 7 after further ageing 206 h.

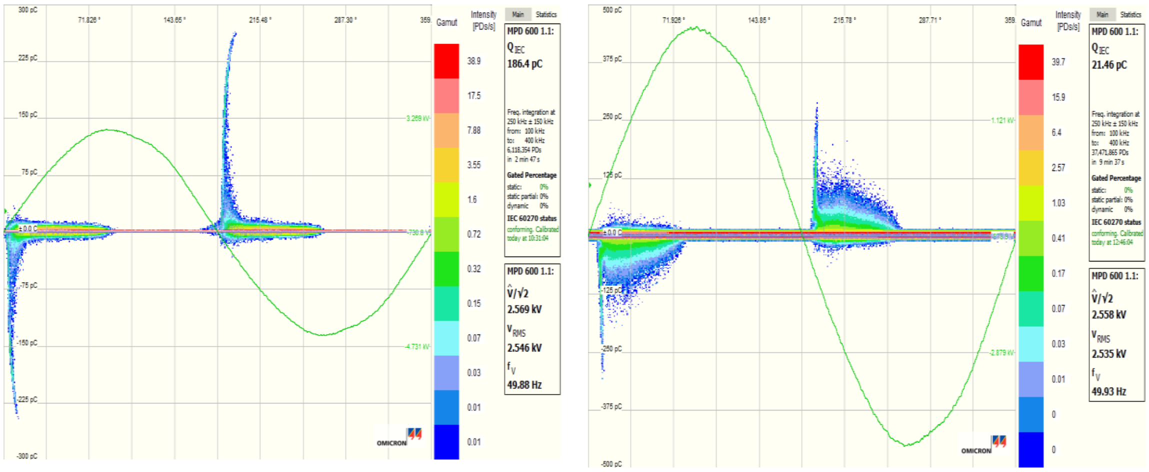

(a) (b)

Figure 4.22: Measured PRPD patterns of the polyethylene sample (III) containing a flat-shaped cavity of diameter 2 mm at various ageing times: (a) a rabbit-like pattern at ageing 10 min and (b) a rabbit-like pattern at ageing 206 h.

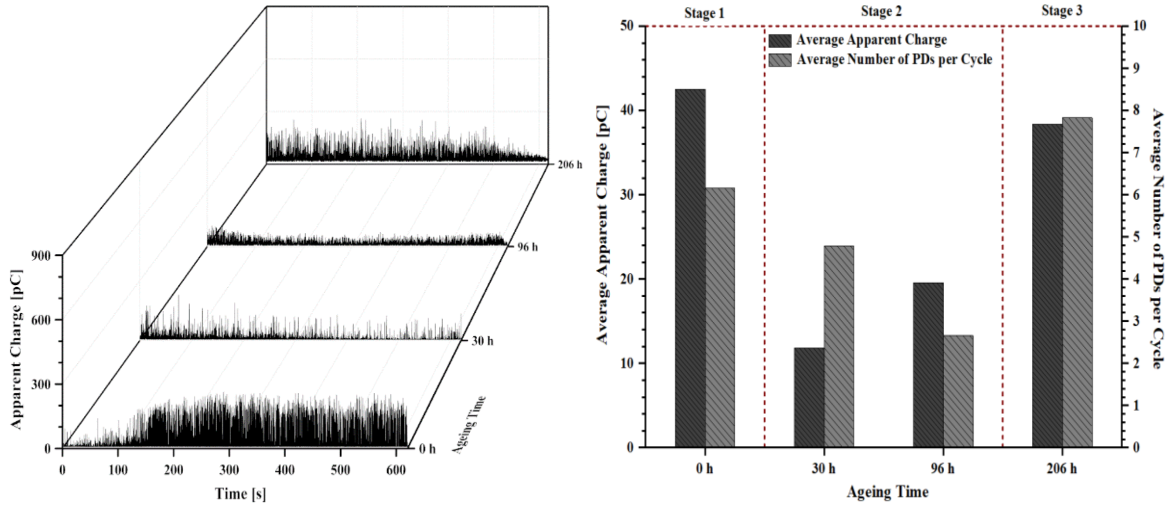

(a) (b)

Figure 4.23: PD data of the polyethylene sample (III) containing a flat-shaped cavity of diameter 2 mm as a function of various ageing times: (a) the scatter distribution of apparent charge and (b) the bar chart between average apparent charge and average number of PDs per cycle.

4.4.9 SEM and EDX analysis: the polyethylene sample (III)

Another investigation into microanalysis on the cavity surface after ageing, the SEM micrograph of localised erosion on the cavity surface was revealed at the localised spot of I as shown in Figure 4.24 (a), which can be subdivided three different areas of the progressive degradation at the localised spots of I-01, I-02 and I-03 as shown in Figure 4.24 (b). All of these spots were analysed the chemical composites in terms of carbon, C, nitrogen, N, oxygen, O, tantalum, Ta, and silicon, Si as shown in Figures 4.25 (a) to 4.25 (c). The proportion of carbon was obtained by just over 87% of all localised spots while a large amount of nitrogen was detected by 7% and 6.6% at the localised spots of I-01 and I-03 respectively, whereas this compound was undetected at the localised spot of I-02. In the percentage of oxygen, the highest ratio was obtained by just under 8 at the localised spot of I-02, compared with this chemical element of 4.6% and 5.2% at the localised spots of I-01 and I-03 respectively. For the chemical compound of tantalum, it was detected a minimum level at the localised spot of I-02, whereas this composite was undetected at the localised spots of I-01 and I-03. In the chemical compound of silicon, it was only found little quantities at the localised spots of I-01, I-02 and I-03 that both tantalum and silicon elements might be might be from contamination during sample preparation for chemical analysis or the inside of a vacuum chamber because the upper layer of the test sample was opened for coating gold before undertaking microanalysis of SEM and EDX instruments.

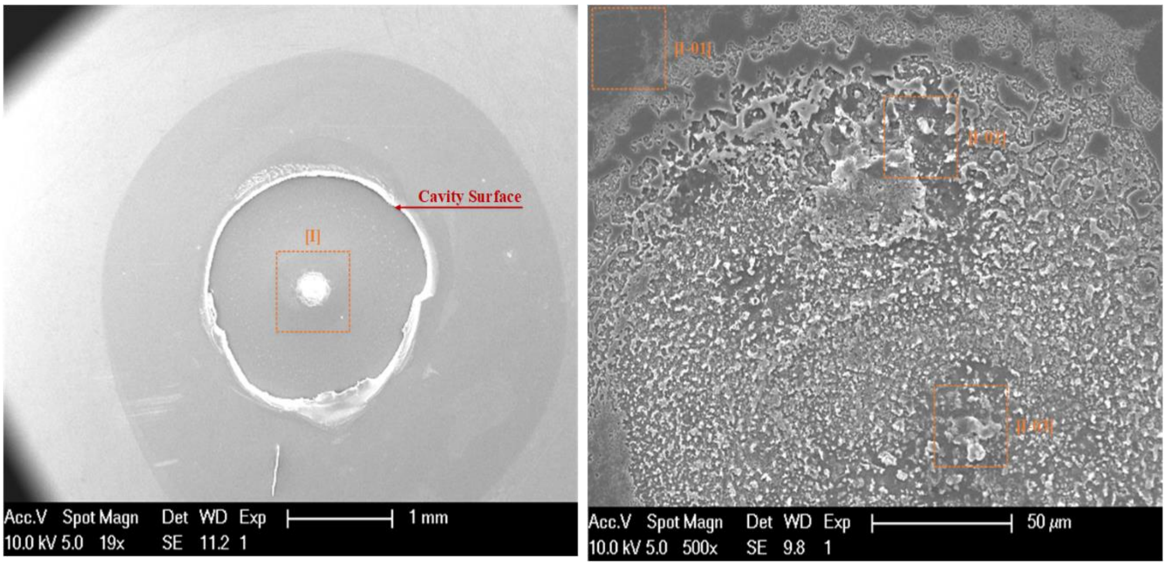

(a) (b)

Figure 4.24: Microanalysis of SEM micrographs: (a) a localised spot of the polyethylene sample (III) containing a flat-shaped cavity of diameter 2 mm at ageing 206 h and (b) a high-magnification at the localised spot of I in the micrograph (a).

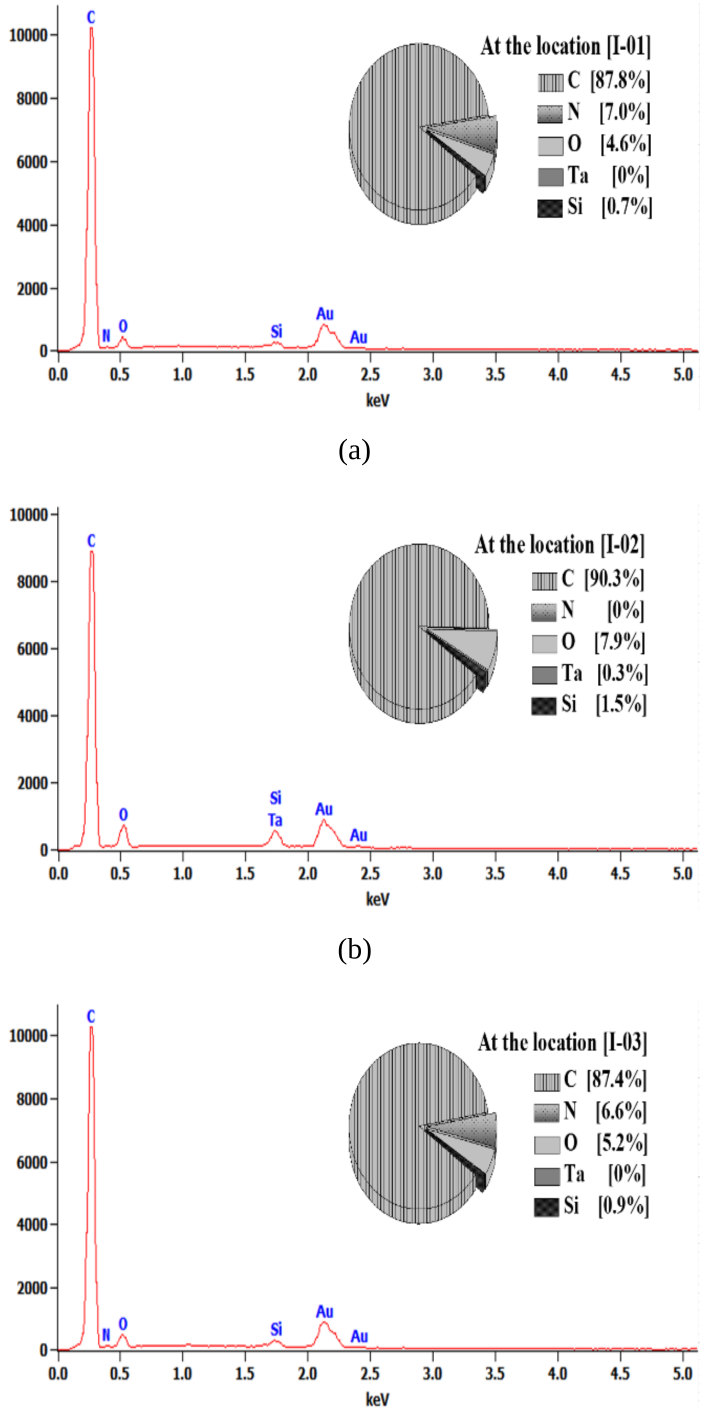

(a)

(b)

(c)

Figure 4.25: EDX analysis of chemical composites in Figure 4.24 (b) at the localised spots of I-01, I-02 and I-03.

4.5 PD characteristics of deterioration mechanisms on the cavity surface

The purpose of this section is to investigate the degradation mechanisms of a cylindrical flat-shaped cavity embedded in polyethylene material by PD activity related to the formation on the cavity surface over a long period of accelerated electrical ageing. The variation in PRPD patterns and PD quantities can be used to diagnose the gradual progression of corrosive by-products on the cavity wall.

4.5.1 Optical microscopy

The morphological changes of a cavity by PD activity during the electrical ageing were investigated into the test sample containing a flat-shaped cavity of diameter 2 mm to find out the distinct PD characteristics related to degradation mechanisms on the cavity surface. The morphology of a virgin cavity was observed before measuring PD as shown in Figure 4.26 (a). Visible evidence of deposited by-products was formed on the inner cavity at ageing 308 h as shown in Figure 4.26 (b) while the progressive deterioration of corrosive by-products was noticed on the cavity surface after further ageing 654 h and 1004 h as shown in Figures 4.26 (c) and 4.26 (d) respectively. It is suggested that localised erosion within the inner cavity resulted from increasing the conductivity on the cavity surface at the localised site by PD bombardment such as the growth of crystals and pits before the electrical tree initiation as reported in other researches [145, 156].

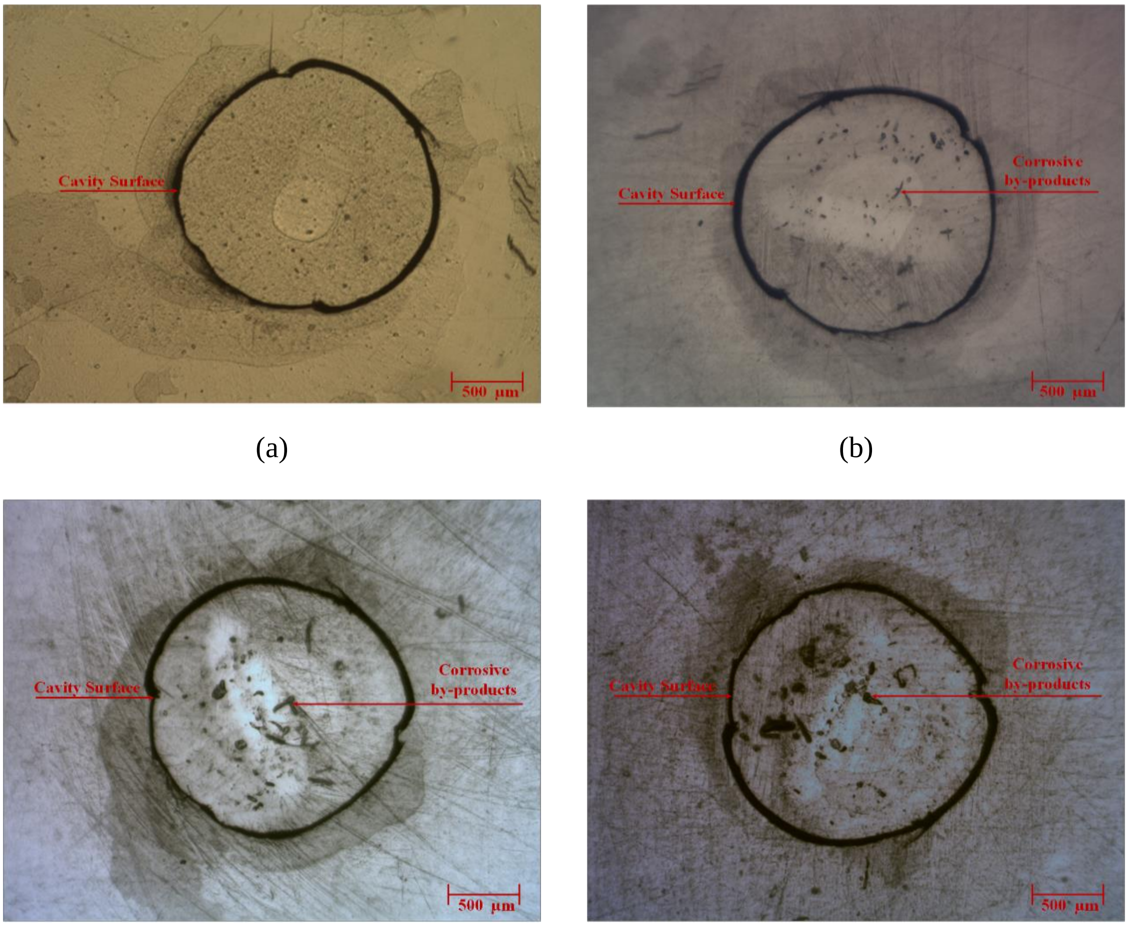

(a) (b)

(c) (d)

Figure 4.26: Morphological changes of the polyethylene sample containing a flat-shaped cavity of diameter 2 mm at various ageing times: top-section views of (a) a virgin cavity, (b) 308 h, (c) 654 h and (d) 1004 h.

4.5.2 Measurement of PD activity

For the apparent charge distribution as a function of various ageing times, the trend showed high magnitude discharges at the initial ageing and followed by minimum magnitude discharges from ageing 30 h to ageing 558 h. The scatter distribution of apparent charge was then detected with large discharges after further ageing 654 h and 1004 h as shown in Figure 4.27 (a). The bar chart between average apparent charge and average number of PDs per cycle can be divided into three main stages at various ageing stages as shown in Figure 4.27 (b). The results show that the average apparent charge was obtained of just over 35 pC at the initial ageing and followed by a steep drop by about 80% during the second stage of ageing while this figure dramatically increased by about 70% during the third stage of ageing. In the average number of PDs per cycle, the trend was obtained just over 10 at the initial ageing. Subsequently, the figure tended to decrease by about 60% during the second stage of ageing and then increased by about 70% during the third stage of ageing. The evolution of PRPD patterns exhibited the rabbit-like shape with a long ear at the initial ageing and this pattern remained unchanged the rabbit-like shape with slight magnitude discharges at ageing 96 h as shown in Figures 4.28 (a) and 4.28 (b). The transition of this PRPD pattern changed to the turtle-like patterns at ageing 308 h and after further ageing just over 1000 h as shown in Figures 4.28 (c) and 4.28 (d). This result indicates that typical PRPD characteristics exhibited as a rabbit-like pattern and a turtle-like pattern, which the transition of PRPD shapes depended on various factors, i.e. gas pressure, gaseous composites, humidity and statistical time lag. It is suggested that the rabbit-like shape with a longer ear resulted from an increase of moisture and statistic time lag of a cavity while the turtle-like shape exhibited after elasped time of ageing due to an increase of the surface conductivity on the cavity wall [209]. Otherwise, the transition of PRPD patterns concerned with the variation in gaseous composites inside a cavity, i.e. oxygen due to the oxidative ageing at the initial stage and the electronegative gases, i.e. CO_2 and H_2O were produced after a prolonged ageing, leading to an increase of CO_2 before an upcoming failure of the test sample [210-211].

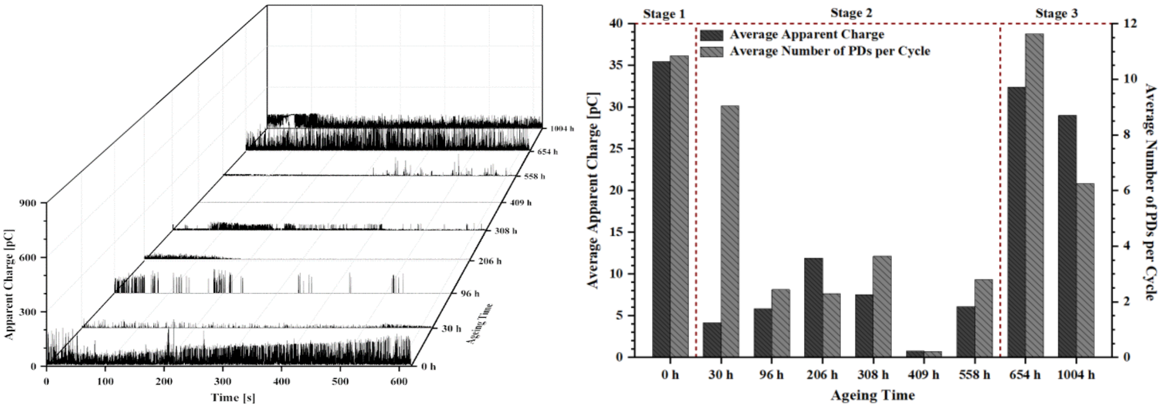

(a) (b)

Figure 4.27: PD data of the polyethylene sample containing a flat-shaped cavity of diameter 2 mm as a function of various ageing times: (a) the scatter distribution of apparent charge and (b) the bar chart between average apparent charge and average number of PDs per cycle.

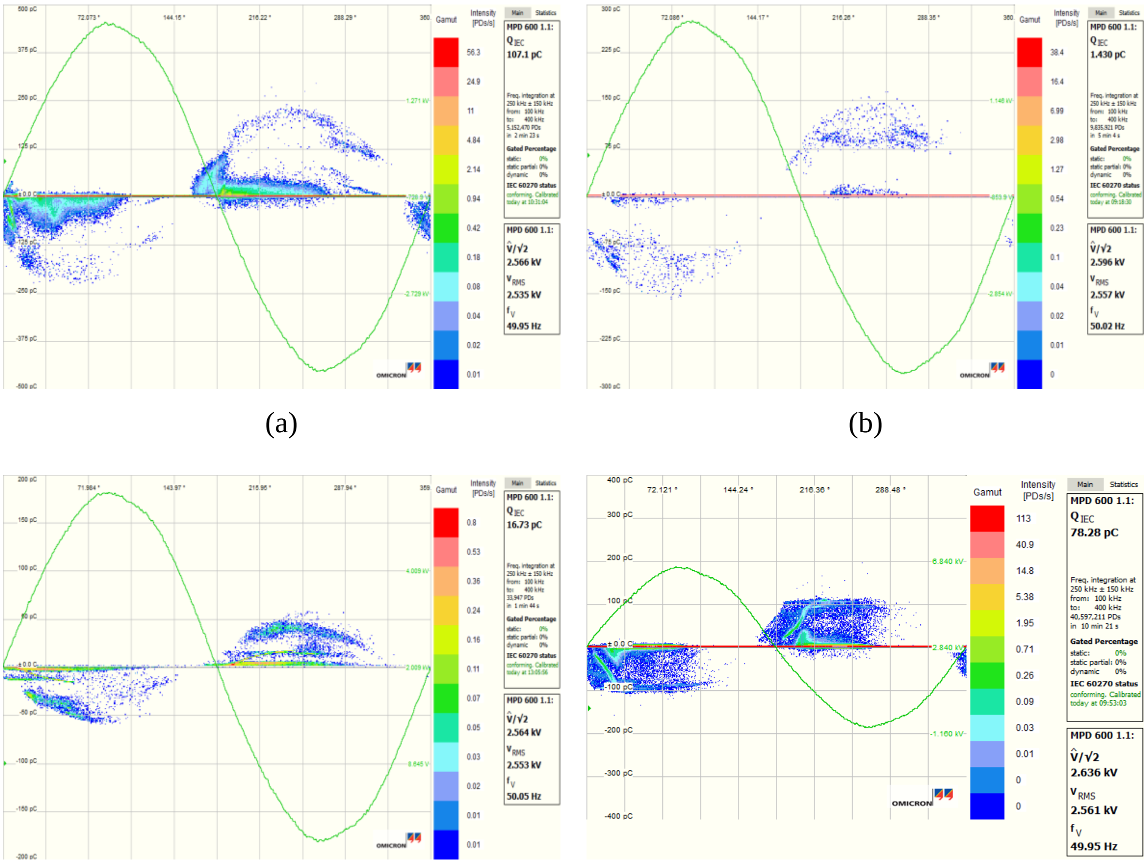

(a) (b)

(c) (d)

Figure 4.28: Variation in measured PRPD patterns of the polyethylene sample containing a flat-shaped cavity of diameter 2 mm at various ageing times: (a) a rabbit-like pattern at ageing 10 min, (b) a rabbit-like pattern at ageing 96 h, (c) a turtle-like pattern at ageing 308 h and (d) a turtle-like pattern at ageing 1004 h.

4.6 PD characteristics of electrical tree initiation on the cavity surface

Another investigation into the test sample containing an air-filled cavity embedded in polyethylene material was undertaken to reveal the progressive erosion site in terms of corrosive by-products and electrical tree initiation on the cavity surface over a prolonged period of electrical ageing.

4.6.1 Optical microscopy

The virgin cavity was observed before measuring PD as shown in Figure 4.29 (a). Visible evidence of corrosive by-products was evolved on the inner cavity during ageing 206 h and 654 h as shown in Figures 4.29 (b) and 4.29 (c) respectively. After further ageing of just over 1000 h, the progressive erosion of corrosive by-products had caused black area within the inner cavity surface, where is marked by a rectangle as shown in Figure 4.29 (d) and a high- magnification at this localised site that the growth of electrical tree initiation was pointed out a progressive cluster of crystals as shown in Figures 4.29 (e).

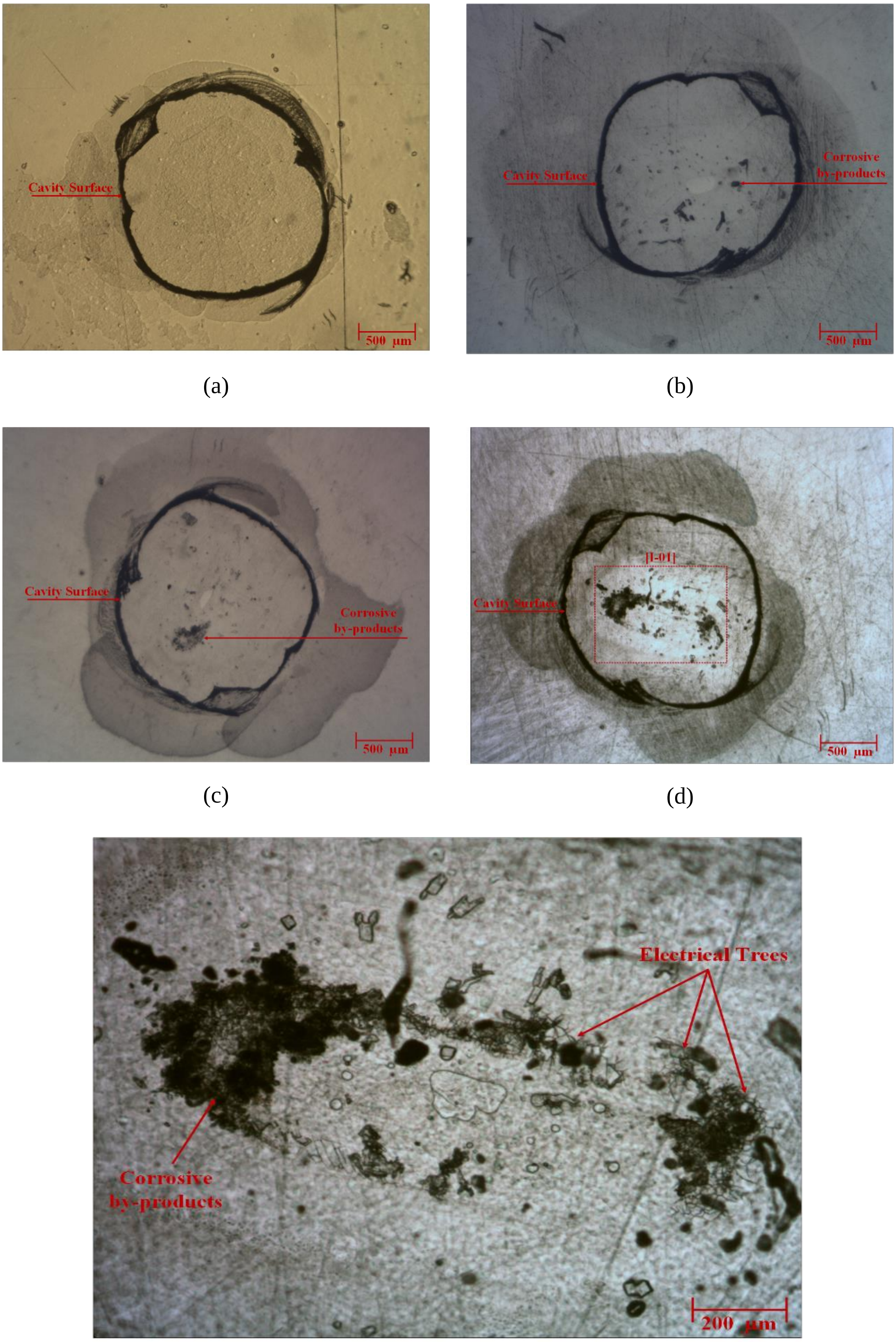

(a) (b)

(c) (d)

(e)

Figure 4.29: Morphological changes of the polyethylene sample containing a flat-shaped cavity of diameter 2 mm at various ageing times: top-section views of (a) a virgin cavity, (b) 206 h, (c) 654 h, (d) 1004 h and (e) a high-magnification in the micrograph (d).

4.6.2 Measurement of PD activity

In the scatter distribution of apparent charge as a function of various ageing times, it showed the high magnitude discharges at the initial ageing and followed by minimum magnitude discharges from ageing 30 h to ageing 409 h. After further ageing 558 h and 654 h, the apparent charge distribution was detected with large discharges. Subsequently, the distribution of magnitude discharges showed a cluster of intense charges between 50 pC and 100 pC at ageing 1004 h as shown in Figure 4.30 (a). The bar chart between average apparent charge and average number of PDs per cycle can be divided into three main stages at various ageing stages as shown in Figure 4.30 (b). The results show that the average apparent charge was obtained just over 12 pC at the initial ageing and followed by a steep drop by about 70% from ageing 30 h to ageing 409 h. In the third stage, the trend dramatically rose by over 80% at ageing 558 h and subsequently dropped by 70% at ageing 654 h while this figure increased by 80% after further ageing of just over 1000 h. As regards the average number of PDs per cycle, the figure was obtained just over 5 at the initial ageing and then tended to decrease by about 60% from ageing 30 h to ageing 409 h. Subsequently, it was obtained just over 5 during further ageing 558 h and 654 h and followed by a steep drop of just under 0.2 during the third stage. The variation in PRPD patterns linked to the rabbit-like pattern with a long ear at the initial ageing while this pattern remained unchanged to exhibit the rabbit-like pattern with a shorter ear at further ageing 308 h and 409 h as shown in Figures 4.31 (a) to 4.31 (c). The transition of this pattern changed to the turtle-like pattern at ageing 654 h as shown in Figure 4.31 (d). After further ageing of just over 1000 h, the wing-like pattern was detected as shown in Figure 4.31 (e). It is suggested that typical PRPD patterns were identified as the rabbit-like pattern and the turtle-like pattern [212] while the wing-like pattern with SPMDs linked to the characteristic tree growth before the PD extinction occurred due to high conductivity in the inside wall of tree channels [213-214].

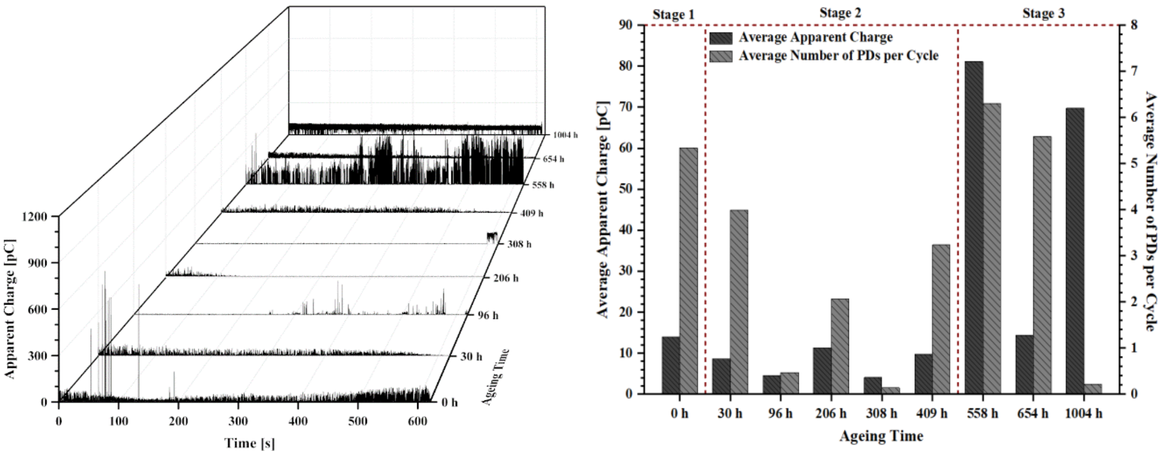

(a) (b)

Figure 4.30: PD data of the polyethylene sample containing a flat-shaped cavity of diameter 2 mm as a function of various ageing times: (a) the scatter distribution of apparent charge and (b) the bar chart between average apparent charge and average number of PDs per cycle.

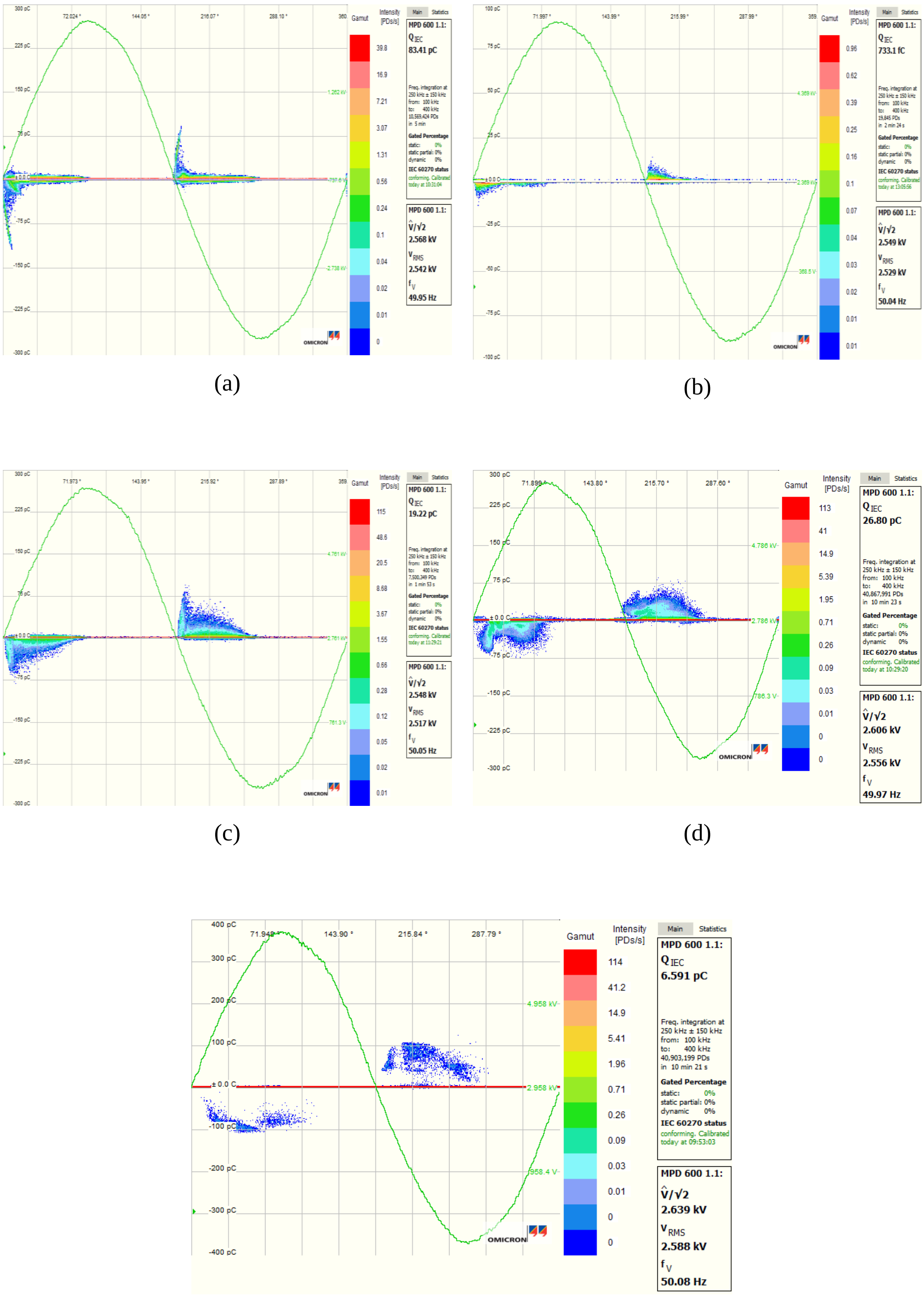

(a) (b)

(c) (d)

(e)

Figure 4.31: Variation in measured PRPD patterns of the polyethylene sample containing a flat-shaped cavity of diameter 2 mm at various ageing times: (a) a rabbit-like pattern at ageing 10 min, (b) a rabbit-like pattern at ageing 308 h, (c) a rabbit-like pattern at ageing 409 h, (d) a turtle-like pattern at ageing 654 h and (e) a wing-like pattern at ageing 1004 h.

4.7 PD characteristics before an upcoming failure of a cavity

An investigation into the morphological change in an air-filled cavity was experimentally undertaken to clarify the time-evolution of PD behaviour related to the mechanism of progressive deterioration in the cavity from localised erosion to upcoming failure due to a prolonged period of ageing.

4.7.1 Optical microscopy

Another investigation into the test sample containing a flat-shaped cavity of diameter 2 mm to clarify the distinct PD characteristics in both PRPD patterns and PD quantities related to the cavity formation from localised erosion to failure due to a long-term of ageing processes with a detailed analysis of an upcoming failure of the test sample. The morphology of a virgin cavity was observed before measuring PD as shown in Figure 4.32 (a). Visible evidence of localised erosion was observed deposited by-products on the inner cavity surface during the ageing processes at 654 h, 1004 h and 1821 h as shown in Figures 4.32 (b) to 4.32 (d). After prolonged ageing of just over 2000 h, the progressive erosion was formed a cluster of corrosive by-products within the inner cavity as shown in Figure 4.32 (e) and followed by total failure of the test sample, where the inside cavity was filled with silicone oil as shown in Figure 4.32 (f). It is considered that an investigation into failure of three layers of polyethylene material was observed the channel of breakdown at the top layer connected with the HV electrode, resulting from the high enhancement of electric fields to exceed the dielectric strength of this layer [215].

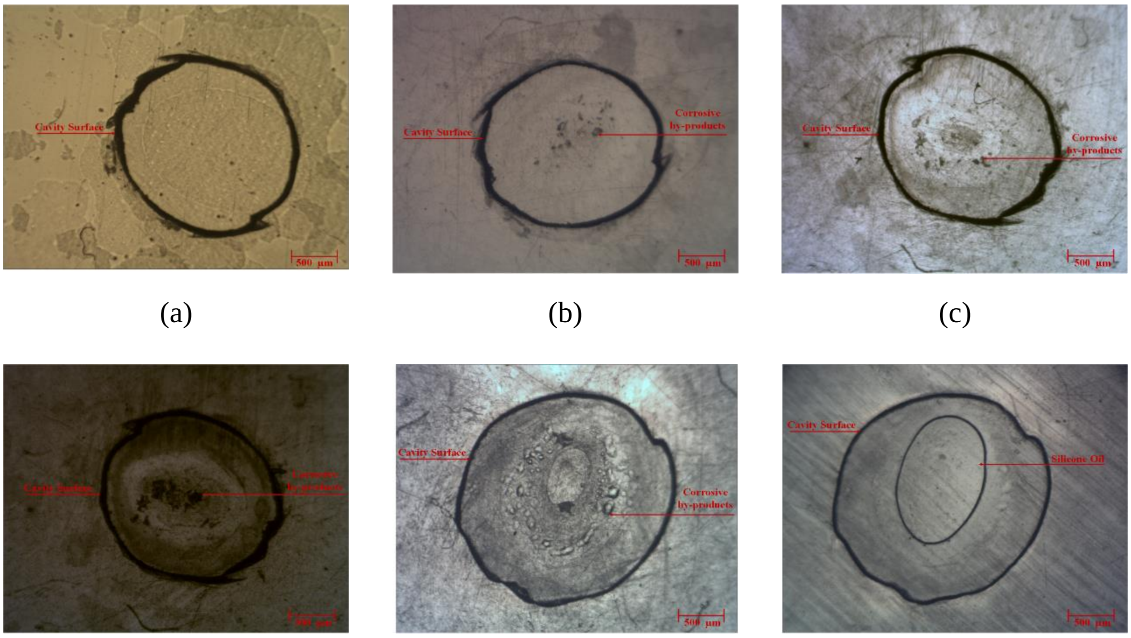

(a) (b) (c)

(d) (e) (f)

Figure 4.32: Morphological changes of the polyethylene sample containing a flat-shaped cavity of diameter 2 mm at various ageing times: top-section views of (a) a virgin cavity, (b) 654 h, (c) 1004 h, (d) 1821 h, (e) 2012 h and (f) 2013 h 30 min.

4.7.2 Measurement of PD activity

The PD characteristics of the variation in PRPD patterns and PD quantities as a function of ageing time were diagnosed degradation stages before an upcoming failure of the test sample. The evolution of PRPD patterns initially exhibited the rabbit-like pattern with a long ear and remained unchanged with a shorter ear after further ageing 308 h as shown in Figures 4.33 (a) and 4.33 (b) respectively. The transition of this pattern changed to the turtle-like pattern after ageing of just over 1000 h as shown in Figure 4.33 (c). After further ageing of just over 1820 h, the PRPD pattern was obtained with the wing-like shape with SPMDs for the positive half-cycle and the turtle-like shape with surface discharges for the negative half-cycle as shown in Figure 4.33 (d). Subsequently, the turtle-like shapes with surface discharges exhibited during ageing processes of just over ageing 2000 h as shown in Figures 4.34 (a) to 4.34 (c) and the occurrence of SPMDs then observed, which corresponded to failure of the test sample as shown in Figure 4.34 (d).

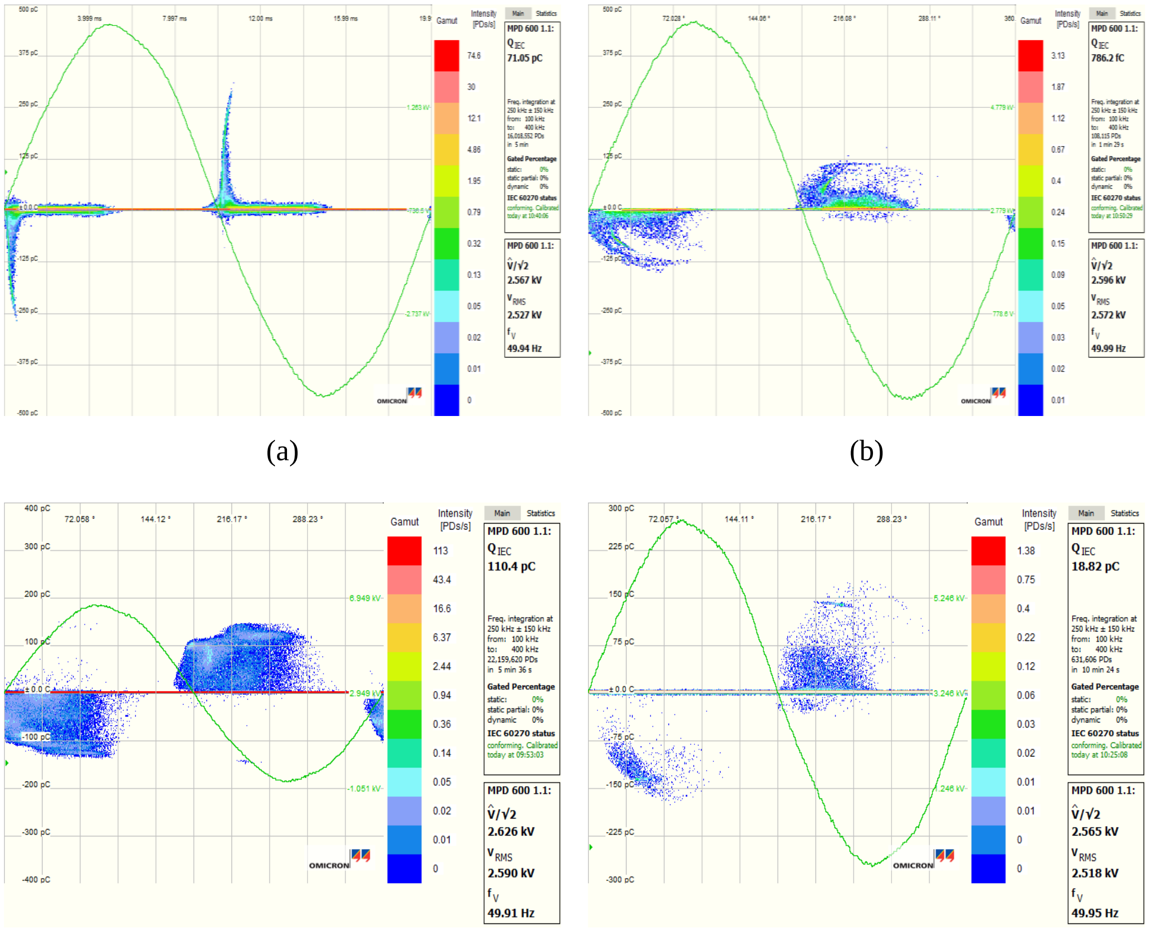

(a) (b)

(c) (d)

Figure 4.33: Variation in measured PRPD patterns of the polyethylene sample containing a flat-shaped cavity of diameter 2 mm at various ageing times: (a) a rabbit-like pattern at ageing 10 min, (b) a rabbit-like pattern at ageing 308 h, (c) a turtle-like pattern at ageing 1004 h and (d) a wing-like pattern at ageing 1821 h.

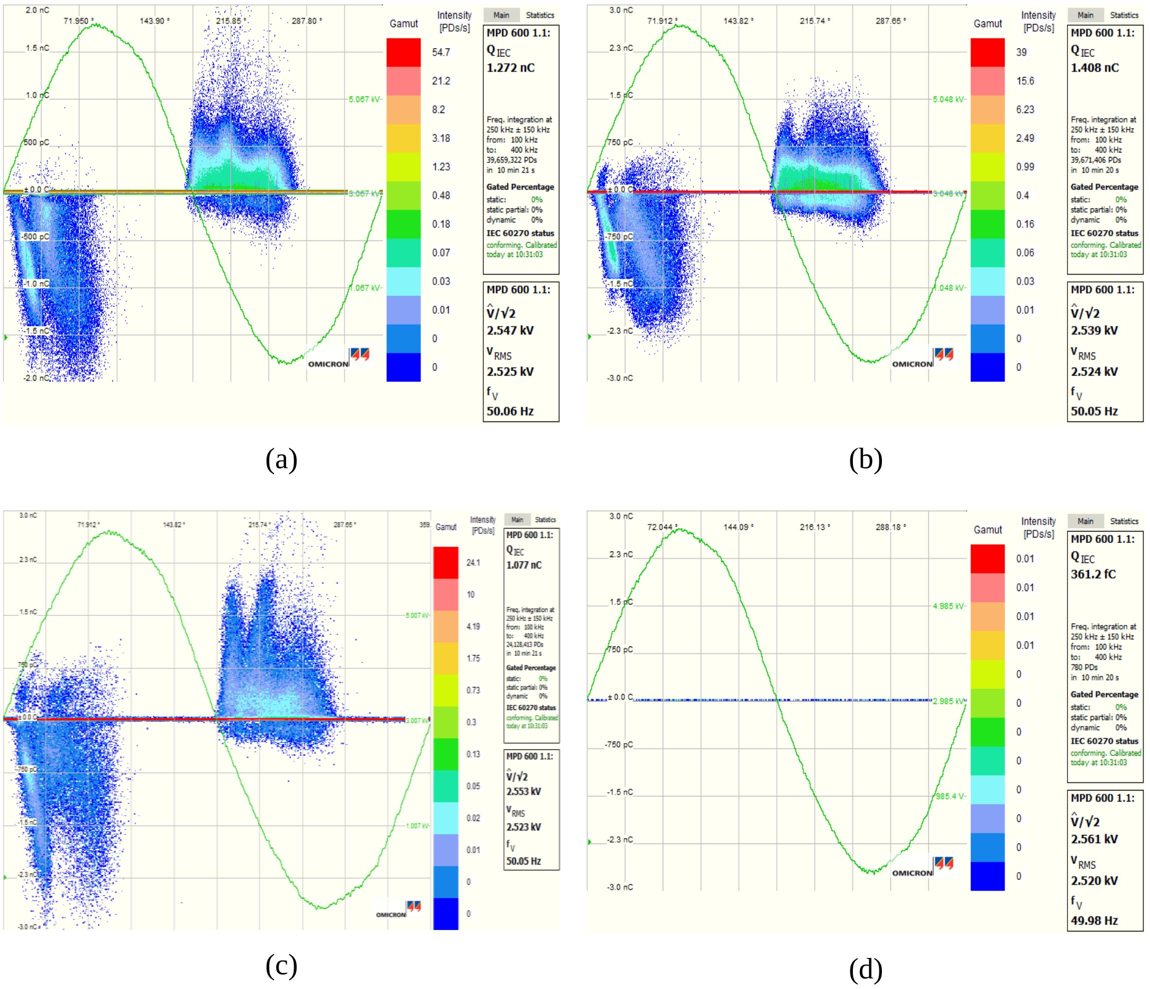

(a) (b)

(c) (d)

Figure 4.34: Variation in measured PRPD patterns of the polyethylene sample containing a flat-shaped cavity of diameter 2 mm at various ageing times: (a) a turtle-like pattern at ageing 2012 h, (b) a turtle-like pattern with surface discharges at ageing 2012 h 30 min, (c) a turtle-like pattern with surface discharges at ageing 2013 h and (d) SPMDs at ageing 2013 h 30 min.

The PD characteristics of the scatter distribution of apparent charge as a function of various ageing times is illustrated as shown in Figure 4.35 (a). The result showed high magnitude discharges at the initial ageing stage and followed by minimum magnitude discharges during ageing processes from 30 h to 654 h. Subsequently, the distribution of apparent charge was detected with large discharges after further ageing 1004 h, 1443 h and 1821 h. With reference to Figure 4.35 (b), the bar chart between average apparent charge and average number of PDs per cycle as a function of various ageing times can be divided into three stages. The average apparent charge was just over 32 pC at the initial ageing stage and followed by a steep drop of about 60% during the second stage. In the third stage, the trend dramatically rose by just over 60% during ageing of 1004 h and 1443 h while this figure followed by a further increase of 80% at ageing 1821 h. As regards the average number of PDs per cycle, the figure was just over 9 during initial ageing and subsequently decreased by about 70% during the second stage of ageing while this amount was just over 6 and followed by about 2 at further ageing times of 1004 h and 1841 h respectively with a steep drop of just under 0.2 during the third stage of ageing. The statistical quantities of measured PRPD patterns prior to failure are detailed in Table 4.2. The result shows that the maximum apparent charge tended to increase with a steep rise of just over 4700 pC at ageing 2013 h and followed by a dramatic drop of just under 1 pC at ageing 2013 h 30 min. With reference to the literature, it is suggested that the variation in the maximum PD magnitude steeply increased before breakdown of the test sample [216-217] due to an increase in electronegative gases in a cavity [116]. The asymmetry of average number of PDs per cycle was detected before failure, where the negative half-cycle was higher than the positive half-cycle. It is likely that the progressive propagation of electrical trees in insulation material from initiation to failure during ageing processes [218]. The characteristic of surface discharge patterns in a void was identified due to the initial growth of pits [219]. The appearance of surface tracking was noticed from the outer cavity surface towards insulation material surroundings from one side of a HV electrode as reported in [220].

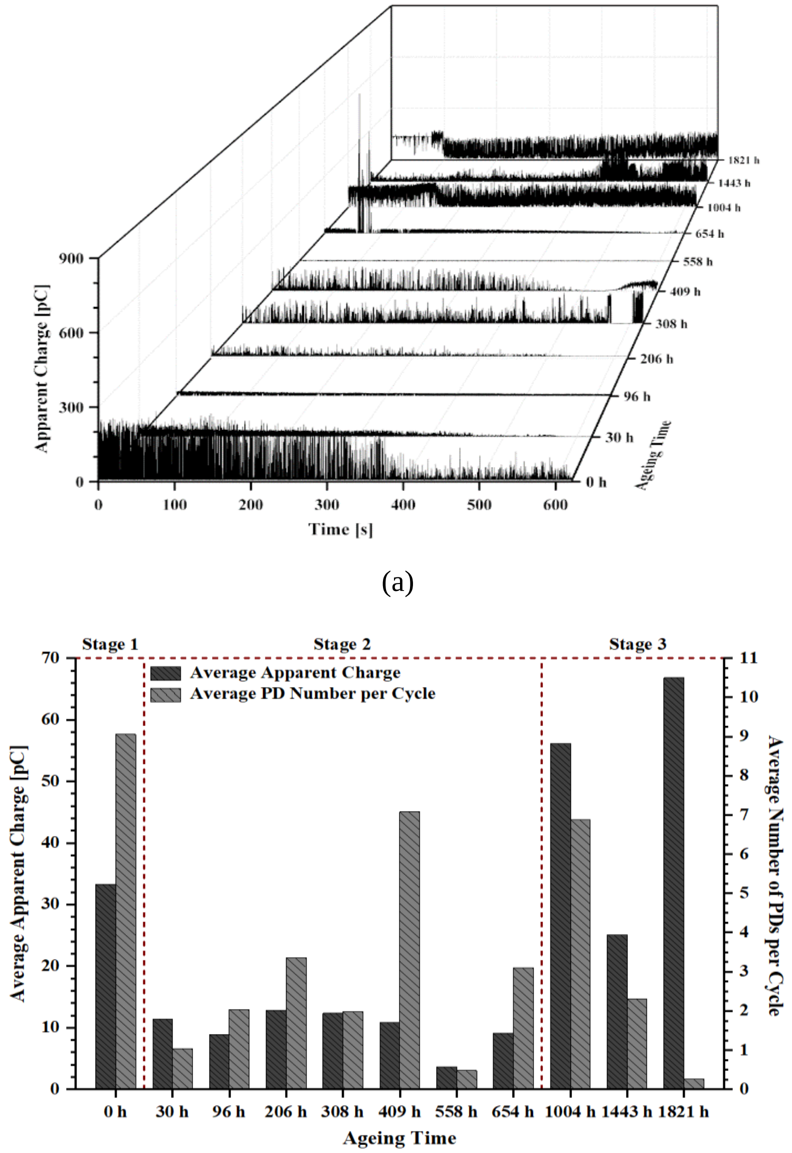

(a)

(b)

Figure 4.35: PD data of the polyethylene sample containing a flat-shaped cavity of diameter 2 mm as a function of various ageing times: (a) the scatter distribution of apparent charge and (b) the bar chart between average apparent charge and average number of PDs per cycle.

Table 4.2: Statistical quantities of measured PRPD patterns before complete failure.

Quantities	**Ageing Time**			
	Fig. 4.34 (a) (2012 h 0 min)	**Fig. 4.34 (b) (2012 h 30 min)**	**Fig. 4.34 (c) (2013 h 0 min)**	**Fig. 4.34 (d) (2013 h 30 min)**
PRPD Patterns	Turtle-like with surface discharges	Turtle-like with surface discharges	Turtle-like with surface discharges	SPMDs
Average Apparent Charge (pC)	326.78	356.62	640.28	0.777
Maximum Apparent Charge (pC)	2876.50	2581.10	4724.30	0.889
Average Number of PDs per Cycle	11.56	11.79	3.93	0.025
Average Number of Positive PDs per Cycle	2.93	3.90	1.54	0.021
Average Number of Negative PDs per Cycle	8.63	7.89	2.38	0.004

4.8 Summary

This chapter reports the experiment results of PD characteristics in a cylindrical flat-shaped cavity embedded in three layers of polyethylene material, which each sample containing a cavity of diameter 2 mm and 0.3 mm in thickness. Measured PDIV characteristics for twenty samples gave the maximum, minimum and average values of 1.787 kV, 1.287 kV and 1.486 kV respectively. All of these samples were aged by increasing the voltage level to 2.5 kV. The results show that PD quantities of the average apparent charge and the average number of PDs per cycle at the initial ageing were higher than the PDIV level. After prolonged ageing, the PD characteristics related to the morphological change in the form of corrosive by-products on the cavity surface were investigated. The results also show that the distinct PRPD patterns exhibited the rabbit-like pattern with a long ear at the initial ageing. The transition of this pattern changed from the turtle-like pattern after ageing just over 400 h to the wing-like pattern with SPMDs, which appeared slight magnitude discharges both positive and negative half-cycle after ageing of just over 1000 h. It is likely that the wing-like pattern is associated with the initial growth of electrical trees on the cavity surface. Also, the various techniques for further diagnosis of degradation processes of a cavity caused by PD activity in terms of physical, thermal and chemical properties were undertaken to clarify the effect of the accelerated ageing. Regarding the dielectric property, the real relative permittivity at 50 Hz almost remained of

2.5 while the trend of tan delta at 50 Hz gradually increased with elapsed time of ageing. With regard to the thermal property, the DSC result shows that the test samples obtained the multiple melting curves after ageing tests. It is possible that the effect of oxidative ageing by PD bombardment changed the chemical bonds in the bulk near to the cavity surface. As regards the chemical analysis, the technique of infrared spectroscopy was used to analyse the chemical composites in both virgin sample and test samples at various ageing times. The result indicates that the new peak was found as carboxylic acids of carbonyl groups at the wavenumber range of 1727 cm^{-1} for all samples after ageing, whereas the absence of this peak was obtained for the virgin sample. It is likely that the chemical chains in bulk of the cavity surface were damaged by the interaction between charge bombardment and chemical reactions inside a cavity during the ageing process. Moreover, microanalysis techniques of SEM and EDX systems were used to reveal the microstructure and chemical elements at the localised erosion site on the cavity surface caused by PD activity. The result shows that the virgin cavity surface was detected an amount of carbon by 100% while the sample after ageing of just over 200 h was noticed localised erosion on the cavity surface, which can be distinguished into three different levels in terms of the surface roughness, the crystal growth and the corrosive by-products. At each of these localised spots, a large amount of nitrogen at the corrosive by-products was identified, compared with the undetectable levels of nitrogen at the locations of the surface roughness and the virgin cavity surface while an amount of oxygen at the corrosive by-product site was higher than the surface roughness site. It is suggested that the variation in gaseous compounds of nitrogen and oxygen inside a cavity was a direct result of ageing, where oxygen was consumed during the initial stage by PD bombardment causing localised erosion on the cavity surface. When oxygen inside a cavity was nearly exhausted due to oxidation reactions, nitrogen ions reacted to induce the progressive growth of pits at the localised erosion site and the initiation of electrical tree growth gradually formed at the localised pits caused by the enhancement of electric fields.

Moreover, this chapter reports analytical results of the relationship between PD characteristics related to the cavity formation, which can be distinguished by analysis of three significant cases in terms of the localised erosion, the electrical tree initiation and the upcoming failure. In the first case of the localised erosion, PD characteristics related to the morphological changes on the cavity surface from the virgin surface to corrosive-by products were investigated for prolonged ageing of just over 1000 h. The result shows that the transition of PRPD patterns changed from the rabbit-like pattern at the initial ageing stage to the turtle-like pattern after ageing of just over 1000 h. In terms of PD quantities, the bar chart between average apparent charge and average number of PDs per cycle can be divided into three main stages as a function of various ageing times that the average apparent charge tended to decrease by about 80% during the first-second stages of ageing and followed by a steep increase of about 70% during the third stage of ageing while the average number of PDs per cycle tended to drop by about 60% during the first-second stages of ageing and then tended to rise by about 70% during the third stage of ageing. The characteristics of typical PRPD patterns can be identified as a rabbit-like pattern and a turtle-like pattern, which the transition of PRPD shapes depended on various factors, i.e. gas pressure, gaseous composites, relative humidity and statistical time lag. It is suggested that an increase of moisture and statistical time lag of a cavity associated with the appearance of rabbit-like shape with a long ear while an increase of surface conductivity on the cavity wall by PD activity resulted in the occurrence of the turtle-like pattern. In the second case of the electrical tree initiation, the cavity formation changed from the virgin cavity to the progressive deposited by-products of electrical tree initiation after ageing of just over 1000 h. The result shows that the evolution of PD characteristics can be identified into three different patterns. In the initial ageing, the transition of PRPD patterns changed from the rabbit-like pattern to the turtle pattern after further ageing 600 h and followed by the wing-like pattern after ageing of just over 1000 h. In the bar chart between average apparent charge and average number of PDs per cycle, it can be divided into three main stages as a function of various ageing times. The result shows that the average apparent charge tended to decrease about 70% during the first second stages of ageing and followed by a steep increase about 80% during the third stage of ageing while the average number of PDs per cycle tended to drop about 60% during the first-second stages of ageing and followed by a steep drop of just under 0.2 at the third stage of ageing. It is likely that PD characteristics of typical cavity discharges were identified as the rabbit-like pattern and the turtle-like pattern while the wing-like patterns with SPMDs linked to the growth of electrical tree initiation. In the third case of the upcoming failure, the PD characteristics related to the morphological changes on the cavity surface were investigated from the virgin cavity to the progressive erosion sites until failure after prolonged ageing of just over 2000 h. The result shows that the variation in PRPD patterns can be distinguished into four different types. In the initial ageing, the transition of PRPD patterns changed from the rabbit-like pattern to the turtle-like pattern after further ageing 1000 h and followed by the wing-like pattern with SPMDs after ageing of just over 1800 h. Subsequently, the turtle-like pattern with surface discharges exhibited before failure of the test sample occurred after ageing of just over 2010 h and followed by the mechanism of SPMDs after ageing 2013 h 30 min. In terms of PD quantities, the bar chart between average apparent charge and average number of PDs per cycle can be divided into three main stages at various ageing times that the average apparent charge tended to decrease by about 60% during the first second stages and followed by a steep increase of about 80% during the third stage while the average number of PDs per cycle tended to drop by about 70% during the first-second stages and followed by a steep drop of just under 0.2 at the third stage of ageing. It is likely that the presence of electrical tree initiation from the cavity surface associated with the wing-like pattern with SPMDs while the turtle-like patterns with surface discharges exhibited before failure of the test sample. In particular, it can be seen that the PD quantities of the maximum PD magnitude rapidly increased before failure while the average number of PDs per cycle was obtained the asymmetry between positive and negative half-cycles.

Chapter 5 Analysis of Degradation Mechanisms by PD Activity within a Spherical Cavity in Silicone Material

The main objective of this chapter is to present both measurement and simulation results based on PD activity in a spherical cavity. The physical parameters of the model based on the experiment result regarding the cavity radius, the material thickness, the applied voltage and the relative permittivity can be defined in a Finite Element Analysis (FEA) model, which is used to find electric field magnitudes in the model of a cavity embedded in insulation material in Section 5.1. In section 5.2, the PD characteristics of PD quantities is analysed from thirty-five test samples in terms of the PDIV, the average number of PDs per cycle, the average apparent charge, the inception electric field and pressure. Also, all of these samples undergo the accelerated ageing, where PD quantities in terms of both average apparent charge and maximum apparent charge as a function of various cavity diameters are compared between measurement and simulation results in Section 5.3. Furthermore, the simulation results of PD characteristics in terms of PRPD patterns, φ-q-n plots and statistic PD quantities as functions of various voltage amplitudes and various ageing times are reproduced to compare the measurement results in Sections 5.4 and 5.5 respectively. A comparison of two silicone samples containing different cavity diameters was undertaken to investigate the PD characteristics of PRPD patterns and PD quantities related to the occurrence of deposited by-products on the cavity wall in terms of liquid droplets and growing protrusions during accelerated ageing processes in Section 5.6. The chemical technique of infrared spectroscopy is used to examine the chemical composites of corrosive by-products inside an enclosed cavity caused by the effect of the accelerated ageing process. An investigation into PD characteristics of the variation in PRPD patterns and PD quantities used to identify the relative level of erosion depth in the vertical cross-section views from various cavity sizes is detailed in Section 5.7. The use of PRPD analysis for diagnosis of degradation processes in a spherical cavity embedded in silicone rubber, which can be distinguished into three significant cases of the cavity formation regarding the localised erosion site, the electrical tree initiation and the upcoming failure. The evolution of PD characteristics in both PRPD patterns and PD quantities is analysed to identify the morphological change of localised erosion on the cavity surface due to the accelerated ageing. Also, an investigation into microanalysis of the deposited by-products, i.e. micro-craters is further examined using chemical techniques of SEM and EDX instruments to reveal the microstructure and chemical composites in bulk at the localised site in Section 5.8. In particular, visible evidence of the electrical tree initiation from the cavity surface is revealed the localised erosion site of corrosive by-products on the cavity wall. Based on the PD results, the variation in distinct PRPD patterns and PD quantities can be analysed to validate a direct link of degradation mechanisms on the cavity surface regarding the electrical tree initiation in Section

5.9. Another investigation into the morphological changes of a spherical cavity from the surface erosion to complete failure is undertaken to diagnose the time-evolution of PRPD patterns and PD quantities related to the cavity formation, which can be distinguished into four different shapes in terms of the surface erosion, the tree growth, the surface discharges prior to failure and complete failure. Also, the simulation of these PRPD patterns and statistical quantities are reproduced for comparison with the measurement result in Section 5.10. A summary of this chapter is provided in the last section.

5.1 Finite Element Analysis (FEA) model of an air-filled cavity

The model of an air-filled cavity in silicone material is designed in a two-dimensional geometry as shown in Figure 5.1 The model is assumed that a PD event inside a cavity occurs, if the electric field magnitude in the centre cavity is governed above the inception value, which can be solved by using an electrostatic equation in Comsol. The physical parameters of this model based on the test sample from the PD measurement consist of a spherical cavity radius embedded in insulation material, the sample thickness, the relative permittivity of a cavity, the relative permittivity of dielectric material and the applied voltage amplitude. The model is used in this work to establish if measured PRPD properties can be simulated.

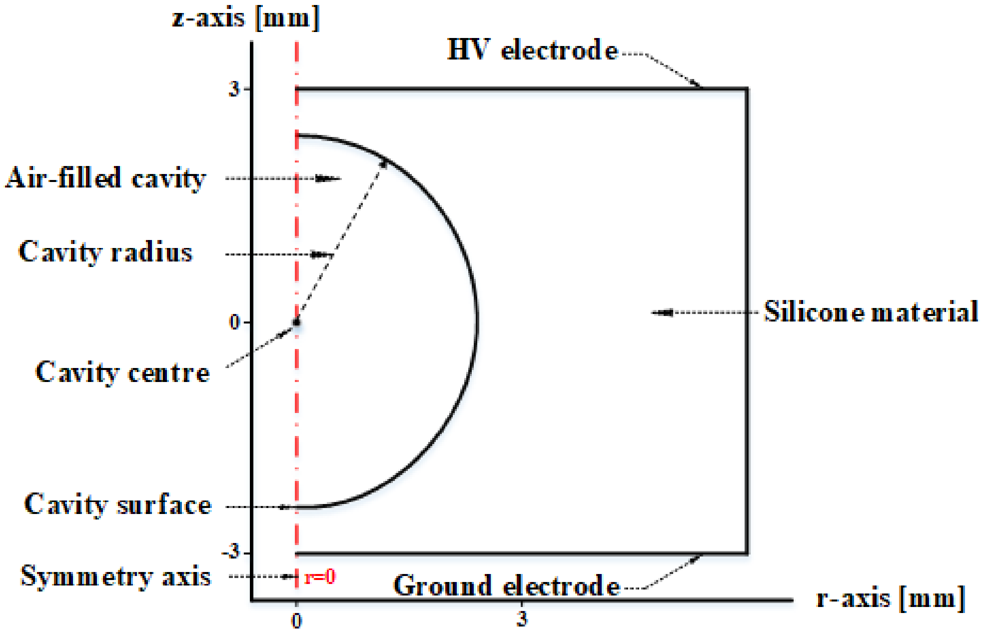

Figure 5.1: Model of the symmetrical axis of a spherical cavity in silicone material in Comsol.

5.2 PDIV characteristics as a function of various spherical cavity diameters

The PD characteristics of PDIV were determined by finding the average value of thirty-five test samples that each samples containing different spherical cavity diameters between 0.5 mm and 2.42 mm and 3 mm in thickness for further detailed sample preparation in Section 3.1.2. All samples, PDIVs were found by increasing the applied voltage until the initiation of a PD event occurred and then the PD data recorded for 10 min. The scatter plot of Figure 5.2 (a) represents the characteristics of PDIV as a function of cavity diameters, where the average inception voltage of these samples was 8.96 kV. The trend values of PDIV tended to increase with the cavity diameters, where the minimum and maximum of inception voltage values were obtained of 4.215 kV and 11.44 kV for cavity diameters of 0.5 mm and 2.42 mm respectively. The measurement of average apparent charge as a function of cavity diameters was compared with the simulation as shown in Figure 5.2 (b). The simulated data of electric field magnitudes and pressure were obtained based on Equation 2.10. For example, the calculation of approximate apparent charge in a spherical cavity embedded in solid dielectric material details in Appendix C.4, where the charge on the cavity wall is transferred from the inner cavity wall to the outer dielectric connected with the ground electrode side. The measured apparent charge tended to be about 137 pC and 465 pC for the cavity diameters of 0.5 mm and 2.42 mm respectively while the simulated apparent charge gradually rose with increasing the cavity sizes from about 2.9 pC to 1.2 nC for the cavity diameters of 0.5 mm and 2.42 mm respectively. The trend of apparent charge at the PDIV level tended to increase with cavity diameters, according to the measurement and simulation results as reported elsewhere [221]. The calculation of apparent charge magnitude as a function of void diameters was determined using Pedersen and Yasui models, where the charges of both models tended to increase with a raising of cavity sizes [106]. A comparison between PD measurement and models, i.e. capacitor and Pedersen models established that the apparent charge tended to increase with varying cavity sizes, where the values of measurement were lower than the simulation data [222]. The inception electric field at the centre point of a cavity as a function of cavity diameters is illustrated in Figure 5.2 (c). The trend tended to increase with the cavity diameters, where the inception values were obtained 1.78 kV/mm and 4.47 kV/mm from the cavity diameters of 0.5 mm and 2.42 mm respectively. It is assumed that when the dipolar charges on the cavity wall remain constantly, an amount of induced charges on the electrodes and an electric field enhancement alongside the upper and lower cavity wall with their bulk material surroundings are proportional to the increased cavity sizes [110]. The gas pressure inside a cavity at the PDIV condition can be calculated through a self-sustained criterion of the streamer discharge in Equation 2.10, which gas pressure inside a cavity as a function of cavity diameters can be determined to compare with the fitted curve of Paschen's law for air as shown in Figure 5.2 (d). The result shows that the calculated pressure tended to increase with the cavity sizes from about 19.7 kPa to 123.3 kPa for cavity sizes of 0.5 mm and 2.42 mm respectively. It should be noted that the behaviour of gas pressure inside a cavity should be below 101.32 kPa at atmosphere, whereas some values of calculated pressure inside a cavity based on the PD measurement were obtained above atmospheric pressure, this occurred for the samples containing cavity diameters between 1.45 mm and 2.42 mm. It is possible that when a virgin sample was measured the PDIV level, the supply voltage was increased slowly until the initial discharge occurred, but the actual inception voltage might be lower than that recorded due to the influence of statistic time lag in a cavity as detailed in the literature [223]. Furthermore, the time evolution of gas pressure in a cavity occurred during the ageing process, it has been reported that the calculated pressure from the inception field can be obtained between 150 kPa and 200 kPa because the variation in gaseous molecules inside a cavity resulted from PD activity and elapsed time of ageing [31].

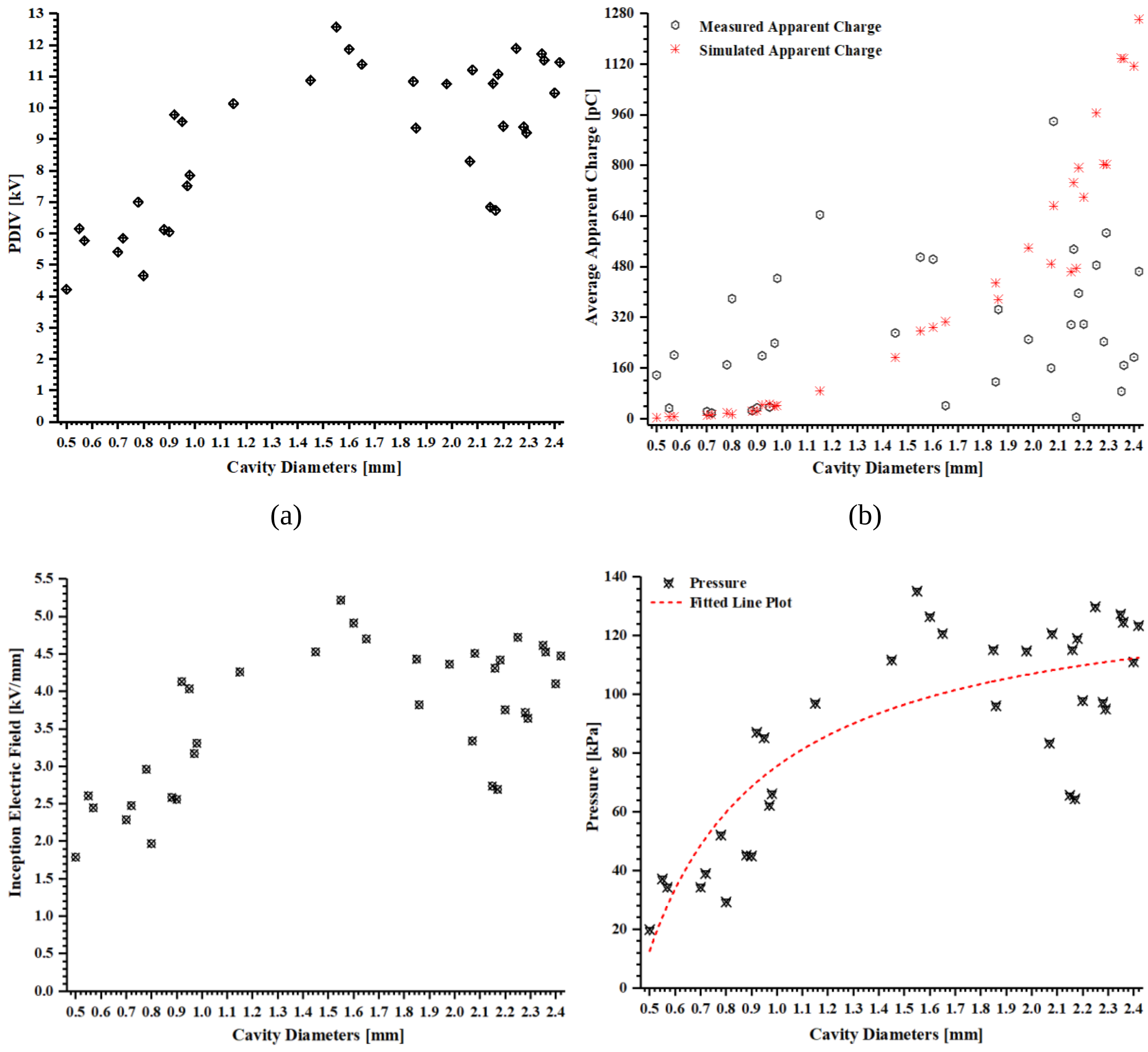

(a) (b)

(c) (d)

Figure 5.2: PD data of thirty-five test samples as a function of different spherical cavity diameters at the inception voltage level: (a) PDIV magnitudes, (b) comparison of average apparent charge between measurement and simulation results, (c) inception electric field magnitudes at a centre cavity and (d) comparison of calculated pressure between the inside cavity and the fitted line plot.

5.3 Accelerated ageing characteristics as a function of various spherical cavity diameters

To determine PD characteristics as a function of ageing for thirty-five different spherical cavity diameters of test samples, the applied voltage was increased by 80% over the average PDIV level. At the beginning of the experiment, each sample had an applied voltage level of 16 kV while PRPD data were acquired for 10 min. Following this, all samples were electrically stressed at the constant voltage level by using multi-test cells for ageing processes as further detailed in Sections 3.3.1 and 3.3.2.

The scatter plots between average apparent charge and maximum apparent charge in both measurement and simulation results as a function of cavity diameters have been compared as shown in Figures 5.3 (a) and 5.3 (b). The results show that the measurement of maximum apparent charge was obtained with an increase from 117 pC to 870 pC for cavity diameters of 0.5 mm and 2.42 mm respectively while the trend of simulation predicted values over the range of 1.76 nC for cavity diameters above 2.42 mm.

Referring to the model in two-dimensional geometric axes in Section 5.1, the symmetry of electric field distribution along the z-axis as a function of different cavity diameters is illustrated in Figure 5.3 (c). The electric field magnitudes tended to slightly decrease with increasing the cavity diameters from 0.5 mm to 2.42 mm while the symmetry of electric field distribution along the r-axis as a function of different cavity diameters is shown in Figure 5.3 (d). The electric field magnitudes tended to slightly reduce with increasing the cavity diameters from 0.5 mm to 2.42 mm while the electric field in the middle cavity was slightly lower than the surrounding dielectric material of the outer cavity surface. Moreover, the electric field distribution in the centre cavity tended to slightly decrease with increasing the cavity diameters, with simulated values of 6.78 kV/mm and 6.25 kV/mm from the cavity diameters of 0.5 mm and 2.42 mm respectively. The result indicates that the magnitudes of maximum apparent charge were slightly higher than the average apparent charge, which slightly raised with increasing the cavity sizes as reported in other researches [221, 225]. Moreover, Comparison between measurement and simulation data of charge magnitudes showed their trend with increasing the cavity diameters [226-227].

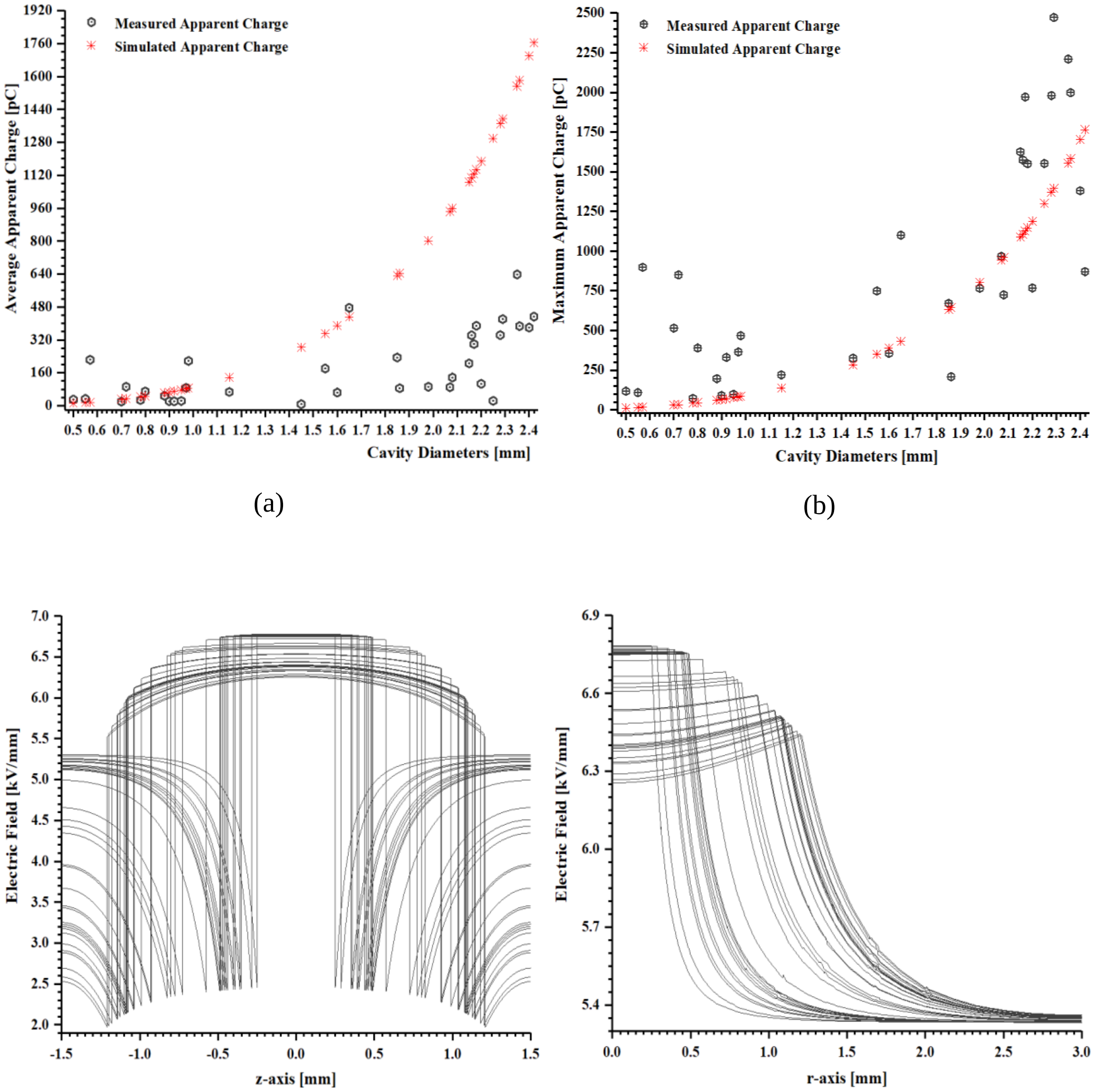

(a) (b)

(c) (d)

Figure 5.3: PD data of thirty-five samples as a function of different spherical cavity diameters at the applied voltage level of 16 kV, 50 Hz: (a) comparison between measurement and simulation magnitudes of average apparent charge, (b) comparison between measurement and simulation magnitudes of maximum apparent charge, (c) and (d) cross-section plots of the symmetric axis of electric field distribution along the z-axis and the r-axis in the FEA model respectively.

5.4 PD characteristics as a function of various voltage amplitudes

The influence of various voltage amplitudes on PD activity was investigated for the sample containing a spherical cavity of diameter 0.80 mm embedded in silicone dielectric material with 3 mm in thickness. The simulation results of PD characteristics in terms of PRPD patterns, φ-q-n plots and statistic PD quantities were reproduced to compare the measurement results.

5.4.1 Measurement of PD activity

The measured PRPD patterns at different applied voltage levels of 14 kV and 16 kV are illustrated as shown in Figures 5.4 (a) and 5.4 (b) respectively that both shaped plots exhibited the rabbit-like patterns and were the symmetry between positive and negative half-cycles, the rabbit-like pattern with a larger ear was detected at 16 kV. The φ-q-n plots at various applied voltage levels of 14 kV and 16 kV were also obtained as shown in Figures 5.5 (a) and 5.5 (b) respectively. The result shows that amounts of average magnitudes of apparent charge and number of PDs at the applied voltage level of 16 kV were higher than the applied amplitude of 14 kV.

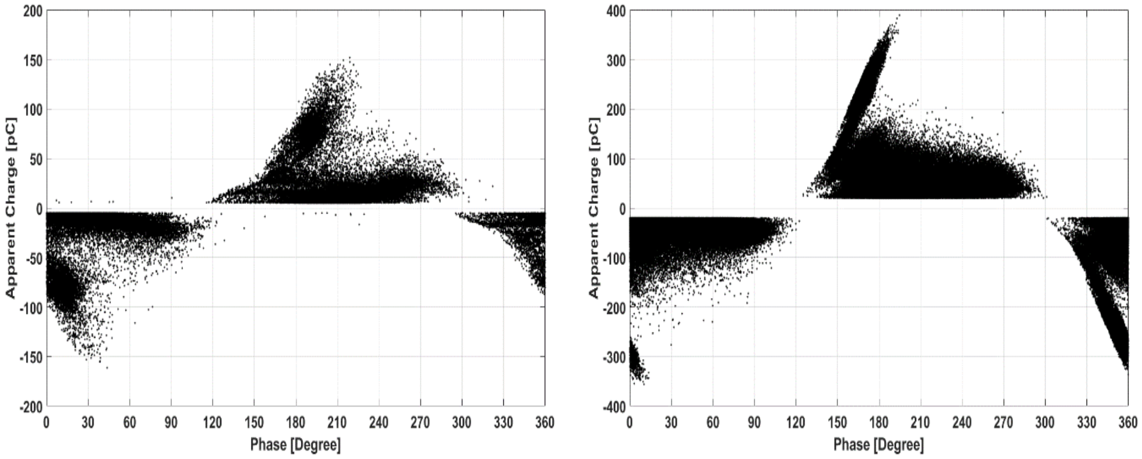

(a) (b)

Figure 5.4: Measured PRPD patterns of the test sample: (a) a rabbit-like pattern at 14 kV and (b) a rabbit-like pattern at 16 kV.

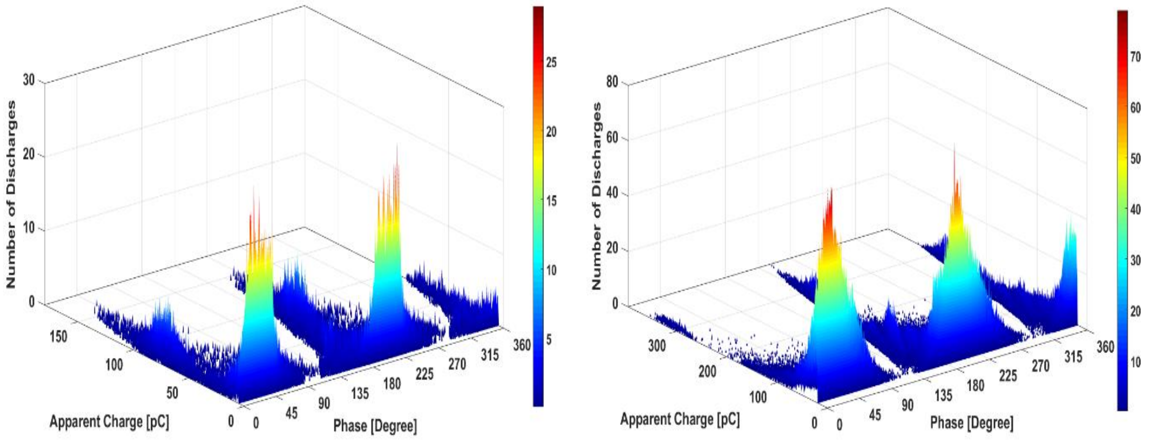

(a) (b)

Figure 5.5: Measured φ-q-n plots of the test sample: (a) a rabbit-like pattern at 14 kV and (b) a rabbit-like pattern at 16 kV.

5.4.2 Simulation of PD activity

A PD model was developed to reproduce the measurement results of both PRPD patterns and PD quantities through Matlab codes in Appendix D.2. The values of physical parameters used in the model for simulation based on the test sample of PD measurement are listed in Table 5.1. The axisymmetric model consisted of a spherical cavity radius of 0.8 mm in a cylindrical dielectric radius with 5 mm and 3 mm in thickness. The relative permittivity of a cavity was 1 and the relative permittivity of dielectric material was 2.8. The simulated PRPD patterns at different applied voltage levels of 14 kV and 16 kV were reproduced the rabbit-like patterns as shown in Figures 5.6 (a) and 5.6 (b) respectively. The φ-q-n plots for these patterns were also exhibited with the symmetry between positive and negative half-cycle as shown in Figures 5.7 (a) and 5.7 (b). The PD statistical quantities of PRPD patterns between measurement and simulation results at different applied voltage amplitudes were compared in Table 5.2. On the one hand, the measurement of PD quantities after increasing the applied voltages from 14 kV to 16 kV shows that the average apparent charge and the maximum apparent charge were obtained 27 pC and 161 pC of 14 kV, and 69 pC and 389 pC of 16 kV while the average number of PDs per cycle was obtained from just over 2.0 to just over 6.8 with the symmetry between the positive and negative half cycles. On the other hand, the simulation of PD quantities at different voltage amplitudes between 14 kV and 16 kV shows that the average apparent charge and the maximum apparent charge were between 47 pC and 164 pC at 14 kV and between 103 pC and 390 pC at 16 kV. The average number of PDs per cycle was obtained from just over 2.0 to just over 6.8 with the symmetry between positive and negative half cycles. This result indicates that there is reasonable agreement for PRPD patterns, φ-q-n plots and PD quantities between measurement and simulation results. Other research has found that the simulation of the rabbit-like pattern was reproduced to match the measurement as functions of various frequency and various voltages, where the factor of work function was adjusted with varying trapped charge rates on the cavity surface [228]. Moreover, the φ-q-n plots between measurement and simulation results as a function of different applied voltage magnitudes were compared for each plot, where the physical model was adjusted the values of the surface conductivity and the electron generation rate to fit the measurement result [229].

Table 5.1: Physical parameters used for a two-dimensional model in Comsol.

Definition	Parameter	Value
Applied voltage amplitude	U_{app}	14 kV, 16 kV
Cavity diameter	d_c	0.8 mm
Dielectric material thickness	d_m	3 mm
Relative permittivity inside a cavity	ε_c	1
Relative permittivity of dielectric material	ε_r	2.8

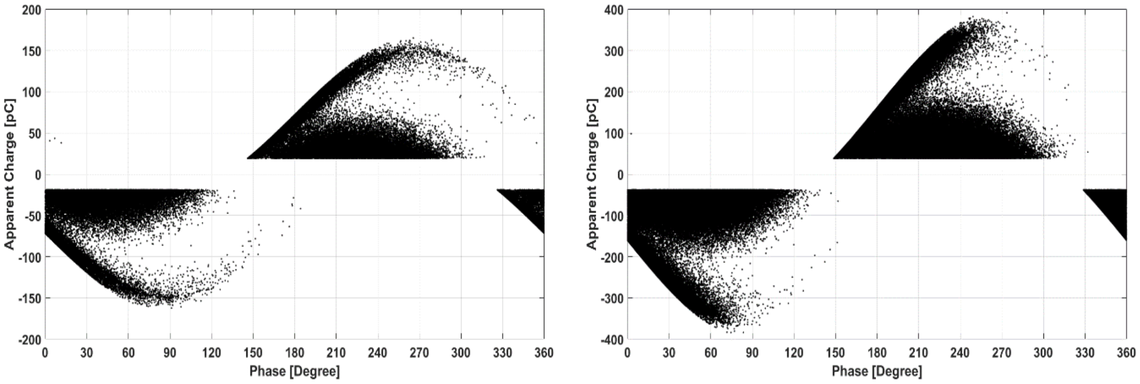

(a)

(b)

Figure 5.6: Simulated PRPD results: (a) 14 kV rabbit-like and (b) 16 kV rabbit-like.

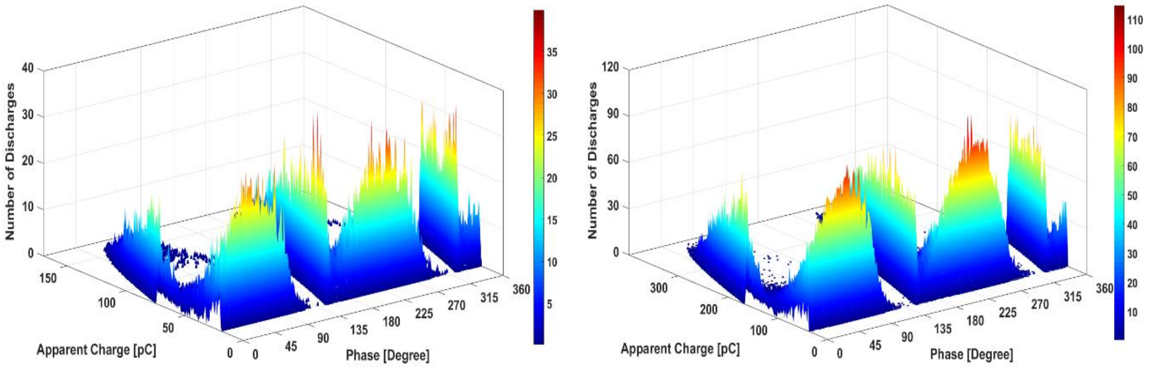

(a)

(b)

Figure 5.7: Simulated φ-q-n plots: (a) 14 kV rabbit-like and (b) 16 kV rabbit-like.

Table 5.2: PD quantities between the measurement and simulation results as a function of various applied voltage amplitudes.

Quantities	**MEASUREMENT**		**SIMULATION**	
Applied voltage (kV)	14	16	14	16
PRPD Patterns	Rabbit-like	Rabbit-like	Rabbit-like	Rabbit-like
Average Apparent Charge (pC)	27.42	69.73	47.43	103.65
Maximum Apparent Charge (pC)	161.41	389.31	164.87	390.87
Average Number of PDs per Cycle	2.08	6.87	2.09	6.86
Average Number of Positive PDs per Cycle	1.02	3.41	1.05	3.43
Average Number of Negative PDs per Cycle	1.06	3.46	1.04	3.43

5.5 PD characteristics of degradation mechanisms as a function of ageing time

PD activity in an air-filled cavity embedded in solid insulation material was undertaken to investigate PD behaviour related to the cavity formation under elapsed time of accelerated ageing from surface erosion and eventually complete failure. The time-evolution of PRPD analysis demonstrated evidence of the formation of an eroded hole. Analysis of PD statistical quantities for distinct patterns is obtained in terms of the apparent charge and the number of PDs per cycle. The physical parameters of the test sample are used to implement an electrostatic Finite Element Analysis (FEA) model, which is used to develop a PD model.

5.5.1 Optical microscopy

Before measuring PD, the morphological changes of the sample containing a spherical cavity with a diameter of 2.40 mm were observed using optical microscope and the sample thickness was measured as approximately 3 mm as shown in Figure 5.8 (a). The morphology of a failed sample after ageing 420 min showed localised erosion on the centre cavity surface as shown in Figure 5.8 (b). It is likely that the localised erosion site in bulk on the cavity wall was bombarded by the interaction between PD activity and gaseous composites inside a cavity and enhanced the electric field magnitude at this localised site [56-57]. These factors led to the initial protrusions on the outer cavity surface and followed by the progressive propagation of electrical trees until complete failure of the sample [14, 230]. Also, the influence of accelerated ageing acted to increase the enhancement of electric fields at the localised site between the cavity wall and the surrounding dielectric material in the vertical direction, which was proportional to increase the cavity sizes [110].

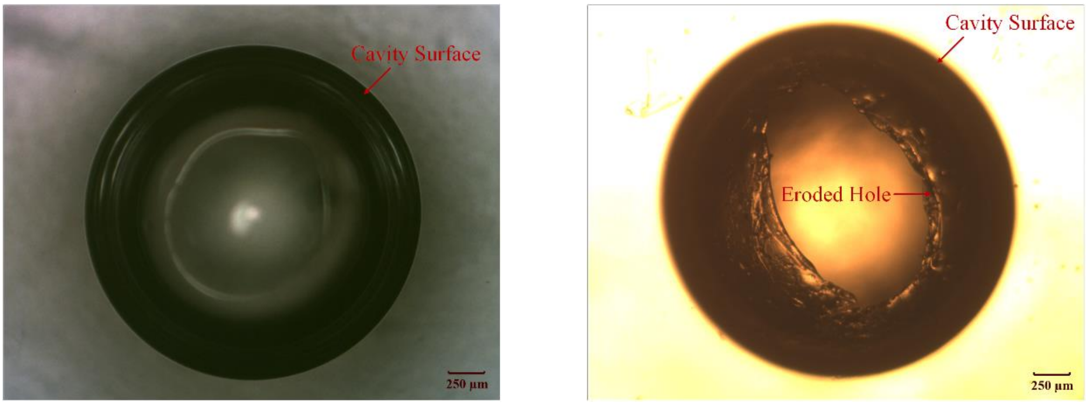

(a) (b)

Figure 5.8: Morphological changes in the sample containing a spherical cavity of diameter 2.40 mm at various ageing times: top-section views of (a) a virgin cavity and (b) an eroded hole formation after failure at ageing 420 min.

5.5.2 Measurement of PD activity

The PRPD characteristic of typical turtle-like pattern exhibited at ageing 30 min as shown in Figure 5.9 (a). The transition of this PRPD pattern was noticed the asymmetry between positive and negative half-cycles after the ageing time of 240 min, where the magnitude discharges of this PRPD pattern for the positive half-cycle were larger than the negative half-cycle. According to an investigation into PD characteristics from a cavity in polyethylene material, the asymmetry of the discharge patterns exhibited in both positive and negative half-cycles is due to the influence of defect locations and ageing stages [232]. Moreover, the asymmetry in discharge magnitudes might cause by the deposition of unequal conductivity on the cavity wall, where the localised erosion site of cracks highly charged by PD activity [233]. After further ageing before failure, the wing-like pattern exhibited after ageing 390 min with SPMDs, which appeared slight magnitude discharges both positive and negative half-cycles as shown in Figure 5.9 (b). It is considered that the typical discharge mechanism within a cavity linked to the turtle-like pattern while the wing-like pattern associated with the growth of electrical trees [14]. When the SPMDs occurred, this was shortly before complete breakdown [124, 234]. The φ-q-n plots for these patterns exhibited as shown in Figures 5.10 (a) and 5.10 (b). The statistical quantities of measured PRPD patterns at each ageing stage are listed in Table 5.3.

The evolution of PD activity was acquired continuously to record every 30 minutes during the electrical ageing until failure of the test sample. The scatter plot between average apparent charge and average number of PDs per cycle between positive and negative half-cycles is illustrated in Figure 5.11 (a) while the maximum PD magnitude and the average number of PDs per cycle are shown in Figures 5.11 (b) and 5.11 (c) respectively. For the PD magnitude, the discharges tended to decrease with elapsed time of ageing. This result is associated with similar PD characteristics before failure of the test sample in the literature [231].

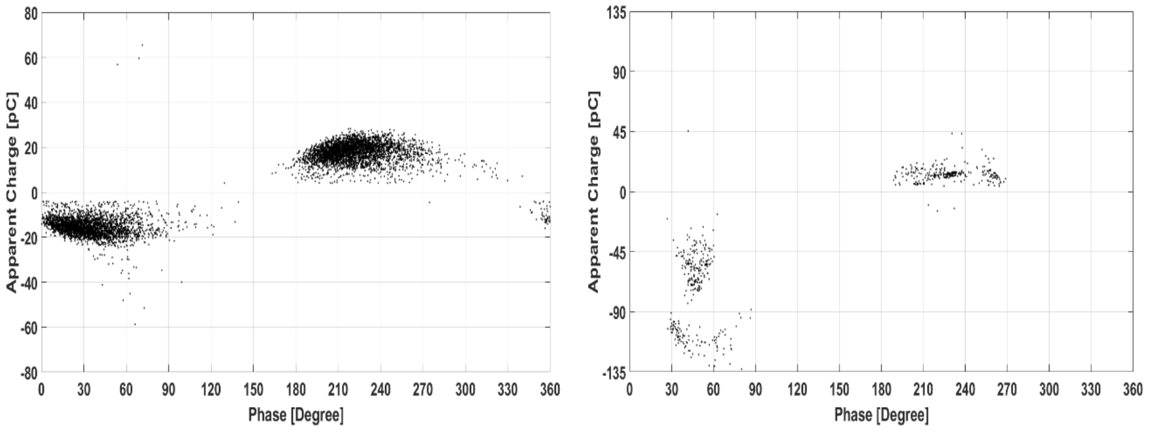

(a) (b)

Figure 5.9: Measured PRPD patterns of the test sample: (a) a turtle-like pattern at ageing 30 min and (b) a wing-like pattern at ageing 390 min.

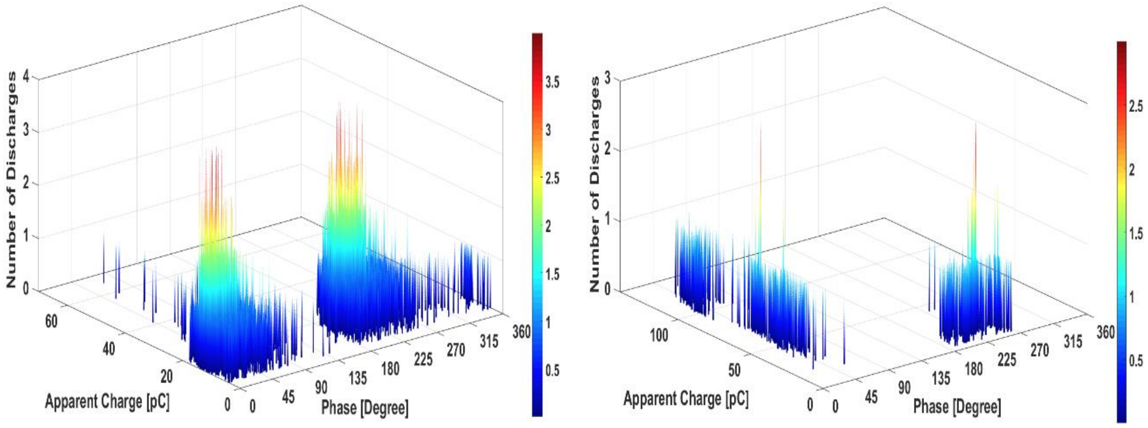

(a) (b)

Figure 5.10: Measured φ-q-n plots of the test sample: (a) a turtle-like pattern at ageing 30 min and (b) a wing-like pattern at ageing 390 min.

Table 5.3: Statistical quantities of measured PRPD patterns at various ageing stages.

Quantities	**Ageing Stages**	
	Fig. 5.9 (a) **(30 min)**	**Fig. 5.9 (b)** **(390 min)**
Elapsed Time to Failure (%)	7.14	92.85
Types of PRPD Patterns	Turtle-like	Wing-like with SPMDs
Average Apparent Charge (pC)	16.59	44.55
Maximum Apparent Charge (pC)	59.43	132.96
Average Number of PDs per Cycle	0.21	0.0181
Average Number of Positive PDs per Cycle	0.10	0.0092
Average Number of Negative PDs per Cycle	0.11	0.0089

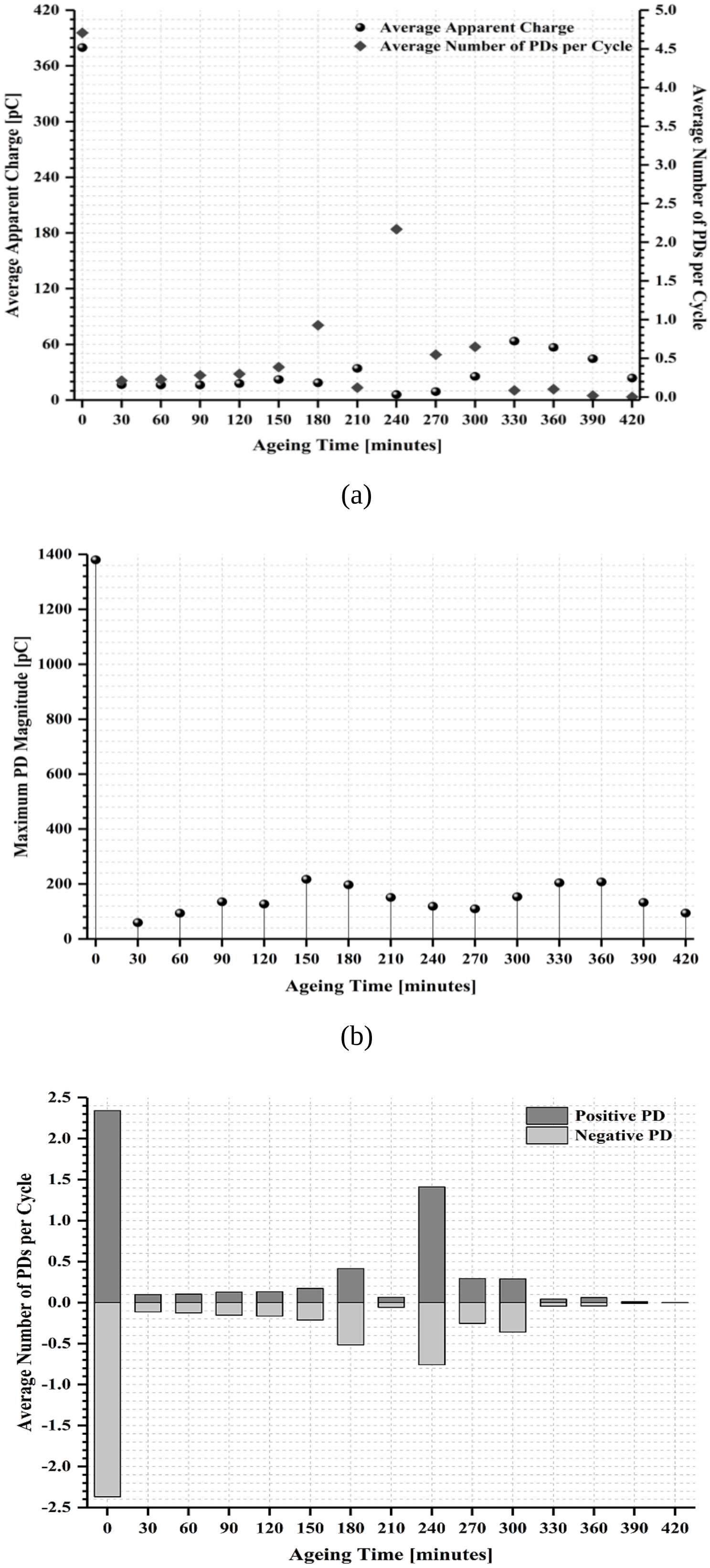

(a)

(b)

(c)

Figure 5.11: Evolution of PD characteristics as a function of ageing time for the sample containing a spherical cavity of diameter 2.40 mm: (a) the scatter plot between average apparent charge and average number of PD per cycle, (b) the maximum PD magnitude and (c) the average number of positive and negative PDs per cycle. Simulation of PD activity

A PD model was developed to reproduce the experimental data from Matlab codes in Appendix D.2. The physical parameters of these axisymmetric models consisted of a spherical cavity radius of 1.2 mm embedded in a cylindrical dielectric radius with 25 mm and 3 mm in thickness. The relative permittivity of a cavity was 1, the relative permittivity of dielectric material was 2.8 and the applied voltage amplitude was 16 kVrms. The simulated PRPD patterns for the turtle-like pattern and the wing-like pattern were reproduced as shown in Figures 5.12 (a) and 5.12 (b) respectively while the φ-q-n plots for these patterns shown in Figures 5.13 (a) and 5.13 (b). The discharge magnitudes were symmetrical between positive and negative half-cycles for the turtle-like pattern while the positive half-cycle was slightly higher than the negative half-cycle for the wing-like pattern. The symmetrical pattern during the initial ageing indicates that the cavity was located in the centre of dielectric material between parallel plate electrodes [229]. The statistical quantities of simulated PRPD patterns are listed in Table 5.4. The simulation results were comparable to the measured PRPD patterns at 30 min and 390 min of ageing. Specifically, the measurement and simulation results for the turtle-like pattern showed reasonable agreement in terms of the shaped pattern, the average apparent charge and the average number of PDs per cycle, whereas the maximum apparent charge obtained a slight difference between the measurement and simulation. In the wing-like pattern, there was reasonable agreement between the simulation and measurement for the average apparent charge and the average number of PDs per cycle, whereas the shaped pattern and the maximum apparent charge showed a discrepancy. It is suggested that the PD characteristics of PRPD patterns exhibited the turtle-like pattern because the changes of deposited by products in a cavity such as surface conductivity and gas conductivity increased while gas pressure decreased during the oxidation reaction at the initial ageing. The simulation of this pattern was reproduced by varying these three parameters [236]. Note that the asymmetric PRPD pattern before failure of the test sample exhibited the wing-like pattern, which discharges of the positive half-cycle were slightly higher than the negative half-cycle as reported by other researcher [14, 237].

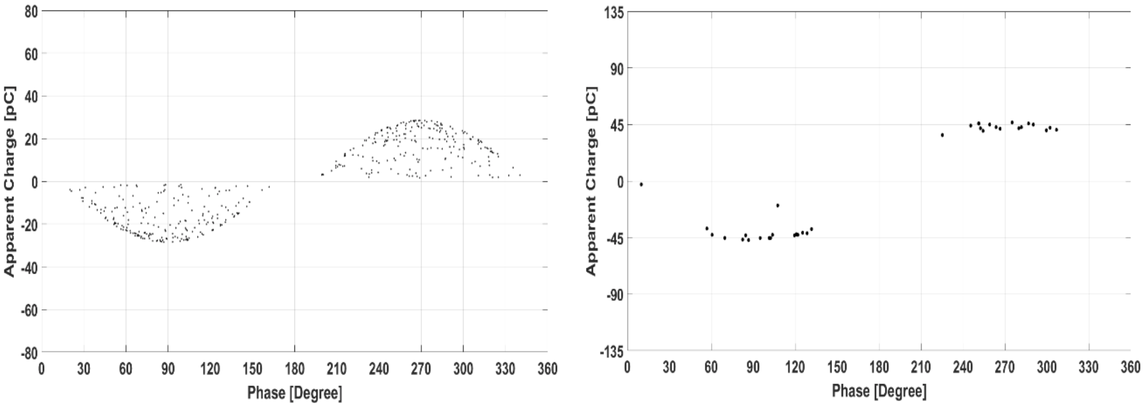

(a) (b)

Figure 5.12: Simulated PRPD results: (a) a turtle-like plot and (b) a wing-like plot.

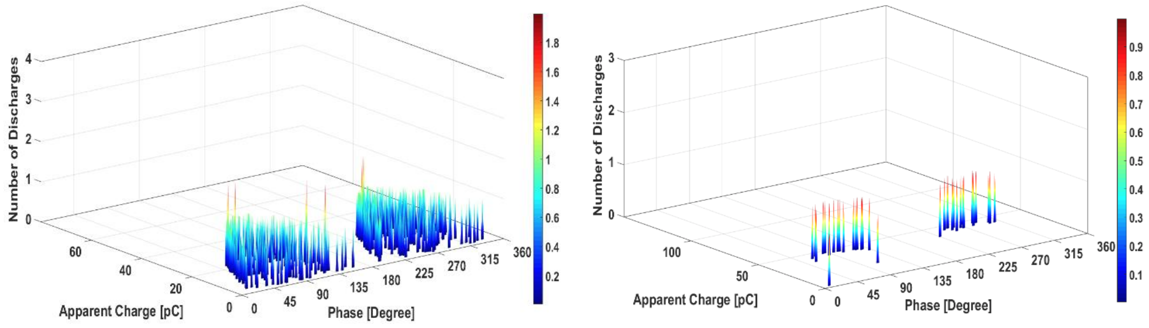

(a)

(b)

Figure 5.13: Simulated φ-q-n plots: (a) a turtle-like plot and (b) a wing-like plot.

Table 5.4: Statistical quantities of simulated PRPD patterns.

Quantities	**Characteristic Models**	
	Fig. 5.12 (a)	**Fig. 5.12 (b)**
Types of PRPD patterns	Turtle-like	Wing-like
Average Apparent Charge (pC)	16.632	41.254
Maximum Apparent Charge (pC)	28.501	46.985
Average Number of PDs per Cycle	0.206	0.0175
Average Number of Positive PDs per Cycle	0.102	0.009
Average Number of Negative PDs per Cycle	0.104	0.0085

5.6 PD characteristics of surface erosion as a function of various cavity sizes

Having established, PD behaviour over an accelerated lifetime for test samples of silicone rubber material with cavities as detailed in section 5.5, this has been used to allow further investigation into morphological and chemical changes at specific points in the ageing process.

5.6.1 Optical microscopy

Comparison of two samples containing different cavity diameters was investigated to find out deposited by-products on the cavity surface during the electrical ageing process. In a cavity diameter of 0.98 mm, the virgin cavity was observed using optical microscopy as shown in Figure 5.14 (a). Visible evidence of liquid droplets inside a cavity was noticed at ageing 30 h as shown in Figure 5.14 (b). After further ageing of 60 h, the inner cavity was obtained the protrusions and localised erosion on the centre cavity surface as shown in Figure 5.14 (c).

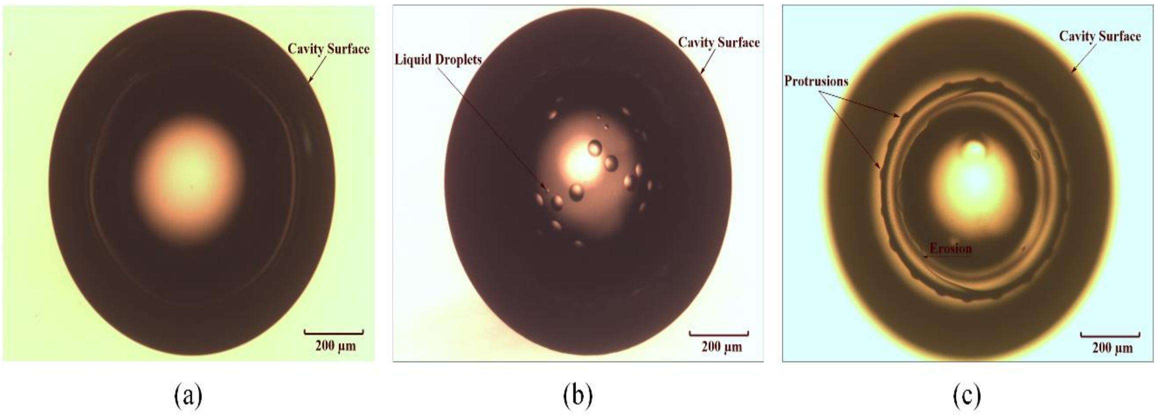

(a) (b) (c)

Figure 5.14: Morphological changes of the sample containing a spherical cavity of diameter 0.98 mm at various ageing times: top-section views of (a) a virgin cavity, (b) liquid droplets on the cavity surface at ageing 30 h and (c) protrusions and localised erosion on the cavity surface at ageing 60 h.

In a cavity diameter of 0.97 mm, the morphological cavity before ageing showed in Figure 5.15 (a). The cavity formation was observed the protrusions and localised erosion on the cavity surface as shown in Figure 5.15 (b), which a high-magnification of this localised site obtained by the deposited by-products of liquid droplets in the centre cavity as shown in Figure 5.15 (c). It is suggested that liquid droplets were formed in bulk of silicone rubber material due to loss of hydrophobicity by PD activity during the ageing process [2].

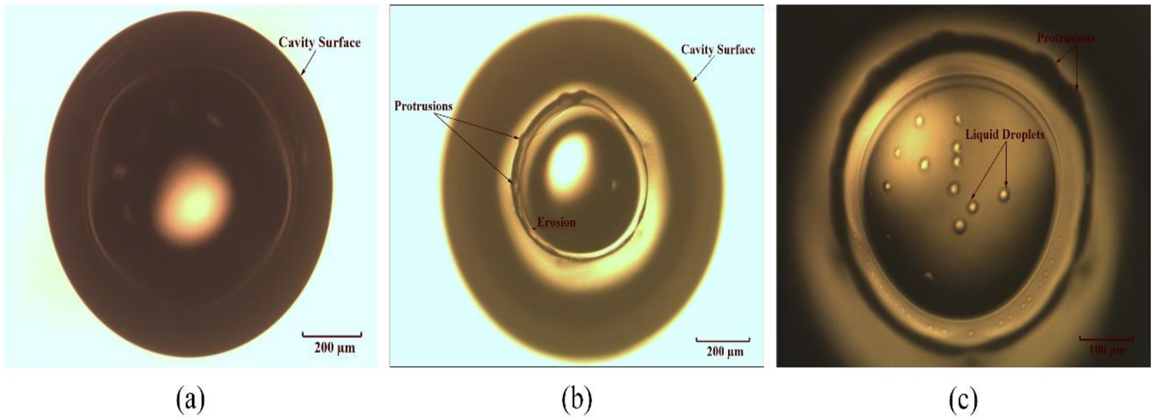

(a) (b) (c)

Figure 5.15: Morphological changes of the sample containing a spherical cavity of diameter 0.97 mm at various ageing times: top-section views of (a) a virgin cavity, (b) protrusions and localised erosion on the cavity surface at ageing 120 h and (c) a high-magnification in the micrograph (b) showing liquid droplets inside the cavity.

5.6.2 Measurement of PD activity

In the initial ageing of 10 min for the sample containing a spherical cavity of diameter 0.98 mm, the typical turtle-like pattern exhibited as shown in Figure 5.16 (a) while the PD quantities of average apparent charge and average number of PDs per cycle were just over 200 pC and 2 respectively. This PRPD pattern remained unchanged, whereas the average apparent charge and the average number of

PDs per cycle decreased just over 90% and 70% respectively after further ageing 60 h as shown in Figure 5.16 (b).

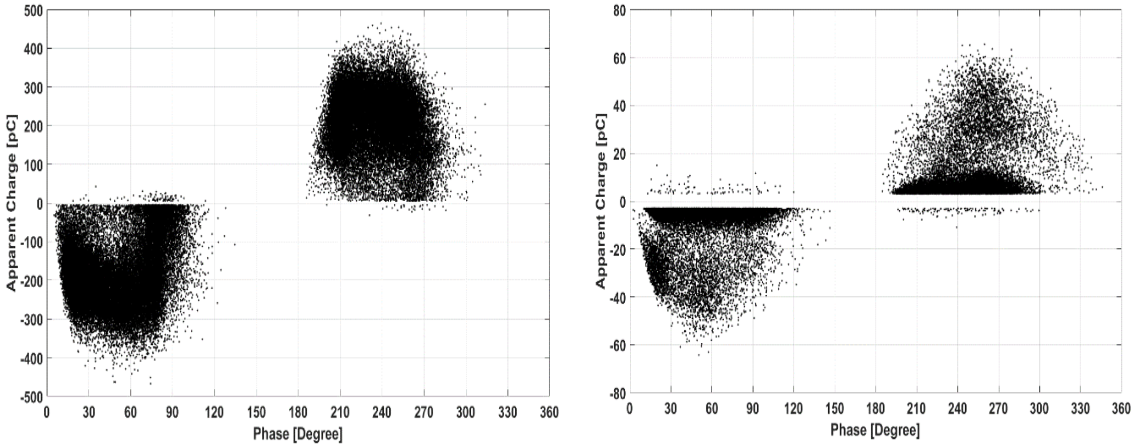

(a) (b)

Figure 5.16: Measured PRPD patterns of the sample containing a spherical cavity of diameter 0.98 mm at various ageing times: (a) a turtle-like pattern at ageing 10 min and (b) a turtle-like pattern at ageing 60 h.

In the initial ageing of 10 min for the sample containing a spherical cavity of diameter 0.97 mm, the turtle-like pattern was detected as shown in Figure 5.17 (a) while the PD statistical quantities of average apparent charge and average number of PDs per cycle were just over 85 pC and 2 respectively. This PRPD pattern remained unchanged, whereas the average apparent charge and the average number of PDs per cycle dropped about 89% and 6.4% respectively after ageing 120 h as shown in Figure 5.17 (b). The statistical quantities of measured PRPD patterns as a function of different spherical cavity diameters at various ageing times are listed in Table 5.5.

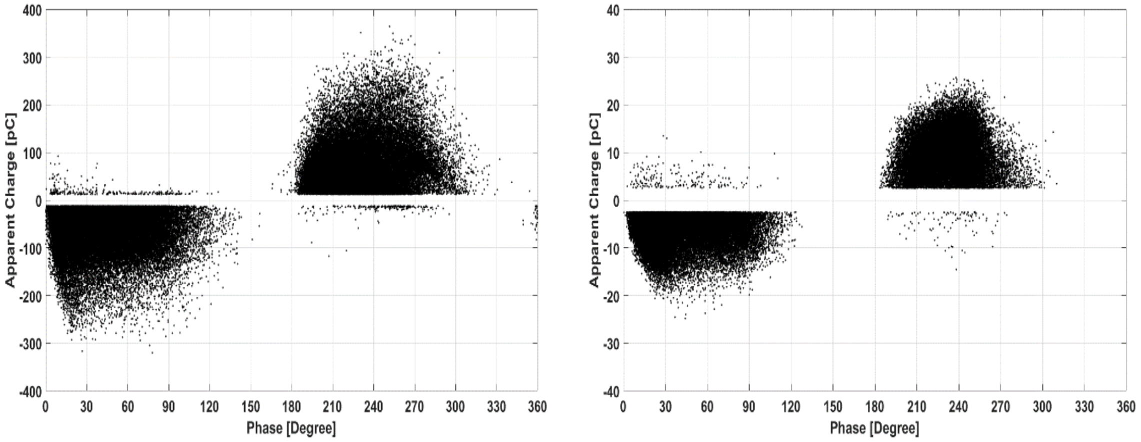

(a) (b)

Figure 5.17: Measured PRPD patterns of the sample containing a spherical cavity of diameter 0.97 mm at various ageing times: (a) a turtle-like pattern at ageing 10 min and (b) a turtle-like pattern at ageing 120 h.

Table 5.5: Statistical quantities of measured PRPD patterns as a function of different spherical cavity diameters at various ageing times.

Quantities	**Ageing Time**			
	Fig. 5.16 (a) (10 min)	**Fig. 5.16 (b) (60 h)**	**Fig. 5.17 (a) (10 min)**	**Fig. 5.17 (b) (120 h)**
Cavity diameter (mm)	0.98		0.97	
PRPD Patterns	Turtle-like	Turtle-like	Turtle-like	Turtle-like
Average Apparent Charge (pC)	217.64	18.31	86.86	9.25
Maximum Apparent Charge (pC)	467.28	65.42	364.18	25.67
Average Number of PDs per Cycle	2.02	0.62	2.03	1.90
Average Number of Positive PDs per Cycle	1.02	0.31	1.03	0.96
Average Number of Negative PDs per Cycle	1.00	0.31	1.00	0.94

5.6.3 Raman spectroscopy

The technique of Raman spectroscopy was used to examine for spectral analysis of chemical by-products inside a cavity caused by PD activity during ageing processes. The infrared spectra were obtained in the wavenumber between 3200 cm^{-1} and 100 cm^{-1}. Comparison of Raman spectra as a function of different cavity diameters at various ageing times is illustrated in Figure 5.18. The spectrum of a virgin sample was obtained to provide for a silicone reference as shown in Figure 5.18 (a). All of these spectral bands are listed in Table 5.6. The Raman results of test samples between a cavity diameter of 0.98 mm at ageing 60 h and a cavity diameter of 0.97 mm at ageing 120 h were obtained at the localised site of corrosive by-products inside each cavities, which these samples were cut along the vertical cross-section view through a middle cavity as shown in Figures 5.18 (b) and 5.18 (c) respectively. It should be noted that the new peak of spectra for the samples after ageing was detected at the wavenumber of 1447 cm^{-1} after ageing 60 h and 120 h, which identified as CH_2 scissoring. It is likely that evidence of the deteriorated region on the cavity surface was formed by the breaking of chemical chains in bulk caused by PD bombardment and high oxygen inside a cavity during oxidative ageing processes [155], where this localised erosion might lead to the growth of tree initiation before an upcoming failure [238]. An investigation into the chemical compounds of tree channels in silicone material is considered that an amount of carbon at the inner wall of electrical tree growth was lower than the localised site of breakdown [239].

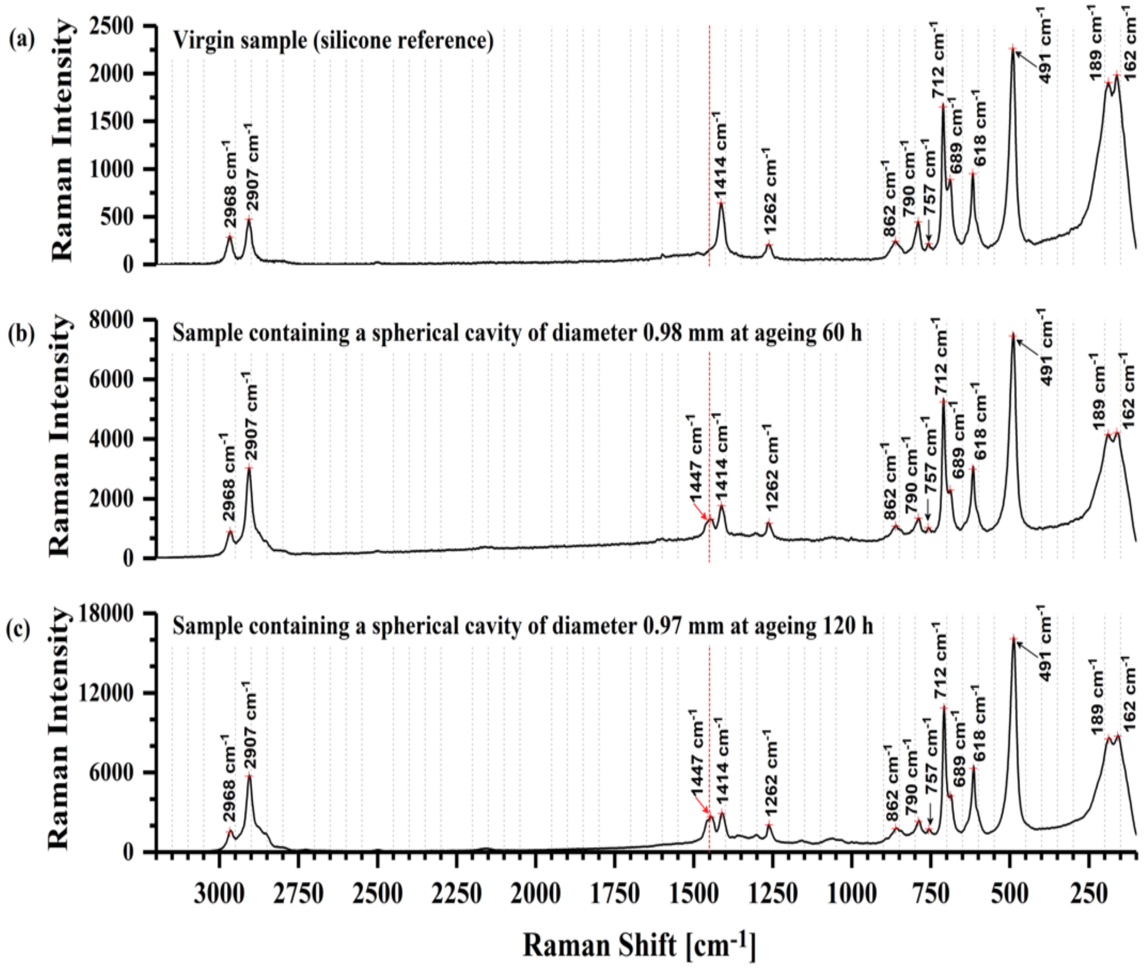

Figure 5.18: Comparison of Raman spectra obtained from various ageing times: (a) a virgin sample, (b) and (c) spectra at the localised spots of corrosive by-products within cavity diameters 0.98 mm and 0.97 mm after ageing for 60 h and 120 h respectively.

Table 5.6: Raman characteristics of infrared bands and their functional groups obtained from silicone material.

Raman Region Bands (cm^{-1})	Frequency Ranges (cm^{-1})	Functional Groups	Ref.
2968 and 2907	2980-2800	CH stretch	[207]
1447	1460-1440	CH$_2$ scissoring	[207]
1414 and 1262	1420-1280	C−N (Amides, Aromatic Amines)	[207]
862	900-820	Si−O stretch	[207]
790 and 757	825-640	C−H bend (Acetylene)	[241]
712 and 689	740-680	C−Si−C stretch	[207]
618	670-620	C=Si stretch	[207]
491	450-550	Si−O− Si symmetric stretch	[240]

5.7 PD characteristics of progressive erosion on the cavity surface as a function of various cavity sizes.

The purpose of this section is to investigate the variation in PRPD patterns related to the progression of localised erosion in the vertical axis of the cavity. Using the source approaches of TGA instrument and dielectric spectroscopy as detailed in Chapter 3, additional measurements were undertaken to characterise changes in thermal and dielectric properties of test samples due to electrical ageing processes.

5.7.1 Optical microscopy

The morphological changes of three samples containing different cavity diameters of 0.50 mm, 0.57 mm and 0.72 mm were investigated to determine the localised erosion depth inside a cavity using the top and vertical views due to degradation processes caused by PD activity. In the sample containing a spherical cavity of diameter 0.50 mm, the morphology of a virgin cavity in the top-section view was undertaken using optical microscopy as shown in Figure 5.19 (a). After further ageing of 30 h, the cavity formation was obtained the deposited by-products of little liquid droplets as shown in Figure 5.19 (b). The cavity of this sample was cut in the vertical cross-section view through the middle cavity to explore the deterioration mechanism inside a cavity, which the shaped cavity in the vertical was 500 µm in height, which equalled the cavity diameter as shown in Figure 5.19 (c). The virgin sample containing a spherical cavity of diameter 0.57 mm in the top-section views showed in Figure 5.20 (a). After further ageing of 60 h, a little cluster of droplets was obtained inside a cavity as shown in Figure 5.20 (b). In the vertical cross-section view, visible evidence of the cavity formation was obtained liquid droplets inside a cavity and erosion depth at the bottom cavity surface with 640 µm in height as shown in Figure 5.20 (c). Another investigation into the virgin sample containing a spherical cavity of diameter 0.72 mm showed in Figure 5.21 (a). The morphology was noticed a large amount of liquid droplets inside a cavity after ageing 120 h as shown in Figure 5.21 (b). This cavity had large liquid droplets inside it and the erosion depth at the bottom cavity surface was 960 µm in height as shown in Figure 5.21 (c). This result indicates that liquid droplets influenced to increase the conductivity on the cavity wall and interacted with PD bombardment to form the gradual progression of localised erosion at the bottom cavity surface. It is possible that the deposited by-product of liquid droplet contained the corrosive compound of nitric acid, which was produced by the reactions between gaseous composites and PD activity within the cavity and reacted in bulk material surroundings, leading to the localised erosion site over a period of ageing. It is suggested that the erosion depth within the cavity caused by an increase of carbonisation due to the enhancement of electric fields at the localised site by PD activity before the tree initiation [242]. Moreover, other research has found that the deterioration mechanism on the surface wall in an enclosed void embedded within epoxy resin was revealed with evidence of breakdown by PD, resulting in carbonisation of the tracking path [243]. An investigation into degradation mechanisms on the surface of silicone material by PD activity was found that the presence of liquid droplets caused by loss of hydrophobicity in the bulk material and increased the conductive surface, leading to the progression of surface erosion by reactions of the electric field enhancement and PD bombardment [244].

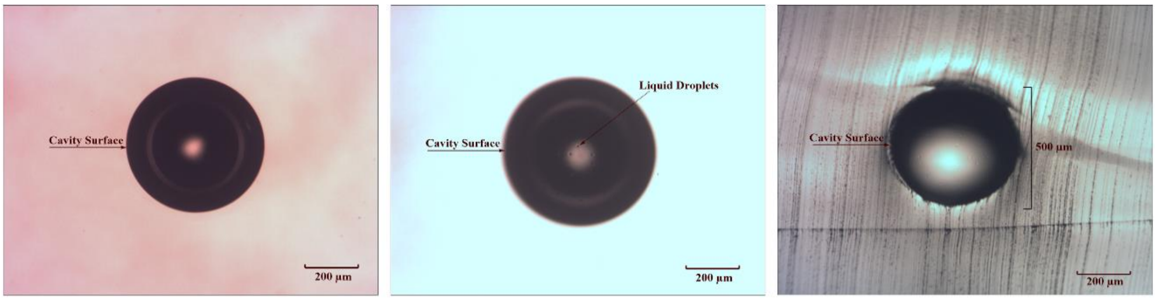

(a) (b) (c)

Figure 5.19: Morphological changes of the sample containing a spherical cavity of diameter 0.50 mm at various ageing times: top-section views of (a) a virgin cavity, (b) liquid droplets within a cavity at 30 h and (c) a vertical cross-section view of the middle cavity at 30 h.

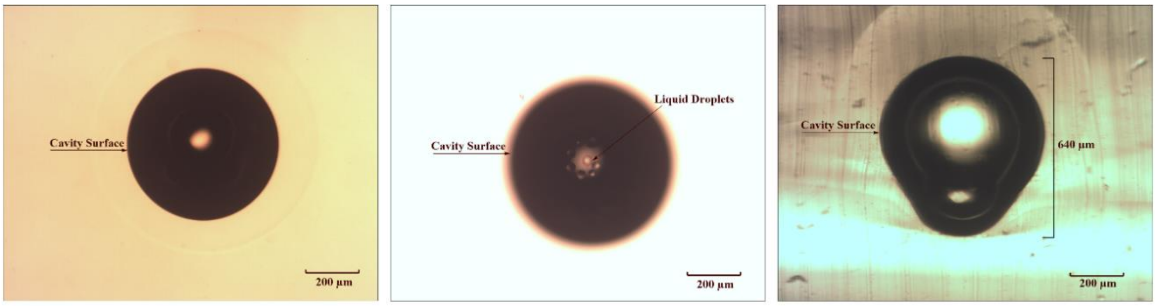

(a) (b) (c)

Figure 5.20: Morphological changes of the sample containing a spherical cavity of diameter 0.57 mm at various ageing times: top-section views of (a) a virgin cavity, (b) liquid droplets within a cavity at 60 h and (c) a vertical cross-section view of the middle cavity at 60 h.

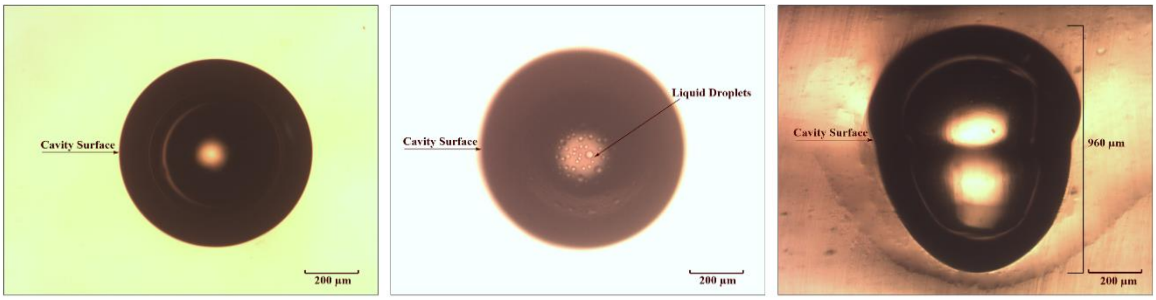

(a) (b) (c)

Figure 5.21: Morphological changes of the sample containing a spherical cavity of diameter 0.72 mm at various ageing times: top-section views of (a) a virgin cavity, (b) liquid droplets within a cavity at 120 h and (c) a vertical cross-section view of the middle cavity at 120 h.

5.7.2 Measurement of PD activity

PD characteristics of three samples containing different cavity diameters of 0.50 mm, 0.57 mm and 0.72 mm were undertaken to find out the variation in PRPD patterns related to the morphological changes inside a cavity due to the effect of accelerated ageing processes. In the sample containing a spherical cavity of diameter 0.50 mm, the PD characteristic of turtle-like pattern was detected in the initial ageing 10 min as shown in Figure 5.22 (a). The PD quantities of average apparent charge and average number of PDs per cycle were obtained just over 29 pC and 2 respectively. After 30 hours, this pattern remained in a turtle-like shape as shown in Figure 5.22 (b), where the average apparent charge and the average number of PDs per cycle decreased just over 56% and 53% respectively. The result shows that there was the symmetry between positive and negative half-cycles at ageing time of 10 min and 30 h.

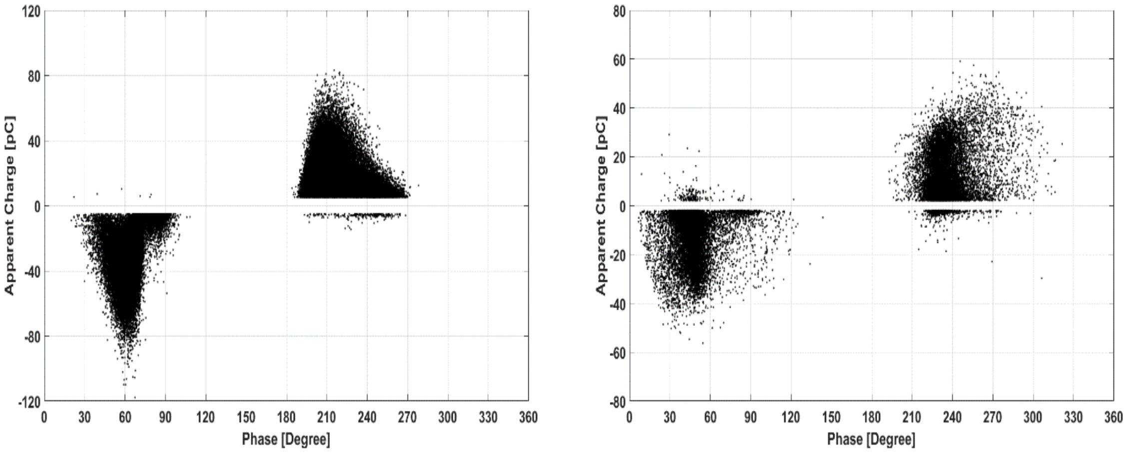

(a) (b)

Figure 5.22: Measured PRPD patterns of the sample containing a spherical cavity of diameter 0.50 mm at various ageing times: (a) a turtle-like pattern at ageing 10 min and (b) a turtle-like pattern at ageing 30 h.

Regarding the sample containing a spherical cavity of diameter 0.57 mm, the rabbit-like pattern exhibited after ageing for 10 min as shown in Figure 5.23 (a) while the average apparent charge and the average number of PDs per cycle were obtained just over 220 pC and 2 respectively. The transition of PRPD shape changed to the wing-like pattern at ageing 60 h as shown in Figure 5.23 (b). The PD quantities of average apparent charge and average number of PDs per cycle dropped just over 90% and 74% respectively while the average number of PDs at ageing time of 10 min and 60 h showed the symmetry between positive and negative half-cycles.

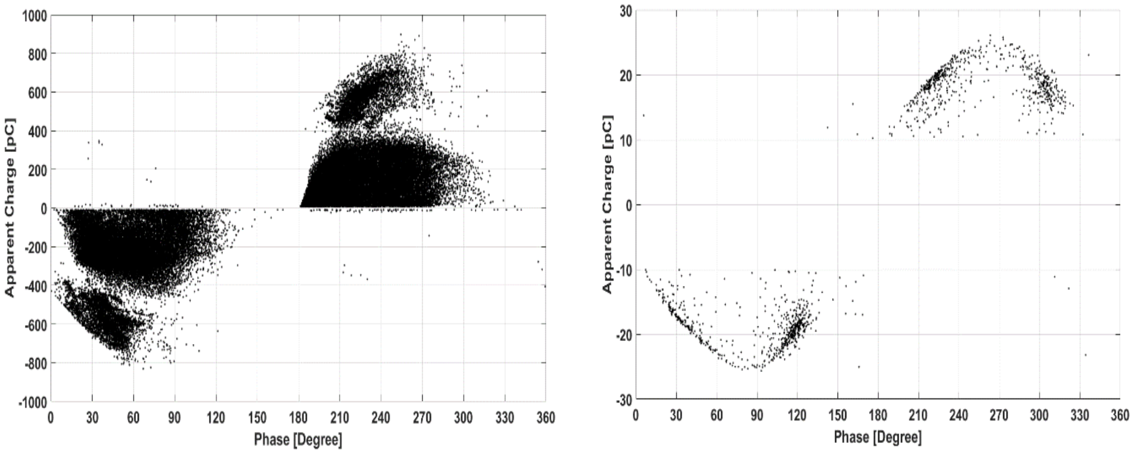

(a) (b)

Figure 5.23: Measured PRPD patterns of the sample containing a spherical cavity of diameter 0.57 mm at various ageing times: (a) a rabbit-like pattern at ageing 10 min and (b) a wing-like pattern at ageing 60 h.

In the sample containing a spherical cavity of diameter 0.72 mm, the turtle-like pattern was undertaken at the initial ageing 10 min as shown in Figure 5.24 (a). The average apparent charge and the average number of PDs per cycle were obtained just over 90 pC and 3.8 respectively. The occurrence of wing-like pattern was observed at ageing 120 h as shown in Figure 5.24 (b). The PD quantities of average apparent charge and average number of PDs per cycle decreased just over 84% and 93% respectively while the wing-like pattern at ageing 120 h showed the asymmetry, where the magnitude discharges of the positive half-cycle were higher than the negative half-cycle. The statistical quantities of measured PRPD patterns as a function of different spherical cavity diameters at various ageing times are listed in Table 5.7.

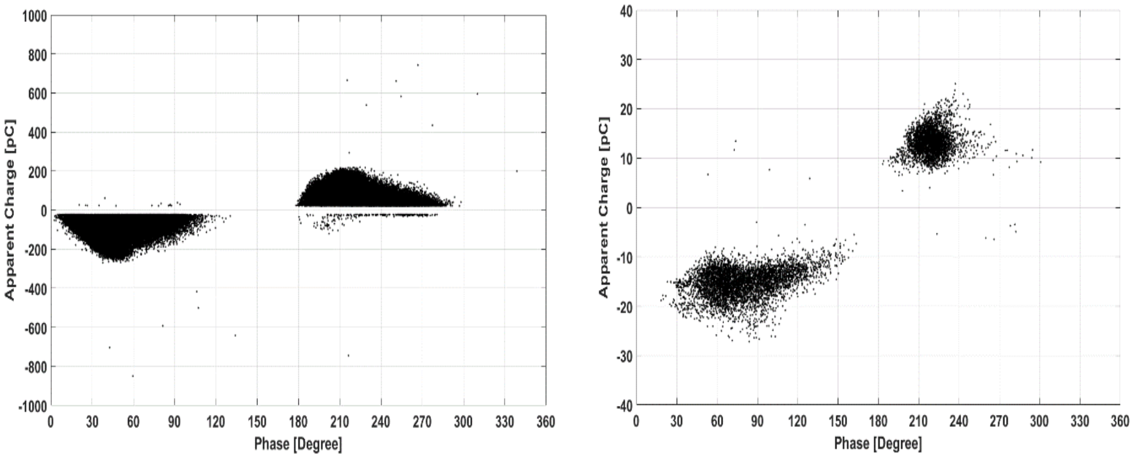

(a) (b)

Figure 5.24: Measured PRPD patterns of the sample containing a spherical cavity of diameter 0.72 mm at various ageing times: (a) a turtle-like pattern at ageing 10 min and (b) a wing-like pattern at ageing 120 h.

Table 5.7: Statistical quantities of measured PRPD patterns as a function of different spherical cavity diameters at various ageing times.

Quantities	**Ageing Time**					
	Fig. 5.22 (a) 10 min	**Fig. 5.22 (b) 30 h**	**Fig. 5.23 (a) 10 min**	**Fig. 5.23 (b) 60 h**	**Fig. 5.24 (a) 10 min**	**Fig. 5.24 (b) 120 h**
Cavity diameter (mm)	0.50		0.57		0.72	
PRPD Patterns	Turtle-like	Turtle-like	Rabbit-like	Wing-like	Turtle-like	Wing-like
Average Apparent Charge (pC)	29.76	12.94	223.19	18.58	92.23	14.48
Maximum Apparent Charge (pC)	117.75	59.09	897.81	26.09	849.85	27.18
Average Number of PDs per Cycle	2.01	0.93	2.04	0.52	3.83	0.26
Average Number of Positive PDs per Cycle	1.01	0.47	1.00	0.26	1.90	0.16
Average Number of Negative PDs per Cycle	1.00	0.46	1.04	0.26	1.93	0.10

5.7.3 Thermogravimetric analysis (TGA)

The technique of thermogravimetric analysis was applied for diagnosing the thermal property of the test samples that the line graph was obtained the relationship between weight loss and temperature. The TGA curve of a virgin sample was obtained to provide a reference as shown in Figure 5.25. The trend slowly decreased the weight of the test sample from 100% at the beginning reaction of 30˚C to 90% at 495˚C and then dropped rapidly to 42% at 900˚C. The TGA plots for samples after ageing were divided into two sets. Two samples were obtained as the first set after ageing 60 h used for a comparison of their thermal reactions. The samples I and II continued to decline by the mass from 100% at 30˚C to 85% at 399˚C and followed by the rapid decrease of 51% at 700˚C. Two samples after ageing 120 h obtained as another set that the samples I and II rapidly declined by weight from 100% at 30˚C to 60% at 583˚C. For all samples, the TGA curves obtained their weight loss at a temperature of 500˚C tended to decrease of 89% for the virgin sample, 79% for the samples after ageing 60 h and 70% for the samples after ageing 120 h. This result indicates that the weight loss of the samples after the accelerated ageing process was slightly higher than the virgin sample, according to comparison of TGA curves for the virgin and aged silicone rubber material caused by depolymerisation of the siloxane matrix during the ageing process [245]. The weight loss rate of silicone elastomer can be divided into three main phases of temperature, which consisted of the low molecular weight silicone at 310˚C, the maximum weight loss due to decomposition of the cross-linked silicone elastomer at 450˚C and the formation of the silica glass, including loss of carbon on the bulk of molecular structures between 630˚C and 670˚C [246]. Note that the influence of electrical ageing might lead to the formation of silica glass on the cavity surface and affect the mechanical properties of the silicone sample and enhance the possibility of mechanical cracking such as micro-craters enhancing the likelihood of growing electrical tree-like structures.

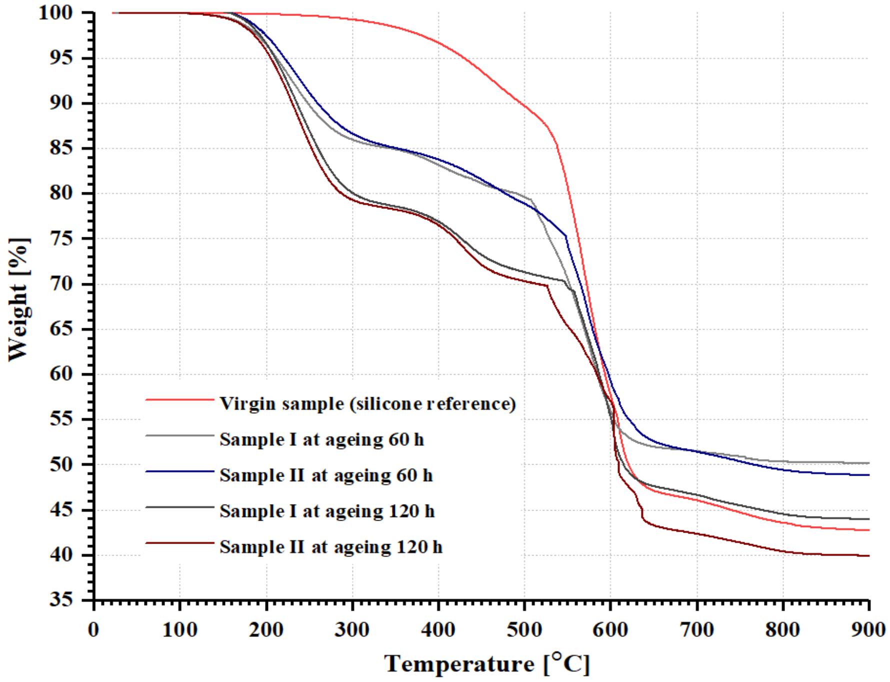

Figure 5.25: TGA curves of silicone samples obtained from various ageing times.

5.7.4 Dielectric spectroscopy

Dielectric spectroscopy was used to diagnose the dielectric property for the test samples. Each sample containing a spherical cavity was analysed in terms of changes in dielectric performance caused by degradation processes in a cavity by charge bombardment. The bar chart between real relative permittivity and tan delta at 50 Hz is illustrated in Figure 5.26 (a). The real relative permittivity and the tan delta of a virgin sample without a cavity were about 2.8 and 0.2×10^{-3} respectively. A comparison of two samples containing different spherical cavity diameters between 1.15 mm and 2.15 mm were undertaken. The result shows that the values of real relative permittivity from cavity diameters of 1.15 mm and 2.15 mm were found to be about 2.72 and 2.65 respectively. Otherwise, the values of tan delta from cavity diameters of 1.15 mm and 2.15 mm were about 1.96×10^{-3} and 3.51×10^{-3} respectively. In the sample containing a spherical cavity of diameter 0.57 mm at ageing 60 h, the real relative permittivity and the tan delta were measured as 2.22 and 0.39×10^{-3}, compared with 2.58 and 0.21×10^{-3} after cleaving the middle cavity in the half. The overall line graphs between the real relative permittivity and the tan delta are illustrated in Figures 5.26 (b) and 5.26 (c) respectively.

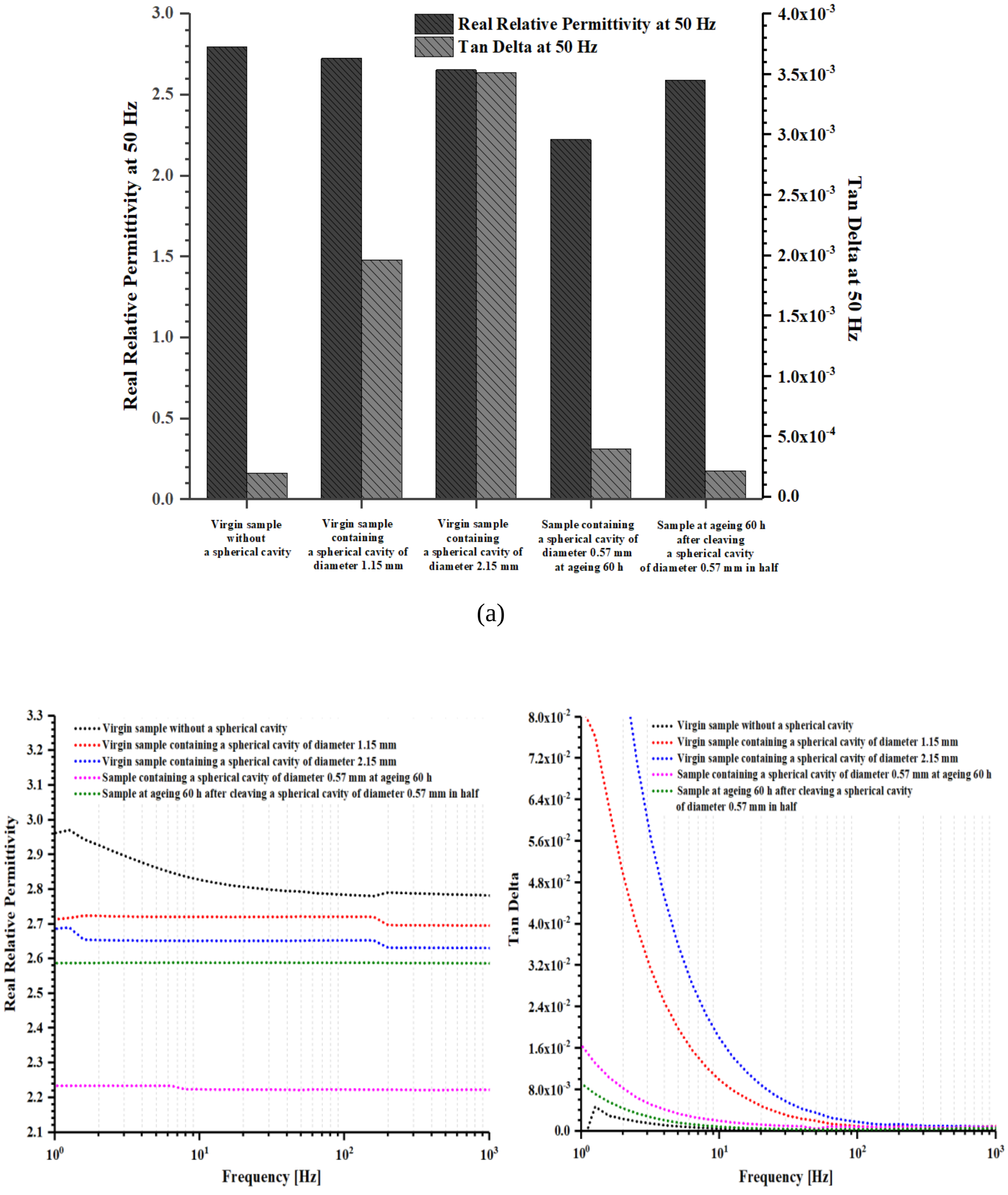

(a)

(b)

(c)

Figure 5.26: Dielectric characteristics of test samples: (a) the bar chart between real relative permittivity and tan delta at 50 Hz, (b) the real relative permittivity as a function of frequency and (c) the tan delta as a function of frequency.

5.8 PD characteristics of micro-craters on the cavity surface

An investigation into PD behaviour related to degradation mechanisms from the wall of an air-filled cavity embedded in solid dielectric material was conducted to reveal the progressive erosion site of micro-craters caused by PD activity. Examination at a microscopic level was also performed using SEM and EDX systems.

5.8.1 Optical microscopy

Before measuring PD, the microscopic photograph of a virgin cavity was observed using optical microscope as shown in Figure 5.27 (a). The cavity formation of localised erosion on the centre cavity surface was noticed after ageing 27 h as shown in Figure 5.27 (b). It is likely that the interaction between PD bombardment and gaseous composites inside the cavity gradually formed the progressive degradation of corrosive by-products on the cavity wall due to the oxidative ageing and the electric fields enhanced at this localised site [11, 51].

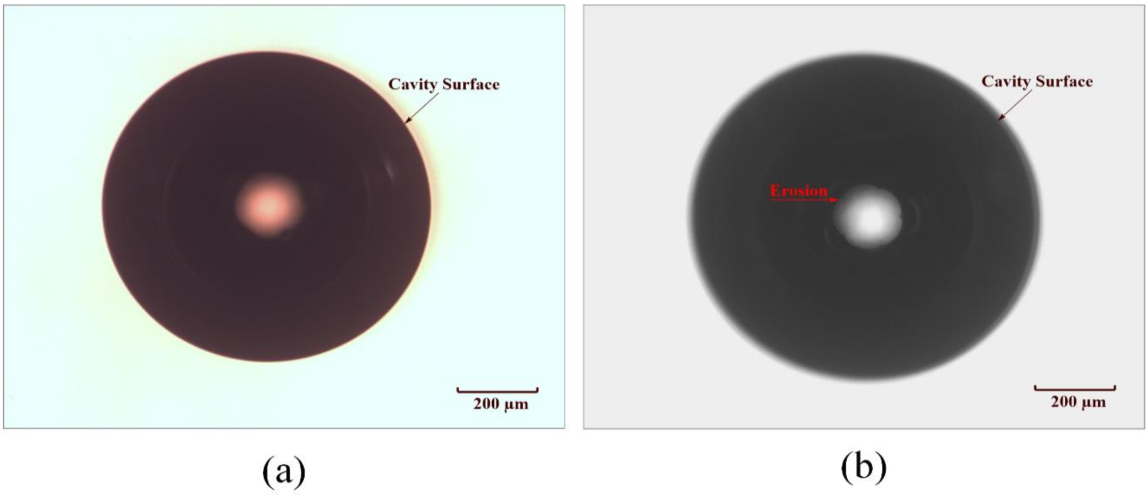

Figure 5.27: Morphological changes of the sample containing a spherical cavity of diameter 0.80 mm: top-section views of (a) a virgin cavity and (b) an eroded cavity formation at ageing 27 h.

5.8.2 SEM and EDX analysis

The combined techniques of scanning electron microscopy (SEM) image and energy dispersive X-ray (EDX) were used to examine corrosive by-products of micro-cracks within a spherical cavity. With reference to Figure 5.28, microanalysis of high-resolution in the SEM image for a virgin cavity at the localised spot I revealed the morphology of the silicone bulk as shown in Figure 5.28 (a). The EDX spectrum of chemical elements at this local site comprised 73% of carbon, 4.9% of oxygen and 22.1% of silicon, no nitrogen was detected as shown in Figure 5.28 (b). The SEM image for deposited by-products within a spherical cavity was noticed micro-craters after ageing 27 h as shown in Figure 5.29 (a). The chemical composites of a micro-crater at the localised spot II consisted 66.93% of carbon, 9.29% of nitrogen, 15.08% of oxygen and 8.69% of silicone as shown in Figure 5.29 (b). It should be noted that the nitrogen compound was obtained at the focal spot of localised erosion in the form of micro-craters on the cavity surface caused by the effect of the oxidative ageing while this composite was undetected at the virgin cavity surface. In the EDX result, the detection of a small amount of aluminium might be from contamination during the sample preparation for chemical analysis or the inside of a vacuum chamber because the enclosed cavity was opened for gold coating before undertaking microanalysis of SEM and EDX. It is considered that the main mixture of gases inside a void contained nitrogen and oxygen in the ratio of 4 to 1 [247]. An investigation into deterioration processes on the surface of silicone rubber material by corona discharges was analysed by X-ray photoelectron spectroscopy (XPS), which revealed an increase of oxygen and a decrease of carbon at the same time due to the oxidation reaction [248]. Moreover, the degradation site on the surface layer of silicone rubber elastomer material after use in high-temperature environments was examined the chemical elements, which consisted of 25.7% of oxygen, 49.7% of carbon, 14.1% of silicon, 9.9% of aluminium and 0.6% of nitrogen [246].

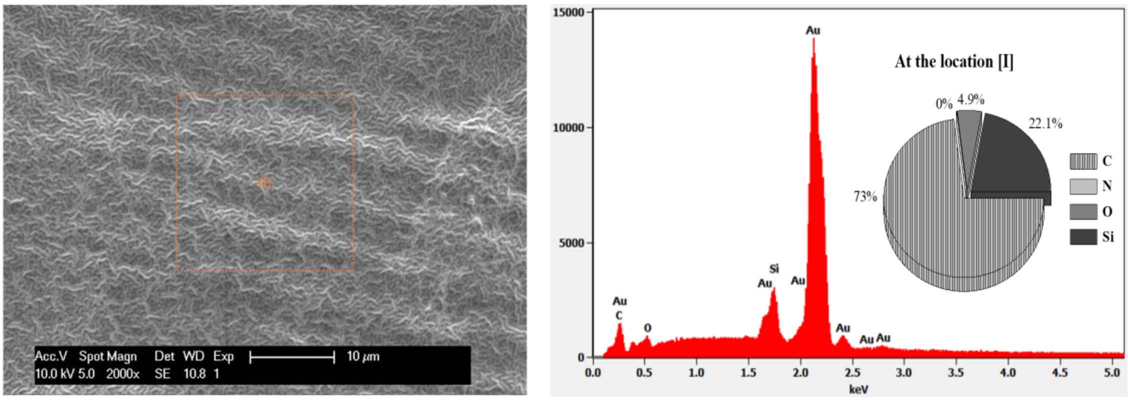

(a) (b)

Figure 5.28: Microanalysis of a virgin sample: (a) SEM image and (b) EDX analysis of chemical composites at the localised spots of I in the micrograph (a).

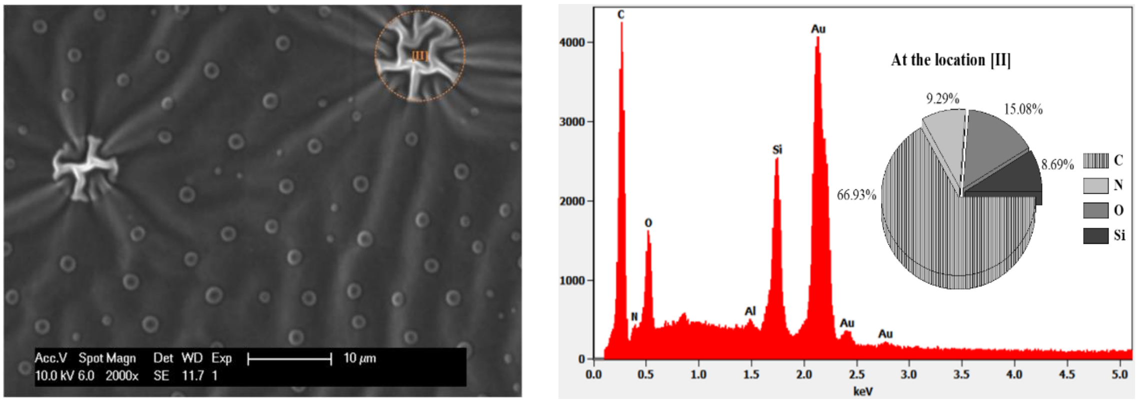

(a) (b)

Figure 5.29: Microanalysis of the sample containing a spherical cavity of diameter 0.80 mm at ageing 27 h: (a) SEM image and (b) EDX analysis of chemical composites at the localised spots of II in the micrograph (a).

5.8.3 Measurement of PD activity

The evolution of PRPD characteristics in the sample containing a spherical cavity of diameter 0.8 mm related to the morphological changes from a virgin cavity to micro-crater initiation was distinguished into three distinct patterns. The measured PRPD of rabbit-like was seen initially after ageing for 2 h and this pattern was detected a larger ear over ageing for 12 h as shown in Figures 5.30 (a) and 5.30 (b) respectively. The PRPD pattern changed to the turtle-like shape after ageing for 20 h as shown in Figure 5.30 (c) and continuously acquired PRPD data until the wing-like pattern exhibited after ageing for 27 h as shown in Figure 5.30 (d). The PD statistical quantities for each pattern are listed in Table 5.8.

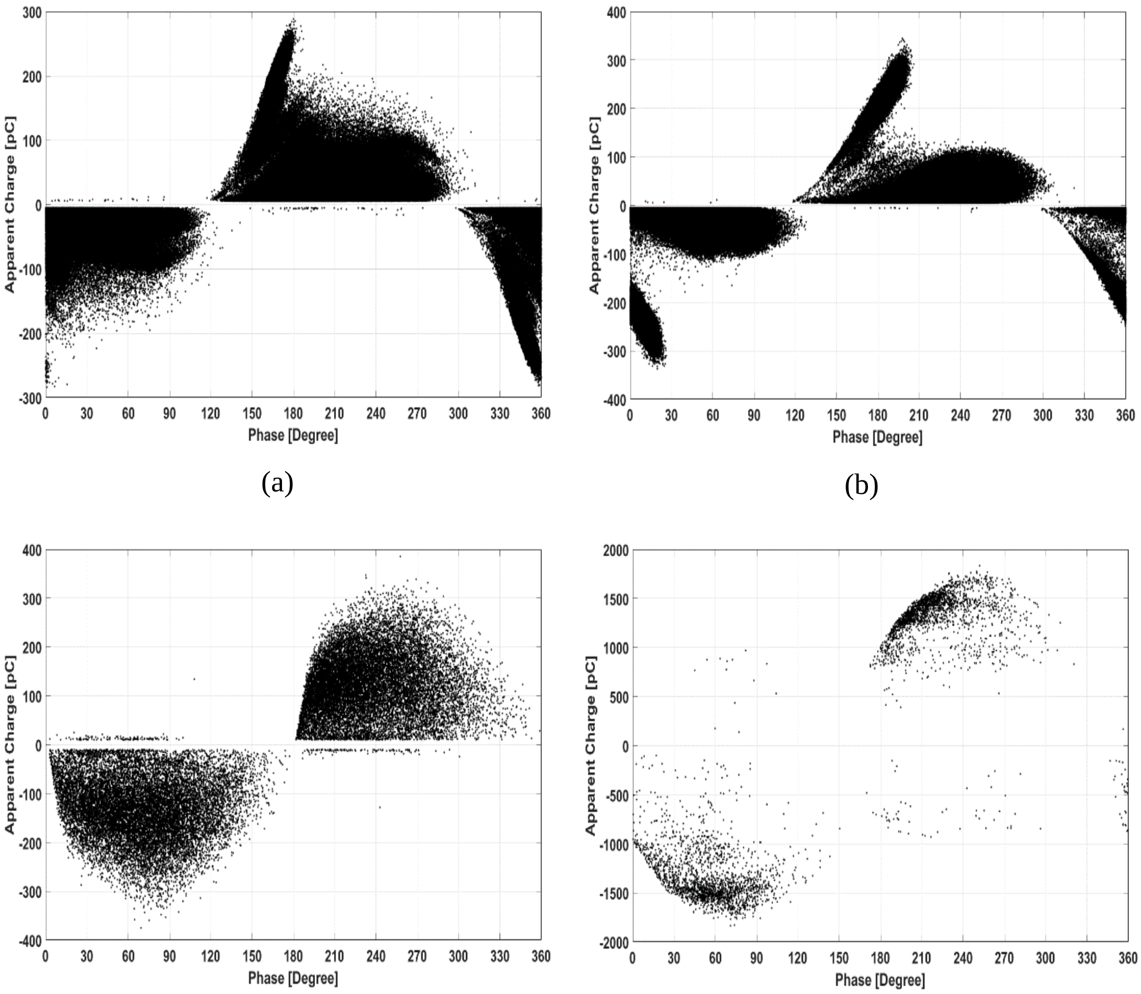

(a) (b)

(c) (d)

Figure 5.30: Variation in measured PRPD patterns of the sample containing a spherical cavity of diameter 0.80 mm at various ageing times: (a) a rabbit-like pattern at ageing 2 h, (b) a rabbit-like pattern at ageing 12 h, (c) a turtle-like pattern at ageing 20 h and (d) a wing-like pattern at ageing 27 h.

Table 5.8: Statistical quantities of measured PRPD patterns at various ageing times.

Quantity	**Ageing Time**			
	Fig. 5.30 (a) (2 h)	**Fig. 5.30 (b) (12 h)**	**Fig. 5.30 (c) (20 h)**	**Fig. 5.30 (d) (27 h)**
PRPD Patterns	Rabbit-like	Rabbit-like	Turtle-like	Wing-like
Average Apparent Charge (pC)	29.74	30.70	117.71	1319.70
Maximum Apparent Charge (pC)	288.34	344.60	385.42	1835.60
Average Number of PDs per Cycle	24.40	30.69	1.16	0.96
Average Number of Positive PDs per Cycle	12.20	15.81	0.57	0.49
Average Number of Negative PDs per Cycle	12.20	14.88	0.59	0.47

An investigation into the evolution of PD characteristics during the electrical ageing was analysed with regard to PD quantities, i.e. the average apparent charge, the maximum PD magnitude and the average number of PDs per cycle as shown in Figure 5.31. The result shows that the scatter plot between average apparent charge and average number of PDs per cycle over ageing 27 h as shown in Figure 5.31 (a). The average apparent charge slightly fluctuated with the magnitude discharges between 30 pC and 100 pC over ageing 14 h and the figure gradually increased from 200 pC at ageing 18 h to just over 1.3 nC at ageing 27 h, while the average number of PDs per cycle highly fluctuate over ageing 18 h and then tended to decrease continuously until elapsed time of ageing 27 h. In the maximum PD magnitude, the trend tended to increase slightly over ageing 26 h while this figure had a steep rise in the discharge magnitudes from just over 1.9 nC at ageing 26.5 h to just over 1.8 nC at ageing 27 h respectively as shown in Figure 5.31 (b). The bar chart is illustrated the average number of positive and negative PDs per cycle as shown in Figure 5.31 (c). The result shows that the reasonable symmetry between positive and negative half-cycles was detected over ageing 27 h, which the magnitudes tended to fluctuate over ageing 15 h and followed by a gradual decrease from just over 4 at ageing 18 h to just under 1 at ageing 27 h.

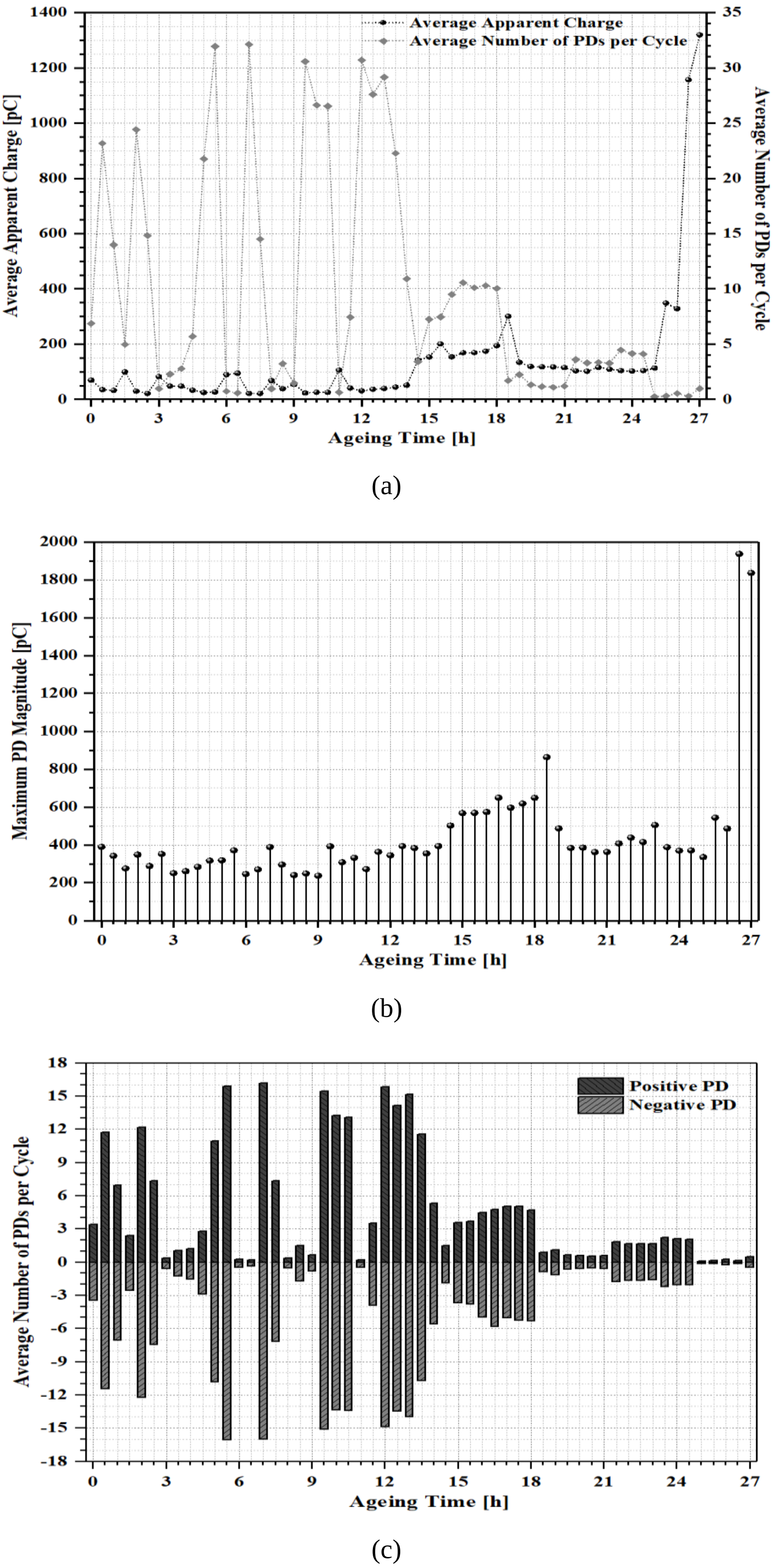

Figure 5.31: Evolution of PD characteristics as a function of ageing time of the sample containing a spherical cavity of diameter 0.80 mm at applied voltage 16 kV, 50 Hz: (a) the scatter plot between average apparent charge and average number of PDs per cycle, (b) the maximum PD magnitude and (c) the average number of positive and negative PDs per cycle.

5.9 PD characteristics of electrical tree initiation on the cavity surface

PD behaviour related to the progressive degradation mechanisms in the cavity was investigated from localised erosion to treeing initiation growing from the wall of an enclosed cavity due to a long-term period of accelerated electrical ageing. Examination in a microstructural level at the localised site was specifically spotted using SEM and EDX techniques.

5.9.1 Optical microscopy

The morphology of a virgin cavity in the top-section view was observed as shown in Figure 5.32 (a). After further ageing of 733 h, the cavity formation was seen deposited by-products of liquid droplets in the centre cavity surface as shown in Figure 5.32 (b). In Figures 5.32 (c) and 5.32 (d), the corrosive by-products inside a cavity were noticed after further ageing 1069 h.

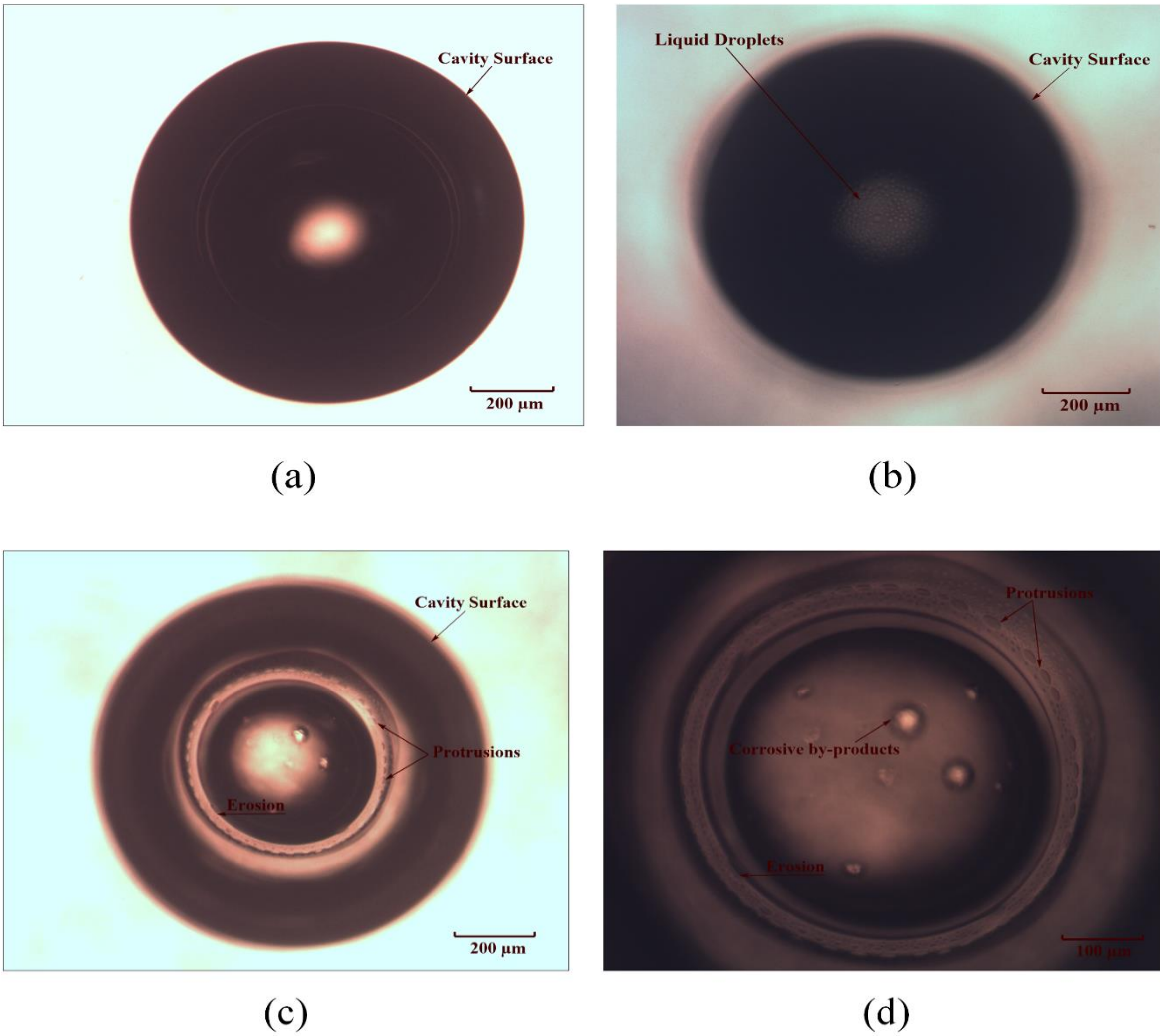

(a) (b)

(c) (d)

Figure 5.32: Morphological changes of the sample containing a spherical cavity of diameter 0.95 mm at various ageing times: top-section views of (a) a virgin cavity, (b) liquid droplets within the cavity at ageing 733 h, (c) an eroded cavity formation at ageing 1069 h and (d) a high-magnification of protrusions within a cavity in the micrograph (c).

Subsequently, the sample was cut in the horizontal cross-section view through the middle cavity. It can be seen that the upper cavity surface was obtained large liquid droplets and the lower cavity surface was obtained little liquid droplets and corrosive by-products as shown in Figures 5.33 (a) and 5.33 (b) respectively. An investigation into electrical tree growth and chemical elements at the localised spots on the cavity surface was undertaken using microanalysis techniques of SEM and EDX as further detailed in Section 5.9.3. It is suggested that the appearance of liquid droplets in a cavity might have evolved due to loss of hydrophobicity during exposure to electrical discharges caused by oxidative degradation mechanisms [249].

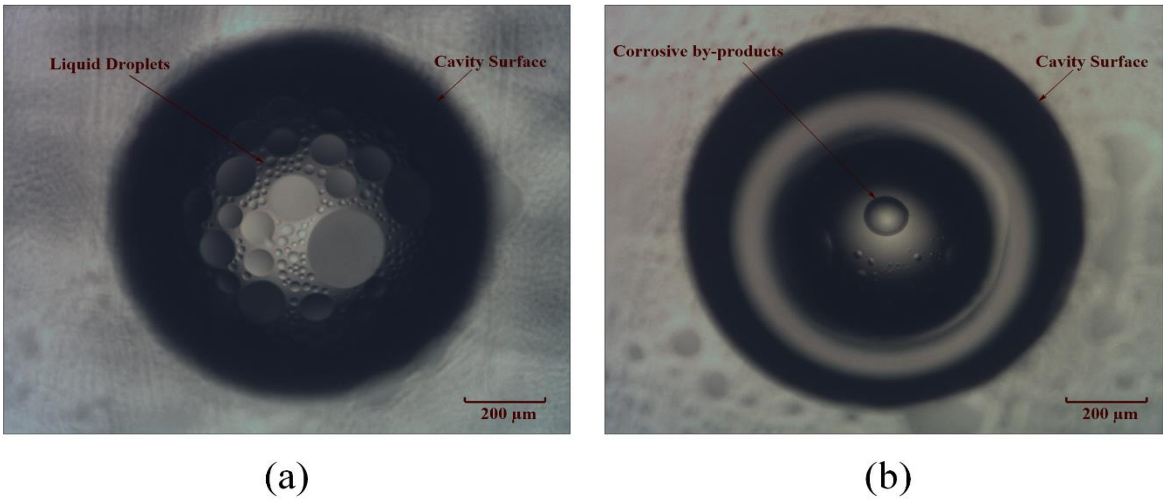

Figure 5.33: Morphological changes of the sample containing a spherical cavity of diameter 0.95 mm at ageing 1070 h: horizontal cross-section views of a middle cavity (a) liquid droplets within the upper cavity surface area and (b) corrosive by-products within the lower cavity surface area.

5.9.2 Measurement of PD activity

The evolution of measured PRPD patterns and PD quantities was correlated with degradation processes of the cavity formation regarding the virgin cavity, the liquid droplets, the corrosive by-products and the electrical tree growth as previously detailed in Section 5.9.1. The typical turtle-like pattern was exhibited after the initial ageing as shown in Figure 5.34 (a). After further ageing, this pattern remained unchanged with slight magnitude discharges as shown in Figure 5.34 (b). The wing-like pattern appeared after ageing for more than 1069 h as shown in Figures 5.34 (c) and 5.34 (d) respectively. The PD quantities of measured PRPD patterns at various ageing times are listed in Table 5.9. It can be seen that there are the highest values of the average apparent charge and the maximum apparent charge during the occurrence of wing-like patterns after ageing for more than 1069 h. Also, the average number of PDs per cycle shows the asymmetry between positive and negative half-cycles during the stage of electrical tree initiation. This result indicates that the relationship between PD quantities and wing-like patterns can be linked to the growth of electrical tree initiation. Other research has found that the PD characteristic of wing-like pattern associated with an upcoming breakdown of the test sample [250].

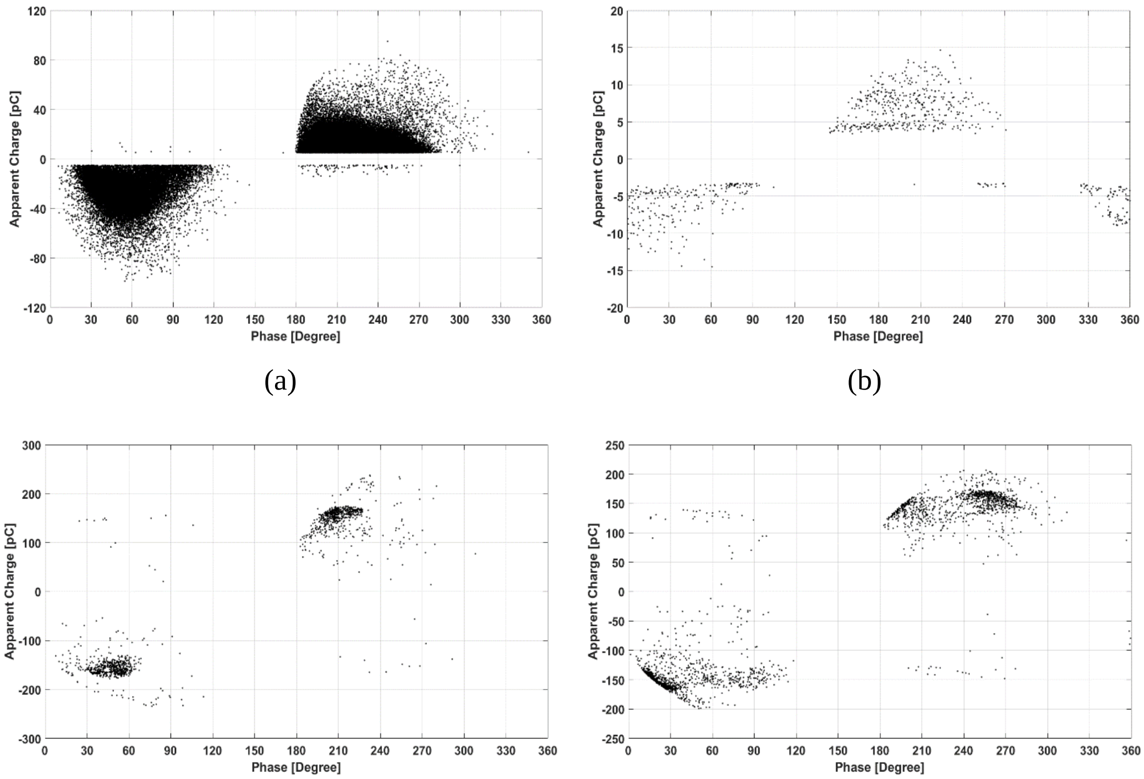

(a) (b)

(c) (d)

Figure 5.34: Variation in measured PRPD patterns of the sample containing a spherical cavity of diameter 0.95 mm at various ageing times: (a) a turtle-like pattern at ageing 10 min, (b) a turtle-like pattern at ageing 733 h, (c) a wing-like pattern at ageing 1069 h and (d) a wing-like pattern at ageing 1070 h.

Table 5.9: Statistical quantities of measured PRPD patterns at various ageing times.

Quantities	**Ageing Time**			
	Fig. 5.34 (a) (10 min)	**Fig. 5.34 (b) (733 h)**	**Fig. 5.34 (c) (1069 h)**	**Fig. 5.34 (d) (1070 h)**
PRPD Patterns	Turtle-like	Turtle-like	Wing-like	Wing-like
Average Apparent Charge (pC)	23.42	5.97	152.90	145.65
Maximum Apparent Charge (pC)	98.74	14.64	237.41	206.58
Average Number of PDs per Cycle	2.076	0.029	0.445	0.102
Average Number of Positive PDs per Cycle	1.043	0.015	0.217	0.051
Average Number of Negative PDs per Cycle	1.033	0.014	0.228	0.051

5.9.3 SEM and EDX analysis

The combined techniques of SEM and EDX systems were used to reveal the progressive deterioration and the electrical tree growth on the cavity surface. The result shows that the upper cavity wall was obtained a large crater and the lower cavity wall was obtained corrosive by-products, i.e. small craters and a cluster of treeing initiation as shown in Figures 5.35 (a) and 5.35 (b) respectively.

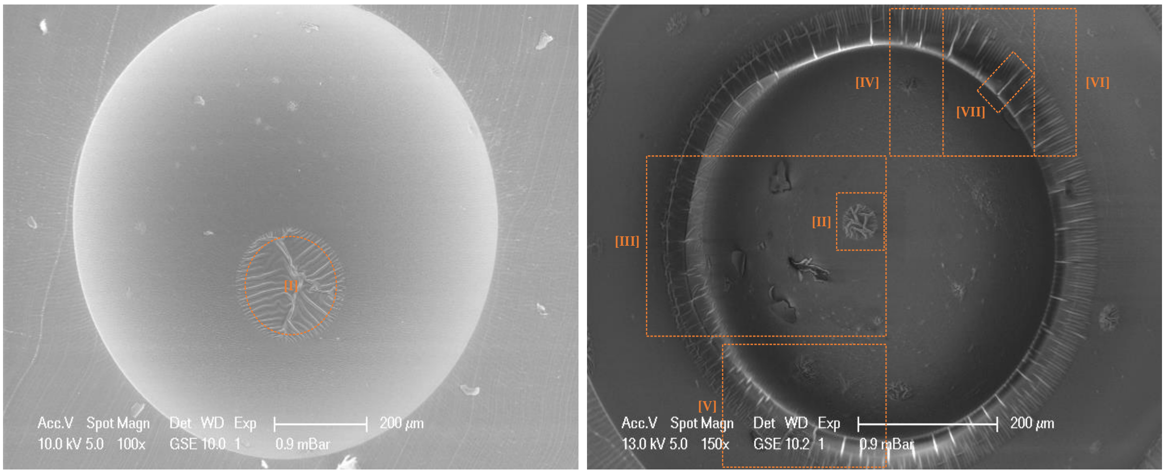

(a) (b)

Figure 5.35: Microanalysis of the sample containing a spherical cavity of diameter 0.95 mm at ageing 1070 h: horizontal cross-section views of a middle cavity (a) the corrosive by-products of a large crater within the upper cavity surface area at the localised spot of I and (b) the corrosive by-products in terms of electrical tree growth, cracks, protrusions within the lower cavity surface area at six localised spots marked by rectangles.

Microanalysis of high-resolution in the SEM image at the localised spots of the lower cavity surface is illustrated in Figure 5.35 (b), which is subdivided into six different locations for analysis of corrosive by-products and a cluster of electrical tree initiation. The crater on the lower cavity surface, which had a smaller size on the upper cavity surface, was the localised spot of II-01 as showed in Figures 5.36 (a). Comparison of different locations on the surface roughness was determined at the localised spots of III-01 with III-02 as showed in Figures 5.36 (b). Also, comparison of different sizes of protrusions was identified at the localised spots of IV-01 and IV-02 as showed in Figures 5.36 (c). Interestingly, visible evidence of a cluster of electrical tree initiation sites was revealed at the localised area of V as showed in Figures 5.36 (d). Moreover, the progressive growth of two trees was focused at the localised spots of VI-01 and VI-02 as showed in Figures 5.36 (e) and the long length of tree growth on the cavity wall was pointed out as showed in Figure 5.36 (f), which the structural dimension of this treeing channel consisted of 2 µm wide and 50 µm in length. Clearly, if these trees grow continuously towards the ground electrode, the sample will undergo complete failure.

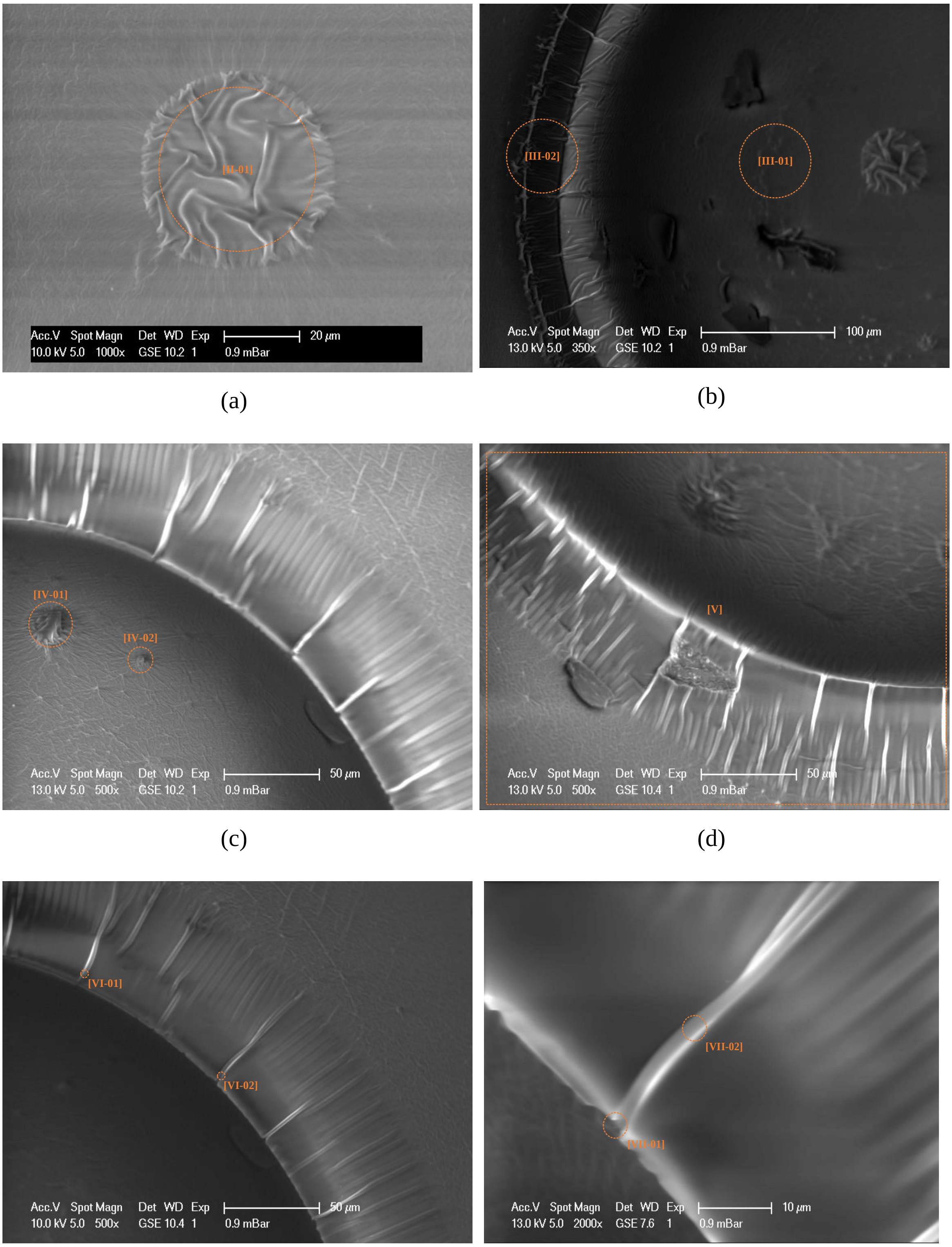

(a) (b)

(c) (d)

(e) (f)

Figure 5.36: Microanalysis of high-resolution images at the localised spots in the SEM micrograph 5.35 (b): (a) a crater at the localised spot of II-01, (b) the surface roughness at the localised spots of III-01 and III-02, (c) the protrusions at the localised spots of IV-01 and IV-02, (d) a cluster of electrical tree growth at the localised area of V, (e) the growth of two trees at the localised spots of VI-01 and VI-02, and (f) the propagation of electrical tree growth at the localised spots of VII-01 and VII-02.

The EDX results correlated to SEM micrographs in Figures 5.35 and 5.36 show that the chemical composites at different locations of corrosive by-products and electrical tree growth, which consist of carbon, nitrogen, oxygen and silicon. In the localised spot I-01 at a large crater of the upper cavity surface in Figure 5.35 (a), the chemical elements comprised 75.8% of carbon, 2.4 % of nitrogen, 12% of oxygen and 9.8% of silicon, compared with 75.4% of carbon, 3.6 % of nitrogen, 11.8% of oxygen and 9.2% of silicon at the localised spot II-01 of the lower cavity surface as shown in Figures 5.37 (a) and 5.37 (b) respectively. It should be noted that the percentage of nitrogen had increased by 1.2%, whereas an amount of carbon, oxygen and silicon had decreased by 0.4%, 0.2% and 0.6 % respectively.

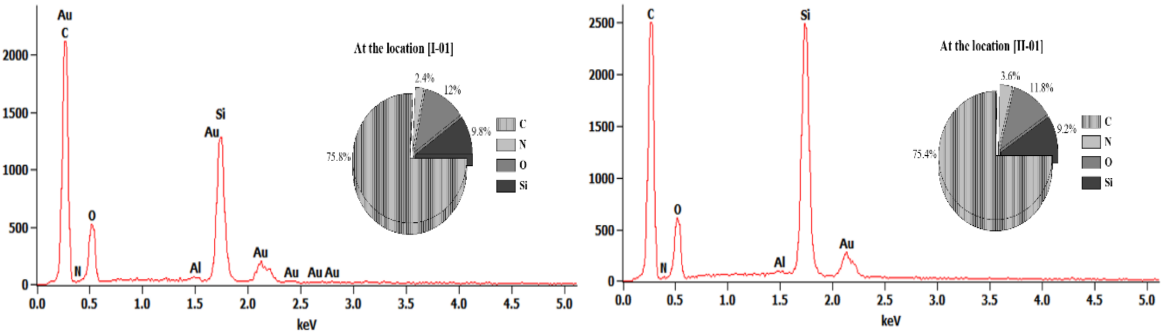

(a) (b)

Figure 5.37: EDX analysis of chemical composites: (a) the localised spot of I-01 in the micrograph 5.35 (a) and (b) the localised spot of II-01 in the micrograph 5.36 (a).

In Figure 5.38, the EDX results at different localised spots in Figure 5.36 show that the surface roughness at the localised spot III-01 was compared with the localised spot III-02, which the proportion of carbon and silicone had dropped by 3.6% and 1.6% respectively. Also, the ratio of nitrogen and oxygen had risen by 0.4% and 4.8%. It is likely that the variation of nitrogen and oxygen act to enhance an increase of the surface roughness due to the oxidative ageing. Furthermore, a comparison of chemical elements of different sizes of protrusions was focused at the localised spots IV-01 and IV-02. The result shows that nitrogen and oxygen were obtained by just over 4% and 12% respectively at the spot IV-01 while these compounds were detected by just under 2% and 11% at the spot IV-02 that the detection of nitrogen at a larger protrusion was higher than a smaller size. In a comparison of the growth of two trees, the result shows that chemical quantities at the localised spot VI-01 were obtained 76.4% of carbon, 2.9% of nitrogen, 11.4% of oxygen and 9.3% of silicon, compared with 76.8% of carbon, 2.7% of nitrogen, 11.3% of oxygen and 9.2% of silicon at the localised spot VI-02. The percentage distribution of elemental components was almost identical at these locations. The focal site on the electrical tree channel at various spots, the result shows that a large amount of nitrogen was detected just over 3% at the initial tree growth of the localised spot VII-01 while this element was only found of 0.7% at the middle channel of the localised spot VII-02. It is suggested that the role of nitrogen contributed to the progressive degradation of localised erosion regarding the growth of pits [58], which the influence of electric fields at the localised site enhanced the propagation of electrical tree growth [56].

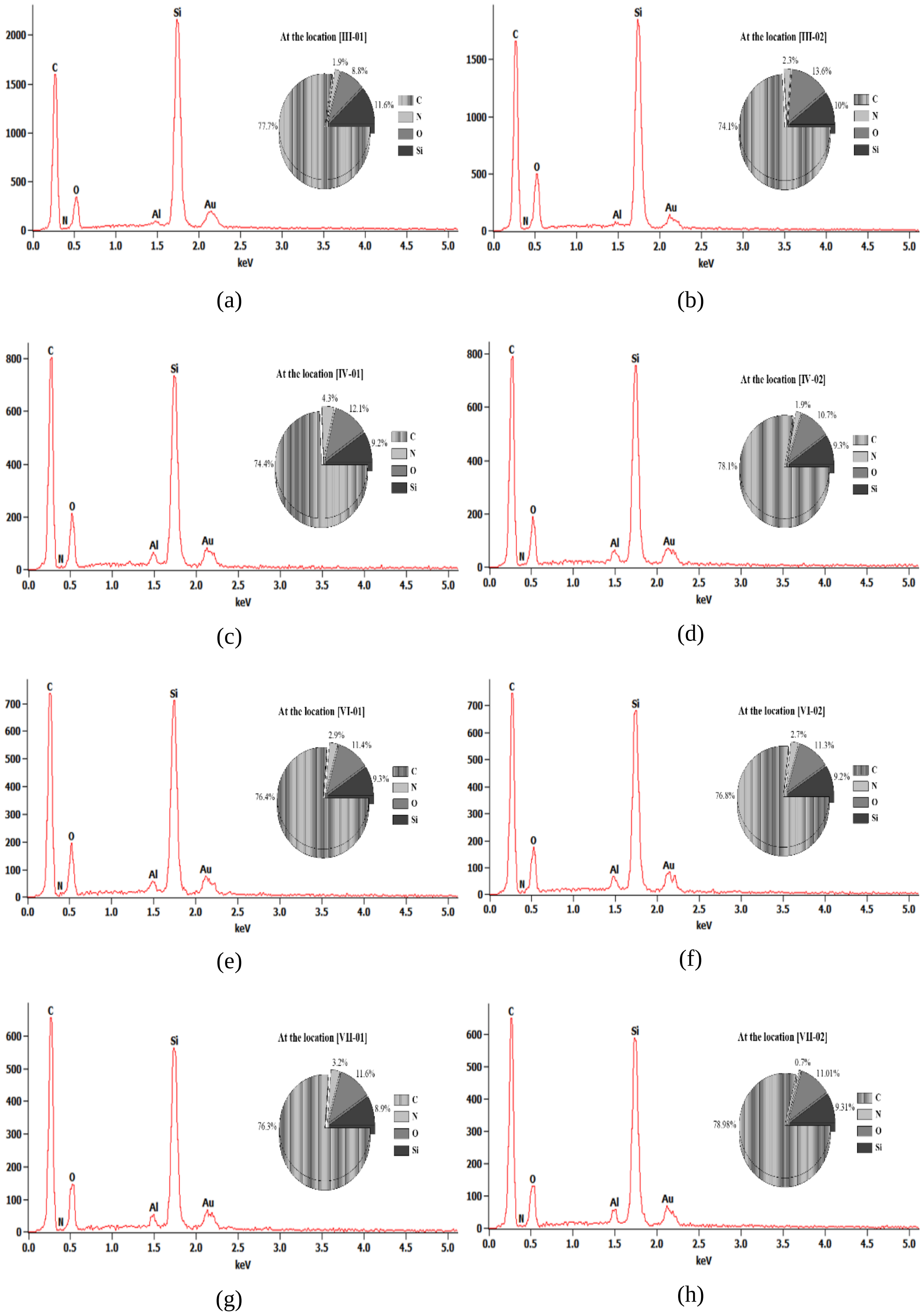

(a) (b)

(c) (d)

(e) (f)

(g) (h)

Figure 5.38: EDX analysis of chemical composites in Figure 5.36 at different localised spots: (a) III-01, (b) III-02, (c) IV-01, (d) IV-02, (e) VI-01, (f) VI-02, (g) VII-01 and (h) VII-02.

5.10 PD characteristics before an upcoming failure of a cavity

By analysis of PRPD pattern data, it is possible to identify likely times to failure of samples under test and therefore undertake morphological analysis before failure.

5.10.1 Optical microscopy

Before measuring PD, the morphology of a virgin cavity was observed using optical microscope as shown in Figure 5.39 (a). In the initial process of ageing, visible evidence of the surface roughness on the inner cavity surface was noticed after ageing 10 h as shown in Figure 5.39 (b). The interaction between PD bombardment and gaseous composites inside a cavity evolved the localised erosion site on the cavity surface and the enhancement of electric fields was spotted at this local site [13]. These factors led to the growth of protrusions out of the cavity wall and the progressive propagation of tree growth until the sample failed after 30 h as shown in Figures 5.39 (c) and 5.39 (d). Subsequently, this sample was cut in the vertical cross-section view of the middle cavity, which revealed the microscopic erosion of growing protrusions on the outer cavity surface and the black bulk inside the cavity as shown in Figures 5.39 (e) and 5.39 (f) respectively.

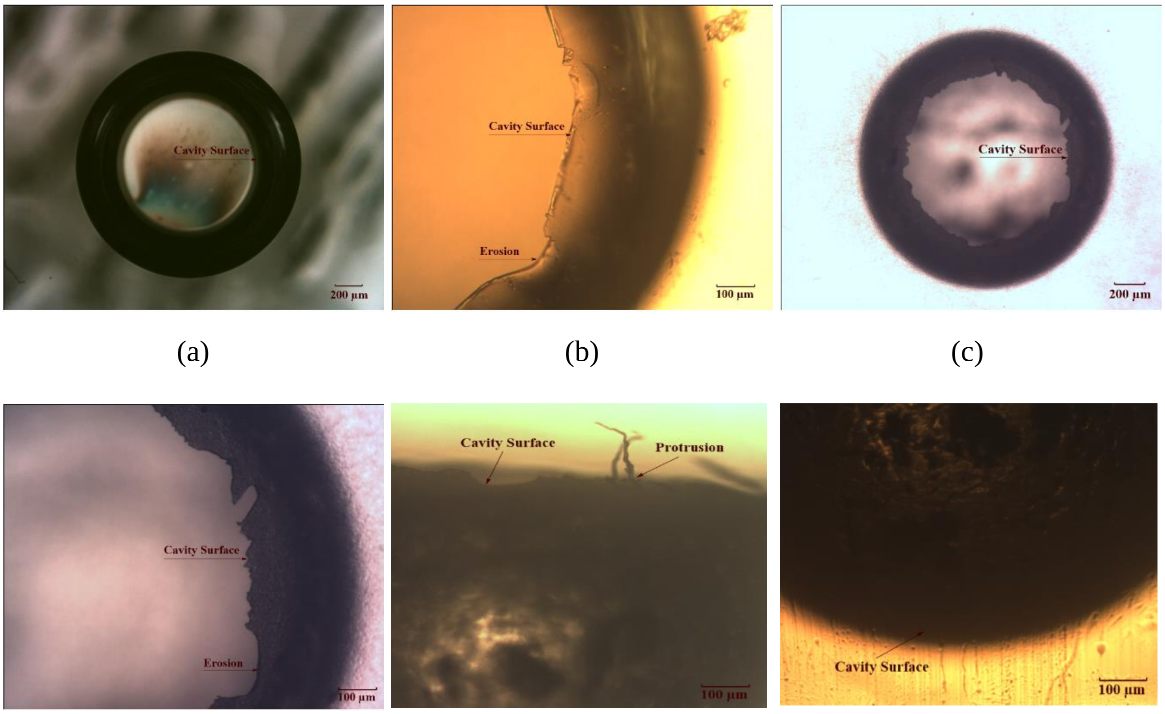

(a) (b) (c)

(d) (e) (f)

Figure 5.39: Morphological changes of the sample containing a spherical cavity of diameter 1.65 mm at various ageing times: top-section views of (a) a virgin cavity, (b) the surface roughness on the inner cavity at ageing 10 h, (c) an eroded cavity formation after failure at ageing 30 h, (d) a high-magnification in the micrograph (c) showing progressive erosion on the inner cavity surface at ageing 30 h; vertical cross-section views of a cavity (e) growing protrusions of the upper cavity surface area and (f) the black bulk in the inner cavity of the lower cavity surface area at ageing 30 h.

The black bulk on the cavity surface is thought to contain chemical by-products: silicone, carbon and oxygen [230]. Some evidence of the growth of pits on the peripheral wall of a cavity in polythene material was reported in [15]. Also, the growth of small pits on the surface of a void in epoxy material was found during the final stage of ageing [251].

5.10.2 Measurement of PD activity

PD behaviour due to the electrical ageing by internal partial discharges inside a spherical cavity of the silicone sample was classified into four main stages with a maximum failure time of 30 h. Figure 5.40 (a) showed the scatter plot of average apparent charge and average number of PDs per cycle over ageing of 30 h. The average apparent charge gradually decreased in the first stage from 97 pC at ageing 0.5 h to 9 pC at ageing 20 h. The trend significantly increased during the second stage to just under 600 pC at 25 h. The average number of PDs per cycle fluctuated during the first-second stages with a maximum value of 7 at ageing 10 h and a minimum value of just below 1 at ageing 22.5 h. In the third-fourth stages, the apparent charge slightly dropped from 190 pC after 26 h to 66 pC after 28 h. There was a sharp rise in the average number of PDs per cycle during the third stage with the average value of 9 at ageing 27 h. There was a sharp reversal during the fourth stage with PDs occurring very infrequently and the average number of PDs per cycle around 10^{-4}.

Maximum values of apparent charge are also shown in Figure 5.40 (b). It can be clearly seen that the highest value of maximum apparent charge was just over 2.5 nC during the second stage. As regards the average numbers of PDs between positive and negative half-cycles as shown in Figure 5.40 (c), there were the reasonable symmetry of PD quantities during the first-second stages. Notable asymmetry arose in the third stage, where the average number of PDs per cycle at ageing 27 h was obtained just under 4 for the positive half-cycle and just over 5 for the negative half-cycle.

The symmetry during the first-second stages, it is likely that a spherical cavity was located in the centre of a homogeneous dielectric material between parallel plate electrodes [229]. The asymmetry during the third stage is thought to be due to the progressive propagation of tree growth [252]. It should be noted that PD activity induced the localised erosion site of protrusions, which gradually evolved on the cavity surface related to high values of the maximum PD magnitude during the second stage as shown in Figure 5.40 (b). It is suggested that an increase in the discharge magnitudes during the growth of electrical trees before an upcoming failure has been observed in other research [231].

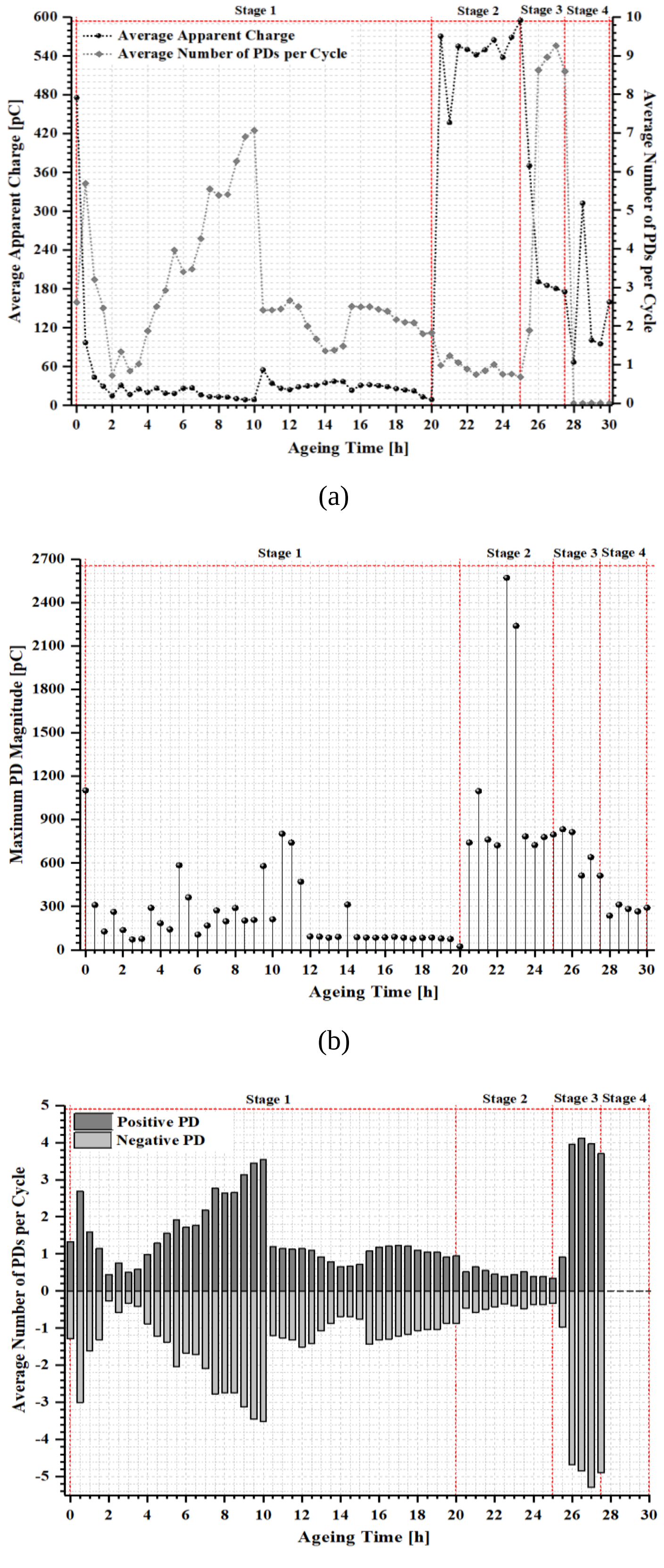

(a)

(b)

(c)

Figure 5.40: Evolution of PD characteristics as a function of ageing time of the sample containing a spherical cavity of diameter 1.65 mm: (a) the scatter plot between average apparent charge and average number of PDs per cycle, (b) the maximum PD magnitude and (c) the average number of positive and negative PDs per cycle.

The evolution of PD activity was acquired continuously to record every 30 minutes during the accelerated ageing until failure of the sample. In the initial stage of ageing, the typical turtle-like shape exhibited as shown in Figure 5.41 (a). Subsequently, the wing-like shape with SPMDs was detected and then transitioned into the rabbit-like shape with surface discharges as shown in Figures 5.41 (b) and 5.41 (c) respectively. Referring to Figure 5.41 (c), it should be noticed that the PD characteristics of this PRPD pattern were combined by two mechanisms between internal and surface discharges, which the internal discharge exhibited the rabbit-like pattern while the surface discharges are marked with a rectangular. The occurrence of SPMDs then observed as shown in Figure 5.41 (d), which corresponded to complete failure of the sample. Similar PRPD patterns have been observed before failure by other researches [253-254]. It is worth noting that SPMDs were noticed in the stages, where the tree formed and the sample failed. Rabbit-like patterns with surface discharges have also been observed prior breakdown of PRPD patterns in an investigation into internal discharges of artificial defects embedded in polymer material [255-256]. The PD statistical quantities at each stage are listed in Table 5.10.

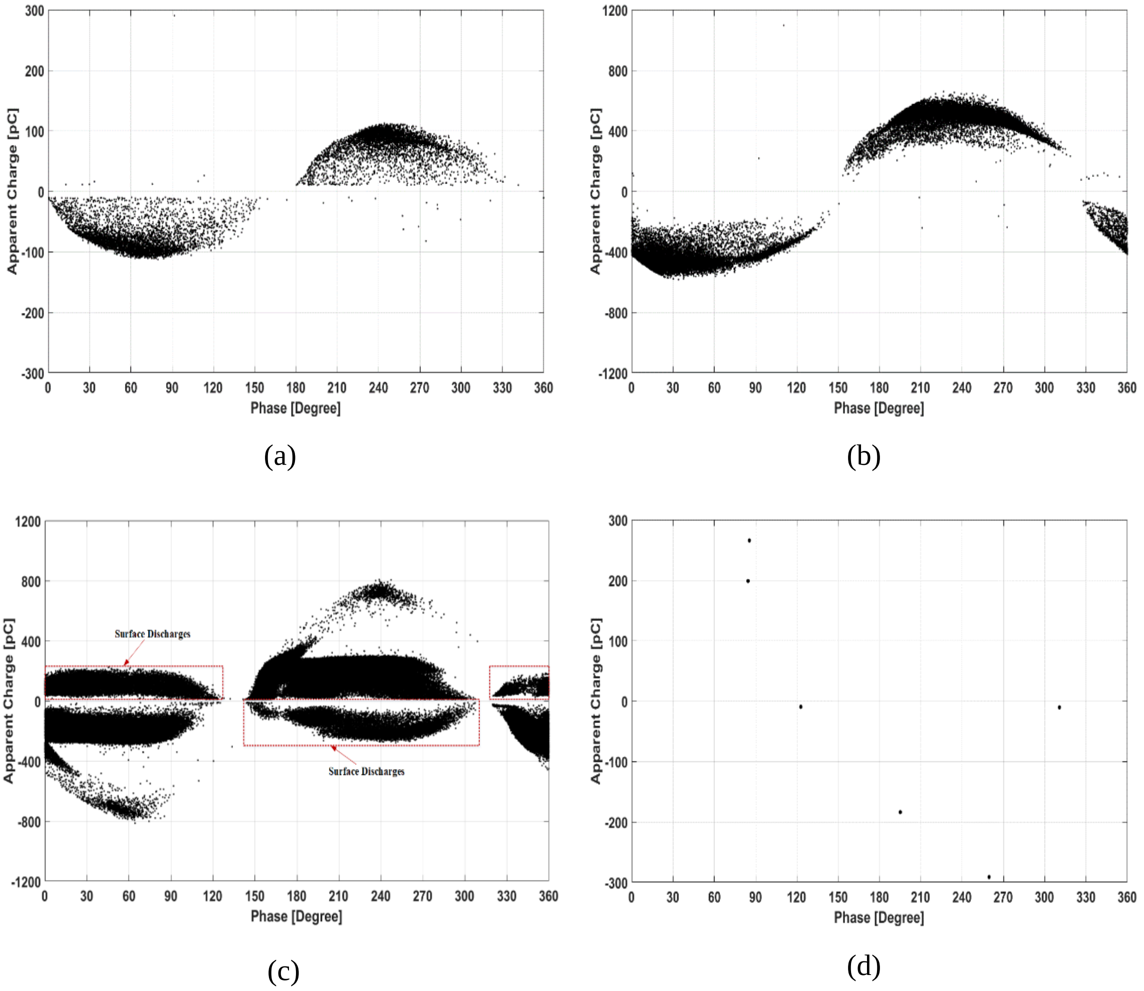

(a) (b)

(c) (d)

Figure 5.41: Variation in measured PRPD patterns of the sample containing a spherical cavity of diameter 1.65 mm at various ageing times: (a) a turtle-like pattern at ageing 4 h, (b) a wing-like pattern at ageing 21 h, (c) a rabbit-like pattern with surface discharges at ageing 26 h and (d) SPMDs at ageing 30 h.

Table 5.10: Statistical quantities of measured PRPD patterns at various ageing times.

Quantities	Ageing Stages			
	Stage 1 **Fig. 5.41 (a)**	**Stage 2** **Fig. 5.41 (b)**	**Stage 3** **Fig. 5.41 (c)**	**Stage 4** **Fig. 5.41 (d)**
Time Elapsed to Failure (%)	13.33	70.00	86.67	100.00
PRPD Patterns	Turtle-like	Wing-like with SPMDs	Rabbit-like with surface discharges	SPMDs
Average Apparent Charge (pC)	20.01	437.38	191.19	159.90
Maximum Apparent Charge (pC)	184.17	1096.30	813.44	291.19
Average Number of PDs per Cycle	1.87	1.22	8.62	1.93E-4
Average Number of Positive PDs per Cycle	0.98	0.65	3.95	1.29E-4
Average Number of Negative PDs per Cycle	0.88	0.57	4.67	0.64E-4

5.10.3 Simulation of PD activity

A PD model was developed to reproduce the PD measurement data through Matlab codes detailed in Appendix D.2. The model assumes that PD activity is governed by the electric fields in the centre location of a cavity, which was found by solving an electrostatic equation in COMSOL. A discharge occurred when the electric field in the centre was above the inception value and a free electron was available. The availability of a free electron was found by comparing the number of electrons generated in a time step against a random number. Discharges were presumed to deposit bipolar surface charge density distributions on the wall of a spherical cavity such that the field in the centre of a cavity was reduced to an extinction value. Free parameters were then adjusted such that the model output matched experimental data [235]. The model can be reproduced the measurement of PRPD patterns for turtle-like patterns, wing-like patterns, rabbit-like patterns and SPMD mechanisms as shown in Figure 5.42. As the model assumes that there was only a single PD source, it is only able to reproduce the rabbit-like PRPD pattern as shown in Figure 5.42 (c), without the curved shapes of surface discharges of the experiment result as shown in Figure 5.41 (c). The statistical quantities of PD measurements and simulations were also compared, which both values are given in Tables 5.10 and 5.11 respectively. The results show that there was reasonable agreement between simulation and measurement for the average apparent charge and the maximum PD magnitude. The average number of PDs per cycle had almost equal values in both simulation and experiment.

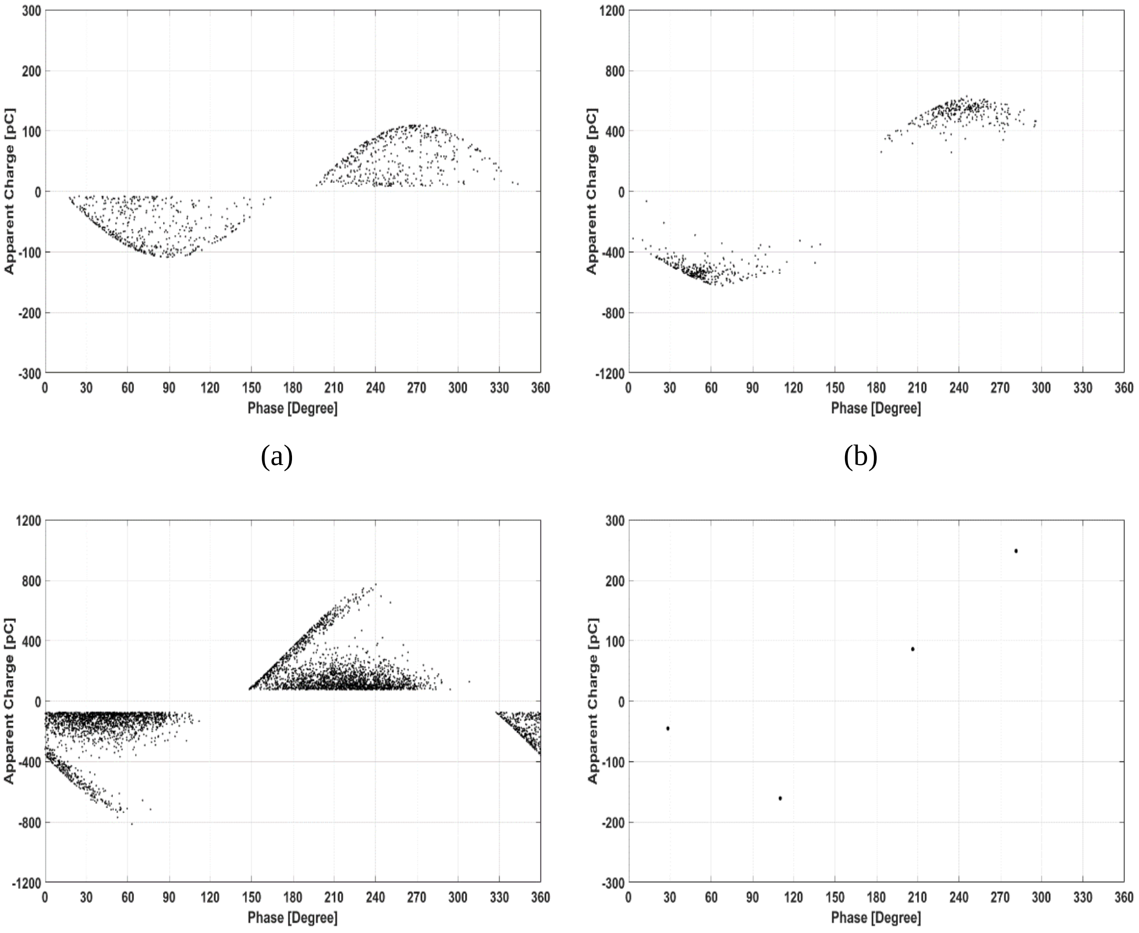

(a) (b)

(c) (d)

Figure 5.42: Variation in simulated PRPD patterns: (a) a turtle-like pattern, (b) a wing-like pattern, (c) a rabbit-like pattern and (d) SPMDs.

Table 5.11: Statistical quantities of simulated PRPD patterns.

Quantities	PRPD Models			
	Model 1 Fig. 5.42 (a)	**Model 2 Fig. 5.42 (b)**	**Model 3 Fig. 5.42 (c)**	**Model 4 Fig. 5.42 (d)**
Average Apparent Charge (pC)	57.51	512.87	188.93	135.30
Maximum Apparent Charge (pC)	109.03	627.77	814.59	248.56
Average Number of PDs per Cycle	1.87	1.24	8.63	8E-3
Average Number of Positive PDs per Cycle	0.94	0.62	4.28	4E-3
Average Number of Negative PDs per Cycle	0.93	0.62	4.35	4E-3

5.11 Summary

The results of both measurement and simulation of PD activity in a spherical cavity embedded in silicone material were presented at various conditions in terms of the PD inception voltage as a function of various cavity diameters, the accelerated ageing test as a function of various cavity diameters, various voltage amplitudes and various ageing times. The PD quantities from thirty-five test samples at the PDIV condition were undertaken to determine the average number of PDs per cycle, the average apparent charge, the inception electric field and pressure, where the simulation results of the average apparent charge as a function of different cavity diameters was in reasonable agreement with the measurement result. Moreover, all of these samples were further used in the accelerated ageing test for analysis of the PD quantities in terms of the average apparent charge, the maximum apparent charge and the simulation result of electric field distribution along the z-axis and the r-axis in the FEA model. The result shows that an amount of maximum apparent charge was in good agreement between measurement and simulation. Furthermore, the simulation of PRPD patterns, φ-q-n plots and PD quantities as functions of various voltage amplitudes and various ageing times were also reproduced, compared to the measurement data with reasonable agreement. Comparison of PD characteristics from two silicone samples containing different cavity diameters of 0.97 mm and 0.98 mm, the PRPD patterns and PD quantities related to the morphological changes caused by PD activity were investigated during the electrical ageing test. The result shows that PRPD characteristics of test samples containing cavity sizes of 0.98 mm and 0.97 mm exhibited the turtle-like patterns at the initial ageing and remained unchanged after further ageing 60 h and 120 h respectively while the PD quantities of average apparent charge and average number of PDs per cycle tended to decrease after elapsed time of ageing. As regards the cavity formation of diameter 0.97 mm, visible evidence of deposited by-products on the cavity surface in the form of liquid droplets and protrusions was noticed after ageing 120 h while the cavity diameter of 0.98 mm was obtained by liquid droplets after ageing 30 h and progressed localised erosion and protrusions after further ageing 60 h. A possible explanation for this result might be that the presence of liquid droplets on the cavity surface caused by the interaction between PD activity and gaseous products in the cavity. The liquid by-product of droplets may contain the chemical compound of nitric acid, which can erode chemical bonds in the bulk material, leading to the localised erosion site by the electric field enhancement and PD bombardment with elapsed time of ageing. With regard to chemical analysis by Raman spectroscopy, the new peak of spectra for the samples after ageing at the localised erosion site in an enclosed cavity can be seen to be due to CH_2 scissoring. It is believed that this peak occurred by the breaking of chemical bonds in bulk on the cavity wall due to the interaction between charge bombardment and gaseous composites inside a cavity during ageing processes. The PD characteristics of three samples containing different cavity diameters: 0.50 mm, 0.57 mm and 0.72 mm were investigated for morphological changes of the erosion depth within a cavity, which each sample was cut through the middle cavity in the vertical view. In the cavity diameter of

0.50 mm, the PRPD pattern exhibited the symmetry of turtle-like pattern at the initial ageing and this pattern remained unchanged after ageing 30 h while PD quantities of the average apparent charge and the average number of PDs per cycle dropped about 56% and 53% after ageing. Regarding evidence of the cavity formation in the vertical view, it remained unchanged at 0.50 mm in height, which equalled the cavity diameter. In the cavity diameter of 0.57 mm, the transition of PRPD patterns changed from the symmetry of rabbit-like patterns at the initial ageing to the wing-like patterns with SPMDs after ageing 60 h while the average apparent charge and the average number of PDs per cycle dropped about 90% and 74% over elapsed time of ageing for 60 h. In this case, visible evidence of liquid droplets was observed inside a cavity with the erosion depth at the bottom cavity wall of 0.64 mm in height. As regards the cavity diameter of 0.72 mm, the PRPD pattern exhibited the turtle-like pattern at the initial ageing. After further ageing 120 h, this pattern was detected the asymmetry of wing-like shape with SPMDs, where little discharge magnitudes for the positive half-cycle were higher than the negative half-cycle. In the PD quantities, the average apparent charge and the average number of PDs per cycle dropped about 84% and 93% over elapsed time of ageing for 120 h. In the morphological change of this cavity, large liquid droplets were obtained inside a cavity with the erosion depth at the bottom cavity surface of 0.96 mm in height. The result of this investigation indicates that the influence of liquid droplets plays a key role to enhance the progressive degradation of the cavity wall, resulting in loss of hydrophobicity and elapsed time of ageing. As regards the thermal analysis, the TGA curves from all samples were obtained their mass loss at a temperature of 500˚C with a decrease of 89% for the virgin sample, 79% for the samples after ageing 60 h and 70% for the samples after ageing 120 h. This result indicates that an amount of weight loss was related to an increase of elapsed time of ageing. Regarding the dielectric property, two samples containing different spherical cavity diameters of 1.15 mm and 2.15 mm were compared the real relative permittivity and the tan delta at 50 Hz. The result shows that the value of real relative permittivity for the smaller cavity size was higher than the larger cavity size while the tan delta for the larger cavity size was higher than the smaller cavity size. In the sample containing the spherical cavity of diameter 0.57 mm at ageing 60 h, the real relative permittivity was lower than the sample after cleaving the middle cavity into the half while the tan delta was higher than the sample after cleaving the middle cavity into the half. In particular, PRPD analysis of a spherical cavity embedded in silicone material can be used for diagnosis of progressive degradation mechanisms on the cavity surface regarding the micro-craters, the electrical tree initiation and the upcoming failure. As regards the cavity formation of diameter 0.80 mm, the transition of distinct PRPD patterns exhibited from the rabbit-like pattern at the initial ageing to the turtle-like pattern after ageing 20 h and followed by the wing-like pattern with the mechanism of SPMDs after ageing 27 h. It is noticed that the occurrence of wing-like patterns associated with the presence of corrosive by-products in terms of micro-craters on the cavity surface, where a cluster of electrical tree initiation might evolve at the localised erosion site. An investigation into microanalysis techniques by SEM and EDX was undertaken to reveal the microstructure and chemical elements of corrosive by-products in the bulk of a cavity caused by charge bombardment. The result shows that the virgin cavity surface comprised the chemical elements by 73% of carbon, 4.9% of oxygen and 22.1% of silicon while deposited by-products on the cavity wall at localised erosion of micro-craters after ageing 27 h consisted 66.93% of carbon, 9.29% of nitrogen, 15.08% of oxygen and 8.69% of silicon. It should be noticed that a large amount of nitrogen was obtained at the localised spot of micro-craters, compared with the undetectable nitrogen in the bulk of the virgin surface. In the cavity formation of diameter 0.95 mm, the PD characteristics of PRPD patterns exhibited the turtle-like pattern at the initial ageing and remained unchanged with slight magnitude discharges after ageing 733 h. The transition of this pattern linked to the wing-like patterns after further ageing 1069 h and 1070 h. Interestingly, the SEM image explored a cluster of electrical tree initiation at the bottom cavity wall, which one of the trees had the structural dimension about 2 µm wide and 50 µm in length. Otherwise, the EDX analysis of various spots at this tree channel was detected a large amount of nitrogen at the focal location of tree initiation, compared with a small number of this compound at the middle channel of treeing growth. Note that the interaction between charge bombardment and gaseous composites, i.e. nitrogen enhanced electrical tree initiation from the cavity wall. In the case of the upcoming failure, an investigation into a spherical cavity of diameter 1.65 mm embedded silicone material was undertaken to find out the cause of its complete failure. The significant variations in PRPD patterns were distinguished into four main stages related to the cavity formation of localised erosion in the form of the surface erosion, the tree growth, the surface discharges prior to failure and complete failure, which growing protrusions on the outer cavity wall were formed over ageing 30 h. The simulation results of distinct PRPD patterns and PD statistic quantities, i.e. the average apparent charge, the maximum apparent charge and the average number of PDs per cycle were also reproduced through a PD model with good agreement with measurement results.

Chapter 6 Conclusions and Future Research

This thesis has investigated the effect of a prolonged period of electrical ageing on cavity morphology, where the cavities have been created in various solid dielectric materials. Changed features of chemical and morphological degradation mechanisms can be correlated with PRPD patterns. Section 6.1 details the main conclusions, resulting from this extensive experimental study. Areas for future work are described in Section 6.2.

6.1 Conclusions

The test samples used in the experiment were produced two different shaped cavities in terms of a cylindrical flat-shaped cavity embedded in polyethylene material and a spherical-shaped cavity embedded in silicone material. The noteworthy results of this research are that the substantial findings contributed to the understanding of progressive degradation mechanisms within the cavity. The key contributions of this study can be summarised the four areas as follows:

Firstly, the variation in PRPD patterns related to the formation on the cavity surface depended on various factors such as gas pressure, gaseous composites, cavity sizes, time-lag of PD events, surface conductivity on the cavity wall and elapsed time of ageing. The typical cavity discharges can be linked to the rabbit-like pattern and the turtle-like pattern while the stage of electrical tree growth can be linked to the wing-like pattern with SPMD mechanism. It is assumed the role of gaseous compounds, i.e. oxygen and nitrogen in the cavity that when all oxygen was consumed by the oxidation reaction, nitrogen was replaced to induce the growth of pits and electrical trees before the upcoming failure. In the LDPE samples, the accumulation of localised erosion on the cavity surface gradually deposited from surface roughness to corrosive by-products of growing crystals and electrical tree initiation due to PD bombardment and electric field enhancement at the localised site during accelerated ageing processes. The variation in PRPD patterns related to the formation on the cavity surface can be distinguished into three main stages. In the initial stage, the rabbit-like pattern with long-ears exhibited due to high amounts of oxygen and statistical time-lag of PD events. In the second stage, the rabbit-like pattern with short-ears changed to the turtle-like pattern due to a low amount of oxygen in the cavity and the high conductivity on the cavity wall after a prolonged period of ageing. It is likely that an amount of nitrogen within the cavity predominantly replaced in this stage because a large amount of oxygen was consumed at the initial stage of ageing. In the third stage, the PD extinction of SPMD mechanism occurred due to the high conductivity on the cavity wall and within the wall of tree channels. In the silicone sample, the evolution of PRPD patterns related to the formation on the cavity surface can be distinguished into four main stages in terms of surface erosion, electrical tree growth, surface discharges prior to failure and upcoming failure. The formation on the cavity surface was gradually degraded from localised erosion to micro-craters before the growth of electrical tree initiation. It is possible that the corrosive by-product of liquid droplets on the cavity surface may contain the chemical compound of nitric acid (HNO_3). This liquid by-product may cause an increase of conductivity on the cavity wall and the progression of localised erosion in the bulk material in the forms of surface erosion, micro-craters and electrical tree growth by addition reactions from PD bombardment and electric field enhancement.

Secondly, an investigation of notable PD characteristics during accelerated electrical ageing was undertaken by analysing both PRPD patterns and PD quantities related to the cumulative formation on the cavity surface. In the initial stage of ageing, the transition of PRPD patterns exhibited from the rabbit-like shape with long ears to the rabbit-like shape with short ears. In the PD quantities, the relationship between average apparent charge and average number of PDs per cycle can be divided into three main stages. The trends of both PD statistical quantities steeply increased at the initial ageing and followed by a gradual decrease of discharge magnitudes during the second stage of ageing. In the final stage, both figures turned to an upward trend. A possible explanation is that the case of PRPD characteristics exhibited the rabbit-like pattern with long ears and the highest level of PD magnitudes because there was a high amount of oxygen content in the cavity during the initial ageing. The progression of deterioration mechanisms on the cavity wall gradually formed in terms of surface roughness, growing crystals and corrosive by-products caused by the interaction between PD bombardment and chemical reactions due to oxidative ageing. Otherwise, the PD characteristics exhibited the rabbit-like patterns with short ears because there were the variation of gas composites within the cavity and a high conductivity on the cavity wall during elapsed time of ageing. The results of SEM and EDX microanalysis indicate that the localised erosion sites of corrosive by-products and growing crystals were spotted with a high amount of nitrogen, compared with the undetectable nitrogen at the virgin surface and the surface roughness. It is possible that much oxygen was consumed during the initial oxidation reaction and replaced by nitrogen after a prolonged period of ageing. In thermal analysis, DSC results indicate that the virgin sample exhibited a single melting peak, compared with multiple melting peaks of samples after various ageing times. The presence of multiple melting peaks is due to the changed mechanism of chemical bonds in the bulk material by the reactions of oxidative ageing and PD activity. Furthermore, chemical analysis of FTIR results indicates that the surface of localised erosion on the cavity wall by PD activity was found a new peak spectrum as carboxylic acids, compared with the undetectable peak of the virgin surface. The occurrence of a new peak spectrum is due to the breaking of chemical bonds in the bulk material of the test sample caused by the interaction of PD bombardment and electric field enhancement. The result indicates that the gradual reduction of oxygen within the cavity during the processes of oxidative ageing affected the transition of discharge mechanisms from rabbit-like patterns with long-ears to rabbit-like patterns with short-ears. In the morphological changes of the cavity, the deposited by-products gradually formed localised erosion on the cavity surface from surface roughness to corrosive by-products in terms of growing crystals and black bulk material with elapsed time of ageing.

Thirdly, the techniques of PRPD analysis can be used to validate localised erosion in terms of growing micro-craters and electrical tree initiation on the cavity surface. Visible evidence of treeing growth from the cavity wall can be disclosed to contribute a hypothesis in the literature and the knowledge in the model of degradation processes within the enclosed cavity. Microanalysis of high-resolution in SEM micrographs at the localised erosion site can reveal the corrosive by-products in terms of a cluster of electrical tree initiation, micro-craters and growing protrusions on the cavity wall. One of treeing channels had in the structural dimension of 2 μm wide and 50 μm in length. EDX results indicate that a large amount of nitrogen was detected at growing micro-craters and electrical tree channels, compared with the undetectable nitrogen in the virgin bulk material. Furthermore, chemical analysis of Raman results indicates that the localised erosion site within the cavity was found a new peaked spectrum as CH_2 scissoring, compared with the undetectable peak of the virgin surface. In thermal analysis, TGA results show that the mass loss of test samples tended to increase with elapsed time of ageing. It is possible that the interaction between chemical reactions and PD activity in the cavity gradually formed the formation of silica glass in bulk silicone material and progressively reacted localised erosion on the cavity wall in forms of growing micro-craters and electrical tree channels during accelerated ageing processes. In the PD characteristics, the notable PRPD patterns show that the asymmetry of wing-like patterns exhibited during the stage of electrical tree growth on the cavity surface.

Fourthly, the characteristic of PD extinction occurred during the stage of an upcoming failure of the test sample, which associated with the appearance of SPMD mechanism with a low number of PDs per cycle as a result of the high conductivity on the cavity wall and the inside wall of tree channels. It can be explained by the fact that when the surface charge decay cumulatively deposited on the cavity wall by the consecutive PD events over a period of ageing, the electric field in the cavity dropped because the physical cavity surface changed to the conductive surface layer. Furthermore, an investigation into the dielectric property indicates that the dielectric loss of test samples tended to increase with elapsed time of ageing. This mechanism caused by the cumulative formation on the cavity surface in the forms of surface roughness, crystals, micro-craters and electrical tree growth by PD activity, which correlated with a gradual accumulation of dielectric loss in the bulk material during electrical ageing processes.

6.2 Further Research

Some worthwhile points should be further considered related to this research as follows:

- The variation in gaseous contents inside the cavity, i.e. oxygen and nitrogen should be precisely determined during procedures for producing the test sample, which the controlled volume of a gaseous-filled cavity can be exactly injected with a syringe used for making a spherical cavity embedded in solid dielectric insulation. Interestingly, an investigation into the proportion in a gaseous-filled cavity between oxygen and nitrogen elements should be determined during the sample preparation before measuring PD for exploring the influence of gaseous composites inside the cavity caused by ageing, leading to the treeing growth from the cavity wall related to PD characteristics.

- The application of high-speed digital camera should be combined in the PD experimental set-up for observing the discharge mechanisms of charge distribution on the cavity surface during PD activity, which the degradation stages can be identified during both initiation and progressive propagation of electrical trees before an upcoming failure of the sample occurs.
- Visible evidence of deposited by-products on the cavity surface by PD activity regarding liquid droplets, surface roughness, craters and electrical trees should be further conducted to analyse their localised microstructures in three-dimensional views by using atomic force microscopy (AFM) instrument. Also, liquid droplets inside the cavity should be clarified the chemical compounds by gas chromatography (GC).
- The occurrence of electrical tree initiation from the cavity wall should be further conducted by using analytical techniques in three-dimensional images, i.e. X-ray computed tomography (XCT) and serial block-face scanning electron microscopy (SBFSEM) instruments for producing the physical microstructure of electrical tree growth from the enclosed cavity in dielectric insulation. These techniques can be applied for exporting data to the model used in Finite Element Analysis (FEA) for finding electric field magnitudes at the localised sites in order to develop improved models of this degradation process.

Appendix A PD Characteristics of a Flat-Shaped Cavity in PET Material

An investigation into PD characteristics of PET sample containing a flat-shaped cavity is conducted to diagnose degradation processes on the cavity surface. The result shows that PD quantities of PDIV and PDEV are determined by finding the average value of twelve test samples. One of the samples was undertaken to investigate the evolution of PRPD analysis related to the morphological changes of a cavity. Furthermore, the chemical analysis by Raman spectroscopy is applied to examine the chemical by-products of the localised erosion sites on the cavity surface under the accelerated ageing test.

A.1 Polyethylene terephthalate (PET)

The sample was made using three layers of PET film with a thickness of 0.3 mm and a flat-shaped cavity diameter of 1.1 mm in the centre of the middle layer, which PET material manufactured by Goodfellow Cambridge Ltd. The chemical structure of PET material comprised by the condensation of ethylene glycol and dimethyl terephthalate as shown in Figure A.1. The characteristic properties of PET film are illustrated in Table A.1.

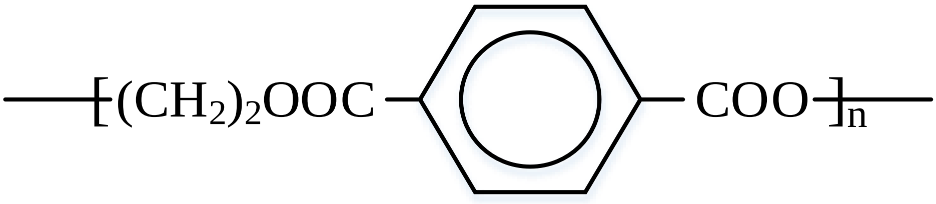

Figure A.1: Chemical structure of PET material [257].

Table A.1: Characteristic properties of PET film [178].

Typical Materials	Dielectric Strength [kV/mm]	Dielectric Constant at 1 MHz	Dissipation Factor at 1 kHz
PET (100 µm in thickness)	17	3.0	0.002

A.2 PD experimental set-up

In the PD measurement, the test sample was placed between parallel brass plate electrodes with a diameter of 10 mm and 20 mm in thickness. The upper electrode was connected to an applied variable HV AC of 20 kV, 50 Hz and the lower electrode was connected to the ground system as shown in Figure A.2.

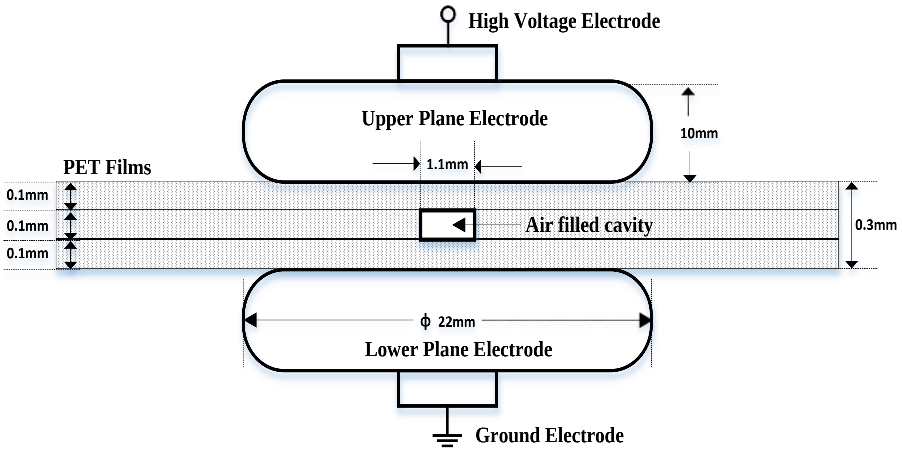

Figure A.2: Schematic arrangement of a test cell and a test sample for the PD measurement.

A.3 Characteristics of PDIV and PDEV levels

The PD measurement in this experiment was conducted by using Omicron Mtronix MPD 600 system, which exhibited PRPD analysis during the electrical ageing process. The applied voltage level for the ageing test was determined by finding the average PDIV of twelve test samples (approximately 2 kV) and multiplying each sample by a factor of 1.5 times (approximately 3 kV), which was set as the samples experienced accelerated ageing. The characteristics of PDIV and PDEV values from twelve PET samples are illustrated in Figure A.3.

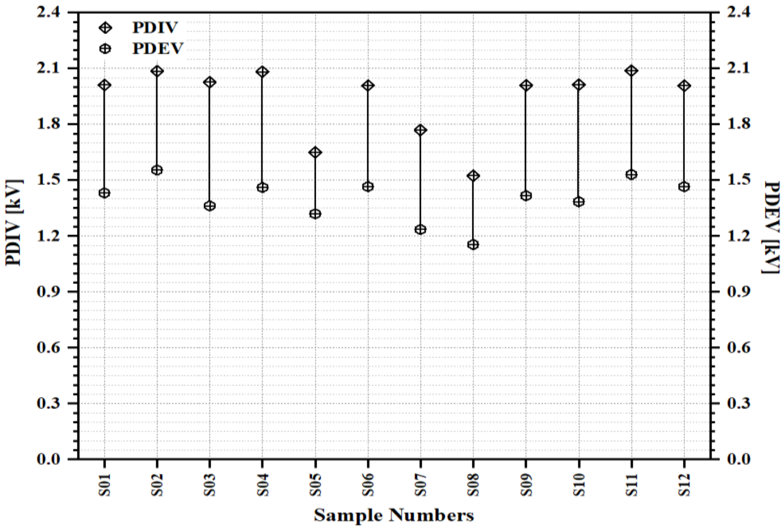

Figure A.3: Characteristics of PDIV and PDEV data obtained from twelve PET samples.

A.4 Optical microscopy

The morphological change was revealed the deteriorated region on the cavity surface. The result shows that the surface roughness was observed after ageing 33 h as shown in Figure A.4 (b). After further ageing of 38 h, visible evidence of the black bulk on the cavity surface occurred as shown in Figure A.4 (b). It is likely that the influence of PD activity and gas composites in a cavity induced the localised erosion site of the black bulk on the cavity wall due to the oxidative ageing [58].

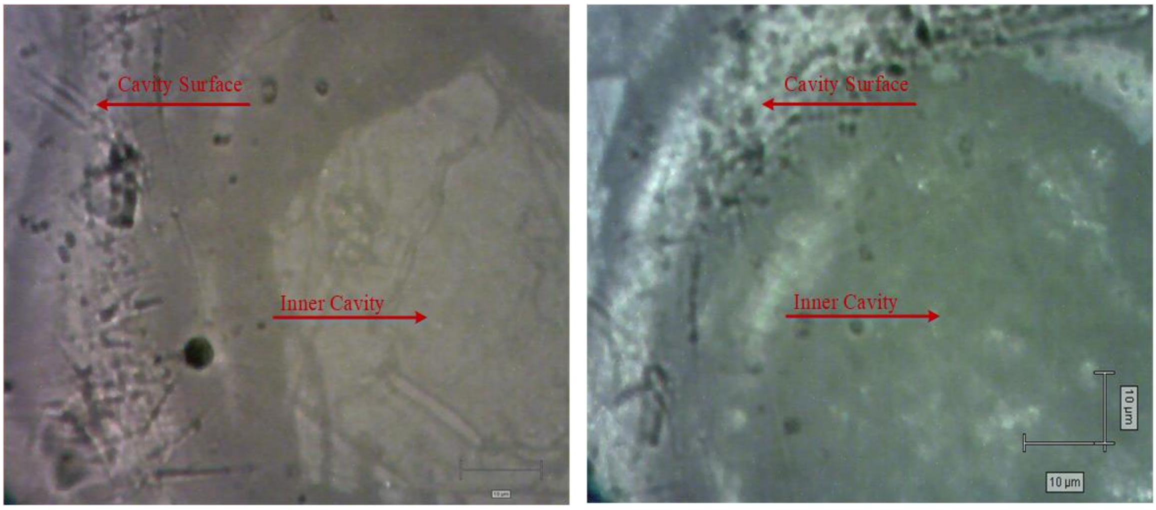

(a) (b)

Figure A.4: Morphological changes of the test sample containing a flat-shaped cavity of diameter 1.1 mm: top-section views of (a) and (b) the morphology of eroded cavity formation after ageing 33 h and 38 h respectively.

A.5 Measurement of PD activity

The PD characteristics were investigated the evolution of PRPD analysis related to the cavity formation during the ageing process. After ageing 1 h, the PRPD pattern linked to the rabbit-like shape, where the charge magnitude exhibited the symmetry between positive and negative half-cycles as shown in Figure A.5 (a). This pattern remained consistent until the transition to growth in the rabbit-eared pattern was observed after ageing 16 h as shown in Figure A.5 (b). The typical turtle-like pattern was noticed after ageing 30 h as shown in Figure A.5 (c). After further ageing of 38 h, the phase relationship in the PRPD pattern was noticed to expand with PD occurring across the entire power cycle as shown in Figure A.5 (d).

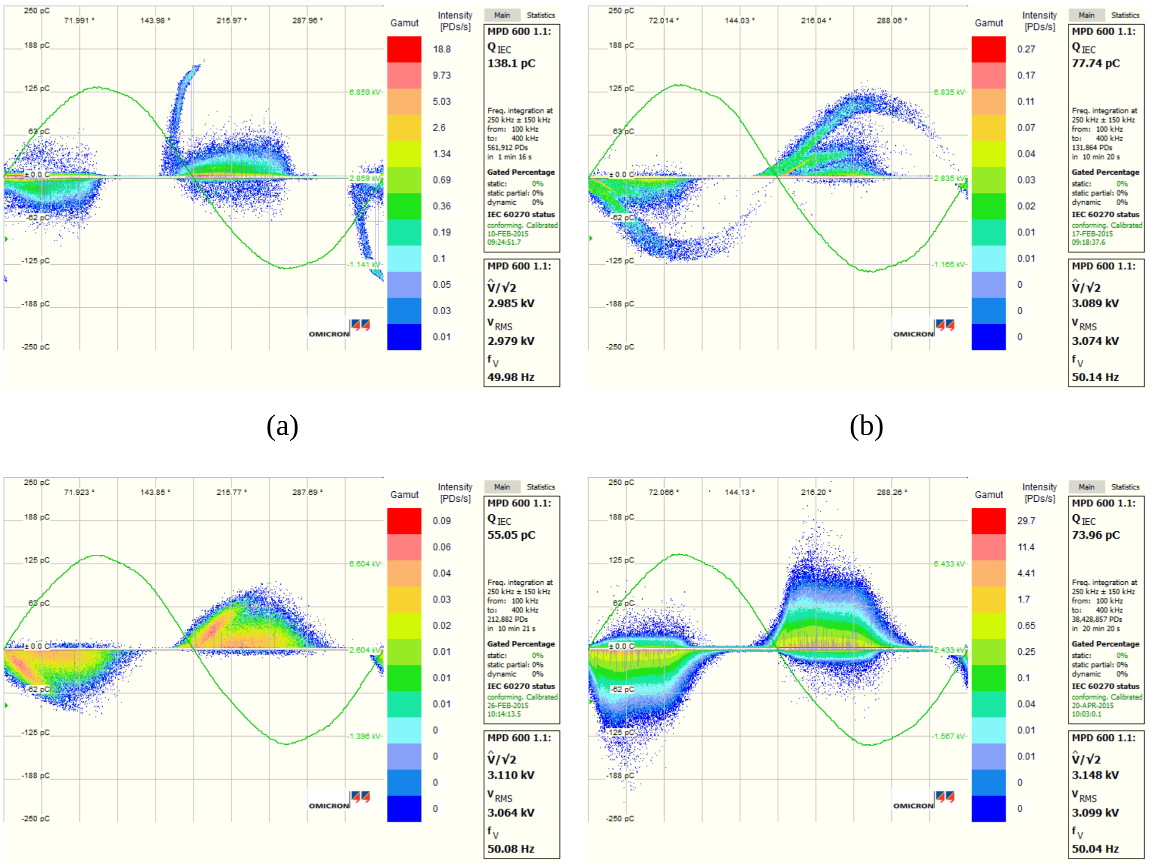

(a)

(b)

(c)

(d)

Figure A.5: Variation in measured PRPD patterns of the test sample containing a flat-shaped cavity of diameter 1.1 mm: (a) a rabbit-like pattern at ageing 1 h, (b) a rabbit-like pattern at ageing 16 h, (c) a turtle-like pattern at ageing 30 h, and (d) a turtle-like pattern at ageing 38 h.

A.6 Raman spectroscopy

Raman spectroscopy was used to analyse chemical by-products at the localised erosion site on the cavity surface caused by the accelerated ageing test. The Raman spectra at different spots on the cavity surface as a function of various ageing times were obtained the wavenumber between 3200 cm^{-1} and 100 cm^{-1} as shown in Figure A.6. The spectrum of a virgin sample was obtained to provide as a spectral reference. The fluorescence of spectra was detected from the sample after ageing, which gradually increased with elapsed time of ageing: 22 h, 33 h and 38 h. The appearance of fluorescence was obtained from the test sample after ageing as reported in other researches [238, 258].

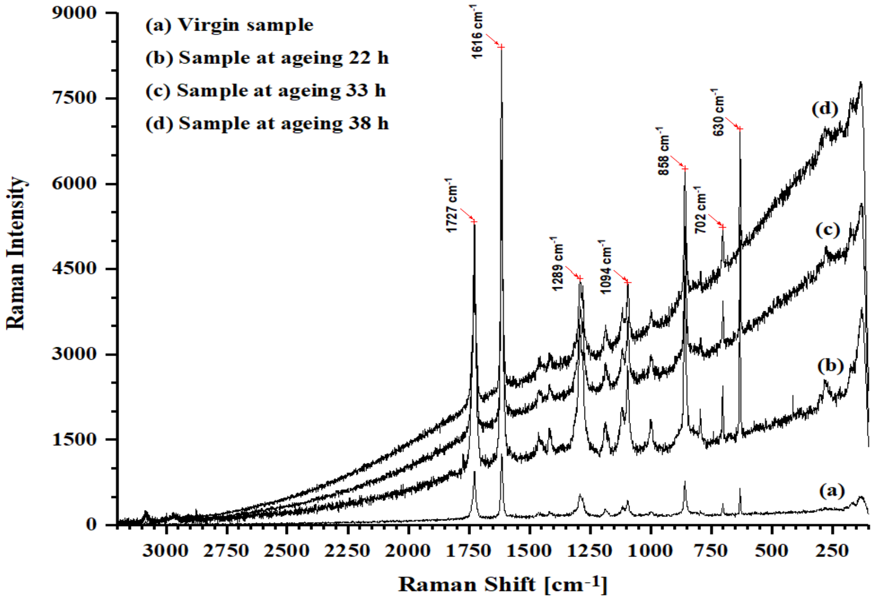

Figure A.6: Comparison of Raman spectra obtained from various ageing times: (a) a virgin sample, (b) 22 h, (c) 33 h, and (d) 38 h.

Appendix B PD Characteristics of a Flat-Shaped Cavity in LDPE Material

An investigation into PD characteristics related to the morphological change of a flat-shaped cavity embedded in polyethylene material was undertaken to identify the stages of degradation processes and failure. The results show that the significant changes between PD characteristics and the cavity formation caused by the accelerated ageing can be distinguished into two significant mechanisms, where the cavity formations were formed localised erosion on the cavity surface in Section B.1 and corrosive by-products before an upcoming failure in Section B.2.

B.1 PD characteristics of deterioration mechanisms on the cavity surface

The deterioration processes of a flat-shaped cavity by PD activity due to a prolonged ageing were undertaken by three polyethylene samples (I) to (III) at the applied voltage level of 2.5 kV, 50 Hz, which each sample containing a flat-shaped cavity of diameter 2 mm in the centre of the middle layer of three layers was investigated the evolution of PD characteristics related to the cavity formation due to a long-term period of electrical ageing.

B.1.1 Optical microscopy: the LDPE sample (I)

In the sample (I), a virgin cavity was observed before measuring PD as shown in Figure B.1 (a). Visible evidence of deposited by-products was formed on the inner cavity surface at ageing 409 h as shown in Figure B.1 (b) and the progressive erosion of corrosive by-products was observed within the centre cavity after further ageing 654 h and 1004 h as shown in Figures B.1 (c) and B.1 (d) respectively. It is suggested that localised erosion within the inner cavity resulted from increasing the conductivity on the cavity surface at the localised site by PD bombardment and the electric field enhancement, leading to growing crystals and pits before the electrical tree initiation as reported in other researches [156].

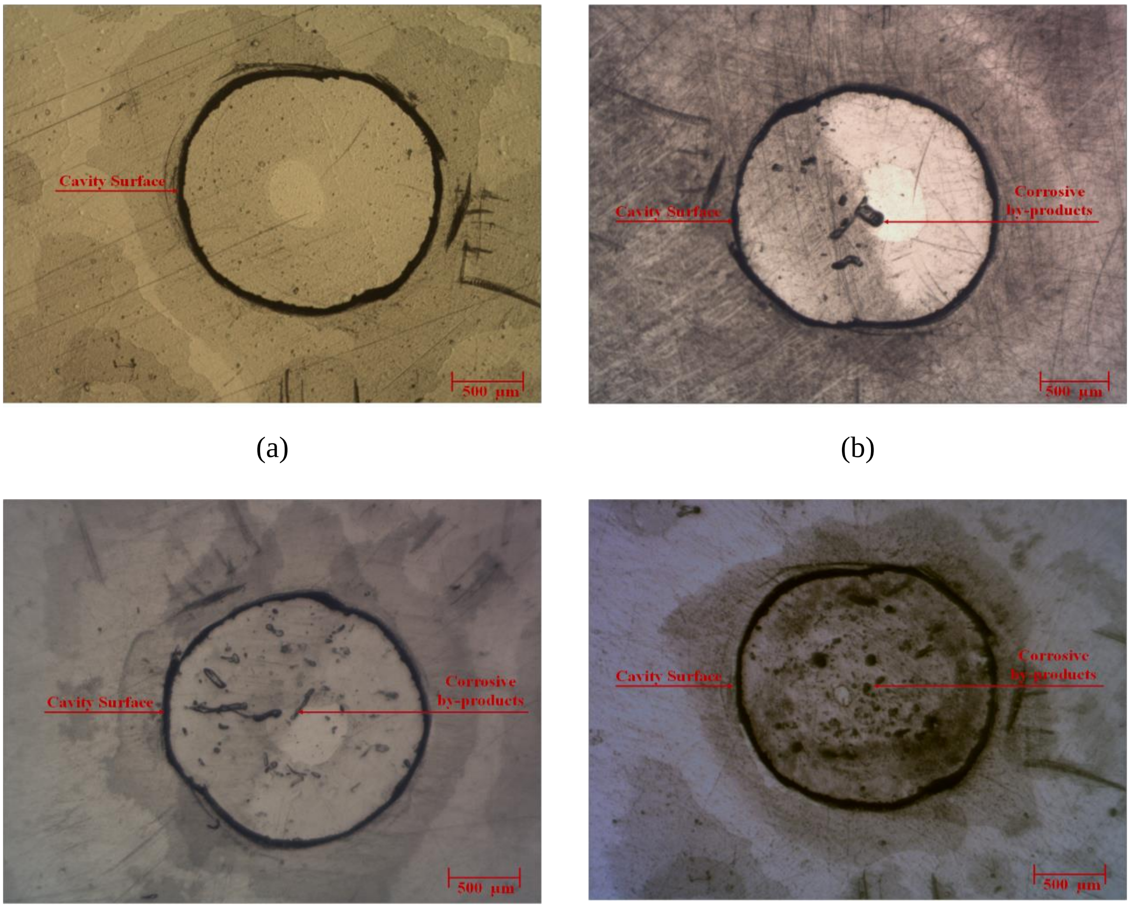

(a) (b)

(c) (d)

Figure B.1: Morphological changes of the LDPE sample (I) containing a flat-shaped cavity of diameter 2 mm at various ageing times: top-section views of (a) a virgin cavity, (b) 409 h, (c) 654 h, and (d) 1004 h.

B.1.2 Measurement of PD activity: the LDPE sample (I)

The characteristics of PRPD patterns exhibited the rabbit-like shape at the initial ageing and this pattern remained unchanged the rabbit-like shapes after ageing 206 h and 409 h as shown in Figures B.2 (a) to B.2 (c) respectively. The transition of this PRPD pattern changed to the turtle-like pattern after further ageing of just over 1000 h as shown in Figure B.2 (d). Otherwise, the scatter distribution of apparent charge as a function of various ageing times showed high magnitude discharges at the initial ageing and followed by minimum magnitude discharges from ageing 30 h to ageing 558 h. Subsequently, the distribution of apparent charge was detected with large discharges at ageing 654 h and 1004 h as shown in Figure B.3 (a). The bar chart between average apparent charge and average number of PDs per cycle can be divided into three main stages at various ageing times as shown in Figure B.3 (b). The result shows that the average apparent charge was obtained just over 30 pC at the initial ageing and followed by a steep drop about 50% during the second stage of ageing while this figure dramatically increased about 25% during the third stage of ageing. In the average number of PDs per cycle, the quantity was obtained just over 12 at the initial ageing and then tended to decrease about 80% during the second stage of ageing while this amount tended to increase about 25% during the third stage of ageing.

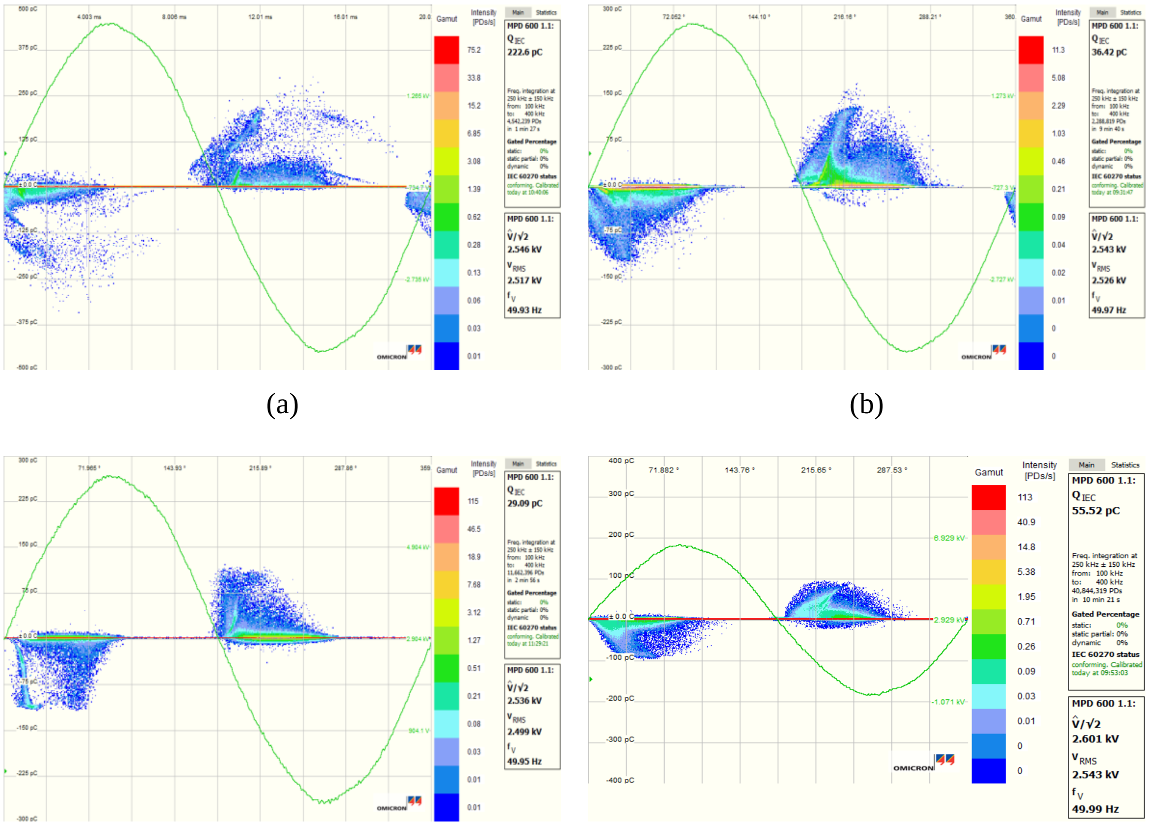

(a) (b)

(c) (d)

Figure B.2: Variation in measured PRPD patterns of the LDPE sample (I) containing a flat-shaped cavity of diameter 2 mm at various ageing times: (a) a rabbit-like pattern at ageing 10 min, (b) a rabbit-like pattern at ageing 206 h, (c) a rabbit-like pattern at ageing 409 h, and (d) a turtle-like pattern at ageing 1004 h.

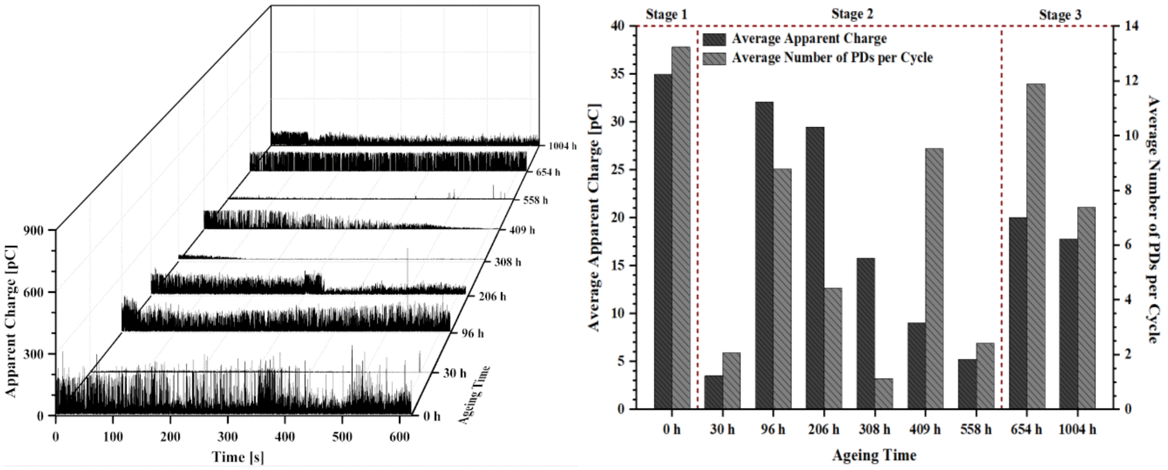

(a) (b)

Figure B.3: PD data of the LDPE sample (I) containing a flat-shaped cavity of diameter 2 mm as a function of various ageing times: (a) the scatter distribution of apparent charge and (b) the bar chart between average apparent charge and average number of PDs per cycle.

B.1.3 Optical microscopy: the LDPE sample (II)

In the sample (II), a virgin cavity was observed before measuring PD as shown in Figure B.4 (a). Visible evidence of deposited by-products was formed on the centre cavity after ageing 96 h as shown in Figure B.4 (b) and the progressive erosion of corrosive by-products was then noticed within the cavity after further ageing 654 h and 1004 h as shown in Figures B.4 (c) and B.4 (d) respectively.

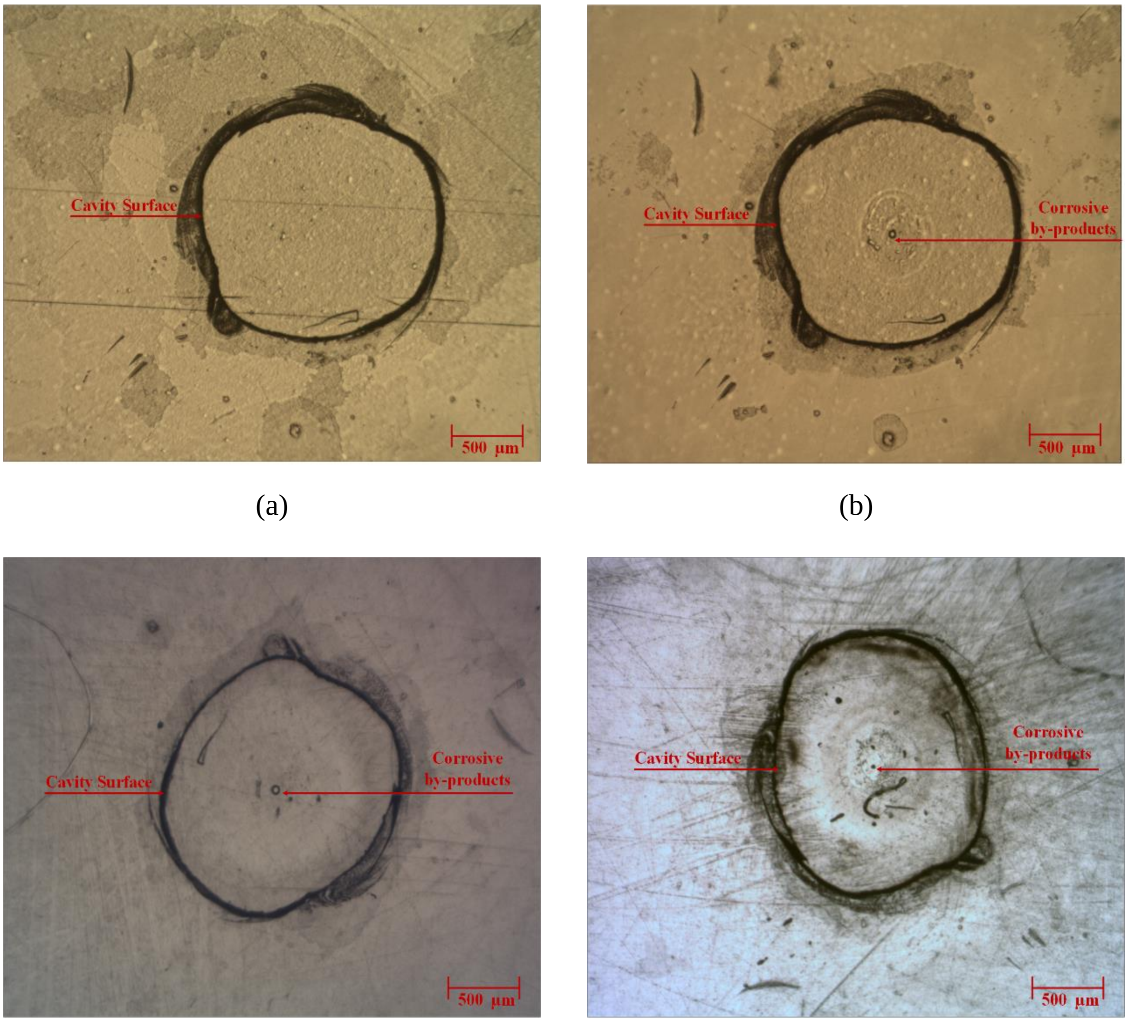

(a) (b)

(c) (d)

Figure B.4: Morphological changes of the LDPE sample (II) containing a flat-shaped cavity of diameter 2 mm at various ageing times: top-section views of (a) a virgin cavity, (b) 96 h, (c) 654 h and (d) 1004 h.

B.1.4 Measurement of PD activity: the LDPE sample (II)

The characteristics of PRPD patterns exhibited the rabbit-like shape with a long ear at the initial ageing and this pattern remained unchanged the rabbit-like shape with slight magnitude discharges at ageing 96 h as shown in Figures B.5 (a) and B.5 (b). The transition of this PRPD pattern changed to the turtle-like patterns after ageing 206 h and further ageing of just over 1000 h as shown in Figures B.5 (c) and B.5 (d). Otherwise, the scatter distribution of apparent charge as a function of various ageing times showed high magnitude discharges at the initial ageing and followed by minimum magnitude discharges during the second-third stages of ageing as shown in Figure B.6 (a). The bar chart between average apparent charge and average number of PDs per cycle can be divided into three main stages at various ageing stages as shown in Figure B.6 (b). The result shows that the average apparent charge was obtained just under 60 pC at the initial ageing and followed by a gradual decrease of about 60% and 80% during the second-third stages of ageing. In the average number of PDs per cycle, the quantity was obtained just over 5 at the initial ageing and then tended to decrease about 60% during the second stage of ageing and followed by a steep increase about 50% after ageing of just over 1000 h during the third stage.

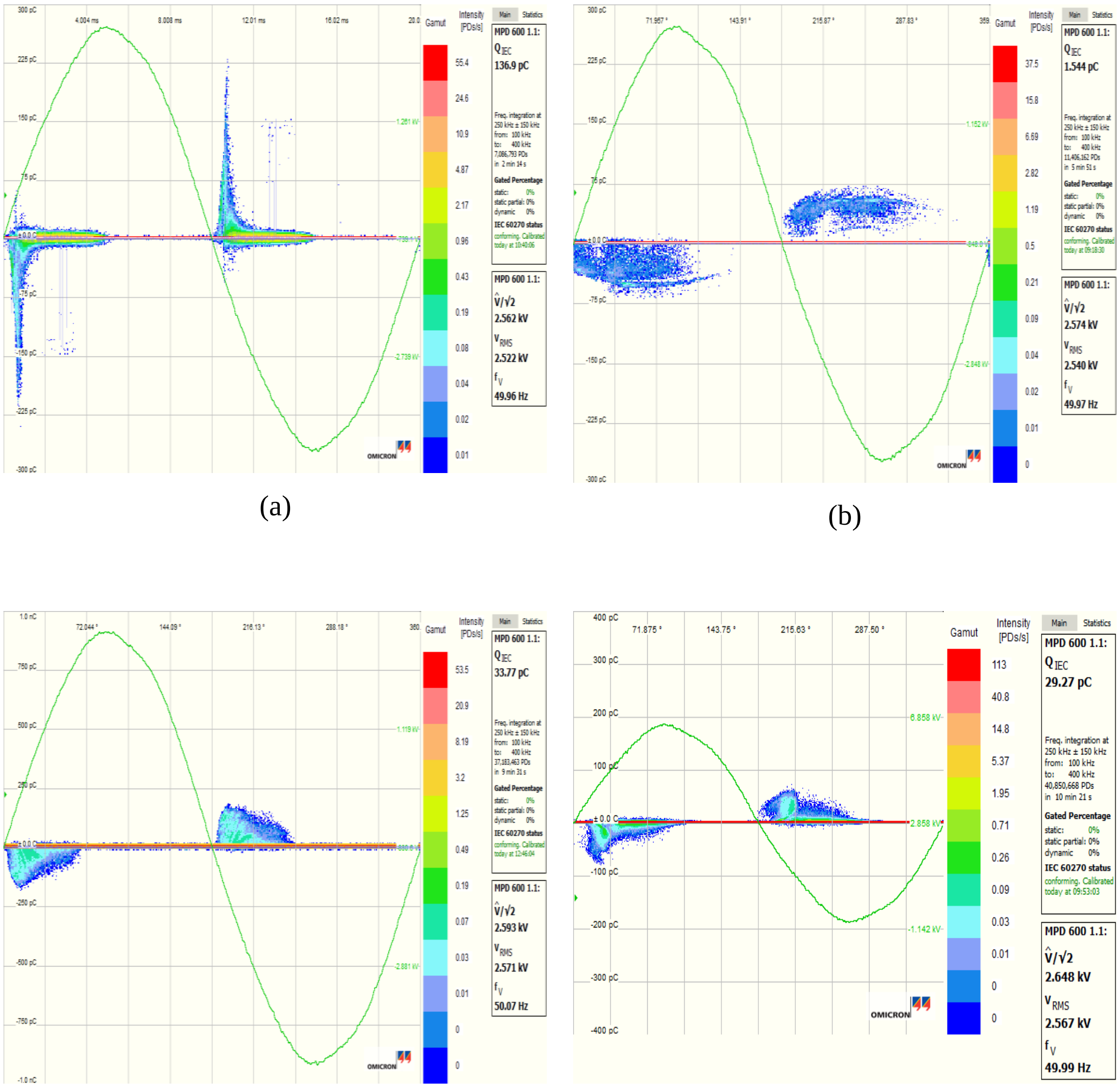

(a)

(b)

(c)

(d)

Figure B.5: Variation in measured PRPD patterns of the LDPE sample (II) containing a flat-shaped cavity of diameter 2 mm at various ageing times: (a) a rabbit-like pattern at ageing 10 min, (b) a turtle-like pattern at ageing 96 h, (c) a rabbit-like pattern at ageing 206 h and (d) a turtle-like pattern at ageing 1004 h.

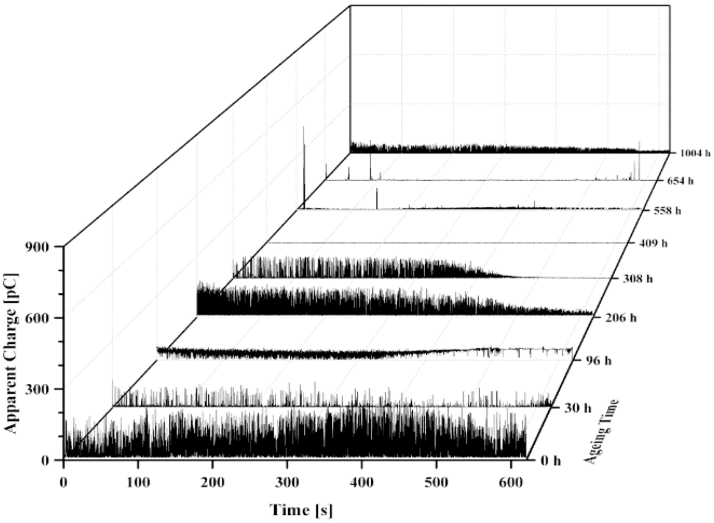

(a)

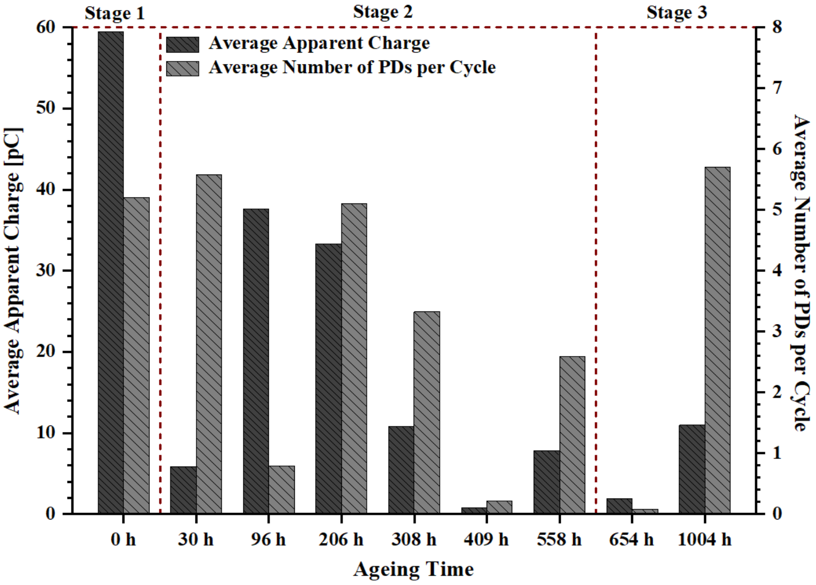

(b)

Figure B.6: PD data of the LDPE sample (II) containing a flat-shaped cavity of diameter 2 mm as a function of various ageing times: (a) the scatter distribution of apparent charge and (b) the bar chart between average apparent charge and average number of PDs per cycle.

B.1.5 Optical microscopy: the LDPE sample (III)

In the sample (III), a virgin cavity was observed before measuring PD as shown in Figure B.7 (a). Visible evidence of deposited by-products was formed on the inner cavity at ageing 308 h as shown in Figure B.7 (b) and the progressive erosion of corrosive by-products was then observed within the cavity after further ageing 654 h and 1004 h as shown in Figures B.7 (c) and B.7 (d) respectively.

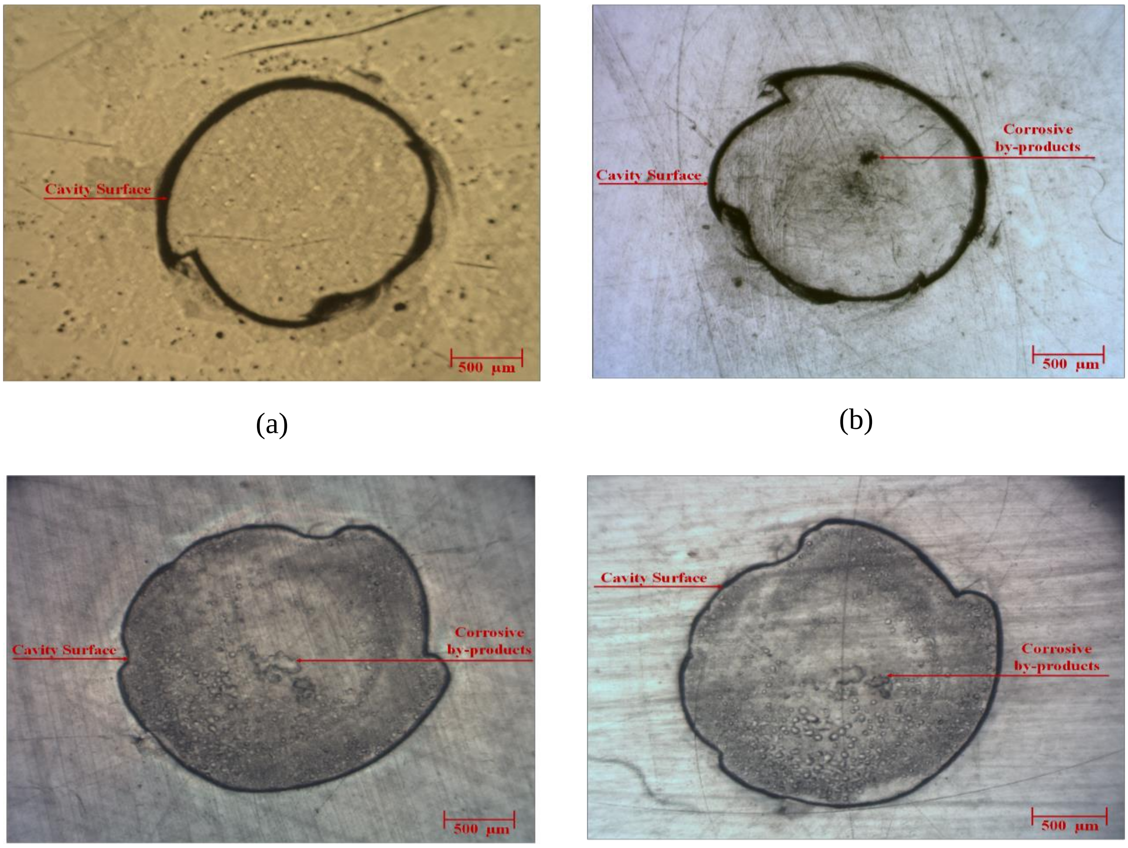

(a) (b)

(c) (d)

Figure B.7: Morphological changes of the LDPE sample (III) containing a flat-shaped cavity of diameter 2 mm at various ageing times: top-section views of (a) a virgin cavity, (b) 308 h, (c) 654 h and (d) 1004 h.

B.1.6 Measurement of PD activity: the LDPE sample (III)

The characteristic PRPD pattern exhibited the rabbit-like shape with a long ear at the initial ageing as shown in Figure B.8 (a). This pattern remained unchanged with a shorter ear at ageing 558 h and 654 h as shown in Figures B.8 (c) and B.8 (c) respectively and subsequently exhibited the rabbit-like pattern with longer ears after further ageing of just over 1000 h as shown in Figure B.8 (d). Otherwise, the scatter distribution of apparent charge as a function of various ageing times showed high magnitude discharges at the initial ageing and followed by minimum magnitude discharges from ageing 30 h to ageing 654 h. Subsequently, the distribution of apparent charge was detected with large discharges after ageing of just over 1000 h as shown in Figure B.9 (a). The bar chart between average apparent charge and average number of PDs per cycle can be divided into three main stages at various ageing times as shown in Figure B.9 (b). The result shows that the average apparent charge was obtained just over 40 pC at the initial ageing and followed by a steep drop about 60% during the second stage of ageing while this figure dramatically increased about 70% during the third stage of ageing. In the average number of PDs per cycle, the trend of this quantity was obtained just over 5 at the initial ageing and then tended to decrease about 60% during the second stage of ageing while this amount tended to increase about 40% during the third stage of ageing.

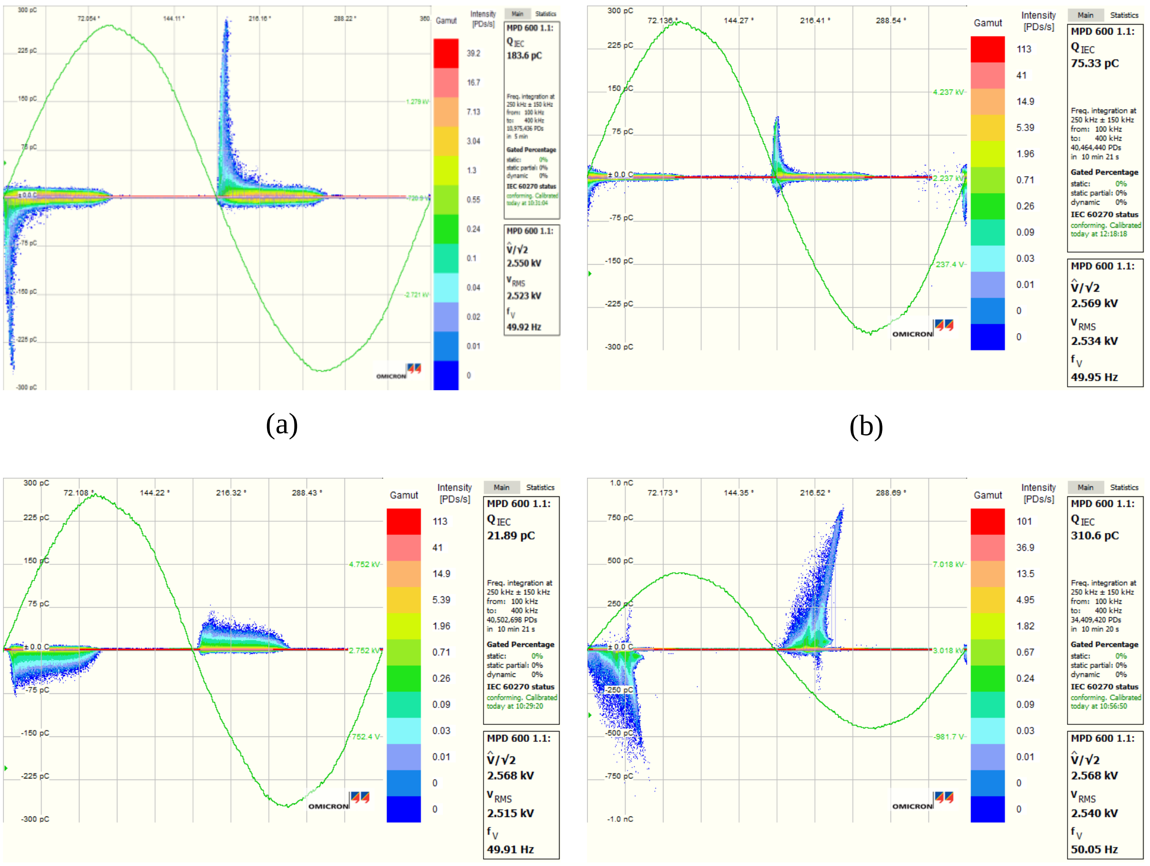

(a)

(b)

(c)

(d)

Figure B.8: Variation in measured PRPD patterns of the LDPE sample (III) containing a flat-shaped cavity of diameter 2 mm at various ageing times: (a) a rabbit-like pattern at ageing 10 min, (b) a rabbit-like pattern at ageing 558 h, (c) a rabbit-like pattern at ageing 654 h and (d) a rabbit-like pattern at ageing 1004 h.

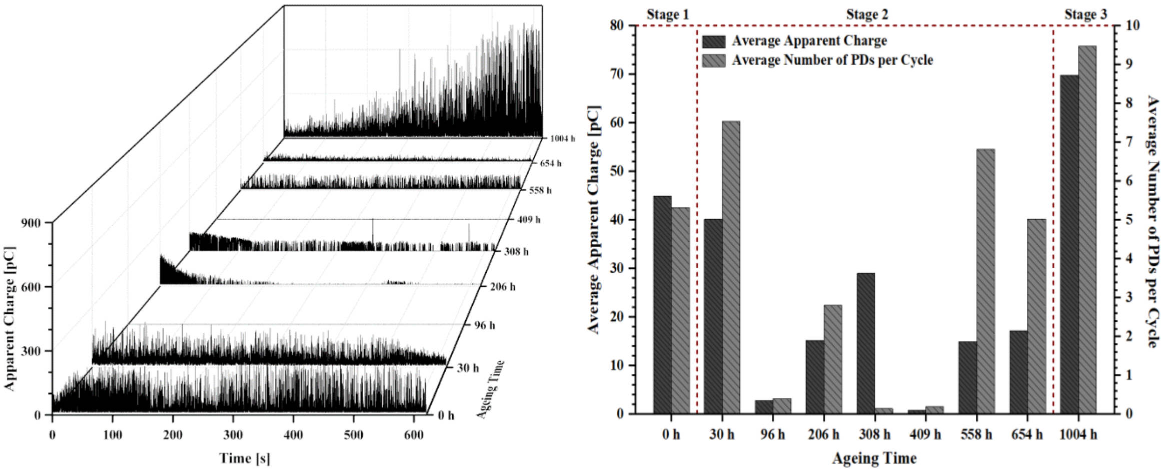

(a)

(b)

Figure B.9: PD data of the LDPE sample (III) containing a flat-shaped cavity of diameter 2 mm as a function of various ageing times: (a) the scatter distribution of apparent charge and (b) the bar chart between average apparent charge and average number of PDs per cycle.

B.2 PD characteristics before an upcoming failure of a cavity

An investigation into the morphological change in an air-filled cavity was experimentally undertaken to reveal PD behaviour related to the mechanism of progressive deterioration in the cavity from localised erosion to upcoming failure due to a long-term period of electrical ageing.

B.2.1 Optical microscopy: the LDPE sample (IV)

In the sample (IV), the morphology of a virgin cavity was observed before measuring PD as shown in Figure B.10 (a). Subsequently, visible evidence of the deposited by-products was observed on the cavity surface during further ageing from 1004 h to 1443 h as shown in Figures B.10 (b) and B.10 (c). After ageing of just over 1821 h, complete failure of the test sample was then noticed with silicone oil within the cavity as shown in Figure B.10 (d).

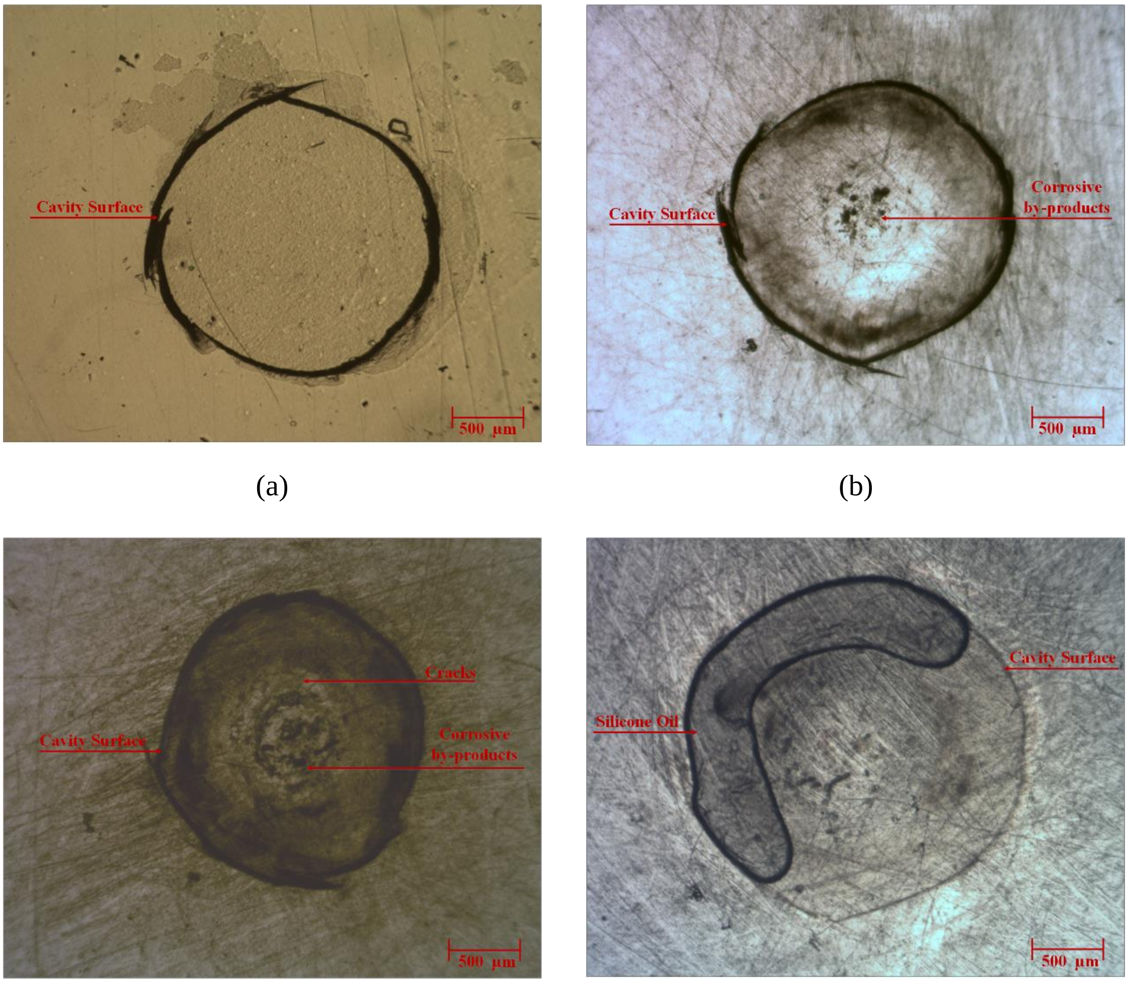

(a) (b)

(c) (d)

Figure B.10: Morphological changes of the LDPE sample (IV) containing a flat-shaped cavity of diameter 2 mm at various ageing times: top-section views of (a) a virgin cavity, (b) 1004 h, (c) 1443 h and (d) 1821 h.

B.2.2 Measurement of PD activity: the LDPE sample (IV)

The characteristic PRPD pattern linked to the rabbit-like shape at the initial ageing as shown in Figure B.11 (a). This pattern still exhibited the rabbit-like shape with high magnitudes of a longer ear after further ageing 206 h and 1443 h as shown in Figures B.11 (b) and B.11 (c) respectively. Subsequently, the transition of PRPD pattern changed to SPMDs, which occurred slight magnitude discharges both positive and negative half-cycles at ageing 1821 h as shown in Figure B.11 (d).

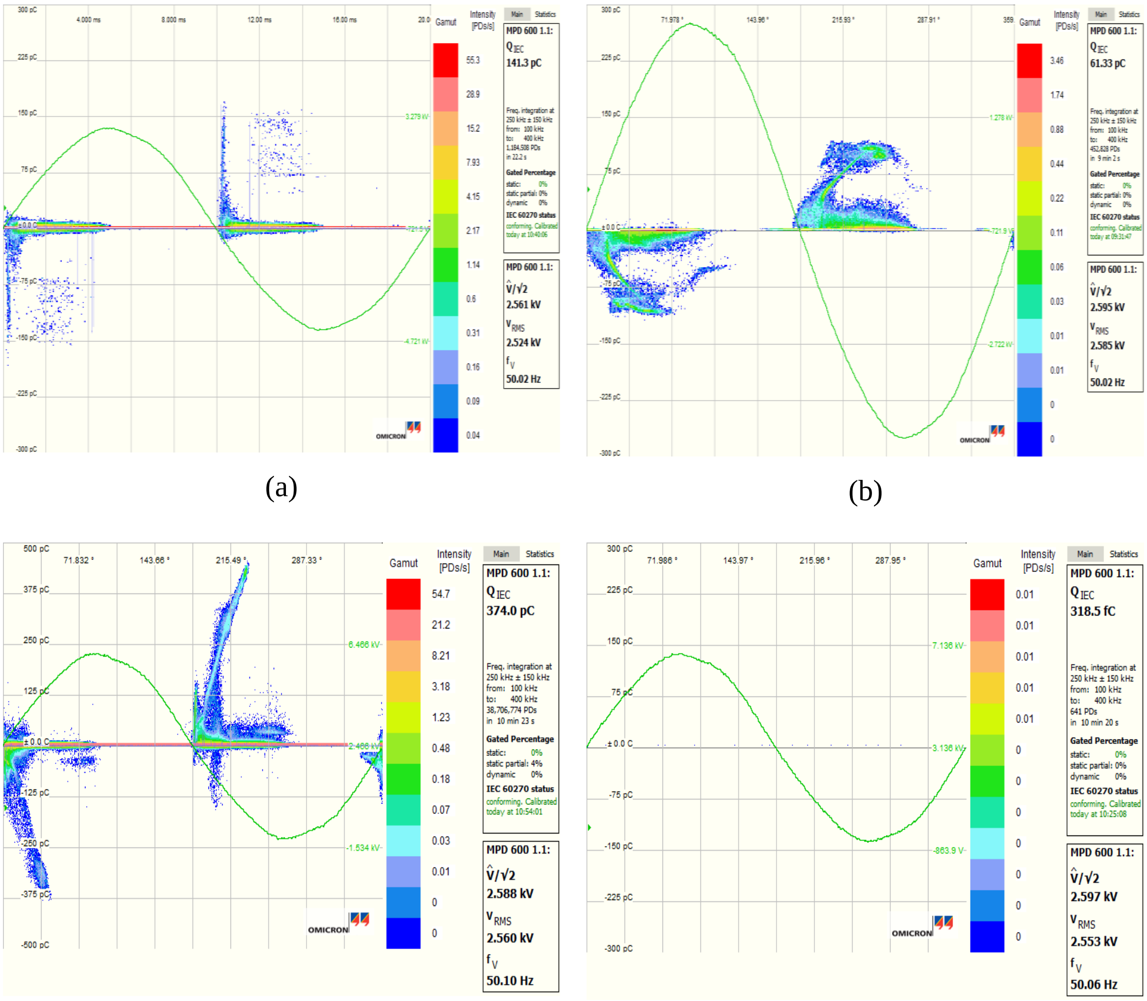

(a) (b)

(c) (d)

Figure B.11: Variation in measured PRPD patterns of the LDPE sample (IV) containing a flat-shaped cavity of diameter 2 mm at various ageing times: (a) a rabbit-like pattern at ageing 10 min, (b) a rabbit-like pattern at ageing 206 h, (c) a rabbit-like pattern at ageing 1443 h and (d) SPMDs at ageing 1821 h.

Otherwise, the scatter distribution of apparent charge as a function of various ageing times showed high magnitude discharges at the initial ageing and followed by minimum magnitude discharges during further ageing of just under 600 h. Subsequently, the distribution of apparent charge was detected with a slight increase of discharge magnitudes from ageing 654 h to ageing 1443 h and followed by minimum discharges after ageing 1821 h as shown in Figure B.12 (a). The bar chart between average apparent charge and average number of PDs per cycle can be divided into four main stages at various ageing times as shown in Figure B.12 (b). The result shows that the average apparent charge was obtained just over 34 pC at the initial ageing and followed by a steep drop about 80% during the second stage of ageing while this figure dramatically increased about 75% during the third stage of ageing and subsequently obtained by minimum magnitude discharges with less than 1 pC at the fourth stage of ageing. In the average number of PDs per cycle, the trend of this quantity was obtained just over 11 at the initial ageing and then tended to decrease about 80% during the second stage of ageing while this amount tended to increase by 90% during the third stage of ageing and followed by undetectable PD events after a prolonged period of ageing for 1821 h.

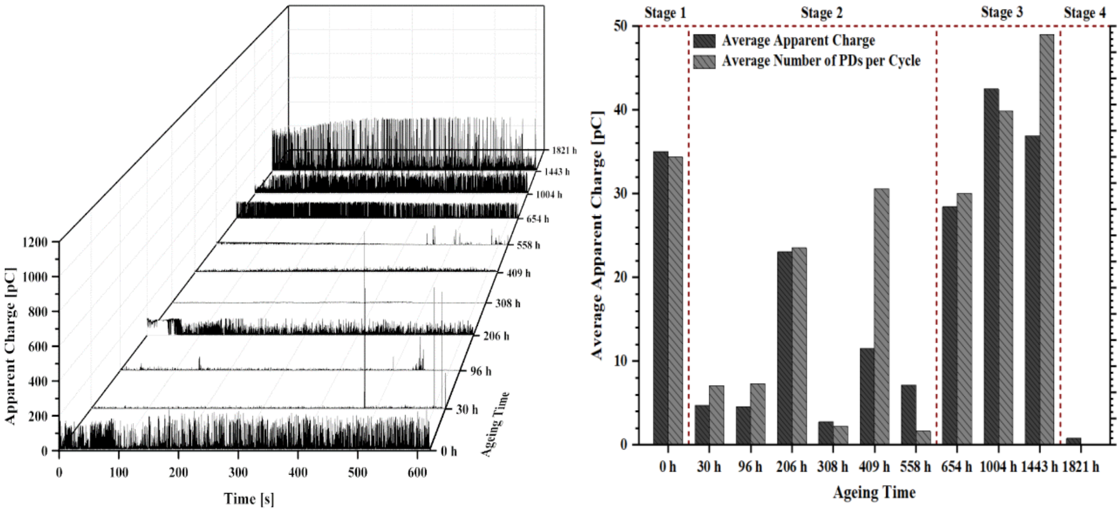

(a) (b)

Figure B.12: PD data of the LDPE sample (IV) containing a flat-shaped cavity of diameter 2 mm as a function of various ageing times: (a) the scatter distribution of apparent charge and (b) the bar chart between average apparent charge and average number of PDs per cycle.

B.2.3 Optical microscopy: the LDPE sample (V)

In the sample (V), a virgin cavity was observed before measuring PD as shown in Figure B.13 (a). Visible evidence of deposited by-products noticed on the cavity surface after further ageing 1004 h and 1443 h as shown in Figures B.13 (b) and B.13 (c) respectively and total failure of the test sample was then observed with silicone oil inside the centre cavity after ageing of just over 1821 h as shown in Figure B.13 (d).

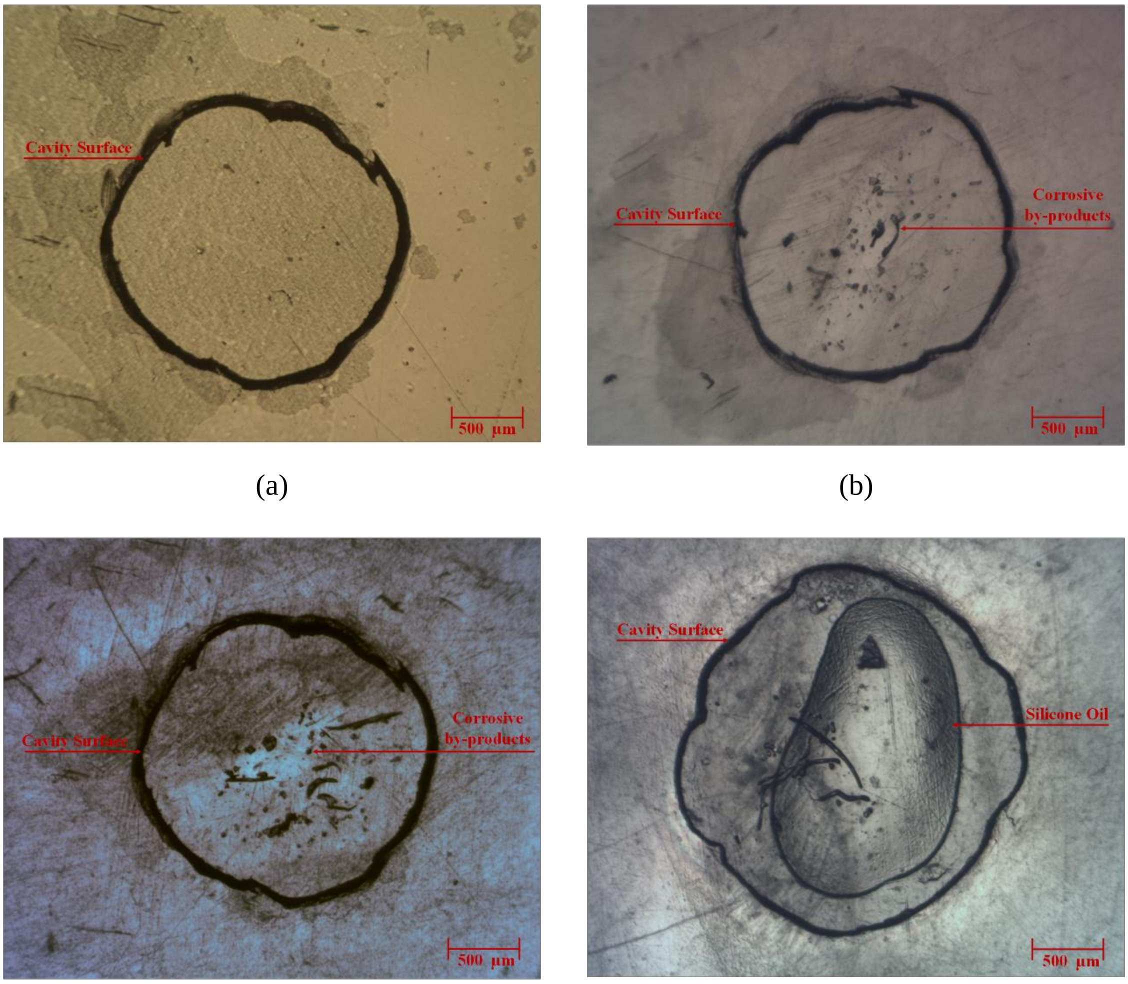

(a) (b)

(c) (d)

Figure B.13: Morphological changes of the LDPE sample (V) containing a flat-shaped cavity of diameter 2 mm at various ageing times: top-section views of (a) a virgin cavity, (b) 1004 h, (c) 1443 h and (d) 1821 h.

B.2.4 Measurement of PD activity: the LDPE sample (V)

The characteristic PRPD pattern exhibited the rabbit-like shape at the initial ageing as shown in Figure B.14 (a). The transition of this pattern turned to the turtle-like pattern with small magnitude discharges at ageing 558 h and this pattern remained unchanged with large magnitude discharges at ageing 1443 h as shown in Figures B.14 (b) and B.14 (c). Subsequently, the characteristic SPMDs appeared with slight magnitude discharges both positive and negative half-cycles at ageing 1821 h as shown in Figure B.14 (d). Otherwise, the scatter distribution of apparent charge as a function of various ageing times showed slight magnitude discharges after ageing of just under 150 h before the distribution of this apparent charge turned to minimum magnitude discharges after further ageing 1821 h as shown in Figure B.15 (a). The bar chart between average apparent charge and average number of PDs per cycle can be divided into four main stages at various ageing times as shown in Figure B.15 (b), which the average apparent charge was obtained just under 18 pC at the initial ageing. The trend of this amount tended to gradually increase at the second stage of ageing and followed by a slight rise of just over 20 pC during the third stage of ageing before this quantity steeply dropped with less than 1 pC during the fourth stage of ageing.

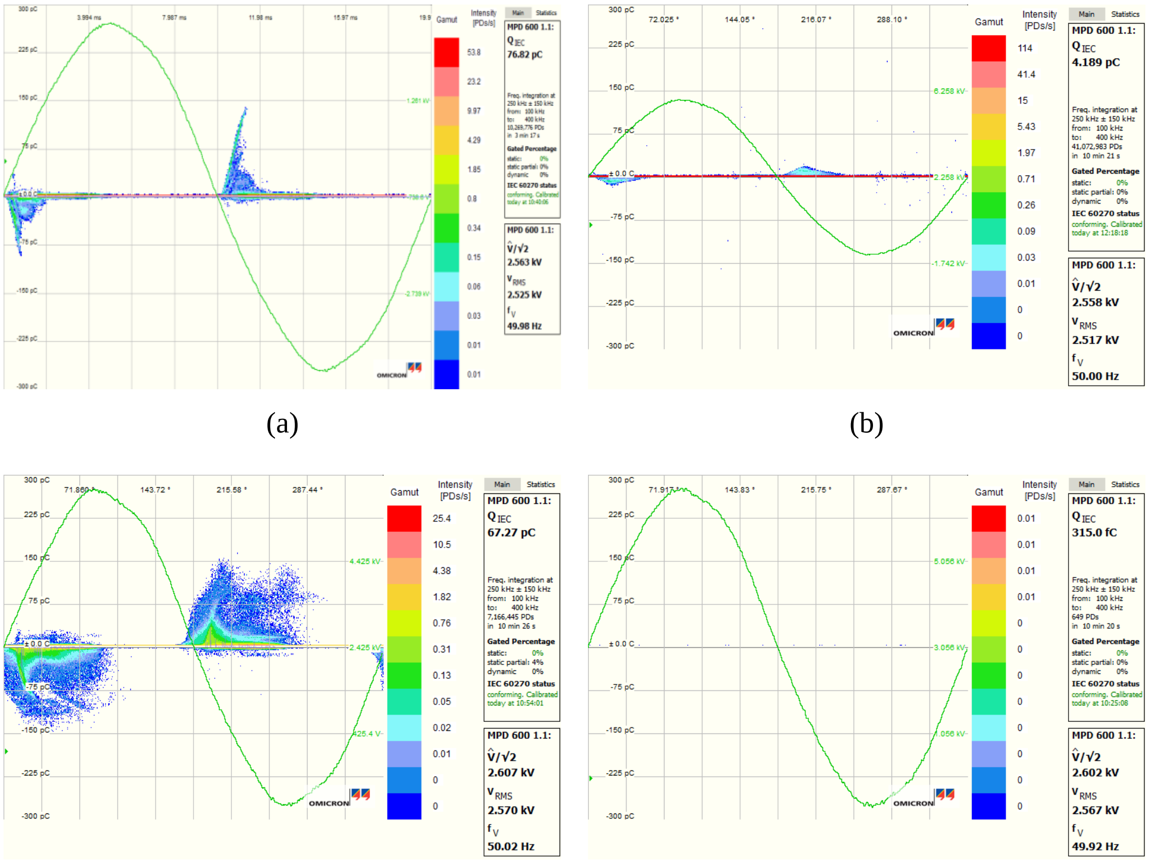

MPD 600 1.1:
Q IEC
76.82 pC
MPD 600 1.1:
V̂/√2
2.563 kV
V RMS
2.525 kV
f V
49.98 Hz

MPD 600 1.1:
Q IEC
4.189 pC
Freq. integration at 250 kHz ± 150 kHz
from: 100 kHz
to: 400 kHz
41,072,983 PDs
in 10 min 21 s
MPD 600 1.1:
V̂/√2
2.558 kV
V RMS
2.517 kV
f V
50.00 Hz

MPD 600 1.1:
Q IEC
67.27 pC
Freq. integration at 250 kHz ± 150 kHz
from: 100 kHz
to: 400 kHz
7,166,445 PDs
in 10 min 26 s
MPD 600 1.1:
V̂/√2
2.607 kV
V RMS
2.570 kV
f V
50.02 Hz

MPD 600 1.1:
Q IEC
315.0 fC
Freq. integration at 250 kHz ± 150 kHz
from: 100 kHz
to: 400 kHz
649 PDs
in 10 min 20 s
MPD 600 1.1:
V̂/√2
2.602 kV
V RMS
2.567 kV
f V
49.92 Hz

(a) (b)

(c) (d)

Figure B.14: Variation in measured PRPD patterns of the LDPE sample (V) containing a flat-shaped cavity of diameter 2 mm at various ageing times: (a) a rabbit-like pattern at ageing 10 min, (b) a turtle-like pattern at ageing 558 h, (c) a turtle-like pattern at ageing 1443 h and (d) SPMDs at ageing 1821 h.

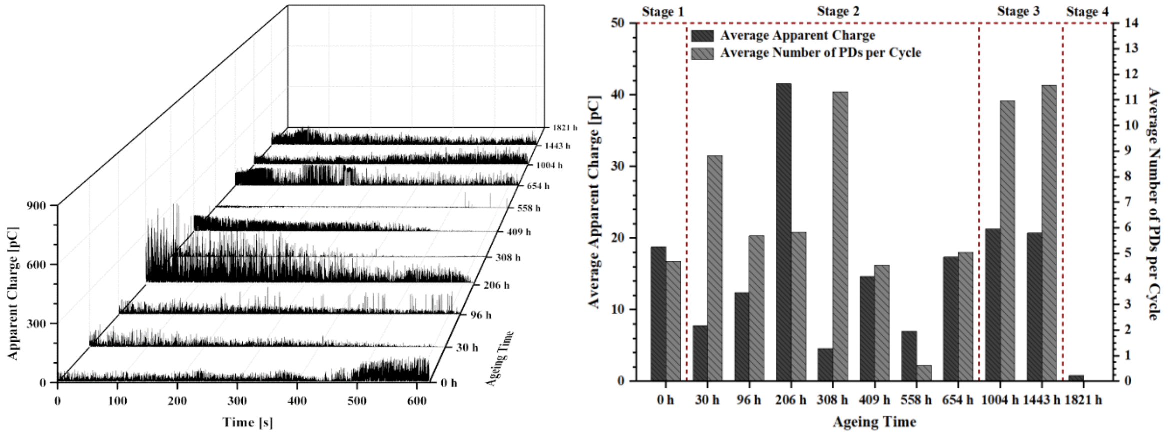

(a) (b)

Figure B.15: PD data of the LDPE sample (V) containing a flat-shaped cavity of diameter 2 mm as a function of various ageing times: (a) the scatter distribution of apparent charge and (b) the bar chart between average apparent charge and average number of PDs per cycle.

B.2.5 Optical microscopy: the LDPE sample (VI)

In the sample (VI), a virgin cavity was observed before measuring PD as shown in Figure B.16 (a). Visible evidence of deposited by-products was noticed on the centre cavity surface after further ageing 1004 h and 1443 h as shown in Figures B.16 (b) and B.16 (c) respectively and complete failure of the test sample was then observed with silicone oil within the cavity after ageing of just over 1821 h as shown in Figure B.16 (d).

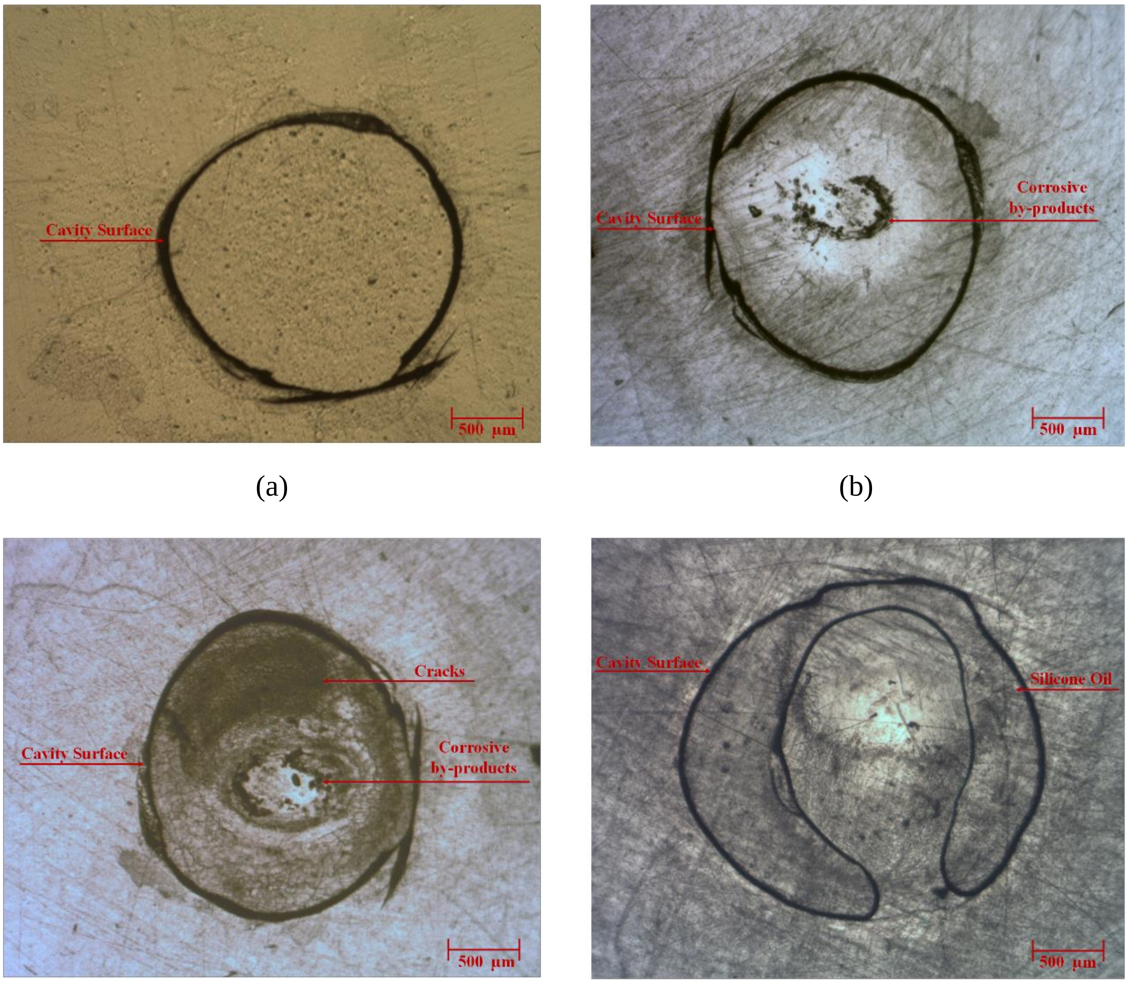

(a) (b)

(c) (d)

Figure B.16: Morphological changes of the LDPE sample (VI) containing a flat-shaped cavity of diameter 2 mm at various ageing times: top-section views of (a) a virgin cavity, (b) 1004 h, (c) 1443 h and (d) 1821 h.

B.2.6 Measurement of PD activity: the LDPE sample (VI)

The characteristic PRPD pattern linked to the rabbit-like shape at the initial ageing as shown in Figure B.17 (a). The shaped pattern still exhibited the rabbit-like shape with large magnitude discharges of a longer ear after further ageing 654 h and 1443 h as shown in Figures B.17 (b) and B.17 (c) respectively. Subsequently, the transition of PRPD patterns changed to SPMDs, which obtained slight magnitude discharges both positive and negative half-cycles at ageing 1821 h as shown in Figure B.17 (d). Otherwise, the scatter distribution of apparent charge as a function of various ageing times showed slight magnitude discharges during ageing of just under 1000 h. Subsequently, the charges showed large magnitude discharges and followed by minimum magnitude discharges after further ageing 1443 h and 1821 h respectively as shown in Figures B.18 (a). The bar chart between average apparent charge and average number of PDs per cycle can be divided into four main stages at various ageing times as shown in Figure B.18 (b). The result shows that the average apparent charge was obtained just under 22 pC at the initial ageing. The trend of this amount tended to gradually decrease during the second stage of ageing and followed by a steep rise of just over 50 pC at ageing 1443 h before this amount steeply dropped with less than 1 pC during the fourth stage of ageing.

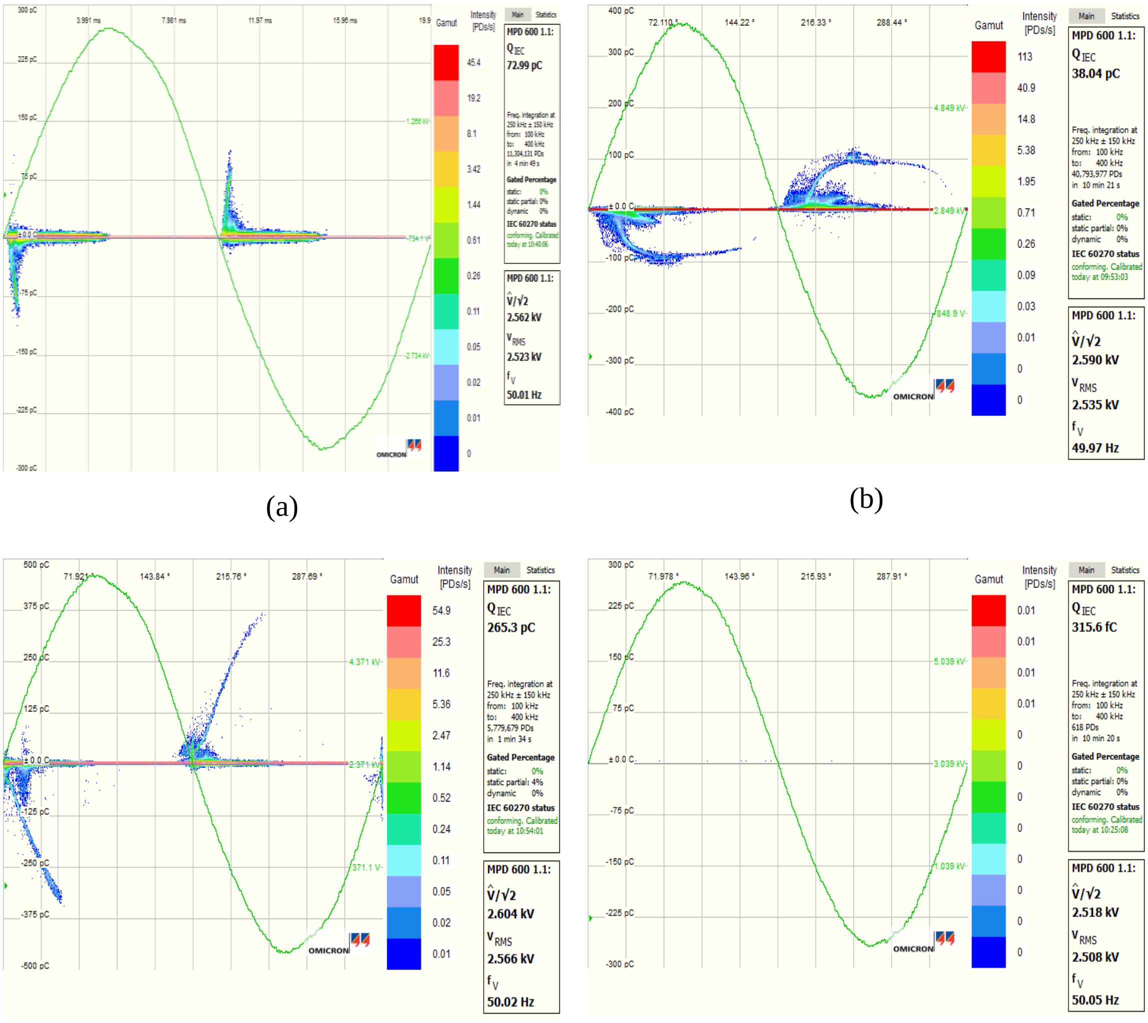

(a) (b)

(c) (d)

Figure B.17: Variation in measured PRPD patterns of the LDPE sample (VI) containing a flat-shaped cavity of diameter 2 mm at various ageing times: (a) a rabbit-like pattern at 10 min, (b) a rabbit-like pattern at ageing 654 h, (c) a rabbit-like pattern at ageing 1443 h and (d) SPMDs at ageing 1821 h.

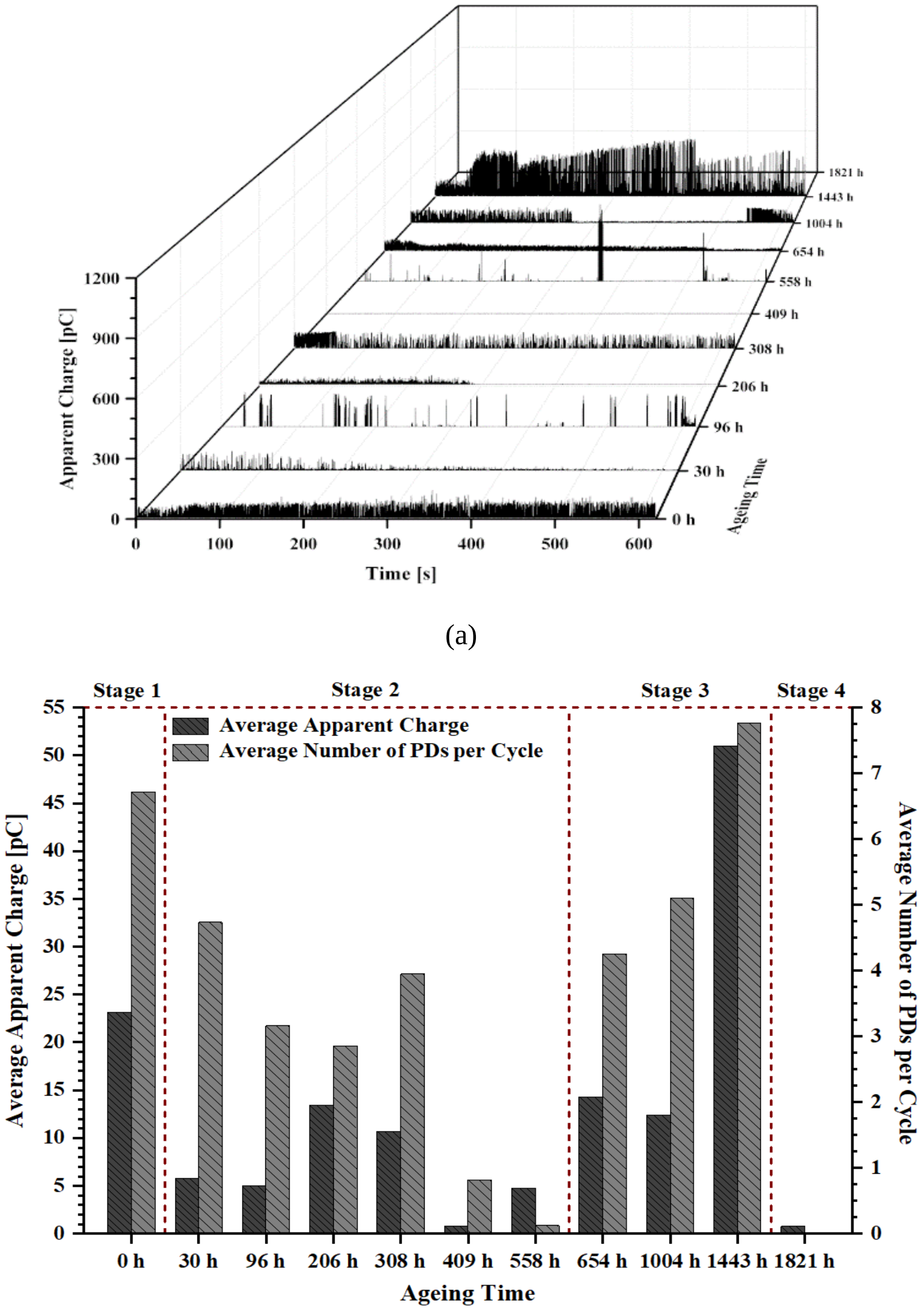

(a)

(b)

Figure B.18: PD data of the LDPE sample (VI) containing a flat-shaped cavity of diameter 2 mm as a function of various ageing times: (a) the scatter distribution of apparent charge and (b) the bar chart between average apparent charge and average number of PDs per cycle.

B.2.7 Optical microscopy: the sample (VII)

In the sample (VII), a virgin cavity was observed before measuring PD as shown in Figure B.19 (a). Noticeable evidence of deposited by-products was observed on the centre cavity surface after further ageing 1004 h and 1443 h as shown in Figures B.19 (b) and B.19 (c) respectively and complete failure of the test sample was then noticed with silicone oil inside the centre cavity after ageing of just over 1821 h as shown in Figure B.19 (d).

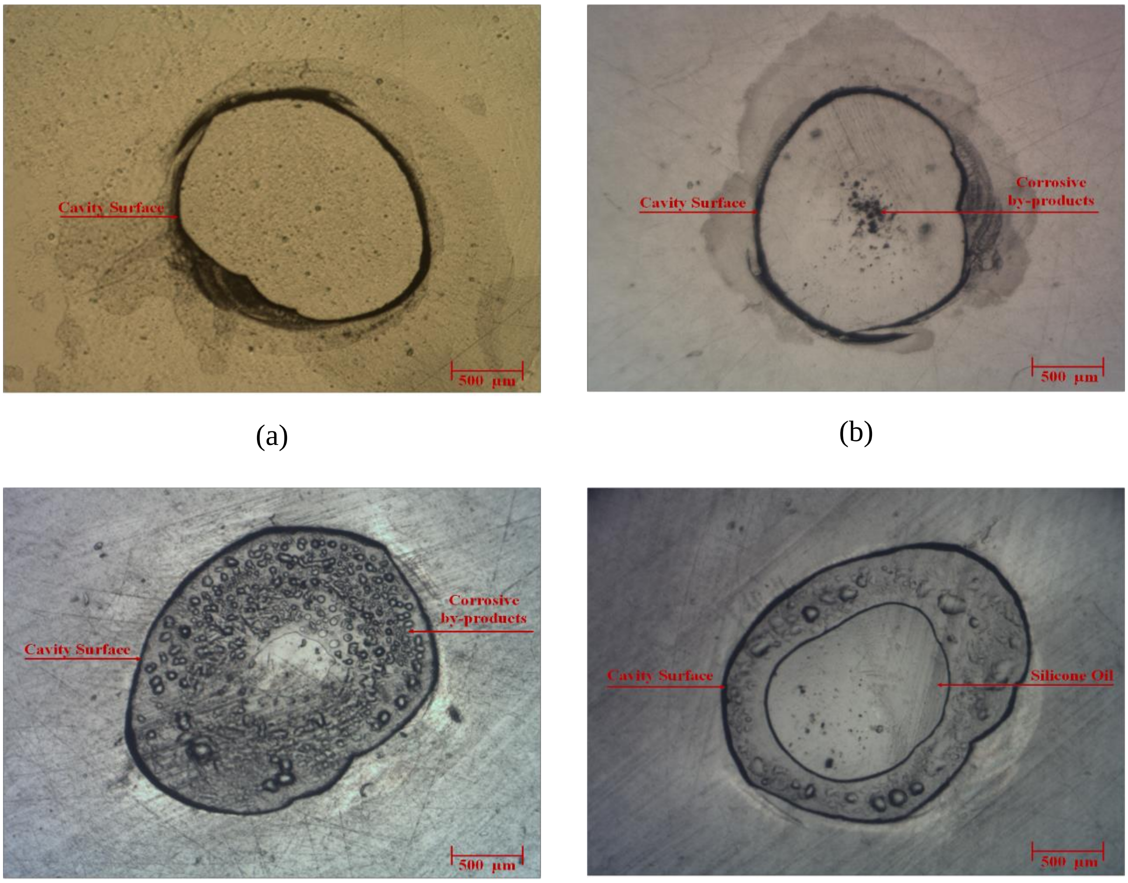

(a) (b)

(c) (d)

Figure B.19: Morphological changes of the LDPE sample (VII) containing a flat-shaped cavity of diameter 2 mm at various ageing times: top-section views of (a) a virgin cavity, (b) 1004 h, (c) 1443 h and (d) 1821 h.

B.2.8 Measurement of PD activity: the LDPE sample (VII)

The characteristic PRPD pattern exhibited the rabbit-like shape at the initial ageing as shown in Figure B.20 (a). The transition of this pattern turned to the turtle-like pattern with small magnitude discharges at ageing 1004 h and this pattern remained unchanged with large magnitude discharges at ageing 1443 h as shown in Figures B.20 (b) and B.20 (c) respectively. Subsequently, the mechanism of SPMDs occurred slight magnitude discharges both positive and negative half-cycles at ageing 1821 h as shown in Figure B.20 (d). The scatter distribution of apparent charge as a function of various ageing times showed slight magnitude discharges after ageing of just under 1005 h. This trend subsequently obtained large magnitude discharges and followed by a steep drop with minimum discharges after ageing 1443 h and 1821 h respectively as shown in Figures B.21 (a). The bar chart between average apparent charge and average number of PDs per cycle can be divided into four main stages at various ageing times as shown in Figure B.21 (b). The result shows that the average apparent charge was obtained just under 25 pC after ageing of just under 1005 h. The trend of this amount dramatically increased after further ageing 1443 h and followed by a steep drop with less than 1 pC during the fourth stage of ageing.

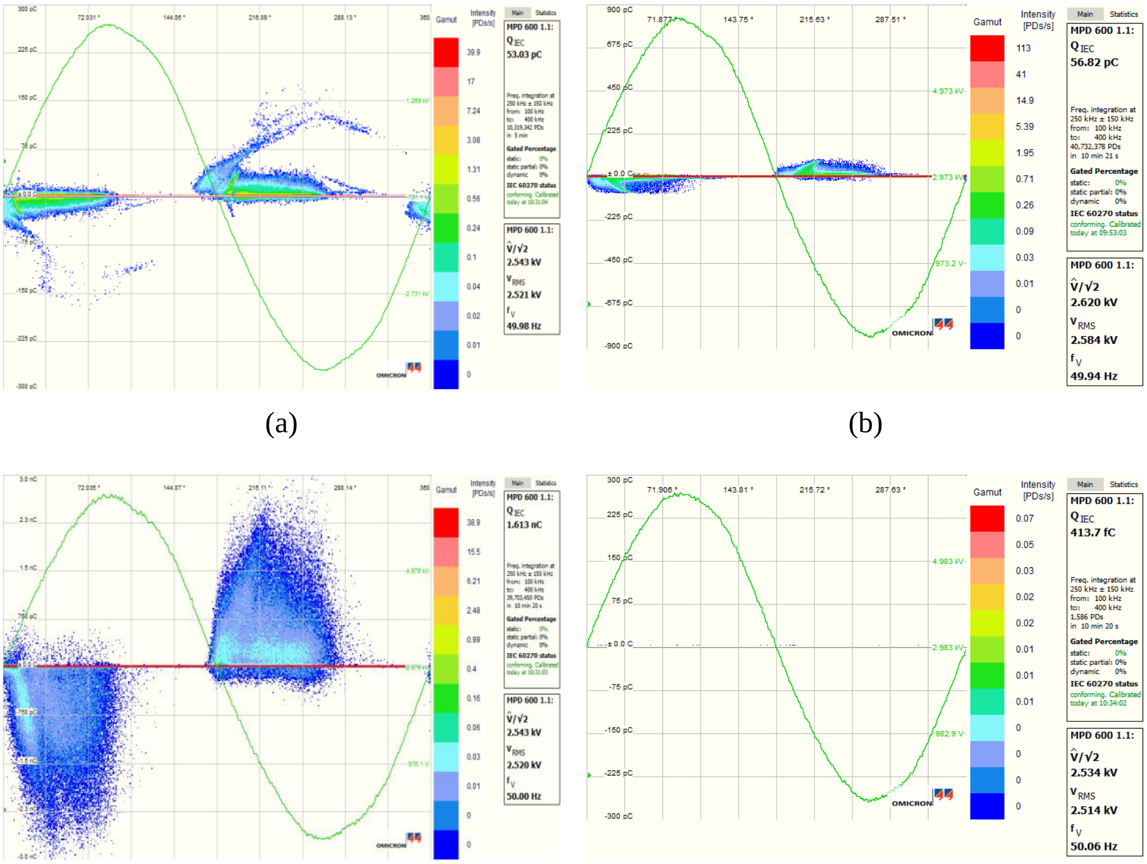

(a) (b)

(c) (d)

Figure B.20: Variation in measured PRPD patterns of the LDPE sample (VII) containing a flat-shaped cavity of diameter 2 mm at various ageing times: (a) a rabbit-like pattern at ageing 10 min, (b) a turtle-like pattern at ageing 1004 h, (c) a turtle-like pattern at ageing 1443 h and (d) SPMDs at ageing 1821 h.

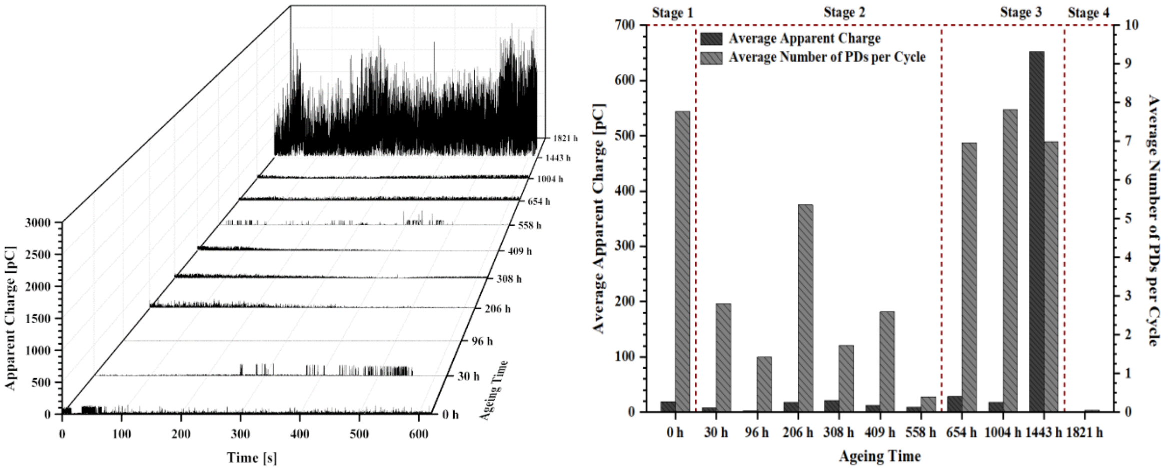

(a) (b)

Figure B.21: PD data of the LDPE sample (VII) containing a flat-shaped cavity of diameter 2 mm as a function of various ageing times: (a) the scatter distribution of apparent charge and (b) the bar chart between average apparent charge and average number of PDs per cycle.

Appendix C Modelling of Physical Cavities

The physical model of a cavity embedded in dielectric material can be simulated to determine electric field magnitudes based on the experiment results in a two-dimensional geometry of the Finite Element Analysis (FEA) by solving the electrostatic equation in Comsol. The models used for this session can be divided into two different cavity shapes embedded in solid dielectric material in terms of a flat-shaped cavity and a spherical-shaped cavity in Sessions C.1 and C.2 respectively. Furthermore, the calculation of inception electric field in a cavity from a flat-shaped cavity and a spherical-shaped cavity can be determined by the physical conditions of the test sample in Session C.3. Moreover, the model of a spherical cavity embedded in solid insulation can be simulated to find out the value of approximate apparent charge by PD activity, where the charge is transferred from the outer cavity wall across parallel plate electrodes in Session C.4. Finally, the model of electrical tree initiation from the wall of a spherical cavity is developed to determine electric field magnitudes based on the physical parameters of the experiment result in Session C.5.

C.1 Modelling of a flat-shaped cavity in solid material

The model of two-dimensional axes of a flat-shaped cavity in polyethylene material was simulated to find out electric field magnitudes and electric equipotential lines at the PDIV level as shown in Figure C.1 (a), where the plots of electric field distributions in the cross-section views along the z-axis and r-axis as shown in Figures C.1 (b) and C.1 (c) respectively. The physical parameters used in this model are listed in Table C.1.

Table C.1: Physical parameters used in the model of a flat-shaped cavity embedded in polyethylene dielectric material.

Definition	Parameter	Value
Applied inception voltage amplitude	U_{inc}	1.5 kV_{rms}
Cavity diameter	d_c	2.0 mm
Cavity height	d_h	0.1 mm
Dielectric material in thickness	d_m	0.3 mm
Relative permittivity in a cavity	ε_c	1.0
Relative permittivity of polyethylene material at 50 Hz	ε_{PE}	2.53

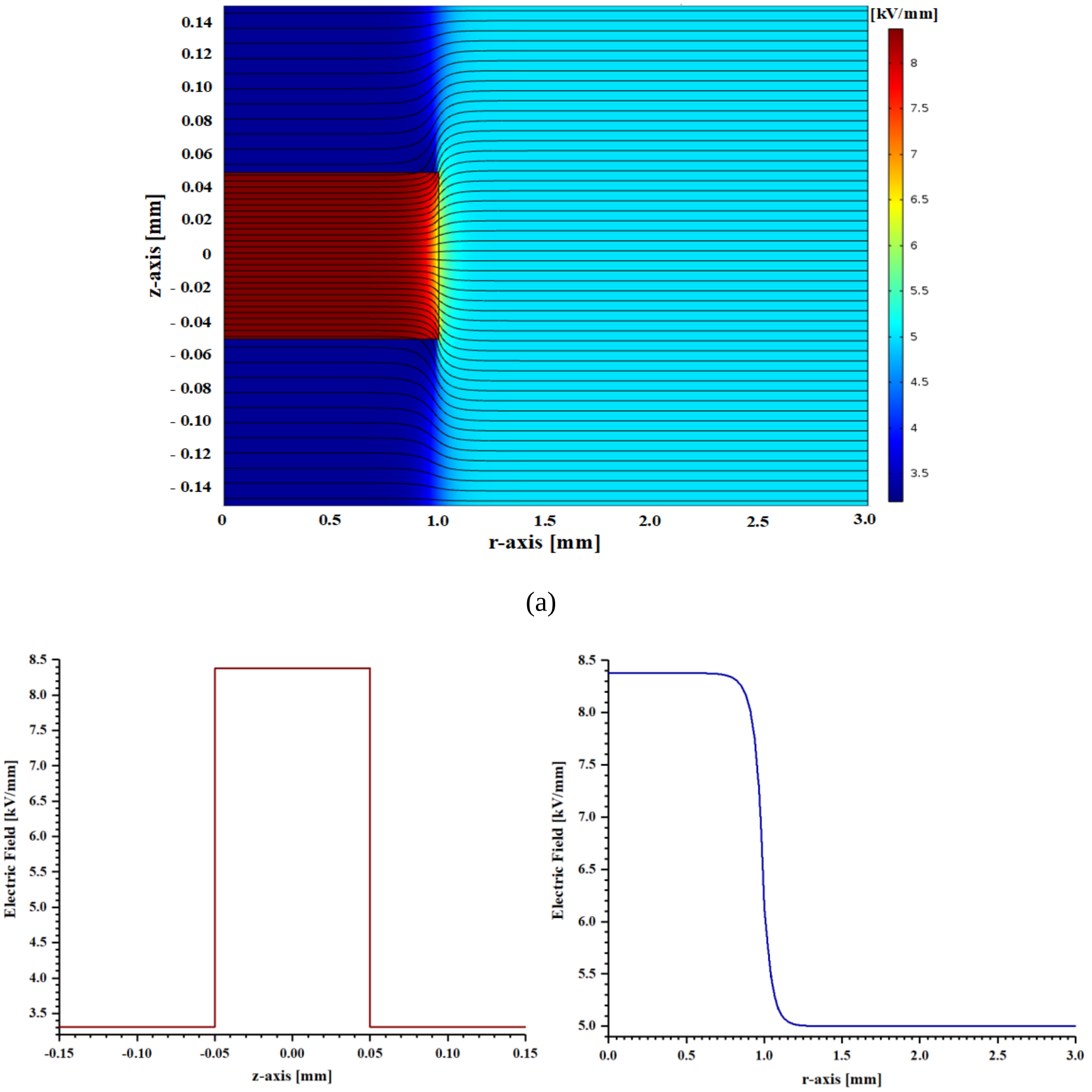

(a)

(b)

(c)

Figure C.1: Simulation of a flat-shaped cavity in solid material at the PDIV level: (a) model of the symmetric axis in the FEA, (b) and (c) plotting electric field magnitudes in cross-section views along the z-axis and the r-axis respectively.

C.2 Modelling of a spherical-shaped cavity in solid material

The model of two-dimensional axes of a spherical-shaped cavity embedded in silicone dielectric material was simulated to find out electric field magnitudes and electric equipotential lines at the PDIV level as shown in Figure C.2 (a), where the plots of electric field distributions in the cross-section views along the z-axis and the r-axis as shown in Figures C.2 (b) and C.2 (c) respectively. The physical parameters used in this model are listed in Table C.2.

Table C.2: Physical parameters used in the model of a spherical-shaped cavity embedded in silicone dielectric material.

Definition	Parameter	Value
Applied inception voltage amplitude	U_{inc}	$10.76\ kV_{rms}$
Cavity diameter	d_c	1.98 mm
Dielectric material in thickness	d_m	3.0 mm
Relative permittivity in a cavity	ε_c	1.0
Relative permittivity of silicone material at 50 Hz	ε_{Si}	2.8

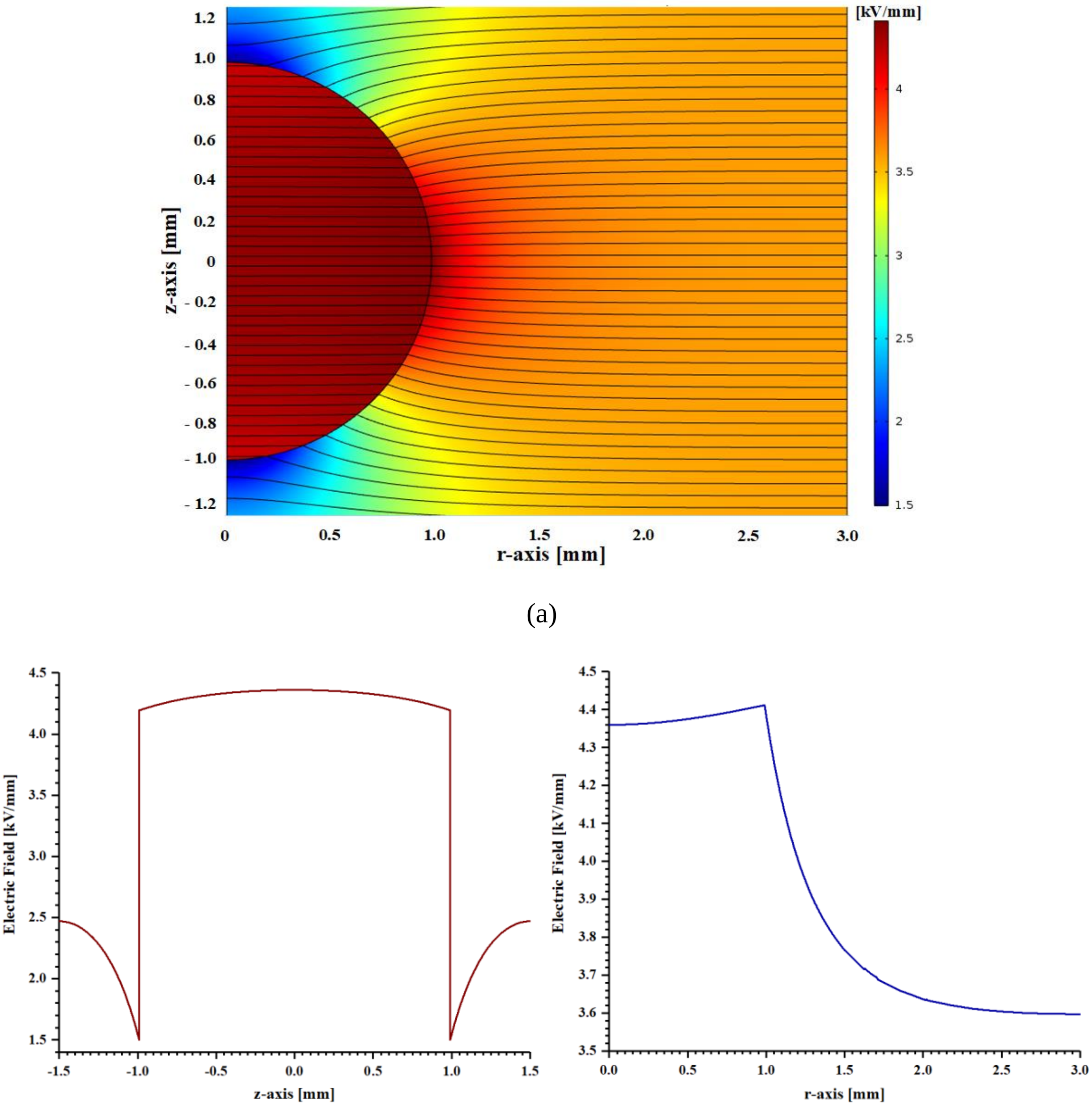

(a)

(b)

(c)

Figure C.2: Simulation of a spherical-shaped cavity in solid material at the PDIV level: (a) model of the symmetric axis in the FEA, (b) and (c) plotting electric field magnitudes in cross-section views along the z-axis and the r-axis respectively.

C.3 Theoretical calculation of inception electric field inside a cavity

The calculation of inception electric field inside a cavity can be approximately determine by the value range between gas pressure and cavity thickness based on the experimental conditions of the test sample, which this amount can be found the constant parameters in terms of A′, B′, and C′ in Table C.3 used for the substitution in Equation B.1. The values of inception electric field magnitude inside a flat-shaped cavity embedded in polyethylene dielectric material and a spherical cavity embedded in silicone dielectric material from the physical parameters of the test samples are given in Tables C.4 and C.5 respectively.

$$\frac{E_{inc}}{P'} = A' + \frac{B'}{(P' \cdot L')^{C}} \tag{B.1}$$

Where E_{inc} is the inception electric field inside a cavity, P′ is the gas pressure inside a cavity, L′ is the cavity thickness, A′, B′, and C′ are the constant parameters in Table C.3. For instance, the cavity thickness, L′ is 1×10^{-4} m and the gas pressure inside a cavity, P′ is 101.32 kPa (1atm). Therefore, the constant parameters for A′, B′, and C′ are 30.25 kV/kPa·m, 3.12 kV and 0.675 respectively.

Table C.3: Constant parameters used for calculation of the inception electric field in a cavity [106].

A′ [kV/kPa·m]	**B′ [kV]**	**C′**	**P′·L′ [kPa·m]**
0	2.789×10^{-10}	3.523	$9\times10^{-5}\leq P\cdot L'\leq 2\times10^{-4}$
329.39	12.077×10^{-6}	2.249	$2.3\times10^{-4}\leq P\cdot L'\leq 8\times10^{-4}$
30.25	3.12	0.675	$9\times10^{-4}\leq P\cdot L'\leq 0.6$
23.24	8.464	0.405	$0.7\leq P\cdot L'\leq 36$

Table C.4: Calculation of the inception electric field inside a flat-shaped cavity embedded in polyethylene dielectric material.

L′ [m]	**P′·L′ [kPa·m]**	**E_{inc}/P′ [kV/kPa·m]**	**E_{inc} [kV/mm]**
1×10^{-4}	101.32×10^{-4}	99.48	10.08

Table C.5: Calculation of the inception electric field inside a spherical-shaped cavity embedded in silicone dielectric material.

L' [m]	$P' \cdot L'$ [kPa·m]	E_{inc}/P' [kV/kPa·m]	E_{inc} [kV/mm]
2×10^{-3}	202.64×10^{-3}	39.41	3.99

C.4 Modelling for an approximate apparent charge of a spherical cavity

The model of PD activity was simulated to determine an approximate apparent charge in a spherical cavity embedded in solid dielectric material, where an amount of induced charge was transferred from the outer cavity wall across parallel plate electrodes. The assumption is that PD activity was governed by electric fields in the centre of a cavity, which was found by solving the electrostatic equation in Comsol. A discharge occurred when the electric field in the centre of a cavity was above the inception value and a free electron was available. Subsequently, Discharges will be deposit bipolar surface charge density distributions on the cavity surface of a spherical cavity such that the field in the centre cavity was reduced to a residual value. The surface charge density at the cavity boundary after a PD event was initially set as reported in the literature [259].

The physical parameters of axisymmetric model consisted of a spherical cavity radius of 0.44 mm embedded in a cylindrical dielectric diameter of 50 mm and 3 mm in thickness. The relative permittivity inside a cavity was 1, the relative permittivity of silicone material at 50 Hz was 2.8 and the inception voltage amplitude was 6.116 kV_{rms}. In the models of Figures C.3 (a) and C.3 (b), the electric field magnitudes in the centre cavity before and after PD events were 2.584 kV/mm and 1.258 kV/mm respectively. The approximate apparent charge was calculated by dividing these filed magnitudes and then multiplying this value by an integrated amount of the surface charge density on the dielectric surface connected with the ground system. Therefore, the simulation of an approximate value for average apparent charge was 23.22 pC while the measurement of average apparent charge was 25.382 pC. This result indicates that there was good agreement between measurement and simulation results.

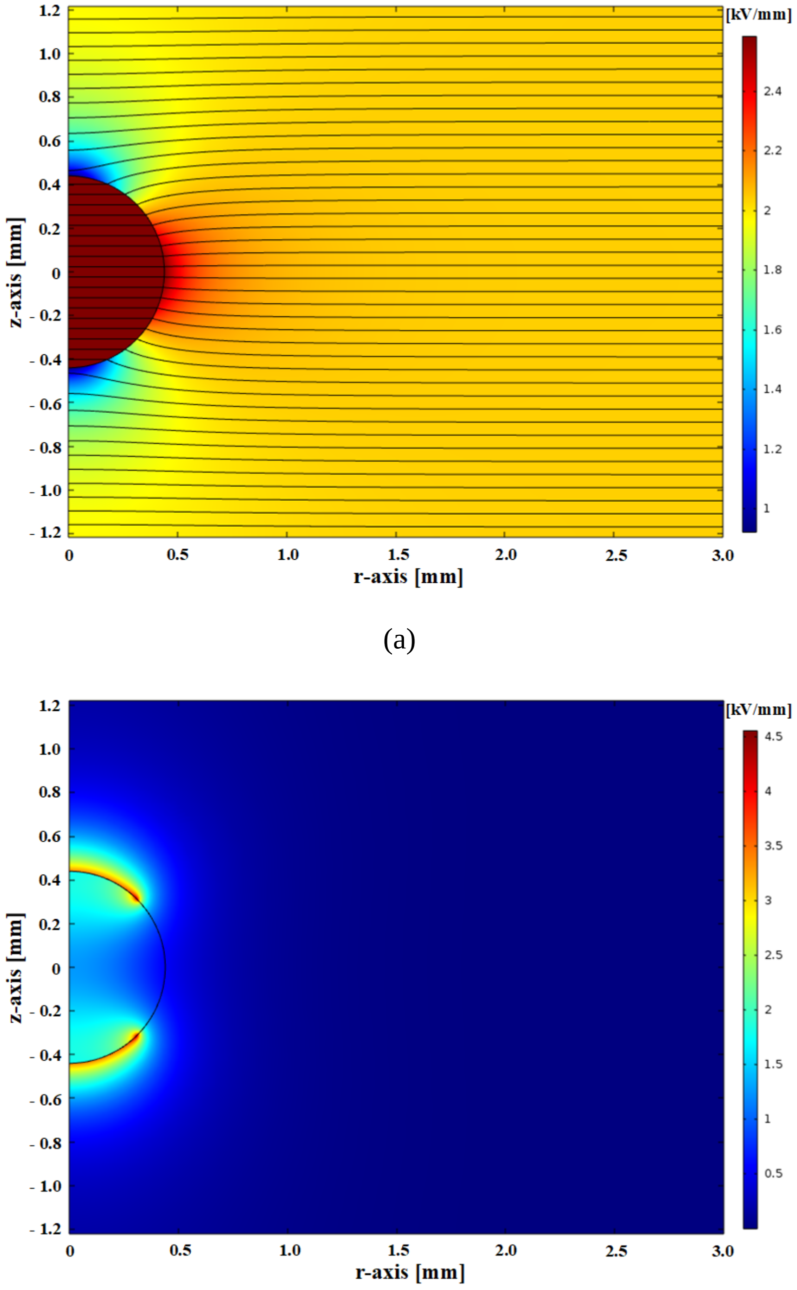

(a)

(b)

Figure C.3: Simulation of a spherical cavity in solid material for approximate apparent charge: (a) before a PD event and (b) after a PD event.

C.5 Modelling of growing electrical tree initiation from the spherical cavity wall

Based on the experiment result, the model of growing electrical tree initiation from the wall of a spherical cavity was developed as shown in Figure C.4, where the growth of electrical tree channel was located at the bottom cavity surface embedded in silicone dielectric material. The physical parameters used in this model based on the experiment result of the micrograph in Figure 5.36 (f) in Section 5.9 are listed in Table C.6. The values of electric field magnitudes within the cavity and the inside treeing channel were 6.75 kV/mm and 5.49 kV/mm respectively while the electric field magnitude within silicone dielectric material was 4.27 kV/mm. The model result shows that the electric field magnitudes inside the treeing channel were lower than the inner cavity. This model relied on the assumption that the width of electrical tree growth was significantly lower than the cavity radius. Therefore, the electrical breakdown strength in the treeing channel was lower than the cavity. Otherwise, the inner wall of treeing channel turned into the conducting surface caused by PD bombardment [252-253].

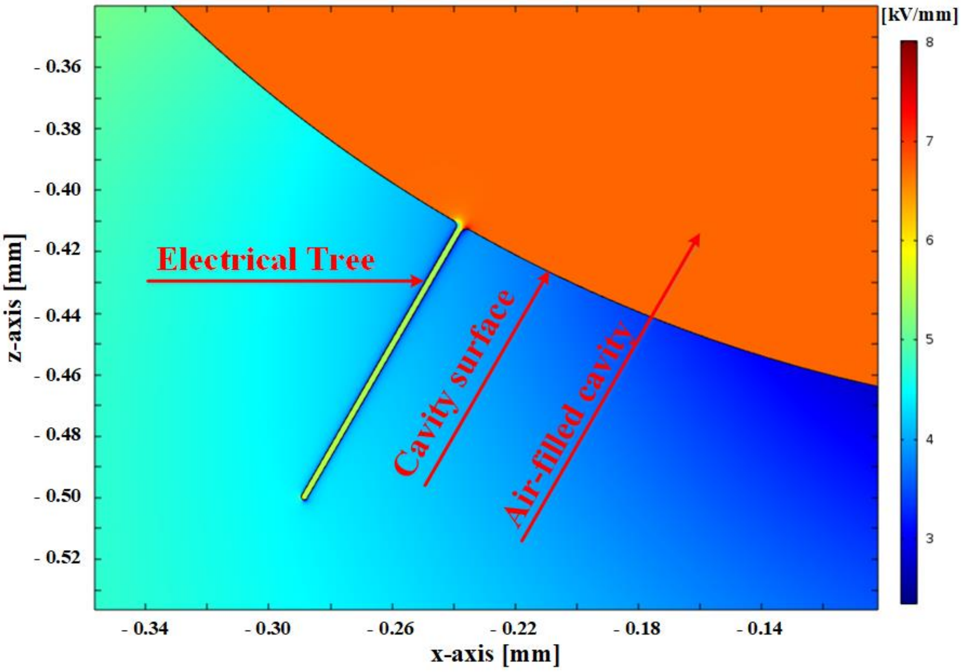

Figure C.4: Simulation of electrical tree initiation from the spherical cavity wall.

Table C.6: Physical parameters used in the model of electrical tree initiation from a spherical cavity embedded in silicone dielectric material.

Definition	Parameter	Value
Applied voltage amplitude	U_{app}	16 kV$_{rms}$
Cavity diameter	d_c	0.95 mm
Treeing length	T_L	0.1 mm
Treeing width	T_w	2.0 µm
Angle of treeing initiation in the Z-axis	T_{az}	30 degrees
Dielectric material in thickness	d_m	3.0 mm
Relative permittivity inside a cavity	ε_c	1.0
Relative permittivity inside a treeing channel	ε_T	1.0
Relative permittivity of silicone material at 50 Hz	ε_{Si}	2.8

Appendix D MATLAB Codes

D.1 MATLAB code for exporting the measured PD data

```
% Main code
clear all;
close all;
clc;

% Importing data
filedir = 'C:\Experiment Data\0001';
phase = importPHData(filedir,'0001');
[t1,q] = importQData(filedir,'0001');
[x,v] = importVData(filedir,'0001');
phase = phase * 360; % Setting phase to be between 0 and 360

% Removing the noise threshold
phase = phase(abs(q) > 1E-12);
q = q(abs(q) > 1E-12);
q = q/1E-12; % Convert to picocolombs

% Plotting 2D PRPD
plot(phase, q,'k.')
ylabel('Apparent Charge [pC]');
xlabel('Phase [Degree]');
xlim([0 360]);
grid on;

% Average and Maximum Apparent Charge [pC]
abs_q = abs(q);
Average_q = mean(abs_q)
q_max = max(abs_q)

% Number of positive and Negative PDs
number_of_PDs = length(q)
number_positive_PDs = sum(q<0)
number_negative_PDs = sum(q>0)

% 2D histogram with 500 bins for q and phase
bin_number = 500;
abs_q_x_axis=linspace(0,q_max,bin_number+1);
qstep=max(abs_q)/bin_number;
phase_y_axis=linspace(0,360,bin_number+1);
pstep=360/bin_number;
[angle_grid,abs_magnitude_grid]=meshgrid(phase_y_axis,abs_q_x_axis);
Density_grid=zeros(size(angle_grid));

for i=1:number_of_PDs
   pos1=round(abs_q(i)/qstep)+1;
   pos2=round(phase(i)/pstep)+1;

   if abs_q(i)~=0
      Density_grid(pos1,pos2)=Density_grid(pos1,pos2)+1;
   end
end
```

```
% plotting phi-q-n pattern;
contour3(angle_grid,abs_magnitude_grid,Density_grid,2*bin_number)
grid on;
colormap(jet);
shading interp
set(gca,'XTick',0:45:360)
xlabel('Phase [Degree]');
ylabel('Apparent Charge [pC]');
zlabel('Number of Discharges');
xlim([0 360]);

% Fuction import_Data_01
function [v_tm, v] = importVData(folder, vUnit);
fileName = sprintf('%s\\%s.V', folder, vUnit);
 file = fopen(fileName, 'rb');

if file == -1
   msg = sprintf('file %s could not be opened', fileName);
   error(msg);
end

fseek(file, 0, 'bof');
v = fread(file, inf, 'float32');
v_tm = 48e-6 * (0:size(v, 1) - 1);

% Fuction import_Data_02
function line_tm = importLineData(folder);
fileName = sprintf('%s\\lineTrigger.TM', folder);
file = fopen(fileName, 'rb');

if file == -1
   msg = sprintf('file %s could not be opened', fileName);
   error(msg);
end

fseek(file, 0, 'bof');
line_tm = fread(file, inf, 'float64');

% Fuction import_Data_03
function phase = importPhData(folder, qUnit);
fileName = sprintf('%s/%s.PH', folder, qUnit);
file = fopen(fileName, 'rb');

if file == -1
   msg = sprintf('file %s could not be opened', fileName);
   error(msg);
end

fseek(file, 0, 'bof');
phase = fread(file, inf, 'float64');

% Fuction import_Data_04
function [q_tm, q] = importQData(folder, qUnit);
fileName = sprintf('%s/%s.Q', folder, qUnit);
file = fopen(fileName, 'rb');

if file == -1
   msg = sprintf('file %s could not be opened', fileName);
   error(msg);
end
```

```
fseek(file, 0, 'bof');
q = fread(file, inf, 'float32', 8);
fseek(file, 4, 'bof');
q_tm = fread(file, inf, 'float64', 4);
```

D.2 MATLAB code for exporting the simulated PD data

```
clear all;
close all;
clc;

% Physical constant parameters
electron_charge =  1.6E-19; %C
phonon_frequency = 5E13; %s-1
k_b = 8.617*1e-5;  % Boltzmann constant in eV
e0= 8.85E-12; % Permittivity of free space
temp = 300; % Temperature at 300K
% Numbers from Comsol
max_applied_field_centre = -1.364E7; % in Volts per m
real_charge_per_change_in_local_field = 5.675/5.08E10;
% Free parameters (these are set so that the models match the experiment result)
% For example, simulation of rabbit-like pattern
apparent_charge_per_change_in_local_field = -1.54E-7/5.08E10;
electron_generation_constant = 1000;
tau_shallow = 2E-3; % detrappable time constant for shallow traps
tau_deep = Inf; % detrappable time constant for deep traps
shallow_fraction = 0.99; % must be between 0 and 1
e_inc = abs(max_applied_field_centre)*0.3;
e_ext = abs(max_applied_field_centre)*0.1;
grid on;

% Specify the time parameters
time_step = 1E-5;  %
ac_frequency = 50; % in Hz
omega = ac_frequency*2*pi;
ac_cycles = 30000; % setting how many AC cycles of PD activity
deep_fraction = 1-shallow_fraction;
% Initital conditions
pd_count = 0; % Count the number of PDs, initially no PDs
e_local_centre = 0; % the local electric field from charge
apparent_charge_list = []; % Record the apparent charge of PDs
phase_angle_list = []; % Record the phase angle of PDs
% Storage arrays
e_field_centre_list = zeros(round(ac_cycles/(ac_frequency*time_step)),1);
e_applied_centre_list = zeros(round(ac_cycles/(ac_frequency*time_step)),1);
e_local_centre_list = zeros(round(ac_cycles/(ac_frequency*time_step)),1);
for time_index = 1:round(ac_cycles/(ac_frequency*time_step))
    time = time_index*time_step;
```

```
    % Applied field in the centre of the void
    e_applied_centre = max_applied_field_centre*sin(omega*time);

    % Total electric field in the centre of the void
    e_field_centre = e_applied_centre + e_local_centre;

    % Store the electric fields at this time
    e_field_centre_list(time_index) = e_field_centre;
    e_applied_centre_list(time_index) = e_applied_centre;
    e_local_centre_list(time_index) = e_local_centre;

    if abs(e_field_centre) > e_inc % if the electric field is high enough

        if pd_count > 0
        % If the electric field is high enough, calculate the electron
        n_e_dot = electron_generation_constant*exp(abs(e_field_centre)/e_inc)*(shallow_fraction*...
        exp(-(time-time_last_pd)/tau_shallow) + deep_fraction*exp(-(time-time_last_pd)/tau_deep));
        else
        % For the very first electron for the first PD just let n_e_dot be random
        n_e_dot = 0.01/time_step;
        end

        if n_e_dot*time_step > rand(1) % if a free electron is available

            % Find the local electric field before PD
            e_local_centre_before_PD = e_local_centre;

            % Find the local electric field required to reduce the field to its extinction value
            e_local_centre = sign(e_field_centre)*e_ext - e_applied_centre;

            % Find the real charge from this PD
            real_charge = apparent_charge_per_change_in_local_field*...
                (e_local_centre - e_local_centre_before_PD);

            % Find the detrappable electron population after this PD
            detrappable_electron_population = abs(real_charge/electron_charge);

            % Record the apparent charge from this PD
            apparent_charge_list(end+1) = apparent_charge_per_change_in_local_field*...
                (e_local_centre - e_local_centre_before_PD);

            % Record the phase angle from this PD
            phase_angle_list(end+1) = mod(omega*time,2*pi)*180/pi;

            % Update the PD counter
            pd_count = pd_count + 1;
            time_last_pd = time;

        end
    end
end


 % Calculation and display PD statistics
 average_apparent_charge = mean(abs(apparent_charge_list*1E12));
 max_apparent_charge = max(abs(apparent_charge_list*1E12));
 pds_per_ac_cycle = pd_count/ac_cycles;
 number_of_positive_pds = sum(apparent_charge_list<0);
 average_number_of_positive_pds = number_of_positive_pds/ac_cycles;
 number_of_negative_pds = sum(apparent_charge_list>0);
 average_number_of_negative_pds = number_of_negative_pds/ac_cycles;

 fprintf('Average Apparent Charge = %f pC\n',average_apparent_charge)
 fprintf('Max Apparent Charge = %f pC\n',max_apparent_charge)
```

```
fprintf('PDs per AC cycle = %f\n',pds_per_ac_cycle)
fprintf('Positive PDS per AC cycle = %f\n',average_number_of_positive_pds)
fprintf('Negative PDS per AC cycle = %f\n',average_number_of_negative_pds)
% Plotting PRPD pattern
plot(phase_angle_list,apparent_charge_list*1E12,'k.')
xlim([0,360])
xlabel('Phase [Degree]')
ylabel('Apparent Charge [pC]')
grid on;
```

List of References

[1] L. A. Dissado and J. C. Fothergill. *Electrical Degradation and Breakdown in Polymers.* IET materials and devices series 9, The Redwood Press, Witlshire, 1992.

[2] T. Tanaka. Aging of polymeric and composite insulating materials. Aspects of interfacial performance in aging. *IEEE Transactions on Dielectrics and Electrical Insulation*, 9(5):704-716, 2002.

[3] N. Can, F. Aras, V. A. Alekperov, and A. Altindal. Investigation on aging mechanism of polyester under combined stresses. *IEEE Electrical Insulation Magazine*, 32(4):38-42, 2016.

[4] G. C Montanari. Insulation diagnosis of high voltage apparatus by partial discharge investigation. In *IEEE International Conference on Properties and Applications of Dielectric Materials (ICPADM)*, pages 1-11, 2006.

[5] C. Laurent and C. Mayoux. Partial discharge – part XI: limitations to PD as a diagnostic for deterioration and remaining life. *IEEE Electrical Insulation Magazine*, 8(2):14-17, 1992.

[6] M. Kosakia, M. Nagaob, N. Shimizuc, and Y. Mizunod. Solid insulation and its deterioration. *Cryogenics*, 38(11):1095-1104, 1998.

[7] G. C. Montanari. Partial discharge measurements: becoming a fundamental tool for quality control and risk assessment of electrical systems. In *IEEE International Symposium on Electrical Insulation (ISEI)*, pages 281-285, 2006.

[8] G. Paoletti and A. Golubev. Partial discharge theory and applications to electrical systems. In *IEEE IAS Pulp and Paper Industry Conference*, pages 124-138, 1999.

[9] B. Fruth. Partial discharge mechanisms in solid insulation systems. In *IEEE International Conference on Conduction and Breakdown in Solid Dielectrics*, pages 297-307, 1992.

[10] J. C. Fothergill, G. C. Montanari, G. C. Stevens, C. Laurent, G. Teyssedre, L. A. Dissado, U. H. Nilsson, and G. Platbrood. Electrical, microstructural, physical and chemical characterization of HV XLPE cable peelings for an electrical aging diagnostic data base. *IEEE Transactions on Dielectrics and Electrical Insulation*, 10(3):514-527, 2003.

[11] T. Tanmaneeprasert and P. L. Lewin. Electrical treeing and ageing characteristics in cavities of low density polyethylene dielectrics on partial discharge. In *IEEE Conference on Electrical Insulation and Dielectric Phenomena (CEIDP)*, pages 975-978, 2016.

[12] T. Tanmaneeprasert and P. L. Lewin. The use of partial discharge analysis for the diagnosis of electrical ageing in polymeric insulation containing cavities. In *IEEE Electrical Insulation Conference (EIC),* pages 383-387, 2016.

[13] T. Tanmaneeprasert and P. L. Lewin. Investigation into accelerated ageing and failure mechanisms of cavities in polyethylene materials using partial discharge techniques. In *IEEE Condition Monitoring and Diagnosis (CMD)*, pages 819-823, 2016.

[14] T. Tanmaneeprasert, P. L. Lewin, and G. Callender. Analysis of degradation mechanisms of silicone insulation containing a spherical cavity using partial discharge detection. In *IEEE Electrical Insulation Conference (EIC)*, pages 233-236, 2017.

[15] J. H. Mason. The deterioration and breakdown of dielectrics resulting from internal discharges. *IET Proceedings of the IEE - Part I: General*, 98(109):44-59, 1951.

[16] J. H. Mason. Breakdown of insulation by discharges. *IET Proceedings of the IEE - Part IIA: Insulating Materials*, 100(3):149-158, 1953.

[17] J. H. Mason. Discharges. *IEEE Transactions on Electrical Insulation*, EI-13(4):211-238, 1978.

[18] G. C Montanari. Fundamental research in electrical insulation and electrical asset management: Is there any link?. In *IEEE International Symposium on Electrical Insulation (ISEI)*, pages 136-147, 2008.

[19] J. H. Mason. Discharge detection and measurements: terminology. *IET Electronics and Power*, 10(9):311, 1964.

[20] P.H.F. Morshuis. *Partial discharge mechanisms: mechanisms leading to breakdown, analysed by fast electrical and optical measurements*. PhD thesis, Delft University of Technology, 1993.

[21] D. M. Hepburn. *The chemical degradation of epoxy resin by partial discharges*. PhD thesis, Glasgow Caledonian University, 1994.

[22] W. Le. *Physical model of PD behaviour and relevant damage growth from micro-cavities in polyethylene-based material under AC voltage*. PhD thesis, Università di Bologna, 2011.

[23] C. Nyamupangedengu. *PD-type-dependent spectral bandwidth in solid polymer dielectrics*. PhD thesis, University of the Witwatersrand, 2011.

[24] N. Freebody. *The use of Raman microprobe spectroscopy in the analysis of electrically aged polymeric insulators*. PhD thesis, University of Southampton, 2012.

[25] D. Adhikari. *Analysis of partial discharge activity in void defects in polymer insulation*. PhD thesis, Glasgow Caledonian University, 2013.

[26] T. Bai. *Degradation process of voids in solid dielectrics under AC applied fields*. MPhil thesis, University of Southampton, 2013.

[27] C. Chang. *Degradation by partial discharge in cavities under AC electric field*. MPhil thesis, University of Southampton, 2015.

[28] P.H.F. Morshuis and F.H. Kreuger. Transition from streamer to Townsend mechanisms in dielectric voids. *Journal of Physics D: Applied Physics*, 23(12):1562-1568, 1990.

[29] E. Gulski, P. H. F. Morshuis, and F. H. Kreuger. Conventional and time-resolved measurements of partial discharges as a tool for diagnosis of insulating materials. In *IEEE International Conference on Properties and Applications of Dielectric Material (ICPADM)*, pages 666-669, 1994.

[30] T. Tanmaneeprasert, P. L. Lewin, and J. A. Hunter. Influence of internal discharges in a cavity within polymeric insulating material caused by partial discharge mechanisms. In *IEEE Conference on Electrical Insulation and Dielectric Phenomena (CEIDP)*, pages 342-345, 2015.

[31] L. Wang, A. Cavallini, G. C. Montanari, and L. Testa, Evolution of PD patterns in polyethylene insulation cavities under AC voltage. *IEEE Transactions on Dielectrics and Electrical Insulation*, 19(2):533-542, 2012.

[32] C. S. Kim, T. Kondo, and T. Mizutani. Change in PD pattern with aging. *IEEE Transactions on Dielectrics and Electrical Insulation*, 11(1):13-18, 2004.

[33] R. Bartnikas. Partial discharges. Their mechanism, detection and measurement. *IEEE Transactions on Dielectrics and Electrical Insulation*, 9(5):763-808, 2002.

[34] Suwarno, Y. Suzuoki, F. Komori, and T. Mizutani. Partial discharges due to electrical treeing in polymers: phase-resolved and time-sequence observation and analysis. *Journal of Physics D: Applied Physics*, 29(11):2922-2931, 1996.

[35] J. Fuhr, B. Fruth, L. Niemeyer, D. Konigstein, M. Hassig, and F. Gutfleisch, “Generic procedure for classification of aged insulating system,” In *IEEE International Conference on Properties and Applications of Dielectric Material (ICPADM)*, pages 35-38, 1991.

[36] K. Wu, T. Ijichi, A. Kojima, F. Komori, and Y. Suzuoki. Influence of PD rest time on φ-q-n patterns from voids. In *IEEE International Conference on Solid Dielectrics (ICSD)*, pages 93-96, 2001.

[37] G. C. Montanari. On line partial discharge diagnosis of power cables. In *IEEE Electrical Insulation Conference (EIC)*, pages 210-215, 2009.

[38] K. Wu, Y. Suzuoki, T. Mizutani, and H. Xie. Model for partial discharges associated with treeing breakdown: III. PD extinction and re-growth of tree. *Journal of Physics D: Applied Physics*, 33(10):1209-1218, 2000.

[39] H. Kaneiwa, Y.Suzuoki, and T. Mizutani. Characteristics of partial discharges in artificial simulated tree channels during tree propagation. *IEEE Transactions on Dielectrics and Electrical Insulation*, 8(1):72-77, 2001.

[40] T. Ishida, Y. Mizuno, M. Nagao, and M. Kosaki. Development and application of partial discharge analysing system for swarming pulsive microdischarges. In *IEEE International Conference on Properties and Applications of Dielectric Material (ICPADM)*, pages 676-679, 1991.

[41] H. Kawakami, N. Kawakubo, Y. Ehara, H. Kishida, and T. Ito. Influence of swarming pulsive micro discharge on tree degradation. In *IEEE Conference on Electrical Insulation and Dielectric Phenomena (CEIDP)*, pages 979-982, 2002.

[42] M. G. Danikas. Small partial discharges and their role in insulation deterioration. *IEEE Transactions on Dielectrics and Electrical Insulation*, 4(6):863-867, 1997.

[43] F. H. Kreuger, E. Gulski, and A. Krivda. Classification of partial discharges. *IEEE Transactions on Electrical Insulation*, 28(6):917-931, 1993.

[44] S. A. Boggs. Partial discharge: overview and signal generation. *IEEE Electrical Insulation Magazine*, 6(4):33-39, 1990.

[45] M. G. Danikas. On the damage of insulating materials below inception voltage. *Journal of Electrical Engineering*, 52(11-12):367-371, 2001.

[46] S. A. Boggs. Partial discharge – part III: cavity-induced PD in Solid Dielectrics. *IEEE Electrical Insulation Magazine*, 6(6):11-16, 1990.

[47] C. Mayoux and C. Laurent. Contribution of partial discharges to electrical breakdown of solid insulating materials. *IEEE Transactions on Dielectrics and Electrical Insulation*, 2(4):641-652, 1995.

[48] K. Wu, Y. Suzuoki, T. Mizutani, and H. Xie. A novel physical model for partial discharge in narrow channels. *IEEE Transactions on Dielectrics and Electrical Insulation*, 16(2):181-190, 1999.

[49] U. Bammert and M. Beyer. Partial discharges measured with an automated system in epoxy resin and polyethylene. *IEEE Transactions on Electrical Insulation*, 23(2):215-225, 1988.

[50] K. Wu, Y. Suzuoki, T. Mizutani, and H. Xie. Model for partial discharges associated with treeing breakdown: II. Tree growth affected by PDs. *Journal of Physics D: Applied Physics*, 33(10):1202-1208, 2000.

[51] P. H. F. Morshuis. Partial discharge mechanisms in voids related to dielectric degradation. *IEE Proceedings – Science, Measurement and Technology,* 142(1):62-68, 1995.

[52] B. A. Fruth and D. W. Gross. Modelling of streamer discharges between insulating and conducting surfaces. In *IEEE International Conference on Conduction and Breakdown in Solid dielectrics*, pages 350-355, 1995.

[53] Y. Murooka, T. Takada, and K. Hiddaka. Nanosecond surface discharge and charge density evaluation part I: review and experiments. *IEEE Electrical Insulation Magazine*, 17(2):6-16, 2001.

[54] R. J. Van Brunt. Physics and chemistry of partial discharge and corona. *IEEE Transactions on Dielectrics and Electrical Insulation*, 1(5):761-784, 1994.

[55] L. Niemeyer, L. Ullrich, and N. Wiegart. The mechanism of leader breakdown in electronegative gases. *IEEE Transactions on Electrical Insulation*, 24(2):309-324, 1989.

[56] P.H.F. Morshuis. Degradation of solid dielectrics due to internal partial discharge: Some thoughts on progress made and where to go now. *IEEE Transactions on Dielectrics and Electrical Insulation*, 12(5):905-913, 2005.

[57] K. Temmen. Evaluation of surface changes in flat cavities due to ageing by means of phase-angle resolved partial discharge measurement. *Journal of Physics D: Applied Physics*, 33(6):603-608, 2000.

[58] T. Tanaka. Internal partial discharges and material degradation. *IEEE Transactions on Electrical Insulation*, EI-21(6):899-905, 1986.

[59] F. H. Kreuger. *Partial discharge detection in high-voltage equipment*. Butterworths, London, 1989.

[60] G. C. Crichton, A. Karlsson, and A. Pedersen. A theoretical derivation of the transients related to partial discharges in ellipsoidal voids. In *IEEE International Symposium on Electrical Insulation (ISEI)*, pages 238-241, 1988.

[61] K. Tsuruta and H. Ebara. Modeling of gas temperature decay after arc discharge in small air gaps. *IEEE Transactions on Electrical Insulation*, 27(3):309-324, 1992.

[62] H. Raether. *Electron avalanches and breakdown in gases*. Butterworths, London, 1964.

[63] L. B. Loeb and J. M. Meek. The mechanism of spark discharge in air at atmospheric pressure. I. *Journal of Applied Physics*, 11(438):438-447, 1940.

[64] A. Pedersen. On the electrical breakdown of gaseous dielectrics-an engineering approach. *IEEE Transactions on Electrical Insulation*, 24(5):721-739, 1989.

[65] F. L. Jones. Ionization processes in the electrical breakdown of gases. *British Journal of Applied Physics*. 5(2):49-53, 1954.

[66] R. Arora and W. Mosch. *High voltage and electrical insulation engineering*. John Wiley & Sons, Hoboken, 2011.

[67] J. M. Meek and J. D. Craggs. *Electrical breakdown of gases*. Clarendon Press, Oxford, 1953.

[68] M. Hoof and R. Patsch. A physical model, describing the nature of partial discharge pulse sequences. In *IEEE International Conference on Properties and Applications of Dielectric Material (ICPADM)*, pages 283-286, 1997.

[69] P. Morshuis and L. Niemeyer. Measurement and simulation of discharge induced ageing processes in voids. In *IEEE Conference on Electrical Insulation and Dielectric Phenomena (CEIDP)*, pages 520-524, 1996.

[70] B. Fruth and L. Niemeyer. The importance of statistical characteristics of partial discharge data. *IEEE Transactions on Electrical Insulation*, 27(1):60-69, 1992.

[71] L. Niemeyer. A generalized approach to partial discharge modeling. *IEEE Transactions on Dielectrics and Electrical Insulation*, 2(4):510-528, 1995.

[72] F. Gutfleisch and L. Niemeryer. Measurement and simulation of PD in epoxy voids. *IEEE Transactions on Dielectrics and Electrical Insulation*, 2(5):729-743, 1995.

[73] A. Cavallini, F. Ciani, and G. C. Montanari. Improved identification level for defects generating partial discharges in solid insulation systems. In *IEEE Conference on Electrical Insulation and Dielectric Phenomena (CEIDP)*, pages 422-425, 2004.

[74] E. Kuffel, W. Zaengl, and J. Kuffel. *High Voltage Engineering: Fundamentals*. Butterworth Heinemann, 2000.

[75] S. A. Boggs and G. C. Stone. Fundamental limitations in the measurement of corona and partial discharge. *IEEE Transactions on Electrical Insulation*, EI-17(2):143-150, 1982.

[76] J. C. Devins. The 1984 J. B. Whitehead memorial lecture the physics of partial discharges in solid dielectrics. *IEEE Transactions on Electrical Insulation*, EI-19(5):475-495, 1984.

[77] I. W. McAllister. Decay of charge deposited on the wall of a gaseous void. *IEEE Transactions on Electrical Insulation*, 27(6):1202-1207, 1992.

[78] K. Wu, C. Pan, Y. Meng, and Y. Cheng. Dynamic behavior of surface charge distribution during partial discharge sequences. *IEEE Transactions on Dielectrics and Electrical Insulation*, 20(2):612-619, 2013.

[79] C. Pan, Y. Meng, and K. Wu. Variation of surface charge distribution in the process of PD degradation. *In IEEE International Symposium on Electrical Insulating Materials (ISEIM)*, pages 117-120, 2011.

[80] C. Pan, K. Wu, Y. Meng, Y. Cheng, and J. Tang. The effect of discharge area variation on stochastic characters of PD magnitude. *IEEE Transactions on Dielectrics and Electrical Insulation*, 24(1):217-226, 2017.

[81] C. Hudon, R. Bartnikas, and M. R. Wertheimer. Spark-to-glow discharge transition due to increased surface conductivity on epoxy resin specimens. *IEEE Transactions on Electrical Insulation*, 28(1):1-8, 1993.

[82] P. H. F. Morshuis and F. H. Kreuger. The evolution of the discharge mechanism in a dielectric bounded cavity due to surface effects. In *IEEE International Conference on Properties and Applications of Dielectric Material (ICPADM)*, pages 672-675, 1991.

[83] H. A. Illias. Measurement and simulation of partial discharges within a spherical cavity in a solid dielectric material. PhD thesis, University of Southampton, 2011.

[84] A. C. Gjaerde and J. Sletbak. Influence of partial discharges on void gas pressure. In *IET International Conference on Partial Discharge*, pages 119-120, 1993.

[85] R. Candela, R. Schifani, and P. Romano. Optimisation of a numerical model for analysis of partial discharge phenomena in a flat cavity. In *IEEE Conference on Electrical Insulation and Dielectric Phenomena (CEIDP)*, pages 689-692, 2001.

[86] A. C. Gjaerde. A phenomenological aging model for combined thermal and electrical stress. *IEEE Transactions on Dielectrics and Electrical Insulation*, 4(6):674-680, 1997.

[87] L. Wang, A. Cavallini, and G. C. Montanari. Time behavior of gas pressure and PD activity in insulation cavities under AC voltage. In *IEEE Conference on Electrical Insulation and Dielectric Phenomena (CEIDP)*, pages 1-4, 2010.

[88] P. H. F. Morshuis and F. H. Kreuger. The spatial distribution and electrical parameters of partial discharges in polyethylene insulation during ageing. In *IEEE International Conference on Conduction and Breakdown in Solid Dielectrics*, pages 209-214, 1992.

[89] H. Ichikawa, K. Ito, Y. Suzuoki, T.Mizutani, and K. Uchida. Partial discharge patterns and degradation diagnosis in polyethylene and polyimide. In *IEEE International Conference on Properties and Applications of Dielectric Materials (ICPADM)*, pages 630-633, 1994.

[90] D. W. Gross and B. A. Fruth. Characteristics of phase resolved partial discharge pattern in spherical voids. In *IEEE Conference on Electrical Insulation and Dielectric Phenomena (CEIDP)*, pages 412-415, 1998.

[91] A. Cavallini and G. C. Montanari. Effect of supply voltage frequency on testing of insulation system. *IEEE Transactions on Electrical Insulation*, 13(1):111-121, 2006.

[92] F. J. Wester, E. Gulski, and J. J. Smit. Detection of partial discharges at different AC voltage stresses in power cables. *IEEE Electrical Insulation Magazine*, 23(4):28-43, 2007.

[93] A. C. Gjaerde. Measurements of void gas pressure during combined thermal and partial discharge ageing of epoxy. *IEE Proceedings – Science, Measurement and Technology*, 142(1):17-21, 1995.

[94] A. C. Gjaerde. The combined effect of partial discharges and temperature on void surfaces. In *IEEE Conference on Electrical Insulation and Dielectric Phenomena (CEIDP)*, pages 550-553, 1997.

[95] R.Schifani, R. Candela, and P. Romano. On PD mechanisms at high temperature in voids included in an epoxy resin. *IEEE Transactions on Dielectrics and Electrical Insulation*, 8(4):589-597, 2001.

[96] H. A. Illias, G. Ghen, and P. L. Lewin. Partial discharge within a spherical cavity in a dielectric material as a function of cavity size and material temperature. *IET Science, Measurement & Technology*, 6(2):52-62, 2012.

[97] J. Sletbak. The influence of cavity shape and sample geometry on partial discharge behavior. *IEEE Transactions on Electrical Insulation*, 3(1):126-130, 1996.

[98] A. Cavallini, M. Conti, G. C. Montanari, and A. Contin. Indexes for the recognition of insulation system defects derived from partial discharge measurements. In *IEEE International Symposium on Electrical Insulation (ISEI)*, pages 511-515, 2002.

[99] G. Ueta, J. Wada, S. Okabe, M. Miyashita, C. Nishida, and M. Kamei. Insulation performance of three types of micro-defects in inner epoxy insulators. *IEEE Transactions on Dielectrics and Electrical Insulation*, 19(3):947-954, 2012.

[100] K. Nakao, T. Kondo, Y. Suzuoki, and T. Mizutani. φ-q-n patterns and current shapes of partial discharges in void. In *IEEE International Symposium on Electrical Insulating Materials (ISEIM)*, pages 665-668, 1998.

[101] A. Krivda and E. Gulski. Influence of aging on classification of partial discharges in cavities. *Japanese Journal of Applied Physics*, 33(10):5942-5949, 1994.

[102] G. C. Montanari, A. Cavallini, and F. Ciani. Partial discharges in internal voids: dependence on defect position with respect to electrodes. In *IEEE Conference on Electrical Insulation and Dielectric Phenomena (CEIDP),* pages 175-178, 2007.

[103] H. Ichikawa, K. Ito, Y. Suzuoki, T.Mizutani, and K. Uchida. Partial discharge patterns and their temporal change in polyethylene and polyimide. Effects of sample condition, chemical structure and gap atmosphere. In *IEEE Conference on Electrical Insulation and Dielectric Phenomena (CEIDP)*, pages 143-148, 1994.

[104] D. Adhikari, D. M. Hepburn, and B. G. Stewart. Comparison of partial discharge characteristics and degradation in several polymeric insulators. *IET Science, Measurement & Technology,* 6(6):474-484, 2012.

[105] J. M. Braun and J. H. Groeger. Determination of gases and gas pressure in GIS spacer voids. In *IEEE Conference on Electrical Insulation and Dielectric Phenomena (CEIDP)*, pages 105-110, 1989.

[106] M. Hikita, M. Kozako, H. Takada, M. Higashiyama, T. Hirose, S. Nakamura, and T. Umemura. Partial discharge phenomena in artificial cavity in epoxy cast resin insulation system. In *IEEE International Symposium on Electrical Insulation (ISEI)*, pages 1-5, 2010.

[107] S. Boggs and J. Densley. Fundamentals of partial discharge in the context of field cable testing. *IEEE Electrical Insulation Magazine*, 16(5):13-18, 2000.

[108] H. N. O, T. R. Blackburn, B. T. Phung, H. Zhang and R. H. Khawaja. Investigation of electric field distribution in power cables with voids. In *IEEE International Conference on Properties and Applications of Dielectric Materials (ICPADM),* pages 637-640, 2006.

[109] G. C. Crichton, P. W. Karlsson, and A. Pedersen. Partial discharges in ellipsoidal and spheroidal voids. *IEEE Transactions on Electrical Insulation*, 24(2):335-342, 1989.

[110] E. Lemke. A critical review of partial-discharge models. *IEEE Electrical Insulation Magazine*, 28(6):11-16, 2012.

[111] W. Hauschild and E. Lemke. *High-voltage test and measuring techniques*. Springer Heidelberg, 2014.

[112] IEC-60270 (Std.): High-voltage test techniques – Partial discharge measurements, 2000.

[113] M. Conti. *Development of artificial intelligence systems for electrical insulation defect identification through partial discharge measurements*. Ph.D. thesis, University of Bologna, 2003.

[114] G. C. Montanari, A. Cavallini, and F. Ciani. Partial discharges in internal voids: Dependence on defect position with respect to electrodes. In *IEEE Conference on Electrical Insulation and Dielectric Phenomena (CEIDP)*, pages 175-178, 2007.

[115] M. Florkowski and B. Florkowska. Phase-resolved rise-time-based discrimination of partial discharges. *IET Generation, Transmission & Distribution*, 3(1):115-124, 2009.

[116] T. Mizutani, T. Kondo, and K. Nakao. Change in partial discharge properties of a void in LDPE. In *IEEE Conference on Electrical Insulation and Dielectric Phenomena (CEIDP)*, pages 257-260, 1999.

[117] K. Wu, F. Komori, and Y. Suzuoki. Effects of oxygen on the formation of rabbit-like PD pattern in a void between metal surfaces. In *IEEE International Symposium on Electrical Insulating Materials (ISEIM)*, pages 37-40, 2001.

[118] K.Wu and Y. Suzuoki. Effects of discharge area on PD patterns in voids. In *IEEE Conference on Electrical Insulation and Dielectric Phenomena (CEIDP)*, pages 227-230, 1999.

[119] N. Hozumi, H. Nagae, Y. Muramoto, M. Nagao, and H. Xie. Time-lag measurement of void discharges and numerical simulation for clarification of the factor for partial discharge pattern. In *IEEE International Symposium on Electrical Insulating Materials (ISEIM)*, pages 29-32, 2001.

[120] Z. Nawawi, Y. Murakami, N. Hozumi, and M. Nagao. Effect of humidity on time lag of partial discharge in insulation gap insulation system. In *IEEE 8th International Conference on Properties and Applications of Dielectric Materials (ICPADM)*, pages 199-203, 2006.

[121] A. Syakur and Suwarno. The influences of humidity on PD characteristics in a void in polyvinyl chloride (PVC). In *IEEE 8th International Conference on Properties and Applications of Dielectric Materials (ICPADM)*, pages 494-497, 2006.

[122] G. Bahder, T. Garrity, M. Sosnowski, R. Eaton, and C. Katz. Physical model of electric aging and breakdown of extruded polymeric insulated power cables. *IEEE Transactions on Power Apparatus and Systems*, PAS-101(6):1379-1390, 1982.

[123] Suwarno, H. Ichikawa, Y. Suzuoki, T. Mizutani, and K. Uchida. Partial discharge patterns of electrical treeing in polyethylene. In *IEEE International Conference on Properties and Applications of Dielectric Materials (ICPADM)*, pages 379-382, 1994.

[124] Y. Ehara, H. Kishida, and T. Ito. Prediction of tree initiation by phase angle analysis of discharge magnitude and discharge luminescence on partial discharge. In *IEEE Conference on Electrical Insulation and Dielectric Phenomena (CEIDP)*, pages 321-324, 2000.

[125] K. Wu, Y. Suzuoki, T. Mizutani, and H. Xie. Model for partial discharges associated with treeing breakdown: I. PDs in tree channels. *Journal of Physics D: Applied Physics*, 33(10):1197-1201, 2000.

[126] N. Hattori, Y. Ehara, H. Kishida, and T. Ito. Pit observation and partial discharge measurement before tree initiation. In *IEEE Conference on Electrical Insulation and Dielectric Phenomena (CEIDP)*, pages 938-941, 2002.

[127] H. Kaneiwa, Y. Suzuoki, and T. Mizutani. Partial discharge characteristics and tree inception in artificial simulated tree channels. *IEEE Transactions on Dielectrics and Electrical Insulation*, 7(6):843-848, 2000.

[128] C. S. Brazel and S. L. Rosen. *Fundamental principles of polymeric materials*. John Wiley and Sons, New Jersey, 2012.

[129] T. A. Osswald and G. Menges. *Materials science of polymers for engineers*. Carl Hanser Verlag, Munich, 2012.

[130] P. C. Painter, and M. M. Coleman. *Essentials of polymer science and engineering*. DEStech, Lancaster, Pennsylvania, 2009.

[131] D. Raabe. Mesoscale simulation of spherulite growth during polymer crystallization by use of a cellular automation. *Acta Materialia*, 52(9):2653-2664, 2004.

[132] J. P. Jones, J. P. Llewellyn, and T. J. Lewis. The contribution of field-induced morphological change to the electrical aging and breakdown of polyethylene. *IEEE Transactions on Dielectrics and Electrical Insulation*, 12(5):951-966, 2005.

[133] R. R. Levier, M. C. Harrison, R. R. Cook, and T. H. Lane. What is silicone?. *Journal of Clinical Epidemiology*, 48(4):513-517, 1995.

[134] G. C. Montanari and L. Simoni. Aging phenomenology and modeling. *IEEE Transactions on Electrical Insulation*, 28(5):755-776, 1993.

[135] T. W. Dakin. Electrical insulation deterioration treated as a chemical rate phenomenon. *IEEE Transactions of the American Institute of Electrical Engineers*, 67(1):113-122, 1948.

[136] L. Simoni. A new approach to the voltage-endurance test on electrical insulation," *IEEE Transactions on Electrical Insulation*. EI-8(3):76-86, 1973.

[137] G. C. Montanari. Notes on theoretical and practical aspects of polymeric insulation aging. *IEEE Electrical Insulation Magazine*, 29(4):34-44, 2013.

[138] A. C. Gjaerde. Multi factor ageing models-origin and similarities. In *IEEE Conference on Electrical Insulation and Dielectric Phenomena (CEIDP)*, pages 199-204, 1995.

[139] L. A. Dissado, J. C. Fothergill, S. V. Wolfe, and R. M. Hill. Weibull statistics in dielectric breakdown; theoretical basis, applications and implications. *IEEE Transactions on Electrical Insulation*, EI-19(3):227-233, 1984.

[140] P. Cygan and J. R. Laghari. Models for insulation aging under electrical and thermal multistress. *IEEE Transactions on Electrical Insulation*, 25(5):923-934, 1990.

[141] G. C. Montanari. Aging and life models for insulation systems based on PD detection. *IEEE Transactions on Dielectrics and Electrical Insulation*, 2(4):667-675, 1995.

[142] A. Contin, E. Gulski, M. Cacciari, and G. C. Montanari. A weibull approach to the investigation of partial discharges in aged insulation systems. In *IEEE International Symposium on Electrical Insulation (ISEI)*, pages 416-419, 1996.

[143] P. Dejean, N. Foulon, M. Goldman, and H. Dejean. Chemical aspects of the ageing of solid insulating materials submitted to partial discharges. In *IEEE International Conference on Conduction and Breakdown in Solid Dielectrics*, pages 181-185, 1992.

[144] G. C. Montanari, A. Motori, A. T. Bulinski, S. S. Bamji, and J. Densley. Application of oxidation induction time and compensation effect to the diagnosis of HV polymeric cable insulation. *IEEE Transactions on Dielectrics and Electrical Insulation*, 3(3):351-360, 1996.

[145] C. Hudon, R. Bartnikas, and M. R. Wertheimer. Chemical and physical degradation effects on epoxy surfaces exposed to partial discharges. In *IEEE International Conference on Properties and Applications of Dielectric Materials (ICPADM)*, pages 811-814, 1994.

[146] T. Tanaka. Tree initiation mechanisms. In *IEEE International Conference on Properties and Applications of Dielectric Materials (ICPADM)*, pages 18-24, 1991.

[147] C. J. Mayoux. Partial-discharge phenomena and the effect of their constituents on polyethylene. *IEEE Transactions on Electrical Insulation*, EI-11(4):139-149, 1976.

[148] Y. Sekii, K. Hirota, and N. Chizuwa. Effects of antioxidants on electrical tree generation in XLPE. In *IEEE International Conference on Solid Dielectrics (ICSD)*, pages 460-464, 2001.

[149] H. Uehara, Y. Sekii, T. Takada, and Y. Cao. Analysis of electrical tree inhibitory effect by antioxidants using quantum chemical calculation. In *IEEE Conference on Electrical Insulation and Dielectric Phenomena (CEIDP)*, pages 1021-1024, 2016.

[150] J. M. Schultz (Ed.). *Properties of solid polymeric materials: treatise on materials science and technology*. Academic Press, New York, 1977.

[151] G. Mazzanti, G. C. Montanari, and S. Serra. Aging model of polyethylene-based materials for HV cables founded on damage inception and growth from air-filled voids. In *IEEE International Conference on Solid Dielectrics (ICSD)*, pages 525-529, 2004.

[152] L. A. Dissado. Understanding electrical trees in solids: from experiment to theory. *IEEE Transactions on Electrical Insulation*, 9(4):483-497, 2002.

[153] N. Shimizu and K. Horii. The effect of absorbed oxygen on electrical treeing in polymers. *IEEE Transactions on Electrical Insulation*, EI-20(3):561-566, 1985.

[154] N. Shimizu and C. Laurent. Electrical tree initiation. *IEEE Transactions on Dielectrics and Electrical Insulation*, 5(5):651-659, 1998.

[155] K. Uchida, H. Asai, N. Shimizu, and T. Takahashi. Initiation mechanism of electrical tree and deteriorated region in polymers. In *IEEE International Conference on Properties and Applications of Dielectric Materials (ICPADM)*, pages 240-243, 1991.

[156] C. Hudon, R. Bartnikas, and M. R. Wertheimer. Surface conductivity of epoxy specimens subjected to partial discharges. In *IEEE International Symposium on Electrical Insulation (ISEI)*, pages 153-155, 1990.

[157] C. Hudon, R. Bartnikas, and M. R. Wertheimer. Analysis of degradation products on epoxy surfaces subjected to pulse and glow type discharges. In *IEEE Conference on Electrical Insulation and Dielectric Phenomena (CEIDP)*, pages 237-243, 1991.

[158] S. I. Reynolds. On the behavior of natural and artificial voids in insulation under internal discharge. *IEEE Transactions of the American Institute of Electrical Engineers, Part III: Power Apparatus and Systems*, 77(3):1604-1608, 1958.

[159] N. S. Tomer, F. Delor-Jestin, L. Frezet, and J. Lacoste. Oxidation, chain scission and cross-linking studies of polysiloxanes upon ageings. *Open Journal of Organic Polymer Materials*, 2(2):13-22, 2012.

[160] C. Batich, D. DePalma, J. Marotta, and G. Latorre. Silicone degradation reactions. *Immunology of Silicones*, 120:13-23, 1996.

[161] K. D. Wolter, J. F. Johnson, and J. Tanaka. Degradation product analysis for polymeric dielectric materials exposed to partial discharges. *IEEE Transactions on Electrical Insulation*, 13(5):327-336, 1978.

[162] K. Chrzan and J. M. Andino. Electrical strength of air containing ozone and nitric oxides produced by intensive partial discharges. *IEEE Transactions on Dielectrics and Electrical Insulation*, 8(4):607-611, 2001.

[163] X. Zhao and Q. Wang. Harnessing large deformation and instabilities of soft dielectrics: theory, experiment, and application. *Applied Physics Reviews 1*, 021304:1-24, 2014.

[164] Q. Wang, L. Zhang, and X. Zhao. Creasing to cratering instability in polymers under ultrahigh electric fields. *Physical Review Letters*, 106(11), 118301:1-4, 2011.

[165] J. H. Mason. Breakdown of solid dielectrics in divergent fields. *IET Proceedings of the IEE – Part C: Monographs*, 102(2):254-263, 1955.

[166] L. A. Dissado and P. J. J. Sweeney. Physical model for breakdown structures in solid dielectrics. *Physical Review B*, 48(22):16261-16268, 1993.

[167] R. Patsch. Electrical and water treeing: a chairman's view. *IEEE Transactions on Electrical Insulation*, 27(3):532-542, 1992.

[168] S. B. Hobdell, S. P. Mainwaring, and R. N. Hampton. An investigation of the factors affecting the growth of bow tie water trees in XLPE insulation systems. In *IEE International Conference on Dielectric Materials, Measurements and Applications*, pages 47-52, 2000.

[169] J. Xu and A. Garton. The chemical composition of water trees in EPR cable insulation. *IEEE Transactions on Dielectrics and Electrical Insulation*, 1(1):18-24, 1994.

[170] L. Huimin, B. Crichton, R. Fouracre, A. Kenwright, and B. Say. An investigation into morphological changes in water treed LDPE. In *IEEE International Conference on Conduction and Breakdown in Solid Dielectrics*, pages 378-382, 1992.

[171] K. Nakamura, M. Hotta, C. shinoda, T. Hashizume, and T. Tani. Influence of bow-tie trees on residual breakdown voltage of dry-cured XLPE power cables after accelerated water immersion aging test. *IEEE International Conference on Properties and Applications of Dielectric Materials (ICPADM)*, pages 363-366, 1994.

[172] R. M. Eichhorn. Treeing in solid extruded electrical insulation. *IEEE Transactions on Electrical Insulation*, EI-12(1):2-18, 1976.

[173] M. S. Mashikian and A. Szarkowski. Medium voltage cable defects revealed by off-line partial discharge testing at power frequency. *IEEE Electrical Insulation Magazine*, 22(4):24-32, 2006.

[174] G. Bahder, T. Garrity, M. Sosnowski, R. Eaton, and C. Katz. Physical model of electric aging and breakdown of extruded polymeric insulated power cables. *IEEE Transaction on Power Apparatus and System*, PAS-101(6):1379-1390, 1982.

[175] R. Vogelsang, T. Farr, and K. Fröhlich. The effect of barriers on electrical tree propagation in composite insulation materials. *IEEE Transactions on Dielectrics and Electrical Insulation*, 13(1):373-382, 2006.

[176] B. X. Du, Z. L. Ma, and Y. Gao. Phenomena and mechanism of electrical tree in silicone rubber. In *IEEE International Conference on Properties and Applications of Dielectric Materials (ICPADM)*, pages 37-40, 2009.

[177] J. C. Fothergill, L. A. Dissado, and P. J. J. Sweeney. A discharge-avalanche theory for the propagation of electrical trees. *IEEE Transactions on Dielectrics and Electrical Insulation*, 1(3):474-486, 1994.

[178] A. S. Vaughan, I. L. Hosier, S. J. Dodd, and S. J. Sutton. On the structure and chemistry of electrical trees in polyethylene. *Journal of Physics D: Applied Physics*, 39(5):962-978, 2006.

[179] N. Rouha and A. Beroual. Physico-chemical diagnosis of EPDM electrical aging by tree phenomenon. *IEEE Transactions on Dielectrics and Electrical Insulation*, 20(5):1577-1583, 2013.

[180] Goodfellow Cambridge Ltd. (2016, January 16). Material properties, Available online: http://www.goodfellow.com.

[181] Ellsworth Adhesives Ltd. (2016, September 12). Products, TDS library, Available online: https://www.ellsworth.com.

[182] J. H. Mason. Enhancing the significance of PD measurements. *IEEE Transactions on Dielectrics and Electrical Insulation*, 2(5):876-888, 1995.

[183] P. Wang, P. L. Lewin, and S. J. Sutton. Calibration of capacitive couplers for online PD detection in HV cables. *IEEE Electrical Insulation Magazine*, 21(3):28-39, 2005.

[184] W. S. Zaengl. Dielectric spectroscopy in time and frequency domain for HV power equipment, I: Theoretical considerations. *IEEE Electrical Insulation Magazine*, 19(5):5-19, 2003.

[185] J. L. Parpal, E. David, G. Delmas, and H. Phuong-Nguyen. DSC measurements on XLPE cables at low and high heating/cooling rates. In *IEEE Conference on Electrical Insulation and Dielectric Phenomena (CEIDP)*, pages 775-780, 1993.

[186] L. Boukezzi, A. Boubakeur, C. Laurent, and M. Lallouani. DSC study of artificial thermal aging of XLPE insulation cables. In *IEEE International Conference on Solid Dielectrics (ICSD)*, pages 146-149, 2007.

[187] H. Czichos, T. Saito, and L. Smith (Eds.). *Springer handbook of materials measurement methods*. Springer, Heidelberg, 2006.

[188] T. D'Amico, C. J. Donahue, and E. A. Rais. Thermal analysis of plastics. *Journal of Chemical Education*, 85(3):404-407, 2008.

[189] C. Chen, Z. Jia, W. Ye, Z. Guan, and Y. Li. Thermo-oxidative aging analysis of HTV silicone rubber used for outdoor insulation. *IEEE Transactions on Dielectrics and Electrical Insulation*, 24(3):1761-1772, 2017.

[190] J. V. Gulmine, P. R. Janissek, H. M. Heise, and L. Akcelrud. Polyethylene characterization by FTIR. *Polymer Testing*, 21(5):557-563, 2002.

[191] P. R. Griffiths. *Infrared and Raman instrumentation for mapping and imaging*. *R. Salzer, et al. (eds.), Infrared and Raman spectroscopic imaging*, Wiley-VCH, Weinheim, 2009.

[192] W. R. C. Somerville, E. C. Le Ru, P. T. Northcote, and P. G. Etchegoin. High performance Raman spectroscopy with simple optical components. *American Journal of Physics*, 78(7):671-677, 2010.

[193] N. A. Freebody, A. S. Vaughan, and A. M. Macdonald. On optical depth profiling using confocal Raman spectroscopy. *Analytical and Bioanalytical Chemistry*, 396(8):2813-2823, 2010.

[194] M. Procházka. *Surface-enhanced Raman spectroscopy, Bioanalytical, Biomolecular and Medical Applications*. Springer, Switzerland, 2016.

[195] J. I. Goldstein, D. E. Newbury, D. C. Joy, C. E. Lyman, P. Echlin, E. Lifshin, L. Sawyer, and J. R. Michael. Scanning electron microscopy and X-ray microanalysis, Springer, America, 2003.

[196] H. Schatten. *The role of scanning electron microscopy in cell and molecular biology: SEM basics, past accomplishments, and new frontiers, Scanning electron microscopy for the life sciences*, Cambridge University Press, New York, 2012.

[197] F. Komori, M. Hikita, Y. Suzuoki, and T. Mizutani. Study of partial discharge occurrence patterns for construction of degradation diagnosis system. In *IEEE International Conference on Properties and Applications of Dielectric Materials (ICPADM)*, pages 224-227, 1997.

[198] P. Morshuis. Assessment of dielectric degradation by ultrawide-band PD detection. *IEEE Transactions on dielectrics and electrical insulation*, 2(5):744-760, 1995.

[199] G. Garcia and C. Mayoux. Some observations on artificial cavities in a cross-linked polyethylene. In *IEEE International Conference on Properties and Applications of Dielectric Materials (ICPADM)*, pages 430-433, 1988.

[200] Y. Suzuoki, Y. Kodani, F. Komori, and T. Kato. Relation between concentration of partial discharge and surface degradation and breakdown. In *IEEE Conference on Electrical Insulation and Dielectric Phenomena (CEIDP)*, pages 404-407, 2008.

[201] L. Wang, A. Cavallini, G. C. Montanari, A. Vaughan, and N. Freebody. PD-induced surface degradation of insulation embedded cavities: microscopic investigation. *IEEE International Symposium on Electrical Insulating Materials (ISEIM)*. pages 121-124, 2011.

[202] T. Liu, J. Fothergill, S. Dodd, L. Dissado, U. H. Nilsson, M. Fu, and F. Perrot. Dielectric spectroscopy study of thermally-aged extruded model power cables. *IEEE International Conference on Solid Dielectrics (ICSD)*, pages 1-4, 2010.

[203] Y. C. Kim, W. AHN, and C. Y. Kim. A study on multiple melting of isotactic polypropylene. *Polymer Engineering and Science*, 37(6):1003-1011, 1997.

[204] N. Shimizu, K. Uchida, and S. Rasikawan. Electrical tree and deteriorated region in polyethylene. *IEEE Transactions on Electrical Insulation*, 27(3):513-518, 1992.

[205] Y. Sekii. Degradation of low-density polyethylene and cross-linked polyethylene by partial discharge. *IEEE Transactions on Electrical Insulation*, 17(1):116-124, 2010.

[206] D. L. Pavia, G. M. Lampman, and G. S. Kriz. *Introduction to spectroscopy: a guide for students of organic chemistry*, Thomson Learning, 2001.

[207] J. B. Lambert, H. F. Shurvell, D. A. Lightner, and R. G. Cooks. *Organic structural spectroscopy*. Prentice-Hall, New Jersey, 1998.

[208] G. C. Montanari, A. Cavallini, L. Testa, S. Serra, and L. A. Dissado. Model of ageing inception and growth from microvoids in polyethylene-based materials under AC voltage. In *IEEE Conference on Electrical Insulation and Dielectric Phenomena (CEIDP)*, pages 29-32, 2008.

[209] K. Wu, Y. Suzuoki, and L. A. Dissado. The contribution of discharge area variation to partial discharge patterns in disc-voids. *Journal of Physics D: Applied Physics*, 37(13):1815-1823, 2004.

[210] T. Mizutani and T. Kondo. PD patterns and PD current shapes of a void in LDPE. In *IEEE International Conference on Properties and Applications of Dielectric Material (ICPADM)*, pages 276-279, 2000.

[211] H. V. P. Nguyen, B. T. Phung, and T. Blackburn. Effects of aging on partial discharge patterns in voids under very low frequency excitation. In *IEEE International Conference on Dielectrics (ICD)*, pages 524-527, 2016.

[212] L. Wang, A. Cavallini, G. C. Montanari, and L. Testa. Patterns of partial discharge activity in XLPE: from inception to breakdown. In *IEEE International Conference on Solid Dielectrics (ICSD)*, pages 1-4, 2010.

[213] K. Wu, H. Xie, Y. Suzuoki, and T. Mizutani. The effect of conductivity distribution in tree channel on PD behavior in electrical tree. In *IEEE International Symposium on Electrical Insulating Materials (ISEIM)*, pages 701-704, 1998.

[214] S. M. Lebedev and E. Gockenbach. Tree-inception in the three-layer dielectrics. In *IEEE Conference on Electrical Insulation and Dielectric Phenomena (CEIDP)*, pages 645-648, 2003.

[215] D. P. Agoris, V. I. Chichikin, O. S. Gefle, S. M. Lebedev, and I. Vitellas. The breakdown study of three-layer solid dielectrics. In *IEEE International Conference on Solid Dielectrics (ICSD)*, pages 434-437, 2011.

[216] E. Gulski and A. Krivda. Influence of aging on classification of PD in HV components. *IEEE Transactions on Dielectrics and Electrical Insulation*, 2(4):676-684, 1995.

[217] A. Krivda and E. Gulski. Classification of discharge patterns during ageing of insulation. In *IEEE International Conference on Conduction and Breakdown in Solid Dielectrics*, pages 254-258, 2002.

[218] T. Kalicki, J. M. Braun, J. Densley, and H. G. Sedding. Pulse-shape characteristics of partial discharge within electrical trees in polymeric materials. In *IEEE Conference on Electrical Insulation and Dielectric Phenomena (CEIDP),* pages 380-383, 1995.

[219] K. Imai. Relationship between surface discharge of Gleitbüschel-type in an artificial void and pit formation. In *IEEE Conference on Electrical Insulation and Dielectric Phenomena (CEIDP)*, pages 141-144, 2003.

[220] G. J. Paoletti and A. Golubev. Partial discharge theory and technologies related to medium voltage electrical equipment. *IEEE Transactions on Industry Applications*, 37(1):90-103, 2001.

[221] M. Budde and M. Kurrat. Partial discharge diagnostics of micro cavities in epoxy insulating materials and their modelling. *IEEE International Symposium on Electrical Insulation (ISEI)*, pages 369-372, 2008.

[222] M. G. Danikas and G. E. Vardakis. The case of Pedersen's theory to model partial discharges in cavities enclosed in solid insulation: a criticism of some of its aspects from an electrical engineers' and from a physicists' point of view. *Journal of Electrical Engineering*, 52(5-6):166-170, 2001.

[223] R. Bodega, P. H. F. Morshuis, M. Lazzaroni, and F. J. Wester. PD recurrence in cavities at different energizing methods. *IEEE Transactions on Instrumentation and Measurement*, 53(2):251-258, 2004.

[224] P. Morshuis, A. Cavallini, G. C. Montanari, F. Puletti, and A. Contin. The behavior of physical and stochastic parameters from partial discharges in spherical voids. In *IEEE International Conference on Properties and Applications of Dielectric Material (ICPADM)*, pages 304-309, 2000.

[225] Z. Lei, J. Song, M. Tian, X. Cui, C. Li, and M. Wen. Partial discharges of cavities in ethylene propylene rubber insulation. *IEEE Transactions on Dielectrics and Electrical Insulation*, 21(4):1647-1659, 2014.

[226] H. B. Burgener, T. H. Teich, and K. Frohlich. Simulations of partial discharges of small microcracks parallel to the electrical field in polymeric materials. In *IEEE Conference on Electrical Insulation and Dielectric Phenomena (CEIDP)*, pages 146-150, 2002.

[227] H. Illias, G. Ghen, and P. L. Lewin. Modeling of partial discharge activity in spherical cavities within a dielectric material. *IEEE Electrical Insulation Magazine*, 27(1):38-45, 2011.

[228] A. Cavallini, R. Ciani, M. Conti, P.F.H. Morshuis, and G. C. Montanari. Modeling memory phenomena for partial discharge processes in insulation cavities. In *IEEE Conference on Electrical Insulation and Dielectric Phenomena (CEIDP)*, pages 723-727, 2003.

[229] H. A. Illias, G. Chen, and P. L. Lewin, The influence of spherical cavity surface charge distribution on the sequence of partial discharge events. *Journal of Physics D: Applied Physics*, 44(24):1-15, 2011.

[230] T. Bai and P. L. Lewin. Degradation behaviour of voids in silicone rubber under applied AC electric fields. In *IEEE Conference on Electrical Insulation and Dielectric Phenomena (CEIDP)*, pages 589-592, 2012.

[231] K. X. Lai, A. Lohrasby, B. T. Phung, and T. R. Blackburn. Partial discharge characteristics of electrical trees prior to breakdown. In *IEEE International Symposium on Electrical Insulating Materials (ISEIM)*, pages 649-652, 2008.

[232] A. Krivda and E. Gulski. Influence of aging on classification of partial discharges in cavities. *Japanese journal of Applied Physics*, 33(10):5942-5949, 1994.

[233] D. M. Ryder. The interpretation of partial electrical discharge measurements with insulation damage and ageing. In *IEEE Conference on Electrical Insulation and Dielectric Phenomena (CEIDP)*, pages 642-647, 1993.

[234] T. Ishida, Y. Mizuno, M. Nagao, and M. Kosaki. Development and application of partial discharge analyzing system for swarming pulsive microdischarges. In *IEEE International Conference on Properties and Applications of Dielectric Material (ICPADM)*, pages 676-679, 1991.

[235] G. Callender, P. Rapisarda, and P. L. Lewin. Investigation of void erosion on partial discharge activity using simulation. In *IEEE International Conference on Dielectrics (ICD)*, pages 1-4, 2016.

[236] T. Shahsavarian and S. M. Shahrtash. Modelling of aged cavities for partial discharge in power cable insulation. *IET Science, Measurement & Technology*, 9(6):661-670, 2015.

[237] T. Ebke, A. Khaddour, and D. Peier. Degradation of silicone gel by partial discharges due to different defects. In *IEE International Conference on Dielectric Materials, Measurements and Applications*, pages 202-207, 2000.

[238] N. A. Freebody, A. S. Vaughan, and P. L. Lewin. Raman microprobe analysis and ageing in dielectrics. *Journal of Physics: Conference Series*, 183(1):1-5, 2009.

[239] N. A. Freebody, I. L. Hosier, and A. S. Vaughan. Raman microprobe analysis of electrical treeing in silicone rubber. In *IEEE International Symposium on High Voltage Engineering (ISH)*, pages 1-6, 2011.

[240] A. H. Kuptsov and G. N. Zhizhin. *Handbook of fourier transform Raman and infrared spectra of polymers*. Elsevier Science, The Netherlands, 1998.

[241] R. L. McCreery. *Raman spectroscopy for chemical analysis*. John Wiley & Sons, New York, 2000.

[242] M. Batalović, K. Sokolija, M. Hadžialić, and N. Batalović. Partial discharges and IEC standards 60840 and 62067: simulation support to encourage changes. *Scientific Journal Technical Gazette*, 23(2):589-598, 2016.

[243] M. G. Danikas, and G. Adamidis. Partial discharges in epoxy resin voids and the interpretational possibilities and limitations of Pedersen's model. *Electrical Engineering,* 80(2):105-110, 1997.

[244] I. J. S. Lopes, S. H. Jayaram, and E. A. Cherney. A study of partial discharges from water droplets on a silicone rubber insulating surface. *IEEE Transactions on Dielectrics and Electrical Insulation*, 8(2):262-268, 2001.

[245] H. Homma, T. Kuroyagi, K. Izumi, C. L. Mirley, J. Ronzello, and S. A. Boggs. Evaluation on surface degradation of silicone rubber using thermogravimetric analysis. In *IEEE International Symposium on Electrical Insulating Materials (ISEIM)*, pages 631-634, 1998.

[246] H. Liu, G. Cash, D. Birtwhistle, and G. George. Characterization of a severely degraded silicone elastomer HV insulator – an aid to development of lifetime assessment techniques. *IEEE Transactions on Dielectrics and Electrical Insulation*, 12(3):478-486, 2005.

[247] S. A. Shcherbanev, I. U. Nadinov, P. Auvray, S. M. Starikovskaia, S. Pancheshnyi, and L. G. Herrmann. Emission spectroscopy of partial discharges in air-filled voids in unfilled epoxy. *IEEE Transactions on Plasma Science*, 44(7):1219-1227, 2016.

[248] A. Toth, I. Bertoti, M. Blazso, G. Banhegyi, A. Bognar, and P. Szaplonczay. Oxidative damage and recovery of silicone rubber surface. I. X-ray photoelectron spectroscopic study. *Journal of Applied Polymer Science*, 52(9):1293-1307, 1994.

[249] H. Hillborg and U. W. Gedde. Hydrophobicity changes in silicone rubbers. *IEEE Transactions on Dielectrics and Electrical Insulation*, 6(5):703-717, 1999.

[250] Suwarno. A comparison between void and electrical treeing discharges in polyethylene. In *IEEE International Conference on Properties and Applications of Dielectric Material (ICPADM)*, pages 493-496, 2000.

[251] Y. Kitamura and S. Hirabayashi. Partial discharge deterioration of epoxy resin for electronic parts. In *IEEE Conference on Electrical Insulation and Dielectric Phenomena (CEIDP)*, pages 485-490, 1985.

[252] T. Kalicki, J. M. Braun, J. Densley, and H. G. Sedding. Pulse-shape characteristics of partial discharge within electrical trees in polymeric materials. In *IEEE Conference on Electrical Insulation and Dielectric Phenomena (CEIDP)*, pages 380-383, 1995.

[253] T. Tanmaneeprasert, P. L. Lewin, and G. Callender. Measuring and simulating partial discharge activity in a spherical cavity during electrical ageing processes. In *IEEE International Conference on Dielectrics (ICD)*, pages 1-4, 2018.

[254] C. Chang, T. Bai, P. L. Lewin, P. H. F. Morshuis, J. A. Pilgrim, A. Cavallini, A. S. Vaughan, G. C. Montanari, and S. Serra. Developing an experimental method for a cavity PD based life model. In *IEEE International Conference on Solid Dielectrics (ICSD)*, pages 780-783, 2013.

[255] J. A. Hunter, L. Hao, D. J. Swaffield, P. L. Lewin, N. Cornish, C. Walton, and M. Michel. Partial discharge in medium voltage three-phase cables. In *IEEE International Symposium on Electrical Insulation (ISEI)*, pages 1-5, 2010.

[256] D. Götz, F. Petzold, H. Putter, S. Markalous, and M. Stephan. Localized PRPD pattern for defect recognition on MV and HV cables. In *IEEE Transmission and Distribution Conference and Exposition (T&D)*, pages 1-4, 2016.

[257] D. I. Bower and W. F. Maddams. *The vibrational spectroscopy of polymers*. Cambridge University Press, New York, 1989.

[258] X. S. Liu, A. S. Vaughan, and G. Ghen. A Raman spectroscopic study of bulk and surface ageing phenomena in polyethylene. In *IEEE Conference on Electrical Insulation and Dielectric Phenomena (CEIDP)*, pages 145-148, 2003.

[259] G. Callender, P. L. Lewin, J. A. Hunter, and P. Rapisarda. Modeling partial discharge in a three-phase cable joint experiment with minimal adjustable parameters. *IEEE Transactions on Dielectrics and Electrical Insulation*, 24(1):279-287, 2017.